

**NIST GCR 09-927**

# **Fire Safety Risks Associated With Leaks in Hydrogen Systems**



**NIST GCR 09-927**

# **Fire Safety Risks Associated With Leaks in Hydrogen Systems**

Prepared for  
*National Institute of Standards and Technology  
Building and Fire Research Laboratory  
Gaithersburg, MD 20899-8202*

By  
Peter B. Sunderland  
*Department of Fire Protection Engineering  
University of Maryland  
College Park, MD 20742*

Grant 60NANB5D1209

December 2009



**U.S. DEPARTMENT OF COMMERCE**  
*Gary Locke, Secretary*

**NATIONAL INSTITUTE OF STANDARDS AND TECHNOLOGY**  
*Patrick D. Gallagher, Director*

### Notice

This report was prepared for the Building and Fire Research Laboratory of the National Institute of Standards and Technology under grant number 60NANB5D1209. The statements and conclusions contained in this report are those of the authors and do not necessarily reflect the views of the National Institute of Standards and Technology or the Building and Fire Research Laboratory.

## **Final Report**

### **Fire Safety Risks Associated with Leaks in Hydrogen Systems**

Grant number: 60NANB5D1209

Grant PI: P.B. Sunderland

Awarded by: National Institute of Standards and Technology  
Building and Fire Research Laboratory  
Gaithersburg, Maryland

Submitted by: P.B. Sunderland  
Assistant Professor  
Department of Fire Protection Engineering  
University of Maryland  
pbs@umd.edu

Submission date: November 18, 2009

Grant period: September 1, 2005 – August 31, 2009

Investigators: Peter B. Sunderland, University of Maryland (PI)  
Richard L. Axelbaum, Washington University (Co-I)  
Beei-Huan Chao, University of Hawaii (Co-I)

NIST Contact: Jiann Yang

## 1. Motivation

Hydrogen presents several unusual fire hazards, including high leak propensity, ease of ignition, and invisible flames. This research concerns experiments, analysis, and computations to identify the hazards of leaks in hydrogen systems that could result in combustion. The work seeks to identify the types of hydrogen leaks that can support flames. A small leak in a hydrogen system could ignite easily, support a flame that is difficult to detect, and lead to a catastrophic failure.

## 2. Objectives

This research seeks an improved understanding of hydrogen fire safety that will lead to hazard reduction in hydrogen systems. Specific objectives include:

1. Measure limits of flaming (at ignition, quenching and blowoff) for hydrogen issuing from circular and slot burners of various sizes.
2. Measure flame quenching limits of hydrogen leaks in plumbing components.
3. Examine material degradation arising from an impinging hydrogen diffusion flame.
4. Prepare analytical and models of spontaneous ignition.
5. Perform CFD analyses of the flames to complement the experiments, yield additional physical insight, and allow the consideration of untested conditions.

## 3. Summary of Progress

- The investigator team has published in *Combustion Theory and Modeling* a manuscript entitled *A Theoretical Study of Spontaneous Ignition of Fuel Jets in an Oxidizing Ambient with Emphasis on Hydrogen Jets*. This paper is attached here in Appendix A.
- The investigator team has published in the *International Journal of Hydrogen Energy* a manuscript entitled *Limits for Hydrogen Leaks that Can Support Stable Flames*. This paper is attached here in Appendix A.
- To date 15 papers and posters on this work have been published at conferences.
- To date 17 oral presentations on this work have been presented. These have been in the U.S., Canada, U.K., and Germany. Six of these presentations have been by graduate students.
- To date one Ph.D. Dissertation and four M.S. Theses have been published on this work.
- An analysis was performed for the spontaneous ignition of a hydrogen (or other gaseous fuel) jet emanating from a slot into an oxidizing ambient (e.g., air). A similarity solution of the flow field was obtained. This was combined with the species and energy conservation equations, which were solved using activation energy asymptotics. Limits of spontaneous ignition were identified as functions of slot width, flowrate, and temperatures of the hydrogen jet and ambient gas. Two scenarios are examined: a cool jet flowing into a hot ambient and a hot jet flowing into a cool ambient. For both scenarios, ignition is favored with an increase of either the ambient temperature or the hydrogen supply temperature. Moreover, for the hot ambient scenario, a decrease in fuel Lewis number also promotes ignition. The Lewis number of the oxidizer only has a weak effect on ignition. Because spontaneous ignition is very sensitive to temperature, ignition is expected to occur near the edge of the jet if the hydrogen is cooler than the ambient gas and near the centerline if the hydrogen is hotter than the ambient gas.
- Quenching and blowoff limits of hydrogen diffusion flames on small burners were observed. Four burner types, with diameters as small as 8  $\mu\text{m}$ , were considered: pinhole burners, curved-wall burners, tube burners, and leaky fittings. In terms of mass flow rate, hydrogen

had a lower quenching limit and a higher blowoff limit than either methane or propane. Hydrogen flames at their quenching limits were the weakest flames recorded to date, with mass flow rates and heat release rates as low as 3.9 mg/s and 0.46 W. The quenching limit for a hydrogen flame at a 6 mm leaky compression fitting was found to be 28 mg/s. This limit was independent of supply pressure (up to 131 bar) and about an order of magnitude lower than the corresponding limits for methane and propane.

- The quenching limit measurements from this project were incorporated into the new SAE J2579 standard for hydrogen vehicles. Hydrogen vehicles for U.S. use will now be required to demonstrate that localized leaks are smaller than our measured quenching limits. We have requested that a similar provision be added to the new NFPA 2, Hydrogen Technologies Code.
- Flames with heat release rates as low as 0.25 W have been observed and photographed. These are believed to be the weakest flames ever observed. The work has applications to fire safety and microcombustors.
- Materials degradation upon exposure to hydrogen diffusion flames has been observed. Hydrogen flames were observed to be more corrosive to metals and silicon carbide fibers than methane flames were.

#### **4. Peer-Reviewed Journal Papers (see full text in Appendix A)**

1. K.B. Lim, B.H. Chao, P.B. Sunderland, R.L. Axelbaum, *A Theoretical Study of Spontaneous Ignition of Fuel Jets in an Oxidizing Ambient with Emphasis on Hydrogen Jets*, **Combustion Theory and Modeling**, 12 (2008) 1179-1196.
2. M.S. Butler, C.W. Moran, P.B. Sunderland, R.L. Axelbaum, *Limits for Hydrogen Leaks that Can Support Stable Flames*, **International Journal of Hydrogen Energy** 34 (2009) 5174-5182.
3. V.R. Lecoustre, C.W. Moran, P.B. Sunderland, B.H. Chao, R.L. Axelbaum, *Experimental and Numerical Investigation of Extremely Weak Hydrogen Diffusion Flames*, **Combustion Symposium**, in preparation.

#### **5. Conference Proceedings and Posters**

1. N.R. Morton, P.B. Sunderland, B.H. Chao, R.L. Axelbaum, *Fire Hazards of Small Hydrogen Leaks*, poster, Bridging the Transition...Hydrogen Internal Combustion Engines Symposium, weststart.org, San Diego (2006).
2. N.R. Morton, P.B. Sunderland, B.H. Chao, R.L. Axelbaum, *Fire Safety Risks Associated with Leaks in Hydrogen Systems*, poster, Annual Fire Conference, NIST, Gaithersburg (2006).
3. M.S. Butler, C.W. Moran, P.B. Sunderland, R.L. Axelbaum, *Quenching Limits of Hydrogen Diffusion Flames*, Eastern States Section of the Combustion Institute, Charlottesville (2007) 8 pp.
4. K.B. Lim, B.H. Chao, P.B. Sunderland, R.L. Axelbaum *An Asymptotic Analysis of Spontaneous Ignition of Hydrogen Jets*, 5<sup>th</sup> U.S. Combustion Meeting, San Diego, 11 pp. (2007).
5. N.R. Morton, P.B. Sunderland, B.H. Chao, R.L. Axelbaum, *Fire Hazards of Small Hydrogen Leaks*, SAE World Congress, Detroit, SAE Paper 2007-01-0429, 4 pp. (2007).
6. N.R. Morton, P.B. Sunderland, B.H. Chao, R.L. Axelbaum, *Fire Hazards of Small Hydrogen Leaks*, The National Hydrogen Association Annual Conference, San Antonio (2007) 8 pp.

7. N.R. Morton, P.B. Sunderland, B.H. Chao, R.L. Axelbaum, *Quenching Limits and Materials Degradation of Hydrogen Diffusion Flames*, 5<sup>th</sup> U.S. Combustion Meeting, San Diego, 8 pp. (2007).
8. M.S. Butler, R.L. Axelbaum, C.W. Moran, P.B. Sunderland, *Flame Quenching Limits of Hydrogen Leaks*, SAE World Congress, Detroit, SAE Paper 2008-01-0726 (2008) 8 pp.
9. M.S. Butler, C.W. Moran, P.B. Sunderland, R.L. Axelbaum, *Fire Safety of Hydrogen Leaks*, Second International Energy 2030 Conference, Abu Dhabi (2008) 10 pp.
10. M.S. Butler, C.W. Moran, P.B. Sunderland, R.L. Axelbaum, *Fire Hazards of Small Leaks in Hydrogen Systems*, Poster, International Association of Fire Safety Science, Karlsruhe (2008).
11. C.W. Moran, M.S. Butler, P.B. Sunderland, B.H. Chao, R.L. Axelbaum, Observations of Normal Gravity Flames that are Weaker than Microgravity Flame Balls, Poster, 32nd International Symposium on Combustion, Montreal (2008).
12. P.B. Sunderland, *Fire Hazards of Small Hydrogen Leaks*, 3<sup>rd</sup> European Summer School on Hydrogen Safety, Ulster (2008) 34 pp.
13. P.B. Sunderland, *Pressure Relief Devices for Hydrogen Vehicles*, 3<sup>rd</sup> European Summer School on Hydrogen Safety, Ulster (2008) 20 pp.
14. V.R. Lecoustre, C.W. Moran, P.B. Sunderland, B.H. Chao, R.L. Axelbaum, *Experimental and Numerical Investigation of Extremely Weak Hydrogen Diffusion Flames*, 6<sup>th</sup> U.S. National Combustion Meeting, Ann Arbor (2009) 12 pp.
15. P.B. Sunderland, *American Perspectives and Regulations for Hydrogen Vehicles*, Progress in Hydrogen Safety Short Course, Ulster (2009) 20 pp.
16. P.B. Sunderland, *Hydrogen Flame Quenching Limits, Extinction, and Materials Degradation*, Progress in Hydrogen Safety Short Course, Ulster (2009) 33 pp.

## 6. Oral Presentations

1. N.R. Morton, *Quenching Limits and Materials Degradation of Hydrogen Diffusion Flames*, 5<sup>th</sup> U.S. Combustion Meeting, San Diego, March 27, 2007.
2. K.B. Lim, *An Asymptotic Analysis of Spontaneous Ignition of Hydrogen Jets*, 5<sup>th</sup> U.S. Combustion Meeting, San Diego, March 28, 2007.
3. P.B. Sunderland, *Quenching, Blowoff, and Spontaneous Ignition Limits of Hydrogen Flames and Jets*, Oral Presentation, NIST Annual Fire Conference, Gaithersburg, April 4, 2007.
4. P.B. Sunderland, *Fire Hazards of Small Hydrogen Leaks*, SAE World Congress, Detroit, April 16, 2007.
5. M.S. Butler, *Quenching Limits of Hydrogen Diffusion Flames*, Eastern States Section of the Combustion Institute, Charlottesville. October 24, 2007.
6. P. B. Sunderland, *Quenching Limits and Materials Degradation of Flaming Hydrogen Leaks*, Department of Mechanical Engineering, University of Texas at Austin, March 18, 2008.
7. P. B. Sunderland, *Fire Hazards of Hydrogen Leaks*, Austin / San Antonio SFPE Chapter, San Marcos, Texas, March 19, 2008.
8. P.B. Sunderland, *Fire Hazards of Hydrogen Leaks*, National Institute of Standards and Technology Annual Fire Conference, Gaithersburg, March 31, 2008.
9. M.S. Butler, *Flame Quenching Limits of Hydrogen Leaks*, SAE World Congress, Detroit, April 15, 2008.
10. P.B. Sunderland, *Pressure Relief Devices for Hydrogen Vehicles*, 3<sup>rd</sup> European Summer School on Hydrogen Safety, Belfast, July 23, 2008.

11. P.B. Sunderland, *Fire Hazards of Small Hydrogen Leaks*, 3<sup>rd</sup> European Summer School on Hydrogen Safety, Belfast, July 23, 2008.
12. P.B. Sunderland, *Fire Hazards of Vehicles Powered by Alternative Fuels Including Hydrogen, CNG, and Electricity*, DC Section of SAE, U.S. Department of Transportation, Washington, Oct. 23, 2008.
13. P.B. Sunderland, *Fire Hazards of Small Hydrogen Leaks*, Johns Hopkins University, Dept. of Mechanical Engineering, Baltimore, Oct. 24, 2008.
14. V.R. Lecoustre, *Experimental and Numerical Investigation of Hydrogen Flame Quenching Limits*, National Institute of Standards and Technology Annual Fire Conference, Gaithersburg, April 29, 2009.
15. P.B. Sunderland, *American Perspectives and Regulations for Hydrogen Vehicles*, Progress in Hydrogen Safety Short Course, Belfast, April 30, 2009.
16. P.B. Sunderland, *Hydrogen Flame Quenching Limits, Extinction, and Materials Degradation*, Progress in Hydrogen Safety Short Course, Belfast, May 1, 2009.
17. V.R. Lecoustre, *Experimental and Numerical Investigation of Extremely Weak Hydrogen Diffusion Flames*, 6<sup>th</sup> U.S. National Combustion Meeting, Ann Arbor, May 18, 2009.

## **7. Theses and Dissertations**

1. Michael S. Butler, *Flame Quenching and Materials Degradation of Hydrogen Leaks*, M.S. Thesis, Department of Mechanical and Aerospace Engineering, Washington University in St. Louis, 50 pp., May, 2008.
2. Vivien R. Lecoustre, *Numerical Investigations of Gaseous Spherical Diffusion Flames*, Ph.D. Dissertation, UMD Department of Mechanical Engineering, anticipated December, 2009.
3. Kian Boon Lim, *An Asymptotic Analysis of Spontaneous Ignition of Hydrogen Jets*, M.S. Thesis, UMD Department of Fire Protection Engineering, 64 pp., May, 2007.
4. Christopher W. Moran, *Flame Quenching Limits of Hydrogen Leaks*, M.S. Thesis, UMD Department of Fire Protection Engineering, 48 pp., May, 2008.
5. Nicholas R. Morton, *Quenching Limits and Materials Degradation of Hydrogen Diffusion Flames*, M.S. Thesis, UMD Department of Fire Protection Engineering, 49 pp., May, 2008.

## **8. Service and Award**

1. Peter B. Sunderland, Excellence in Oral Presentation, for *Fire Hazards of Small Hydrogen Leaks*, SAE World Congress, Detroit, 2007.
2. Peter B. Sunderland, Editorial Co-Chair, Hydrogen Vehicle Fire Safety, SAE World Congress, 2008.

## **APPENDIX A**

### **Reprints of Publications**

## Quenching limits of hydrogen diffusion flames

*M.S. Butler<sup>1</sup>, C.W. Moran<sup>2</sup>, P.B. Sunderland<sup>2</sup>, R.L. Axelbaum<sup>1</sup>*

<sup>1</sup>*Dept. of Energy, Environmental, and Chemical Engineering, Washington Univ., St. Louis MO  
63130, USA*

<sup>2</sup>*Dept. of Fire Protection Engineering, Univ. of Maryland, College Park MD 20742, USA*

This study examines the types of hydrogen leaks that can support combustion. Hydrogen, methane, and propane diffusion flames on round burners and leaky compression fittings were observed. Measurements included limits of quenching and blowoff for round burners with diameters of 0.006 - 3.175 mm. The measured mass flow rates at the quenching limits were found to be generally independent of burner diameter. In terms of mass flow rate, hydrogen had the lowest quenching limit and the highest blowoff limit of the fuels considered. The quenching limits for hydrogen diffusion flames on round burners with thick walls were found to be higher than for thin walls. The minimum mass flow rate of hydrogen that can support combustion from a leaking compression fitting was found to be independent of pressure and about an order of magnitude lower than the corresponding methane and propane flow rates. The implications for fire safety are discussed.

### **Introduction**

Concerns about the emissions of greenhouse gases have led to extensive consideration of hydrogen as an energy carrier. Hydrogen presents several unusual fire hazards, including high leak propensity, ease of ignition, and invisible flames. The scenario of interest in this work is that a small leak in a hydrogen system might ignite, support a flame that is difficult to detect, and degrade containment materials to the point of a catastrophic failure. This study includes experiments and analysis to identify which hydrogen leaks can support flames.

A Department of Energy report [1] found that hydrogen containment was the chief safety concern associated with using hydrogen as a transportation fuel and documented several catastrophic hydrogen fires.

Quenching and blowoff limits bound the leak flow rates that can support combustion. Measurements of propane quenching and blowoff flow rates were made by Matta et al. [2]. Quenching limits for methane were performed by Cheng et al. [3]. Blowoff measurements for hydrogen, methane and propane were performed by Kalghatgi [4].

Research has been done in evaluating leak flow rates of hydrogen, methane, and propane. Swain and Swain [5] modeled and measured leak rates for diffusion, laminar, and turbulent flow regimes. They found that combustible mixtures in an enclosed space resulted more quickly for propane and hydrogen leaks than for methane leaks. Their supply pressures were the same for all fuels.

Thus motivated, the objectives of this work are to measure limits of sustained combustion, both

at quenching and blowoff, for hydrogen on round burners and lower flaming limits for hydrogen, methane and propane on leaky compression fittings.

### Flame Quench Scaling

A scaling analysis was developed to interpret measured flame quenching limits. These limits are the minimum flow rates required to support a diffusion flame.

The stoichiometric length  $L_f$  of laminar gas jet diffusion flames on round burners is:

$$L_f/d = a Re = a \rho u_0 d / \mu, \quad (1)$$

where  $d$  is the burner inside diameter,  $a$  is a dimensionless fuel-specific empirical constant,  $Re$  is Reynolds number,  $u_0$  is the average fuel velocity in the burner,  $\rho$  is fuel density, and  $\mu$  is fuel dynamic viscosity. The scaling of Eq. (1) arises from many theoretical and experimental studies, including Roper [6], Sunderland et al. [7], and references cited therein. Constant  $a$  here is assigned values measured by Sunderland et al. [7], as listed in Table 1.

The base of an attached jet diffusion flame is quenched by the burner. Its standoff distance can be approximated as one half of the quenching distance of a stoichiometric premixed flame. Such quenching distances typically are reported as the minimum tube diameter,  $L_q$ , through which a premixed flame can pass. It is assumed here that a jet flame can be supported only if its stoichiometric length is greater than half this quenching distance:

$$L_f \geq L_q / 2. \quad (2)$$

Measurements of  $L_q$ , shown in Table 1, are taken from Kanury [8]. When combined, Eqs. (1) and (2) predict the following fuel flow rate,  $m_{fuel}$ , at the quenching limit:

$$m_{fuel} = \pi \rho u_0 d^2 / 4 = \pi L_q \mu / (8 a). \quad (3)$$

Equation (3) indicates that the fuel mass flow rate at the quenching limit is a fuel property that is independent of burner diameter. When values of  $L_q$ ,  $\mu$ , and  $a$  from Table 1 are inserted into Eq. (3), the predicted fuel flow rates at quenching shown in Table 1 are obtained.

**Table 1: Selected fuel properties of hydrogen, methane, and propane. Values for  $a$  are from Sunderland et al. [7],  $L_q$  and  $S_L$  are from Kanury [8], and  $\mu$  is from Weast and Astle [9].**

Fuel	$a$	$L_q$ [mm]	$S_L$ [cm/s]	$\mu$ [g/m-s]	$m_{fuel}$ [mg/s] predicted
H <sub>2</sub>	0.236	0.51	291	8.76e-3	0.008
CH <sub>4</sub>	0.136	2.3	37.3	1.09e-2	0.085
C <sub>3</sub> H <sub>8</sub>	0.108	1.78	42.9	7.95e-3	0.063

### Experimental

Two different burner configurations are considered here: round burners and leaky compression fittings.

There is generally a limited range of flow rates for which a flame can be established on the present burners. Above this range, the flow is said to be above its blowoff limit. This limit occurs when the flow velocity in the flammable region of the flame becomes greater than the burning

velocity of the mixture. Below this range, the flow is said to be below the quenching limit. Quenching occurs when there is too much heat loss for combustion to be sustained.

### Round Burners

Three different types of round burners were considered for this work: tube burners, pinhole burners, and curved-wall pinhole burners. Each had a range of flow passage diameters. All tests were performed at ambient lab pressure, and flow was delivered via a pressure regulator and a flow controlling valve.

The tube burners were made from stainless steel hypodermic tubes, oriented vertically. Tube inside diameters were 0.006, 0.016, 0.033, 0.047, and 0.087 mm. These burners resemble microinjectors that may be used in future, small scale microelectromechanical power generators [7].

The pinhole burners were stainless steel nozzles that are manufactured for solid-stream spray generation. The top of all the burners except the two smallest ones is a curved surface with a hole passing through its axis as shown in Figure 1. The two smallest burners had holes in planar, not curved, surfaces. It is expected that the variation of quenching flow rate as a result of this slight curvature is on the order of the error associated with measurement. The hole diameters were 0.008, 0.127, 0.356, 0.530, 0.711, 0.838, 1.016, 1.397, 1.778, 2.388, and 3.175 mm.

The curved-wall pinhole burners were constructed of stainless steel tubes with two outside diameters: 1.59 and 6.35 mm. A radial hole was drilled in each tube. Hole sizes were 0.406, 0.533, 0.737, 0.864, and 1.016 mm (small tubes) and 0.406, 1.753, 2.464 and 3.124 mm (large tubes).

Figure 1 shows a false-color image of a hydrogen flame on a 0.356 mm pinhole burner just prior to extinction. The photo was taken in a dimly lit room with an f-number of 4.2,  $f/4.2$ , and an exposure time of 30 s. The flame was still very faint after using these settings, so a digital contrast enhancement was applied. The hydrogen quenching distance of Table 1 suggests that steady hydrogen diffusion flames should be anchored about 0.25 mm above the burner surface. Figure 1 shows this is reasonable for the present flames near their quenching limits.

Certain complications are unique to these experiments. The present small flow rates could not be accurately measured using conventional flow meters. Instead, a glass soap-bubble meter was installed upstream of the burners. Tests performed with varying air moisture contents found

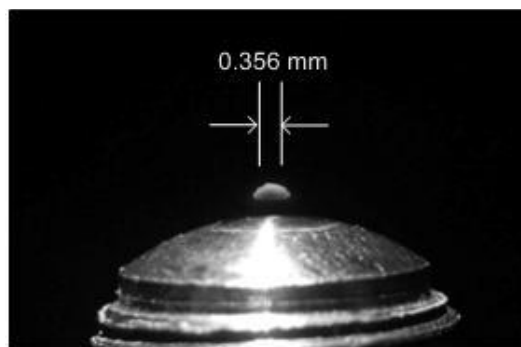


**Figure 1: False-color image of hydrogen flame over a 0.356 mm orifice.**

quenching flow rate to be generally independent of air moisture content. Hydrogen flame detection was complicated by their dimness, especially at low flow rates, but this was resolved by using thermocouples to detect flames. K-type thermocouples were chosen to avoid catalysis, and were placed several flame lengths above the flames to avoid disturbances.

Quenching flow rates were measured by first establishing a flame slightly larger than that shown in Figure 1. The flow rate was then decreased slowly until flame extinction. A soap bubble was then introduced for flow rate measurement. Each burner was allowed to warm to just above room temperature to prevent water condensation on the burner surface. This is because water condensation was found to disturb flow from the small burners, sometimes extinguishing the flames. Tests performed with different burner temperatures found quenching flow rate to be largely independent of burner temperature.

The fuel flow rate at blowoff was measured by first establishing a stable, large flame. The flow rate was then increased until the flame first lifted and then extinguished. For these tests the flames were detected visually.

### Leaky Fittings

Quenching limits were also measured for leaky compression fittings. These involved 6.35 mm outside diameter stainless steel tubes. Each tube entered a tube union fitting, which was a stainless steel Swagelok® compression fitting. The end of the union opposite the tube was sealed. This configuration simulates a possible unintended leak in a fuel line. One fitting (burner 1) was intentionally overtightened to introduce a leak. The fitting was originally made correctly using the manufacturer's instructions and an application of soap produced no bubbles for hydrogen at 5.52 bar. The fitting was then tightened an additional 0.75 turns. Burner 2 had a front ferrule that was intentionally scratched to simulate possible damage during installation, but was otherwise made according to manufacturer instructions. Both overtightened and scratched fittings are occasionally encountered in plumbing systems.

For the leaky fitting tests, pressure was varied to find quenching limits. Flow was measured using a rotameter that was calibrated with a soap bubble meter. For methane and propane, the minimum flaming flow rate was found by slowly increasing the pressure until an external pilot flame produced a visible flame near the leak. The experiments were done in a dim room so that methane and propane flames were readily visible. Thermocouples verified that even the smallest methane and propane flames were visible.

For hydrogen an audible pop was always found to occur at ignition. For the lowest flow rates, this pop was followed by extinction when the external flame was removed. Such extinction was confirmed with thermocouples. At slightly higher pressures, this pop was followed by steady burning. Near the quenching limits, hydrogen flames were never visible, even under darkened laboratory conditions.

Several orientations were tested to see the effect of burner orientation on the minimum flow rate. Each test was repeated to establish repeatability.

## **Results**

### Round Burners

Figure 2 shows a summary of all the limit data for tube burners. The blowoff flow rates increase with tube burner diameter, and the quenching flow rates are relatively flat. The

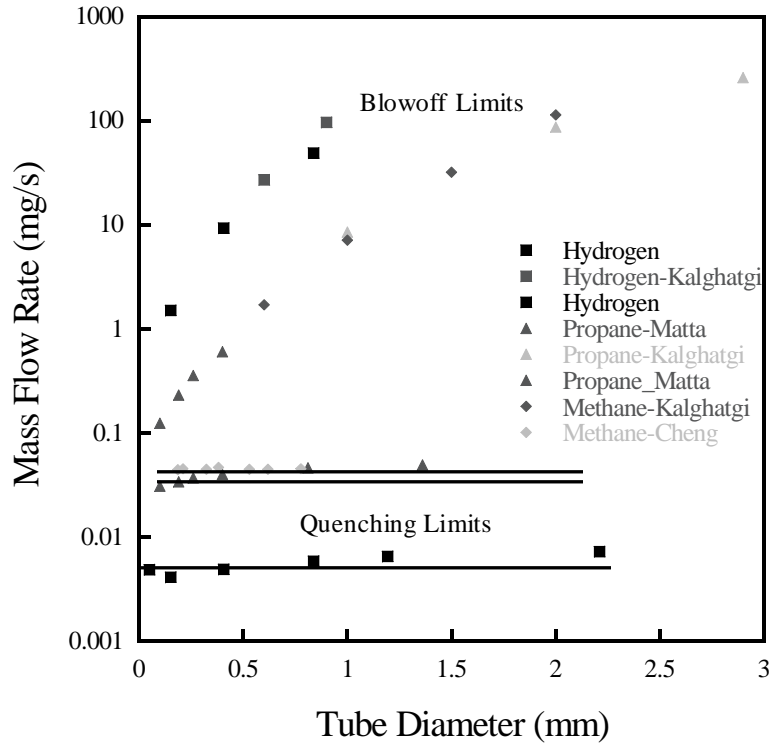


**Figure 2: Plot of quenching and blowoff limits versus tube diameter.**

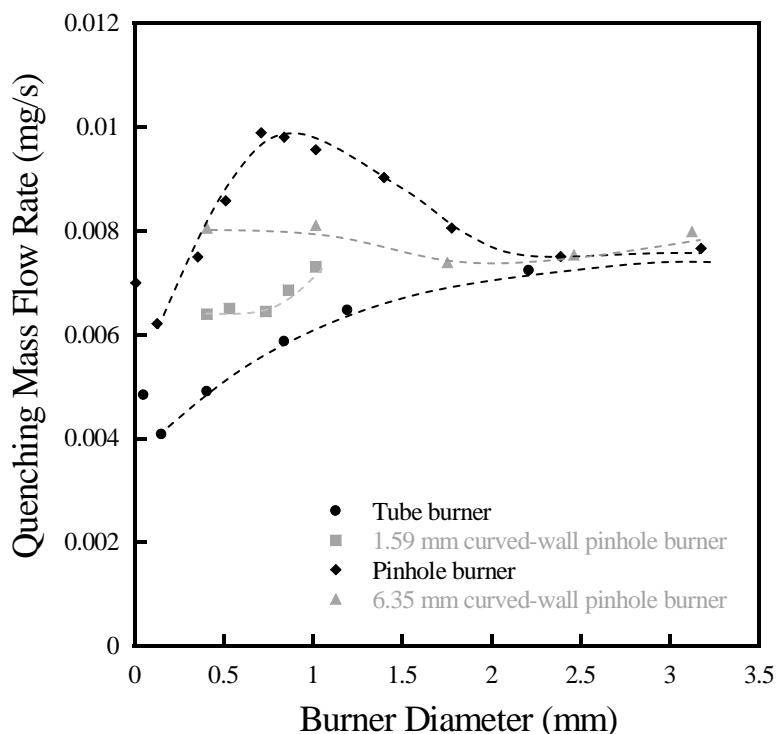
limits of combustion in Figure 2 are much wider for hydrogen than for propane or methane. The hydrogen quenching limits are about an order of magnitude lower than those for methane and propane, while hydrogen blowoff limits are about an order higher than those of the others. The data from Matta et al [2], Cheng et al. [3], and Kalghatgi [4] show that the limits for methane and propane are very similar. For all fuels, the quenching limits are nearly independent of burner diameter, whereas blowoff limits increase with increasing diameter. The independence of quenching limit from burner diameter is consistent with the analysis presented above, see Eq. (3).

Figure 3 shows the present hydrogen quenching limits. Data are included for all three types of burners. The theory of Eq. (3) predicts that the quenching flow rate is independent of burner diameter. It appears from Figure 3 that the scaling analysis did roughly predict the average quenching flow rate for hydrogen, although there is clearly another mechanism not accounted for in the calculation.

The tube burners show the same trend as the data from Matta et al. [2]; there is a slight increase in quenching flow rate with increasing burner size. It is reasonable to conclude that there is more heat loss to the burner with increasing burner size; with more heat loss, the quenching flow rate will increase to account for the weaker flame.

The pinhole burners show the upper limit for quenching flow rates. These flows are around 0.008 mg/s, as predicted. This plot does not exhibit the same trend as the tube burners because approximately the same amount of heat loss occurs independent of burner size. The hump in Figure 3 for orifice burners is under investigation.

The effect of curvature was investigated by using the curved-wall pinhole burners. It was



**Figure 3: Plot of quenching mass flow rates versus burner diameter for hydrogen.**

expected that with increasing curvature, a flame would experience less wall heat loss. This should result in a stronger flame and a lower quenching flow rate. This is exactly what was observed in the two curved-wall burners. The 6.35 mm burners act more like pinhole burners, whereas the 1.59 mm burners act more like tube burners; the 6.35 mm curved-wall burners have higher average quenching flow rates than the 1.59 mm curved-wall burners.

Both the tube and pinhole burners have an increase in quenching flow rate for the smallest burners. This is because the velocity at the burner outlet is large enough to weaken the stability of the flame.

### Leaky Fittings

The leaky fittings were observed for hydrogen, methane, and propane in vertical, inverted, and horizontal orientations. Figure 4 shows the effect of burner orientation on the minimum flaming flow rate for Burner 1. It is seen that the orientation of the leak does not have an effect on the quenching limit of hydrogen because these flames were so small at their limits. Burner orientation did have an effect on propane and methane with a horizontal configuration requiring the highest flow rate and inverted orientation requiring the lowest. The inverted orientation required the lowest flow rate of all fuels as this kept the flame the farthest away from the burner so that less heat was lost to the burner.

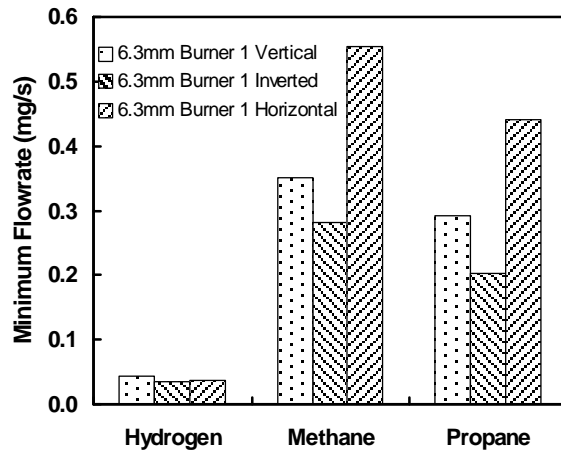


**Figure 4. Minimum flaming flow rate for Burner 1 in vertical, horizontal and inverted orientations**

Figure 5 shows the minimum flaming flow rate for hydrogen, propane, and methane for the vertical burner orientation. The minimum flow rate necessary for sustained flaming is plotted with respect to pressure. The data in Figure 5 were obtained by adjusting the torque on a leaky fitting. Thus the data at higher pressures result from a fitting with a higher torque.

Within experimental uncertainties, the data of Figure 5 are independent of pressure for all three fuels. The mean minimum flow rate for a flaming hydrogen leak is 0.040 mg/s. The hydrogen flow rate was about an order of magnitude lower than for the other fuels due to its low quenching distance and low molecular weight. This behavior is similar to that seen in the round burners above, in Figure 2.

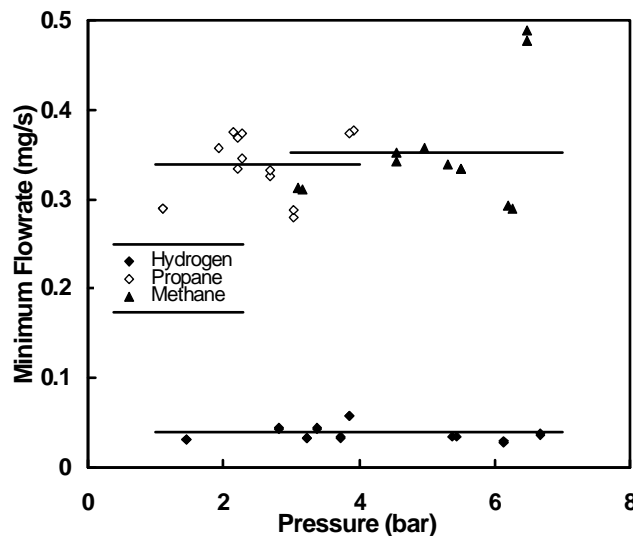


**Figure 5. Minimum flaming flow rate versus pressure in the vertical orientation.**

The minimum hydrogen flaming flow rate for round burners (Figure 2) is about an order of magnitude lower than that for leaky fittings (Figure 5). This is attributed to additional burner heat losses in the leaky fittings, where flames burn near concave metal surfaces.

## Conclusions

The quenching and blowoff limits for hydrogen on round burners were measured and compared to published values for other gases. Hydrogen diffusion flames on tube burners had much wider limits of combustion than propane and methane. It has been shown that the quenching flow rates for all these gases are largely independent of burner size.

For hydrogen the quenching flow rate was found to depend on burner type, owing to differences in wall heat loss. Tube burners had the lowest quenching flow rates, orifice burners had the highest, and radial burners fell in-between, as expected.

The minimum flow rate necessary for sustaining a hydrogen flame at a leaky compression fitting is 0.040 mg/s. This is about an order of magnitude lower than for propane or methane. The minimum mass flow rate for all fuels is nearly independent of pressure.

The round burner and leaky compression fitting experiments yielded similar results in that they both found that the lower limits of combustion for hydrogen were about an order of magnitude lower than those for propane and methane. The two experiments differed in that their lower combustion limits were off by an order of magnitude owing to different amounts of heat loss.

## Acknowledgments

This work is supported by NIST under the technical direction of J. Yang. Helpful discussions with B.H. Chao are appreciated.

## References

- [1] L.C. Cadwallader, J.S. Herring, *Safety Issues with Hydrogen as a Vehicle Fuel*, Report INEEL/EXT-99-00522 prepared for U.S. Department of Energy (1999).
- [2] L.M. Matta, Y. Neumeier, B. Lemon, B.T. Zinn, *Characteristics of Microscale Diffusion Flames*, Proc. Combust. Inst. 29 (2002) 933-938.
- [3] T.S. Cheng, C.P. Chen, C.S. Chen, Y.H. Li, C.Y. Wu, Y.C. Chao, *Characteristics of Microjet Methane Diffusion Flames*, Combust. Theory Modeling 10 (2006) 861-881.
- [4] G.T. Kalghatgi, *Blow-Out Stability of Gaseous Jet Diffusion Flames. Part I: In Still Air*, Combustion Science and Technology, 26:5, 233-239 (1981).
- [5] M.R. Swain, M.N. Swain, *A Comparison of H<sub>2</sub>, CH<sub>4</sub>, and C<sub>3</sub>H<sub>8</sub> Fuel Leakage in Residential Settings*, Int. J. Hydrogen Energy 17:807-815 (1992).
- [6] F.G. Roper, *The Prediction of Laminar Jet Diffusion Flame Sizes: Part 1. Theoretical Model*, Combust. Flame 29:219-226 (1977).
- [7] P.B. Sunderland, B.J. Mendelson, Z.G. Yuan, D.L. Urban, *Shapes of Buoyant and Nonbuoyant Laminar Jet Diffusion Flames*, Combust. Flame 116:376-386 (1999).
- [8] A.M. Kanury, *Introduction to Combustion Phenomena*. Gordon and Breach, New York, p. 131 (1975).
- [9] R.C. Weast, M.J. Astle, *CRC Handbook of Chemistry and Physics*, 59th edition, CRC Press, Inc. West Palm Beach, p. F-58 (1979).
- [10] B.R. Munson, D.F. Young, T.J. Okiishi, *Fundamentals of Fluid Mechanics*, Wiley, Hoboken, NJ, p. 359 (2002).
- [11] N.R. Morton, P.B. Sunderland, B.H. Chao, R.L. Axelbaum, *Quenching Limits and Materials Degradation of Hydrogen Diffusion Flames*, 5th U.S. Combustion Meeting, San Diego (2007).
- [12] M.Y. Bahadori, U. Hegde, L. Zhou, *Liftoff and Blowoff of Jet Diffusion Flames*, Paper AIAA-2002-1078, Aerospace Sciences Meeting, Reno, Nevada, January 14-17, 2002.

5<sup>th</sup> US Combustion Meeting  
 Organized by the Western States Section of the Combustion Institute  
 and Hosted by the University of California at San Diego  
 March 25-28, 2007

## An asymptotic analysis of spontaneous ignition of hydrogen jets

*Kian Boon Lim<sup>1</sup>, Beei-Huan Chao<sup>2</sup>, Peter B. Sunderland<sup>1</sup>, Richard L. Axelbaum<sup>3</sup>*

<sup>1</sup>*Dept. of Fire Protection Engineering, Univ. of Maryland, College Park, MD 20742, USA*

<sup>2</sup>*Dept. of Mechanical Engineering, Univ. of Hawaii, Manoa, HI 96822, USA*

<sup>3</sup>*Dept. of Mechanical and Aerospace Engineering, Washington Univ., St. Louis, MO 63130, USA*

Analytical work is presented for the spontaneous ignition of a hydrogen jet emanating from a slot into air. A similarity solution of the flow field was obtained. This was combined with the species and energy conservation equations, which were solved using activation energy asymptotics. Limits of spontaneous ignition were identified as functions of slot width, flow rate, and temperatures of the hydrogen jet and ambient air. Two scenarios are examined: a cool jet flowing into a hot ambient and a hot jet flowing into a cool ambient. For both scenarios, ignition is favored with an increase of either the ambient temperature or the hydrogen supply temperature. Moreover, for the hot ambient scenario, a decrease in fuel Lewis number also promotes ignition. The Lewis number of the oxidizer only has a weak effect on ignition. Because spontaneous ignition is very sensitive to temperature, ignition is predicted to occur near the edge of the jet if the hydrogen is cooler than the air and on the centerline if the hydrogen is hotter than the air.

### Nomenclature

$a_T$	constant representing the temperature increase through reaction
$B$	pre-exponential factor
$c_p$	specific heat at constant pressure
$D$	mass diffusion coefficient
$Da$	Damköhler number
$\tilde{Da}$	reduced Damköhler number
$E$	activation temperature
$f$	nondimensional streamfunction
$Le$	Lewis number
$p$	pressure
$Pr$	Prandtl number
$q_F$	heat of combustion per unit mass of fuel
$R$	ideal gas constant
$Sc$	Schmidt number
$T$	temperature
$u$	flow velocity in the $x$ (streamwise) direction
$v$	flow velocity in the $y$ (transverse) direction
$W$	molecular weight
$x$	streamwise spatial coordinate
$X$	ignition location in the $x$ direction from the exit of the slot
$x_0$	distance from the fictitious origin of the jet to the exit of the crack
$y$	transverse spatial coordinate ( $y = 0$ along the centerline)
$Y$	mass fraction

**Greek**

$\alpha$	parameter defined as $\alpha = (\tilde{T}_\infty - \tilde{T}_0) / \tilde{Y}_{F,0}$
$\varepsilon$	small parameter, defined as $\varepsilon = \tilde{T}_\infty^2 / \tilde{E}$ , used for asymptotic expansion
$\phi_O$	perturbation of oxidizer concentration in the inner, reaction region
$\theta$	perturbation of temperature in the inner, reaction region
$\gamma$	parameter defined as $\gamma = (\tilde{T}_0 - \tilde{T}_\infty) / \tilde{Y}_{O,\infty}$
$\lambda$	thermal conductivity
$\mu$	viscosity
$\nu$	stoichiometric coefficient
$\rho$	gas density
$\psi$	streamfunction
$\eta$	similarity variable
$\xi$	stretched spatial coordinate, defined in Eq. (24)
$\zeta$	stretched spatial coordinate in the inner, reaction region (inner variable)

**Subscripts**

0	value of variables at the exit of the crack
<i>F</i>	fuel
<i>f</i>	frozen solution
<i>O</i>	oxidizer
<i>T</i>	temperature
$\infty$	ambient condition

**Superscripts**

$\sim$	nondimensional quantity
$\wedge$	rescaled nondimensional quantity

**1. Introduction**

Hydrogen jets flowing into heated air ignite spontaneously at an air temperature of 943 K [1]. This is cooler than for most other fuels [2], including gasoline and methane, and is not much higher than the autoignition temperature of stoichiometric hydrogen/air mixtures, 858 K [1]. Hydrogen is under consideration as a major new fuel carrier. Occasional unintended hydrogen leaks will be unavoidable, and some may involve heated hydrogen and/or air. Thus an improved understanding of limits of spontaneous ignition of hydrogen jets is sought here, with the aid of activation-energy asymptotics.

Asymptotic flame theories can provide valuable insights into combustion reactions [4-6]. Im et al. [7,8] analyzed thermal ignition in supersonic hydrogen/air mixing layers and obtained ignition characteristics over a wide range of conditions. An investigation of different combustion regimes by Damköhler-number and activation-energy asymptotics in a stagnant mixing layer was performed by Lee and Chung [9].

Zheng and Law [10] identified ignition limits of premixed hydrogen-air flames where ignition was by heated counterflow. Toro et al. [11] examined in detail the structure of laminar hydrogen jet flames both experimentally and numerically. Chaos et al. [12] examined Lewis-number effects in unsteady laminar hydrogen jet flames. Liu and Pei [13] examined autoignition and explosion limits of hydrogen-oxygen mixtures in homogenous systems.

The present analysis considers the spontaneous ignition of a jet of hydrogen or other gaseous fuel leaking through a crack into air. The crack is taken to be straight and long, yielding a two-dimensional flow field. The ignition analysis identifies limits of spontaneous ignition.

The objectives of this work are to:

- 1) develop a model of spontaneous ignition for two cases: a cool fuel jet flowing into heated air and a heated fuel jet flowing into cool air,
- 2) identify limits of spontaneous ignition as functions of slot width, flow rate, fuel Lewis number, and temperatures of the fuel jet and the ambient air, and
- 3) identify the location of ignition.

## 2. Formulation

The problem of interest is a steady, isobaric laminar jet of fuel (e.g. hydrogen) at temperature  $T_0$  issuing from a rectangular slot into an oxidizing environment (e.g. atmospheric air) at a temperature of  $T_\infty$ , as shown schematically in Fig. 1. Spontaneous ignition occurs when either  $T_0$  or  $T_\infty$  is sufficiently high that the weak reaction between the fuel and the oxidizer transitions to a vigorous burning flame. This study analyzes the ignition state as a function of various physical properties including Lewis number,  $T_0$ ,  $T_\infty$ , the flow velocity at the slot exit,  $u_0$ , and the width of the slot. The slot is considered sufficiently long that end effects are negligible. The reaction chemistry is simulated by a single-step, overall, irreversible reaction with second order Arrhenius kinetics and a high activation energy.

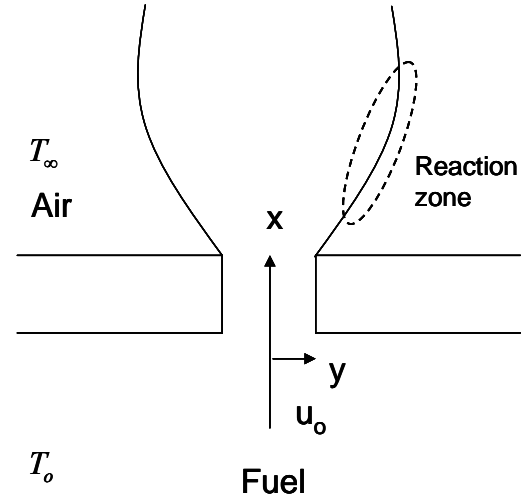


Figure 1: Schematic of slot and hydrogen leak.

With the above problem definition, conservation of mass and momentum are given by

$$\frac{\partial(\rho u)}{\partial x} + \frac{\partial(\rho v)}{\partial y} = 0 \quad , \quad (1)$$

$$\rho u \frac{\partial u}{\partial x} + \rho v \frac{\partial u}{\partial y} - \frac{\partial}{\partial y} \left( \mu \frac{\partial u}{\partial y} \right) = 0 \quad , \quad (2)$$

which are to be solved subject to the boundary conditions

$$y = 0 \quad , \quad x = x_0 : \quad u = u_0 \quad ; \quad x > x_0 : \quad \partial u / \partial y = 0 \quad , \quad v = 0 \quad , \quad (3)$$

$$y \rightarrow \infty : \quad u \rightarrow 0 \quad . \quad (4)$$

Introducing a streamfunction  $\psi$  of the form

$$\rho u = \rho_\infty u_0 (\partial \psi / \partial y) \quad , \quad \rho v = -\rho_\infty u_0 (\partial \psi / \partial x) \quad , \quad (5)$$

such that the continuity equation is satisfied, transforming the coordinates from  $(x, y)$  to  $(\tilde{x}, \eta)$  where

$$\tilde{x} = x/x_0 \quad , \quad \eta = \sqrt{\rho_\infty u_0 / (6 \mu_\infty x_0)} \tilde{x}^{-2/3} \int_0^y (\rho / \rho_\infty) dy \quad , \quad (6)$$

and defining

$$\psi = \sqrt{6\mu_\infty x_0 / (\rho_\infty u_0)} \tilde{x}^{1/3} f(\eta) \quad , \quad (7)$$

Eqs. (2) – (4) are transformed to

$$(f'''/2) + f f''' + f'^2 = 0 \quad . \quad (8)$$

$$\eta = 0 : \quad f = f'' = 0 \quad f' = 1 \quad ; \quad \eta \rightarrow \infty : \quad f' \rightarrow 0 \quad . \quad (9)$$

A similarity solution is assumed to exist so that  $f$  is a function of  $\eta$  only. Solving Eqs. (8) – (9) following Schlichting [14] and Bickey [15] yields  $f = \tanh \eta$ .

Applying the coordinate transformation and the solution of the momentum equation to the energy and species conservation equations, we obtain

$$\frac{1}{Pr} \frac{\partial^2 \tilde{T}}{\partial \eta^2} + 2(\tanh \eta) \frac{\partial \tilde{T}}{\partial \eta} - 6(\operatorname{sech}^2 \eta) \tilde{x} \frac{\partial \tilde{T}}{\partial \tilde{x}} = -Da \tilde{x}^{4/3} \tilde{Y}_F \tilde{Y}_O \tilde{T}^{-1} \exp(-\tilde{E}/\tilde{T}) \quad , \quad (10)$$

$$\frac{1}{Sc_F} \frac{\partial^2 \tilde{Y}_F}{\partial \eta^2} + 2(\tanh \eta) \frac{\partial \tilde{Y}_F}{\partial \eta} - 6(\operatorname{sech}^2 \eta) \tilde{x} \frac{\partial \tilde{Y}_F}{\partial \tilde{x}} = Da \tilde{x}^{4/3} \tilde{Y}_F \tilde{Y}_O \tilde{T}^{-1} \exp(-\tilde{E}/\tilde{T}) \quad , \quad (11)$$

$$\frac{1}{Sc_O} \frac{\partial^2 \tilde{Y}_O}{\partial \eta^2} + 2(\tanh \eta) \frac{\partial \tilde{Y}_O}{\partial \eta} - 6(\operatorname{sech}^2 \eta) \tilde{x} \frac{\partial \tilde{Y}_O}{\partial \tilde{x}} = Da \tilde{x}^{4/3} \tilde{Y}_F \tilde{Y}_O \tilde{T}^{-1} \exp(-\tilde{E}/\tilde{T}) \quad , \quad (12)$$

which are to be solved subject to

$$\eta = 0 \quad , \quad \tilde{x} = 1 : \quad \tilde{T} = \tilde{T}_0 \quad , \quad \tilde{Y}_F = \tilde{Y}_{F,0} \quad , \quad \tilde{Y}_O = 0 \quad , \quad (13)$$

$$\eta = 0 \quad , \quad \tilde{x} > 1 : \quad \partial \tilde{T} / \partial \eta = \partial \tilde{Y}_F / \partial \eta = \partial \tilde{Y}_O / \partial \eta = 0 \quad , \quad (14)$$

$$\eta \rightarrow \infty : \quad \tilde{T} \rightarrow \tilde{T}_\infty \quad , \quad \tilde{Y}_F \rightarrow 0 \quad , \quad \tilde{Y}_O \rightarrow \tilde{Y}_{O,\infty} \quad . \quad (15)$$

In the above,

$$\begin{aligned} \tilde{T} &= \frac{c_p T}{q_F} \quad , \quad \tilde{Y}_F = Y_F \quad , \quad \tilde{Y}_O = \frac{\nu_F W_F}{\nu_O W_O} Y_O \quad , \quad Da = \frac{6x_0 \nu_O c_p p B}{W_F q_F R u_0} \\ \tilde{E} &= \frac{c_p E}{q_F} \quad , \quad Pr = \frac{\mu}{\lambda / c_p} \quad , \quad Sc_j = \frac{\mu}{\rho D_j} \quad , \quad Le_j = \frac{\lambda / c_p}{\rho D_j} \quad . \end{aligned}$$

The values of  $c_p$ ,  $\rho \lambda$ ,  $\rho \mu$ , and  $\rho^2 D_j$  are considered constant. The ideal gas equation of state has been adopted here.

In the non-reactive limit, solving Eqs. (10) – (15) gives the frozen solutions,

$$\tilde{T}_f = \tilde{T}_\infty + (\tilde{T}_0 - \tilde{T}_\infty) (\operatorname{sech}^{2Pr} \eta) / \tilde{x}^{1/3} \quad , \quad (16)$$

$$\tilde{Y}_{F,f} = \tilde{Y}_{F,0}(\operatorname{sech}^{2Sc_F} \eta) / \tilde{x}^{1/3} \quad , \quad (17)$$

$$\tilde{Y}_{O,f} = \tilde{Y}_{O,\infty}[1 - (\operatorname{sech}^{2Sc_O} \eta) / \tilde{x}^{1/3}] \quad . \quad (18)$$

### 2.1. Cool jet flowing into a hot ambient ( $T_\infty > T_0$ )

In the presence of a weak reaction, the temperature is increased from its frozen value by a small,  $O(\varepsilon)$  amount where  $\varepsilon = \tilde{T}_\infty^2 / \tilde{E}$  while the reactant concentrations are reduced from their respective frozen values by an  $O(\varepsilon)$  amount. Because ignition is primarily controlled by temperature, ignition occurs near  $\eta \rightarrow \infty$  if successful. Away from this high temperature region, the reaction is frozen. In the outer, chemically frozen region, the outer solutions are similar to Eqs. (16) – (18) but with an  $O(\varepsilon)$  change in their values. In the inner, reactive region, defining a stretched inner variable as

$$\zeta = \tilde{Y}_{F,0}(\operatorname{sech} \eta)^{2Pr} / (\varepsilon \tilde{x}^{1/3}) \quad , \quad (19)$$

and substituting into Eqs. (10) – (12) yields, when  $Le_F$  is sufficiently smaller than unity, as for hydrogen,

$$\zeta^2 (\partial^2 \theta / \partial \zeta^2) = -\tilde{D}a \zeta^{Le_F} \exp(\theta - \alpha \zeta) \quad , \quad (20)$$

where  $\alpha = (\tilde{T}_\infty - \tilde{T}_0) / \tilde{Y}_{F,0}$  and the reduced Damköhler number is defined as

$$\tilde{D}a = Da \tilde{Y}_{O,\infty} \tilde{x}^{4/3} [\tilde{Y}_{F,0} / (\varepsilon \tilde{x}^{1/3})]^{1-Le_F} \exp(-\tilde{E} / \tilde{T}_\infty) / (4Pr \tilde{T}_\infty) \quad . \quad (21)$$

The boundary conditions required to solve this equation can be found by matching the inner and outer solutions as

$$\zeta = 0 : \quad \theta = 0 \quad ; \quad \zeta \rightarrow \infty : \quad \partial \theta / \partial \zeta \rightarrow 0 \quad , \quad \theta \rightarrow a_T \quad (22)$$

For the case of  $Le_F$  close to unity, Eq. (20) is modified to

$$\zeta^2 (\partial^2 \theta / \partial \zeta^2) = -\tilde{D}a (\zeta - \theta) \exp(\theta - \alpha \zeta) \quad . \quad (23)$$

### 2.2. Hot jet flowing into a cool ambient ( $T_0 > T_\infty$ )

For the case of a hot jet issuing into a cold ambient, any ignition will occur near the jet centerline,  $\eta = 0$ . Moreover, because the jet will be cooled by the cold ambient gas along the flow, ignition is expected to occur near the slot exit. The analysis is similar to that in Section 2.1, except that  $\varepsilon = \tilde{T}_0^2 / \tilde{E}$  and the inner variables are defined as

$$\zeta = \eta \sqrt{Pr \tilde{Y}_{O,\infty} / \varepsilon} \quad , \quad \xi = \tilde{Y}_{O,\infty} (\tilde{x} - 1) / (3\varepsilon) \quad , \quad (24)$$

leading to

$$\frac{\partial^2 \theta}{\partial \zeta^2} - 2 \frac{\partial \theta}{\partial \xi} + \frac{1}{Le_O} \frac{\partial^2 \phi_O}{\partial \zeta^2} - 2 \frac{\partial \phi_O}{\partial \xi} = 0 \quad , \quad (25)$$

$$\frac{\partial^2 \theta}{\partial \zeta^2} - 2 \frac{\partial \theta}{\partial \xi} = -\tilde{D}a(\phi_O + Le_O \zeta^2 + \xi) \exp[\theta - \beta(\zeta^2 + \xi)] \quad , \quad (26)$$

with the initial and boundary conditions

$$\theta(\xi=0) = \phi_O(\xi=0) = 0 \quad , \quad (27)$$

$$\zeta = 0 \text{ and } \zeta \rightarrow \infty, \xi > 0 : \quad \partial \theta / \partial \zeta = \partial \phi_O / \partial \zeta = 0 \quad , \quad (28)$$

where  $\gamma = (\tilde{T}_0 - \tilde{T}_\infty) / \tilde{Y}_{O,\infty}$  and the reduced Damköhler number is

$$\tilde{D}a = \varepsilon [Da \tilde{Y}_{F,0} / (\tilde{T}_0 \tilde{Y}_{O,\infty})] \exp(-\tilde{E} / \tilde{T}_0) \quad . \quad (29)$$

Ignition is considered successful when the heat generation through reaction is sufficient to compensate the heat loss from the jet to the ambient at any location, and the ignition criterion is given by

$$(\partial \theta / \partial \xi)_{\zeta=0} \geq \beta \quad \text{or} \quad \partial \theta / \partial \zeta \geq 2\beta\zeta \text{ at any } \xi \quad . \quad (30)$$

### 3. Results

#### 3.1. Cool jet flowing into a hot ambient ( $T_\infty > T_0$ )

Equations (20) and (23), subject to Eqs. (21) – (22), were solved by a fourth order Runge-Kutta method. The results are shown in Fig. 2, a plot of the reaction temperature increase versus reduced Damköhler number. This reveals the lower and middle branches of an S-curve [4]. In each such curve, there is a maximum value of  $\tilde{D}a$  above which a solution does not exist. For values of  $\tilde{D}a$  smaller than this critical value, there are two solutions for each  $\tilde{D}a$ . The critical value of  $\tilde{D}a$  represents the transition from weak reaction to vigorous burning, and is defined as the ignition state. The lower branch, showing an increase of temperature with higher reaction rate, is the physically realistic branch. The middle branch represents conditions that are not physically possible. Spontaneous ignition is predicted for any  $\tilde{D}a$  greater than this critical value.

Three curves are included in Fig. 2, each with a different value of  $\alpha = (\tilde{T}_\infty - \tilde{T}_0) / \tilde{Y}_{F,0}$ . Fig. 2 indicates that a decrease in  $\alpha$  reduces the critical  $\tilde{D}a$  at ignition, which means that ignition is favored. Such a decrease can be accomplished either by increasing the reactant mass fraction in the fuel supply,

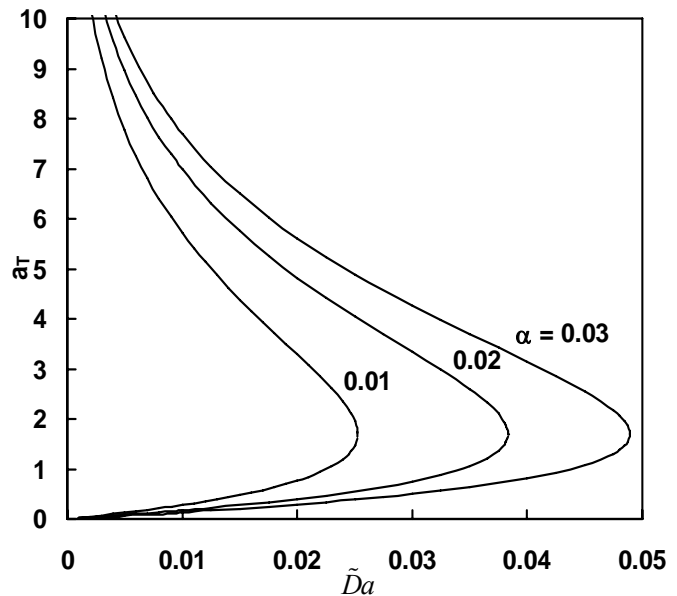


Figure 2:  $a_T$  versus  $\tilde{D}a$  for varying  $\alpha$ , with  $Le_F = 0.6$  and constant  $\tilde{T}_\infty$ .

$\tilde{Y}_{F,0}$ , or by increasing the jet temperature,  $\tilde{T}_0$ . Both findings are physically realistic.

Parameter  $\alpha$  also can be changed by variations in the ambient temperature,  $\tilde{T}_\infty$ , but this changes  $\tilde{Da}$  simultaneously. To investigate the effects of  $\tilde{T}_\infty$  variations at fixed  $\tilde{Da}$  requires a rescaling. The rescaling is performed here by specifying a reference value of  $\tilde{T}_\infty$  as  $\hat{T}_\infty$ , defining rescaled parameters  $\hat{\varepsilon} = (\hat{T}_\infty)^2 / \tilde{E}$ ,  $\hat{a}_T = (\tilde{T}_\infty^2 / \hat{T}_\infty^2) a_T$  and

$$\hat{Da} = Da \tilde{Y}_{O,\infty} \tilde{x}^{4/3} [\tilde{Y}_{F,0} / (\hat{\varepsilon} \tilde{x}^{1/3})]^{(1-Le_F)} \exp(-\tilde{E} / \hat{T}_\infty) / (4Pr\hat{T}_\infty) \quad , \quad (31)$$

and plotting the results in terms of rescaled variables  $\hat{a}_T$  and  $\hat{Da}$ . The results are shown in Fig. 3. Here an increase in  $\tilde{T}_\infty$ , which increases  $\alpha$  without changing  $\hat{Da}$ , is seen to favor ignition. This also is physically realistic because more heat is transferred to the cold fuel flow at a higher rate when the ambient is at a higher temperature. By the same reason, when the kinetic data are unchanged, an increased  $\tilde{T}_\infty$  yields ignition to occur nearer the edge of the jet. Note that the Damköhler number shown after Eq. (15) is a function of the radial distance from the virtual origin of the jet.

The influence of reactant Lewis number on ignition is considered in Fig. 4. Here  $Le_F$  is defined as the mixture thermal diffusivity divided by the mass diffusivity of fuel into the mixture. A decrease in  $Le_F$  for fixed  $\hat{Da}$  is seen to favor ignition. This occurs because a smaller  $Le_F$  implies that fuel species diffuse more quickly into the hot oxidizer. A fuel such as a mixture of hydrogen and nitrogen has a small  $Le_F$ . Nayagam and Williams [16] found that in a one-dimensional model of steady motion of edges of reaction sheets, increasing the Lewis number decreases the propagation velocity at small Damköhler numbers.

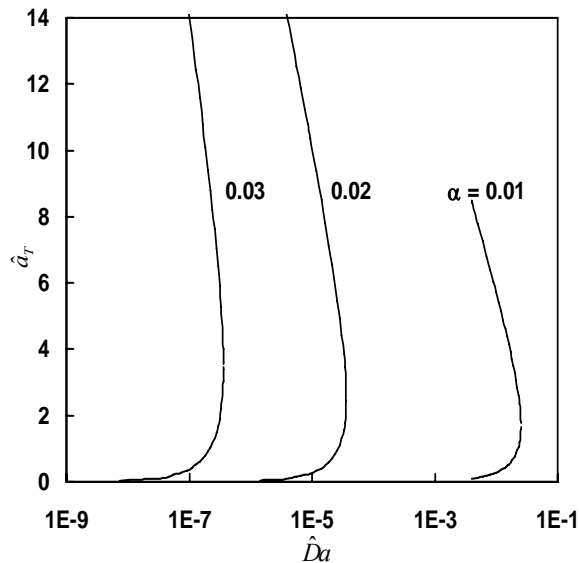


**Figure 3:**  $\hat{a}_T$  versus  $\hat{Da}$  for varying  $\alpha$ , with  $Le_F = 0.6$ .

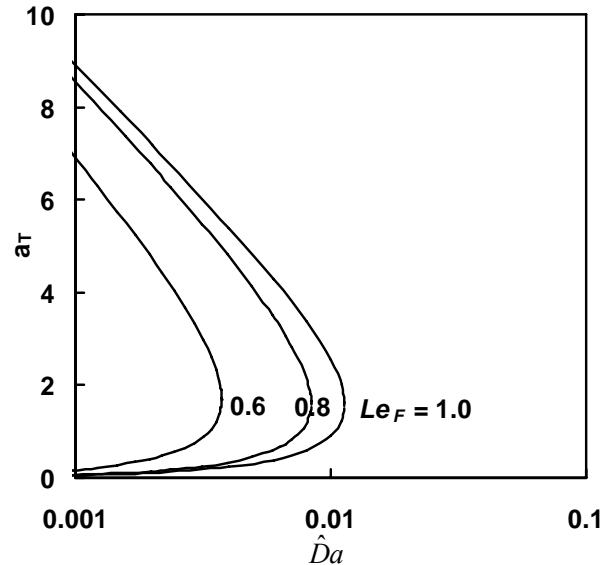


**Figure 4:**  $a_T$  versus  $\hat{Da}$  for varying  $Le_F$ , with  $\alpha = 0.02$ ,  $\tilde{T}_0 = 0.0358$ , and  $\tilde{E} = 1.79$ .

### 3.2. Hot jet flowing into a cool ambient ( $T_0 > T_\infty$ )

Eqs. (25) – (28) were solved by the Crank-Nicholson method and the resulting matrix was inverted by LU decomposition. Selected results are shown in Figs. 5 and 6. In Fig. 5,  $\theta_{\max}$  represents the maximum value of temperature increase through reaction before ignition occurs. The corresponding ignition location,  $X$ , is shown in Fig. 6.

Three curves are included in Figs. 5 and 6, each with a different value of  $\gamma$ , where  $\gamma = (\tilde{T}_0 - \tilde{T}_\infty) / \tilde{Y}_{O,\infty}$ . These curves do not have the shape of an S-curve because the solutions are derived from a partial differential equation, in contrast to the ordinary differential equation of the cool jet. On each curve, by increasing the reaction rate,  $\tilde{D}a$ , a smaller temperature increase and a shorter ignition location is observed before ignition, as is reasonable to expect. A higher value of  $\tilde{D}a$  yields an increased heat generation rate, which compensates for some heat loss from the hot jet to the cold ambient, favors ignition, and moves the point of ignition closer to the jet exit. In contrast, a reduction in  $\tilde{D}a$  weakens the reaction and makes ignition more difficult such that both  $\theta_{\max}$  and  $X$  increase. Although an increase of  $X$  provides longer residence time for the reaction so that ignition can occur at a smaller  $\tilde{D}a$ , the reaction rate decreases with  $X$  because the jet is cooled by the cold ambient, as can be seen from the reaction term of Eq. (26). A sharp increase in  $\theta_{\max}$  and  $X$ , as shown the low  $\tilde{D}a$  side of the  $\gamma = 0.3$  curves in Figs. 5 and 6, means that the reduction of reaction rate dominates over the residence time increase, and defines the smallest  $\tilde{D}a$  for which ignition occurs.

Figures 5 and 6 also indicate that a decrease in  $\gamma$  for any fixed  $\tilde{D}a$  favors ignition, as ignition occurs at a lower temperature increase,  $\theta_{\max}$ , and at a shorter ignition location,  $X$ . More importantly, a decrease in  $\gamma$  permits ignition at a lower value of  $\tilde{D}a$ . Such a decrease can be

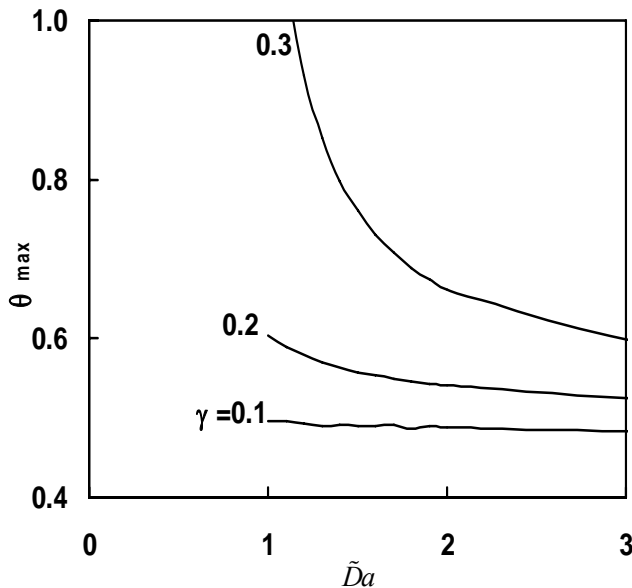


Figure 5 :  $\theta_{\max}$  versus  $\tilde{D}a$  for varying  $\gamma$ , with  $Le_o=1.0$  and constant  $\tilde{T}_0$ .

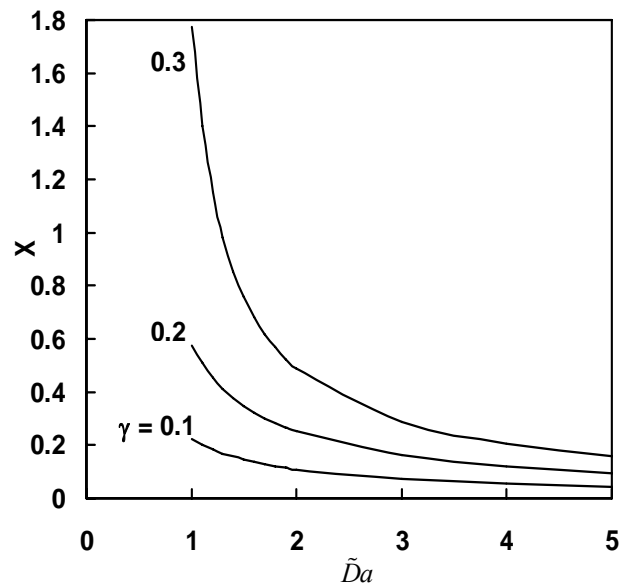


Figure 6 :  $X$  versus  $\tilde{D}a$  for varying  $\gamma$ , with  $Le_o = 1$ .

accomplished either by increasing the reactant mass fraction in the oxidizer supply,  $\tilde{Y}_{O,\infty}$ , or by increasing the ambient temperature,  $\tilde{T}_\infty$ . Both findings are physically realistic.

Parameter  $\gamma$  also can be changed by variations in the jet temperature,  $\tilde{T}_0$ , but this changes  $\tilde{D}a$  simultaneously. To investigate the effects of  $\tilde{T}_0$  variations at fixed  $\tilde{D}a$  requires a rescaling similar to that performed in Section 3.1. The rescaling is performed here by specifying a reference value of  $\tilde{T}_0$  as  $\hat{T}_0$ , defining rescaled parameters  $\hat{\varepsilon} = (\hat{T}_0)^2 / \tilde{E}$ ,  $\hat{\theta}_{\max} = (\tilde{T}_0 / \hat{T}_0)^2 \theta_{\max}$  and

$$\hat{D}a = \hat{\varepsilon} [Da \tilde{Y}_{F,0} / (\hat{T}_0 \tilde{Y}_{O,\infty})] \exp(-\tilde{E} / \hat{T}_0) \quad , \quad (32)$$

and plotting the results in terms of rescaled variables  $\hat{\theta}_{\max}$  and  $\hat{D}a$ . The results are shown in Figs. 7 and 8. Here an increase in  $\tilde{T}_0$ , which increases  $\gamma$  without changing  $\hat{D}a$ , is seen to favor ignition because ignition can occur at a lower reaction rate, or lower  $\hat{D}a$ . This also is physically realistic. Ignition is predicted to occur near the centerline if the fuel is hotter than the air because this is where the highest temperature is attained.

The effects of oxidizer Lewis number on spontaneous ignition are considered in Fig. 9. This plot shows that decreased  $Le_O$  makes ignition more difficult. For an increase in the mass diffusivity of the oxidizer (or a decreased  $Le_O$ ) at a fixed value of  $\tilde{D}a$ ,  $\theta_{\max}$  increases. In addition, the minimum  $\tilde{D}a$  for ignition increases with decreased  $Le_O$ . This differs from the ignition behavior with respect to fuel Lewis number in the cool jet case (Fig. 4). In a cool jet, there is unlimited heat transfer from the hot ambient gas to preheat the fuel so that a higher fuel diffusion rate (lower  $Le_F$ ) results in a higher fuel concentration in the reaction region, more heat generation through the reaction and, hence, easier ignition. In the hot jet, only limited heat is

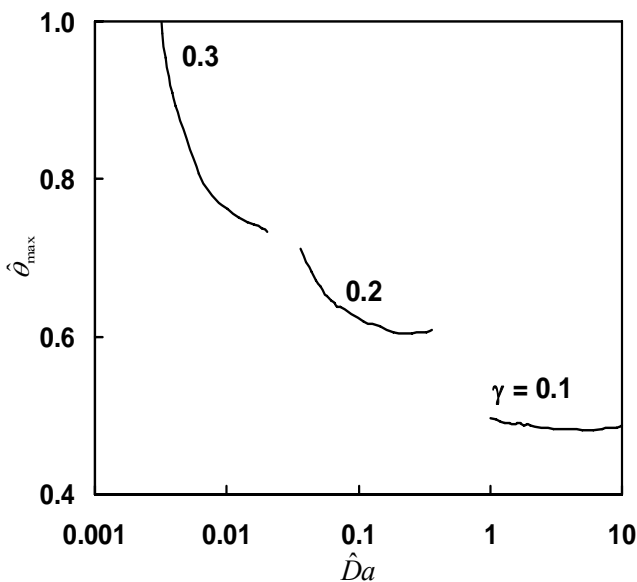


Figure 7 :  $\hat{\theta}_{\max}$  versus  $\hat{D}a$  for varying  $\gamma$ , with  $Le_o = 1$ .

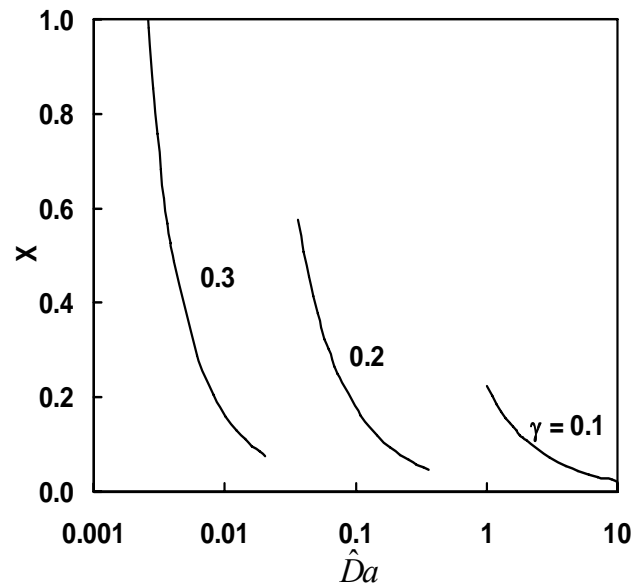


Figure 8 :  $X$  versus  $\hat{D}a$  for varying  $\gamma$ , with  $Le_o = 1$ .

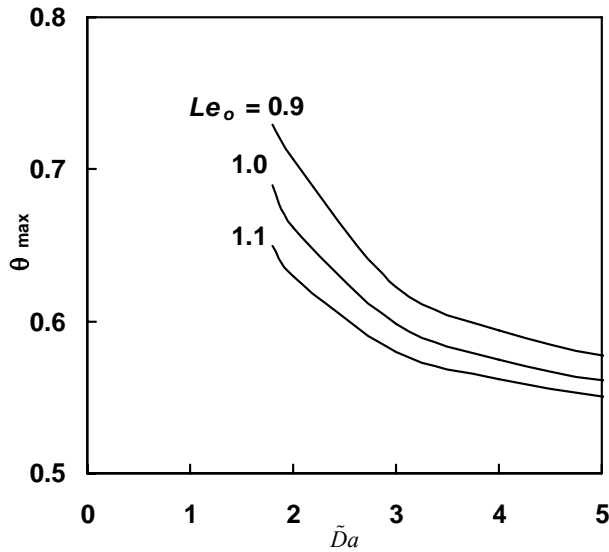


Figure 9 :  $\theta_{\max}$  versus  $\tilde{D}a$  for varying  $Le_o$ , with  $\gamma = 0.3$ .

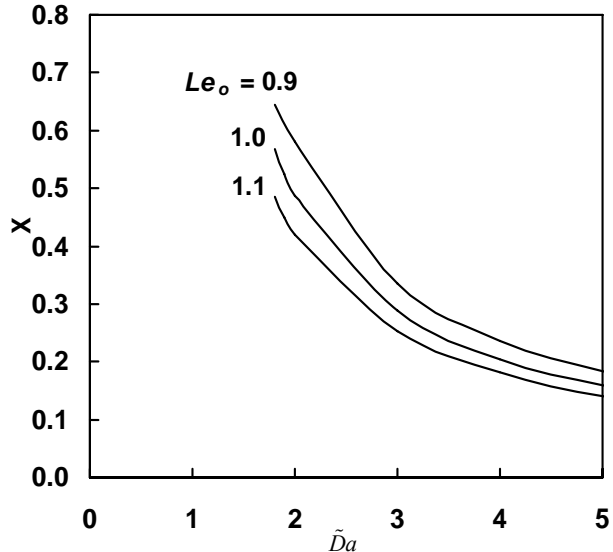


Figure 10 :  $X$  versus  $\tilde{D}a$  for varying  $Le_o$ , with  $\gamma = 0.3$ .

available from the fuel flow. An increased oxidizer mass diffusivity increases the transport rate of oxidizer to the center of the jet, thus requiring more heat to preheat the oxidizer, decreasing the temperature in the hot zone, and making ignition more difficult. Furthermore, unlike the cool jet case, the Lewis number of the oxidizer only has a weak effect on the ignition state (see Fig. 9) because ignition occurs near the jet exit if successful. In the reaction region, the flow velocity is high such that streamwise convection dominates over transverse diffusion. Moreover, because  $Le_O$  is close to unity for oxygen in air, the effect of  $Le_O$  in a hot-hydrogen cold-air system is secondary. As in Fig. 8, the effect of  $Le_O$  on the ignition location is similar to that on the ignition state, shown in Fig. 10.

#### 4. Conclusions

The spontaneous ignition of a hydrogen jet emanating from a slot into air has been considered analytically. A similarity solution of the flow field was obtained, which was combined with the species and energy conservation equations. Solutions were found using activation energy asymptotics.

The analysis yielded limiting conditions for spontaneous ignition of fuel jets. For a cool jet flowing into a hot ambient, ignition is found to be a strong function of ambient temperature and fuel Lewis number. Ignition was favored by an increase in ambient temperature or a decrease in Lewis number. For the hot jet scenario, ignition was significantly affected by the jet temperature, but only weakly affected by the oxidizer Lewis number.

Because spontaneous ignition is very sensitive to temperature, ignition is predicted to occur near the edge of the jet if the fuel is cooler than the air and on the centerline if the fuel is hotter than the air.

The present model can be extended to studies of flame extinction and to circular jet configurations.

## Acknowledgment

This work was supported by NIST grant 60NANB5D1209 under the technical management of J. Yang.

## References

- [1] CRC Handbook of Chemistry and Physics, R.C. Weast, ed., CRC Press, West Palm Beach (1979).
- [2] E.C. Magison, *Electrical Instruments in Hazardous Locations*, 2<sup>nd</sup> Edition, Instrument Society of America, Pittsburg, Pennsylvania, p304, 1972.
- [3] J. Hord, Is Hydrogen a Safe Fuel?, *International journal of hydrogen energy*, 3:157, 1978.
- [4] F.A. Williams, *Combustion Theory*, 2nd Edition, Addison-Wesley Publishing Company, Redwood City, CA, p76-84, 1985.
- [5] N. Peters, *Turbulent Combustion*, Cambridge University Press, Cambridge, England, p178-186, 2000.
- [6] A. Liñán, F.A. Williams, *Fundamental Aspects of Combustion*, Vol. 34 of Oxford Engineering Science Series, Oxford University Press, New York, p57-81, 1993.
- [7] H.G. Im, S.R. Lee, C.K. Law., Ignition in the Supersonic Hydrogen/Air Mixing Layer with Reduced Reaction Mechanisms, AIAA-1994-548 Aerospace Sciences Meeting and Exhibit, 32nd, Reno, NV, Jan 10-13, 1994
- [8] H.G. Im, B.H. Chao, J.K. Bechtold, C.K. Law, Analysis of Thermal Ignition in the Supersonic Mixing Layer, *AIAA Journal* 32, p341-349, 1994.
- [9] S.R. Lee, S.H. Chung, On the structure of Hydrogen Diffusion Flames with Reduced Kinetic Mechanisms, *Combustion Science Tech.*, 96, p247.
- [10] X.L. Zheng, C.K. Law, Ignition of Premixed Hydrogen/Air by Heated Counterflow under Reduced and Elevated Pressures, *Combustion and Flame* p136-168, 2004.
- [11] V.V. Toro, A.V. Mokhov, H.B. Levinsky, M.D. Smooke, Combined Experimental and Computational Study of Laminar, Axisymmetric Hydrogen-air Diffusion Flames, *Proc. Combust. Inst.* 30:485, 2005.
- [12] M. Chaos, R.-H. Chen, E.J. Welle, W.L., Roberts, Fuel Lewis Number Effects in Unsteady Burke Schumann Hydrogen Flames, *Combust. Sci. Tech.* 177:75, 2005.
- [13] Y., Liu, P., Pei , Asymptotic analysis on autoignition and explosion limits of hydrogen-oxygen mixtures in homogeneous systems, *International journal of hydrogen energy* , Vol. 31, No. 5, pp. 639-647, 2006.
- [14] H. Schlichting, *Boundary-Layer Theory*, Seventh Edition, McGraw-Hill, Inc., p. 127-200, 1979.
- [15] W. Bickey, The Plane Jet, *Phil. Mag. Ser. 7*, 23: 727, 1939.
- [16] V. Nayagam, F.A. Williams, Lewis-number effects on edge-flame propagation, *Journal of fluid mechanics*, 458: 219-228, 2002.

## **FIRE HAZARDS OF SMALL HYDROGEN LEAKS**

N.R. Morton<sup>1</sup>, P.B. Sunderland<sup>1</sup>, B.H. Chao<sup>2</sup>, R.L. Axelbaum<sup>3</sup>

This study examines the types of hydrogen leaks that can support combustion and the corrosive effects of hydrogen flame exposure to aluminum, galvanized steel, stainless steel, and SiC fibers. Hydrogen, methane, and propane diffusion flames on round burners were observed. Measurements included limits of quenching and blowoff for burners with diameters of 0.36 — 1.78 mm. The measured mass flowrates at the quenching limits were found to be independent of burner diameter. In terms of mass flowrates, hydrogen had the lowest quenching limit and the highest blowoff limit of the fuels considered. Hydrogen flames were found to be more corrosive than methane flames to aluminum, galvanized steel, and SiC fibers.

### **1. Introduction**

Concerns about the emissions of greenhouse gases have led to extensive consideration of hydrogen as an energy carrier. Hydrogen presents several unusual fire hazards, including high leak propensity, ease of ignition, and invisible flames. The scenario of interest in this work is that a small leak in a hydrogen system might ignite, support a flame that is difficult to detect, and degrade containment materials to the point of a catastrophic failure. This study includes experiments and analysis to identify which hydrogen leaks can support flames. Material degradation by hydrogen and methane flames also is examined here.

A Department of Energy report [1] found that hydrogen containment was the chief safety concern associated with using hydrogen as a transportation fuel and documented several catastrophic hydrogen fires.

Quenching and blowoff limits bound the leak flowrates that can support combustion. Measurements of propane quenching and blowoff flowrates were made by Matta et al. [2]. Quenching limits for methane were performed by Cheng et al. [3].

Research has been done in evaluating leak flow rates of hydrogen, methane, and propane. Swain and Swain [4] modeled and measured leak rates for diffusion, laminar, and turbulent flow regimes. They found that combustible mixtures in an enclosed space resulted more quickly for propane and hydrogen leaks than for methane leaks. Their supply pressures were the same for all fuels.

Khan et al. [5] examined the effects of raised temperatures on carbon fabric/epoxy composites, a likely material for high pressure storage tanks. Pehr [6] discusses

<sup>1</sup>Dept. of Fire Protection Engineering, Univ. of Maryland, College Park MD

<sup>2</sup>Dept. of Mechanical Engineering, Univ. of Hawaii, Manoa HI

<sup>3</sup>Dept. of Mechanical and Aerospace Engineering, Washington Univ., St. Louis MO

some of the issues associated with hydrogen containment. Utgikar and Thiesen [7] discuss the impact of hydrogen on materials, and the safety of hydrogen fuel tanks.

Thus motivated, the objectives of this work are to (1) measure limits of flaming (at quenching and blowoff) for hydrogen, methane, and propane issuing from circular burners of various sizes, and (2) examine material degradation arising from exposure to hydrogen and methane diffusion flames.

## 2. Flame Quench Scaling

A scaling analysis was developed to interpret measured flame quenching limits. These limits are the minimum flow rates required to support a diffusion flame. This analysis also yields a dimensionless crack parameter that indicates how close a given leak is to the quenching limit.

The stoichiometric length  $L_f$  of laminar gas jet diffusion flames on round burners is:

$$L_f / d = a Re = a \rho u_0 d / \mu, \quad (1)$$

where  $d$  is burner inside diameter,  $a$  is a dimensionless fuel-specific empirical constant,  $Re$  is Reynolds number,  $u_0$  is the average fuel velocity in the burner,  $\rho$  is fuel density, and  $\mu$  is fuel dynamic viscosity. The scaling of Eq. (1) arises from many theoretical and experimental studies, including Roper [8], Sunderland et al. [9], and references cited therein. Constant  $a$  here is assigned values measured by Sunderland et al. [9], as listed in Table 1.

**Table 1: Selected fuel properties of hydrogen, methane, and propane. Values for  $a$  are from Sunderland et al. [9],  $L_q$  and  $S_L$  are from Kanury [10], and  $\mu$  is from Weast and Astle [11].**

Fuel	$a$	$L_q$ [mm]	$S_L$ [cm/s]	$\mu$ [g/m-s]	$m_{fuel}$ [mg/s] predicted	$m_{fuel}$ [mg/s] measured
H <sub>2</sub>	0.236	0.51	291	8.76e-3	0.008	0.021
CH <sub>4</sub>	0.136	2.3	37.3	1.09e-2	0.085	0.112
C <sub>3</sub> H <sub>8</sub>	0.108	1.78	42.9	7.95e-3	0.063	0.031

The base of an attached jet diffusion flame is quenched by the burner. Its standoff distance can be approximated as one half of the quenching distance of a stoichiometric premixed flame. Such quenching distances typically are reported as the minimum tube diameter,  $L_q$ , through which a premixed flame can pass. It is assumed here that a jet flame can be supported only if its stoichiometric length is greater than half this quenching distance:

$$L_f \geq L_q / 2 \text{ to support a flame.} \quad (2)$$

Measurements of  $L_q$ , shown in Table 1, are taken from Kanury [10]. When combined, Eqs. (1) and (2) predict the following fuel flowrate,  $m_{fuel}$ , at the quenching limit:

$$m_{\text{fuel}} = \pi \rho u_0 d^2 / 4 = \pi L_q \mu / (8 a) . \quad (3)$$

Equation (3) indicates that the fuel mass flow rate at the quenching limit is a fuel property that is independent of burner diameter. When values of  $L_q$ ,  $\mu$ , and  $a$  from Table 1 are inserted into Eq. (3), the predicted fuel flowrates at quenching shown in Table 1 are obtained.

A crack parameter can now be derived. Assuming fully-developed, incompressible laminar flow in the burner,

$$u_0 = d^2 \Delta p / (32 \mu L_b) , \quad (4)$$

where  $\Delta p$  is the pressure drop across the burner and  $L_b$  is the burner flow passage length [12]. Equation (4) is valid for many laboratory burners. However, compressed hydrogen storage systems at pressures of up to 350 bar require more advanced models of leak flowrates such as those in [4].

Combining Eqs. (1), (2), and (4) yields, for leaks that are fully-developed, incompressible and laminar,

$$CP = a \rho d^4 \Delta p / (16 \mu^2 L_b L_q) \geq 1 \text{ to avoid flame quenching,} \quad (5)$$

where  $CP$  is the dimensionless quenching crack parameter.

### 3. Experimental

#### 3.1 Quenching and Blowoff

Quenching and blowoff limits of hydrogen, methane, and propane diffusion flames were measured. These tests involved five burners with inside diameters of 0.356, 0.711, 0.838, 1.397, and 1.778 mm. All tests were performed in quiescent air at 1.01 bar.

The burners were stainless steel nozzles that are manufactured for spray generation. The top of each burner is a curved surface with a hole passing through its axis. Fuel was delivered to each burner via a pressure regulator, a metering valve, and a rotameter.

For the quenching limit measurements, a flame approximately 5 mm long was ignited. The flow was then reduced until the flame extinguished. This was done several times for each burner and each fuel. The flames were small enough, and the experiments were done quickly enough, that there was no noticeable increase in the temperature of the burners. Measurement of the hydrogen quenching limits required special care, as small hydrogen flames are nearly invisible even in a darkened lab. Methods to identify quenching for hydrogen flames included passing paper above the burner and increasing the flowrate.

Also measured were the blowoff limits of each fuel for each burner. Blowoff limits were measured by igniting a flame and then increasing the flow rate until the flame lifted off and extinguished. The tests were performed quickly to ensure burner temperatures remained close to ambient.

Blowoff occurs when velocities in the flammable regions exceed the burning velocity. For laminar flames the relevant burning velocity is the laminar flame speed, which is shown in Table 1, however most of the present flames were turbulent just before blowoff.

### 3.2 Materials Degradation

Materials degradation tests were performed on specimens of six different materials: aluminum alloy 1100, galvanized 1006-1008 carbon steel, 304 stainless steel, 316 stainless steel, SiC yarn and SiC filament. These materials were chosen owing to their common use in gas storage systems. The specimens were approximately 100 mm long, with diameters as given in Table 2.

**Table 2: Wire and fiber specimen diameters.**

Material	Diameter (mm)
Aluminum Alloy 1100	1.01
Galvanized 1006-1008 Carbon Steel	1.04
304 Stainless Steel	1.04
316 Stainless Steel	1.01
SiC yarn	1.14
SiC filament	0.015

The burners for these tests were stainless steel tubes with inside diameters of 2.43 mm. The flames were approximately 15 mm long, and are shown in Fig. 1. These images were recorded using a Nikon D100 Digital Camera with a 60 mm focal length lens, and with ISO 1600, direct sunlight white balance, 50 ms shutter time, and f/3.8.

The samples were installed horizontally in hydrogen and methane diffusion flames at a height of 7 mm. This height was near the flame mid-height and was low enough in the methane flame to avoid soot deposition.

## 4. Results

The images of Fig. 1 show sample hydrogen and methane diffusion flames. The methane flame exhibits the familiar blue and yellow regions of hydrocarbon diffusion flames. The hydrogen flame is much dimmer and is visible only in a darkened room.

### 4.1 Quenching and Blowoff Limits

The measured fuel mass flowrates at quenching and blowoff are presented in Fig. 2. Results are shown for hydrogen, methane, and propane and are plotted as a function of burner diameter.

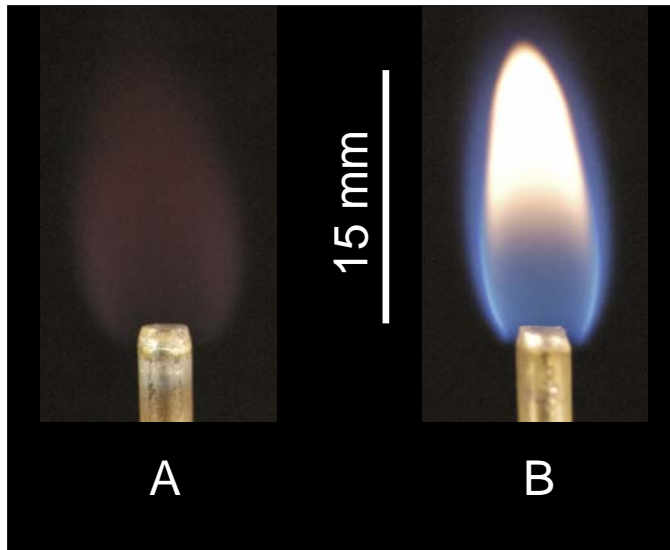


**Figure 1: Color images of (A) hydrogen flame and (B) methane flame.**

Figure 2 shows that burner mass flowrate at the quenching limit is independent of burner diameter. This finding is supported by the prediction of Eq. (3). Mass flowrates at the quenching limits increase from hydrogen to propane to methane. Results averaged for all burner diameters are shown in Table 1. The predictions of Eq. (3), also given in Table 1, capture the trends of the quenching experiments. It may be possible to improve the agreement by using different published values of quenching distances of premixed flames. The prediction may also be improved by using the available standoff distances of these fuels, instead of quenching distance, as the length scale in the analysis.

Matta et al. [3] measured quenching limits for propane, and found that flowrate is nearly independent of burner tube diameter. The prediction [3] uses to correlate the quenching data uses the standoff distance as the length scale for the analysis. Ref. [3] also noted that the predicted flow velocity for the flammable mixtures will be larger than the local flame speed at blowoff. The measurements from the present study were found to be lower for the quenching regime, but similar for blowoff.

Cheng et al. [2] measured quenching velocities for methane, and makes use of flame length correlations and measurements of standoff distance to predict when quenching will occur. The measurements from the present study were found to be smaller than the quenching measurements and predictions from [2].

The blowoff measurements in Fig. 2 show that mass flowrate at blowoff increases with burner diameter. Blowoff mass flowrates increase from methane to propane to hydrogen. This is qualitatively supported by the laminar flame speeds shown in Table 1.

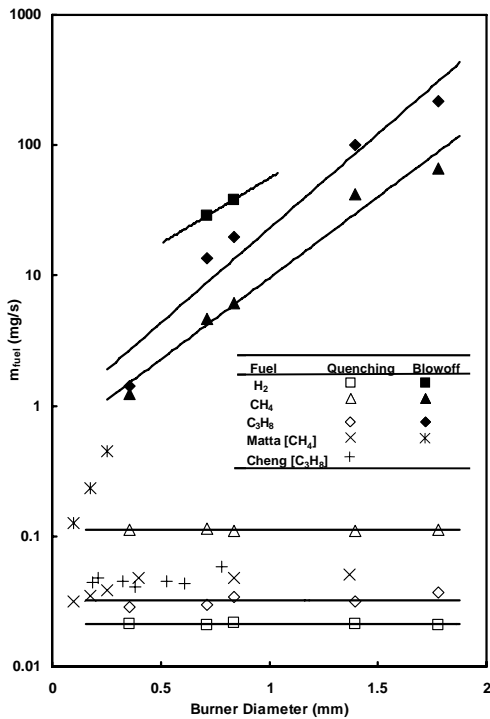


Figure 2. Measured fuel mass flowrate at the quenching and blowoff limits versus burner diameter. The lines are the fits of the present experiments.

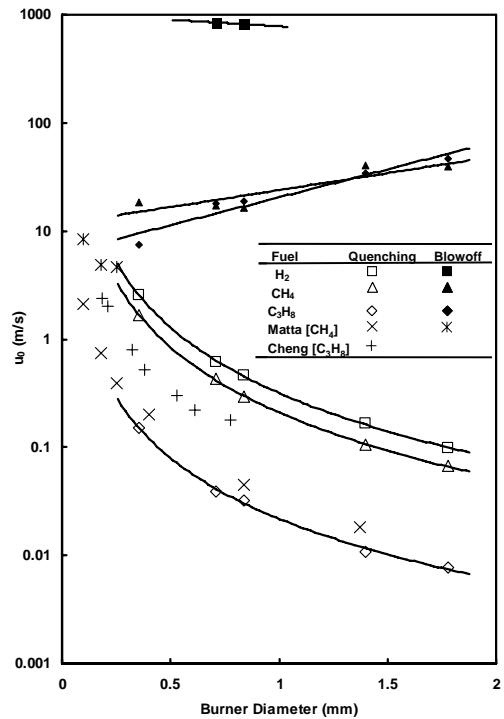
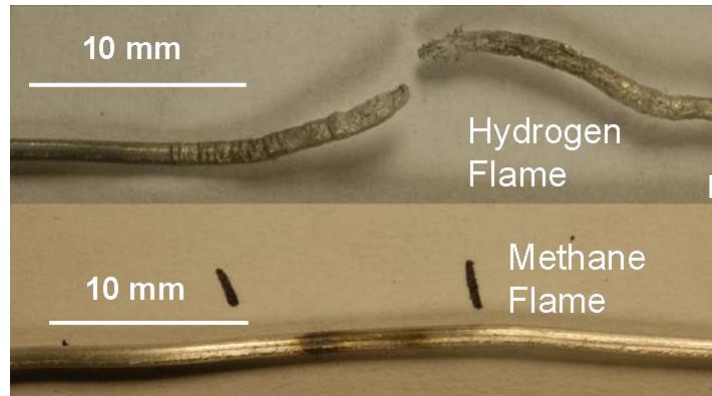


Figure 3. Measured fuel velocity at the quenching and blowoff limits versus burner diameter. The curves shown are fits of the present experiments.

Figure 3 shows the same measurements and correlations of Fig. 2 when the ordinate is changed to fuel velocity. This figure suggests a regime may exist at the smallest burner diameters where the blowoff limit is lower than the quenching limit. Burners smaller than those considered here will need to be tested to further evaluate this.

#### 4.1 Material Degradation

Aluminum alloy 1100 showed very different effects when exposed to hydrogen and methane flames. Figure 4 includes images of the aluminum samples after the 8 hour exposure. The hydrogen flame caused severe warping, as well as noticeable oxidation of the aluminum wire, after one hour. As the test continued, the distortion became more and more severe, as did the degree of oxidation, until the aluminum wire failed. The wire in the methane flame for the same exposure time did not reveal these effects. There is some slight discoloration where some soot deposited from the methane flame, but nothing approaching what was observed for they hydrogen exposure.



**Figure 4: Aluminum wires following 8 hours of exposure to (A) hydrogen flame and (B) methane flame.**

Another material that showed significant differences upon flame exposure is galvanized carbon steel. The sample exposed to a hydrogen flame showed more significant corrosion than the sample in the methane flame, see Fig. 5.

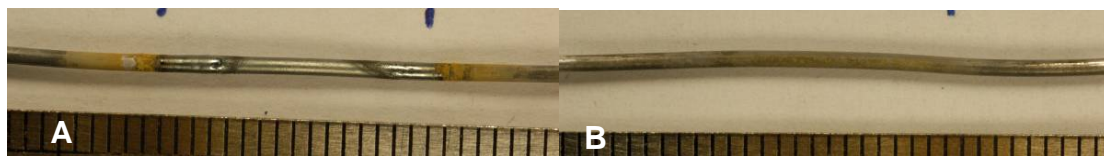


**Figure 5: Galvanized 1006-1008 Carbon steel following one hour of exposure to (A) hydrogen flame and (B) methane flame. The scale markings are in mm.**

A test of one hour exposure of the fiber yarn showed that it performed similarly in both hydrogen and methane flames. Several individual filaments failed during both exposures, but most remained intact.

Individual SiC filaments were observed to burn through during exposure to either hydrogen or methane flames. Filaments in the hydrogen and methane flames were observed to fail in 15 and 116 minutes, respectively.

## 5. Conclusions

The quenching and blowoff limits for hydrogen, methane, and propane have been measured for small round burners. Materials degradation of exposure to hydrogen and methane diffusion flames was observed. The conclusions of this study are:

The measured fuel mass flow rate at the quenching limits is independent of burner diameter. This is consistent with a simple scaling analysis based on a premixed flame quenching distance.

Hydrogen has a lower mass flowrate at quenching and a higher mass flowrate at blowoff than either methane or propane.

Hydrogen flames caused faster corrosion than methane flames on aluminum alloy 1100, galvanized steel, and SiC filaments.

## 6. Acknowledgements

This work was supported by NIST grant 60NANB5D1209 under the technical management of J. Yang. The assistance of K.B. Lim, V. Lecoustre, and C. Moran is appreciated.

## 7. References

- [1] Cadwallader, L.C. and Herring, J.S., Safety Issues with Hydrogen as a Vehicle Fuel, Report INEEL/EXT-99-00522, prepared for U.S. Department of Energy (1999).
- [2] Matta, L.M., Neumeier, Y., Lemon, B., Zinn, B.T., Characteristics of Microscale Diffusion Flames. Proceedings of the Combustion Institute v. 29. n.1, p 933-938 (2002).
- [3] Cheng, T.S., Chen, C.P., Chen, C.S., Li, Y.H., Wu, C.Y., Chao, Y.C., Characteristics of Microjet Methane Diffusion Flames. Combustion Theory and Modeling v.10, n. 5, p. 861-881 (2006).
- [4] Swain, M.R., Swain, M.N., A Comparison of H<sub>2</sub>, CH<sub>4</sub>, and C<sub>3</sub>H<sub>8</sub> Fuel Leakage in Residential Settings, Int. J Hydrogen Energy 17:807-815 (1992).
- [5] Khan, R., Kan, Z., Al-Sulaiman F., Merah, N., Fatigue Life Estimates in Woven Carbon Fabric/Epoxy Composites at Non-Ambient Temperatures. Journal of Composite Materials Vol. 36, No. 22, p. 2517-2535 (2002).
- [6] Pehr, K. Aspects of Safety and Acceptance of LH<sub>2</sub> Tank Systems in Passenger Cars. Int. J. Hydrogen Energy Vol. 21, No. 5, pp. 387-395 (2006).
- [7] Utgikar, V.P., Thiesen, T., Safety of compressed hydrogen fuel tanks: Leakage from stationary vehicles. Technology in Society 27:315-320 (2005).
- [8] Roper, F.G., The Prediction of Laminar Jet Diffusion Flame Sizes: Part I. Theoretical Model. Combust. Flame 29:219-226 (1977).
- [9] Sunderland, P.B., Mendelson, B.J., Yuan, Z.-G., Urban, D.L., Shapes of Buoyant and Nonbuoyant Laminar Jet Diffusion Flames, Combust. Flame 116:376-386 (1999).
- [10] Kanury, A.M., Introduction to Combustion Phenomena. Gordon and Breach, New York, p. 131 (1975).
- [11] Weast, R.C., Astle, M.J., CRC Handbook of Chemistry and Physics, 59th edition, CRC Press, Inc. West Palm Beach, p. F-58 (1979).
- [12] Munson, B.R., Young, D.F., Okiishi, T.H., Fundamentals of Fluid Mechanics, Wiley, Hoboken, NJ, p. 359 (2002).
- [13] Odegard, Ben C., Thomas, George J., Testing of High Pressure Hydrogen Composite Tanks. Proceedings of the 2001 DOE Hydrogen Program Review. Livermore, CA, USA.
- [14] Bahadori, M. Y., Hegde, U., Zhou, L., Liftoff and Blowoff of Jet Diffusion Flames, Paper AIAA-2002-1078, Aerospace Sciences Meeting, Reno, Nevada, January 14-17, 2002.

# Fire Hazards of Small Hydrogen Leaks

N.R. Morton, P.B. Sunderland  
University of Maryland

B.H. Chao  
University of Hawaii

R.L. Axelbaum  
Washington University

Copyright © 2007 SAE International

## ABSTRACT

This study examines the types of hydrogen leaks that can support combustion and the effects on stainless steel of long term hydrogen flame exposure. Experimental and analytical work is presented. Hydrogen diffusion flames on round burners were observed. Measurements included limits of quenching, blowoff, and piloted ignition for burners with diameters of 0.36 - 1.78 mm. Results are compared to measurements for methane and propane. A dimensionless crack parameter was identified to correlate the quenching limit measurements. Flow rates were 0.019 - 40 mg/s for hydrogen, 0.12 - 64 mg/s for methane, and 0.03 - 220 mg/s for propane. Hydrogen flames were found to be corrosive to 316 stainless steel tubing.

## INTRODUCTION

Concerns about the emissions of greenhouse gases have led to extensive consideration of hydrogen as an energy carrier. Hydrogen presents several unusual fire hazards, including high leak propensity, ease of ignition, and invisible flames. This research concerns experiments and analysis to identify which hydrogen leaks can support flames. A small leak in a hydrogen system could ignite easily, support a flame that is difficult to detect, and degrade containment materials to the point of a catastrophic failure. Hydrogen leaks can develop in pressure vessels, piping, seals, valves, pressure regulators, and pressure relief devices.

A Department of Energy report (Cadwallader and Herring, 1999) found that hydrogen containment was the chief safety concern associated with using hydrogen as a transportation fuel. This report documents several catastrophic hydrogen fires.

Research in hydrogen combustion has increased recently, but no study to date has characterized the types of hydrogen leaks that can support a flame. Absent such information, it may be difficult for the designers of a

hydrogen system to perform a cost-benefit analysis of protection against leaks.

Research has been done in quantifying leak flow rates, comparing hydrogen to methane and propane. Swain and Swain (1992) modeled and measured leak rates for diffusion, laminar, and turbulent flow regimes. They found that combustible mixtures in an enclosed space resulted more quickly for propane and hydrogen leaks than for methane leaks. However their supply pressures were the same for all fuels and thus did not reflect plans for hydrogen systems in vehicles with pressures of up to 700 bar.

The present research seeks to determine the relative fire hazards of small hydrogen leaks compared to those of methane and propane. The modeling and experimentation focus primarily on small burners and flames near the quenching limit. Experiments also consider the corrosive effects associated with the exposure of 316 stainless steel to hydrogen and methane flames.

Thus motivated, the objectives of this work are to (1) measure limits of flaming (at ignition, quenching and blowoff) for hydrogen, methane, and propane issuing from circular burners of various sizes, and (2) examine material degradation arising from hydrogen and methane diffusion flames.

## FLAME QUENCHING THEORY

A theoretical model was developed to predict flame quenching limits. These limits are the minimum flow rates sufficient to support a diffusion flame. This theory also yields a dimensionless crack parameter that indicates how close a given leak is to the quenching limit.

The stoichiometric length  $L_f$  of a laminar gas jet diffusion flames on a round burner is:

$$L_f/d = a Re = a \rho u_0 d / \mu, \quad (1)$$

where  $d$  is burner inside diameter,  $a$  is a dimensionless fuel-specific empirical constant,  $Re$  is Reynolds number,  $u_0$  is the average fuel velocity in the burner,  $\rho$  is fuel density, and  $\mu$  is fuel dynamic viscosity. The scaling of Eq. (1) arises from many theoretical and experimental studies, including Roper (1977), Sunderland et al. (1996), and references cited therein. Constant  $a$  here is assigned values measured by Sunderland et al. (1996), as listed in Table 1.

Table 1: Selected fuel properties of hydrogen, methane, and propane. Values for  $a$  are from Sunderland et al. (1996),  $L_q$  and  $S_L$  are from Kanury (1975), and  $\mu$  is from Weast and Astle (1979).

Fuel	$a$	$L_q$ [mm]	$S_L$ [cm/s]	$\mu$ [g/m-s]
H <sub>2</sub>	0.236	0.51	291	8.76e-3
CH <sub>4</sub>	0.136	2.3	37.3	1.09e-2
C <sub>3</sub> H <sub>8</sub>	0.108	1.78	42.9	7.95e-3

The base of an attached jet diffusion flame is quenched by the burner. Its standoff distance can be approximated as one half of the quenching distance of a stoichiometric premixed flame. Such quenching distances typically are reported as the minimum tube diameter,  $L_q$ , through which a premixed flame can pass. It is assumed here that a jet flame can be supported only if its stoichiometric length is greater than half this quenching distance:

$$L_f \geq L_q / 2 \text{ to support a flame.} \quad (2)$$

Measurements of  $L_q$ , shown in Table 1, are taken from Kanury (1975). When combined, Eqs. (1) and (2) predict the following fuel flowrate,  $m_{fuel}$ , at the quenching limit:

$$m_{fuel} = \pi \rho u_0 d^2 / 4 = \pi L_q \mu / (8 a). \quad (3)$$

Eq. (3) indicates that the fuel mass flow rate at the quenching limit is a fuel property that is independent of burner diameter.

A crack parameter can now be derived. Assuming fully-developed laminar flow in the burner,

$$u_0 = d^2 \Delta p / (32 \mu L_b), \quad (4)$$

where  $\Delta p$  is the pressure drop across the burner and  $L_b$  is the burner flow passage length (Munson et al., 2002).

Combining Eqs. (1), (2), and (4) yields

$$CP = a \rho d^4 \Delta p / (16 \mu^2 L_b L_q) \geq 1 \text{ to support a flame,} \quad (5)$$

where  $CP$  is the dimensionless crack parameter.

## EXPERIMENTAL

Two types of measurements were made. Quenching and blowoff limits of small-scale hydrogen, methane, and propane flames were measured. These tests involved five hemispherical burners of different diameters. Materials degradation tests were also performed, using tube burners. Flowrates were measured with calibrated rotameters.

The quenching and blowoff limit burners are hemispherical stainless steel nozzles that are manufactured for spray generation. At the apex of the hemisphere is a drilled hole of the specified diameter.

Fuel flow was commenced and ignited, creating a flame approximately 5 mm in size. The flow was then reduced until the flame extinguished. This was done several times for each burner and each fuel. The flames were small enough, and the experiment was done quickly enough, that there was no noticeable increase in the temperature of the stainless steel burners.

Inverted burns also were performed, in which the jet direction was downward. Hydrogen performed essentially the same; the quench limit was largely independent of burner orientation. Methane required less fuel to sustain a flame in the inverted position, and propane required a significantly larger flowrate to sustain an inverted flame.

Also measured were the blowoff flows of each fuel for each burner. Blowoff is achieved when the flammable regions flow faster than the laminar flame speed, which is shown in Table 1. Blowoff limits were measured by igniting a flow of fuel and then increasing the flow rate until the flame lifted off and extinguished.

Tests were also conducted to determine the corrosive effects of these flames on 316 stainless steel. For these tests the flames considered were those of Fig. 1.

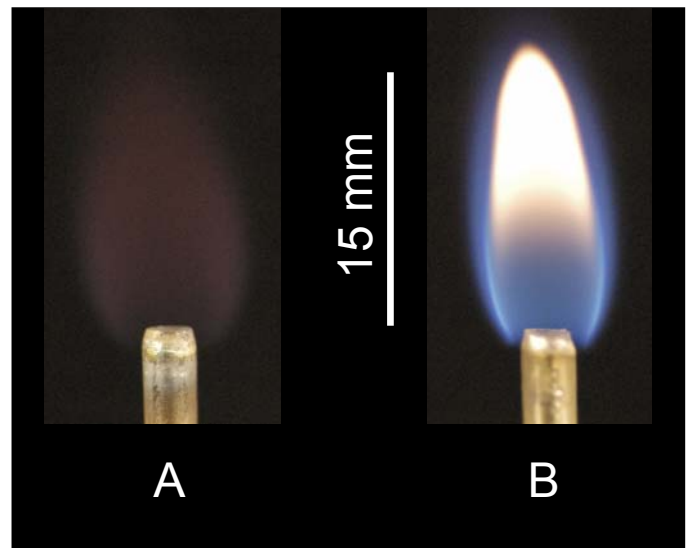


Figure 1: Color images of a representative hydrogen flame (A) and methane flame (B).

## RESULTS

Typical hydrocarbon flames burn much brighter than do hydrogen flames, as shown in Fig. 1.

The results of the quenching and blowoff studies are presented in Figs. 2 and 3. These figures also include the predictions of quenching limits from Eq. (3). Figure 2 shows the fuel mass flow rate versus diameter, while Figure 3 shows fuel velocity versus diameter for the same tests.

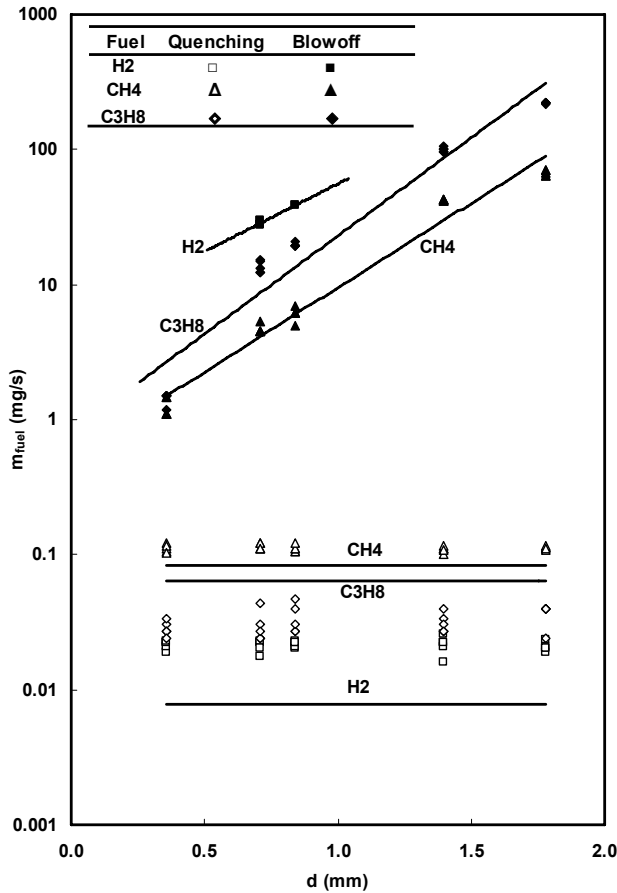


Figure 2: Measured fuel mass flowrate at the quenching and blowoff limits versus burner diameter. The lower set of three lines are the quenching limit theory of Eq. (3) for the fuels as shown. The upper set of three lines are the best fits of the blowoff measurements for the fuels as shown.

Figure 2 shows that burner mass flowrate at the quenching limit is independent of burner diameter. This finding is supported by the present theory. Hydrogen requires the smallest mass flowrate, which is expected given the wide flammability limits of hydrogen compared to methane and propane. Propane requires slightly higher mass flow rates, and methane requires the highest. The theory of Eq. (3) captures the trends of the quenching experiments, but its predicted quenching limits do not agree very well with measurements except for methane. It may be possible to improve this agreement

by using different published values of quenching distances of premixed flames.

Fig. 2 demonstrates the important finding that for each fuel there is a critical mass flowrate below which combustion is impossible. Using these results, given the flowrate of a leak, it is readily known whether the leak is flammable.

The blowoff data show that methane will reach blowoff at the lowest mass flowrate, propane next, and hydrogen will require the most mass flow to achieve blowoff. These observations are qualitatively supported by the laminar flame speeds shown in Table 1.

Figure 3 shows the same measurements of Fig. 2 where the ordinate is changed to fuel velocity. This figure suggests a regime may exist at the smallest burner diameters where the blowoff limit is lower than the quenching limit. Burners smaller than those considered here will need to be tested to further evaluate this.

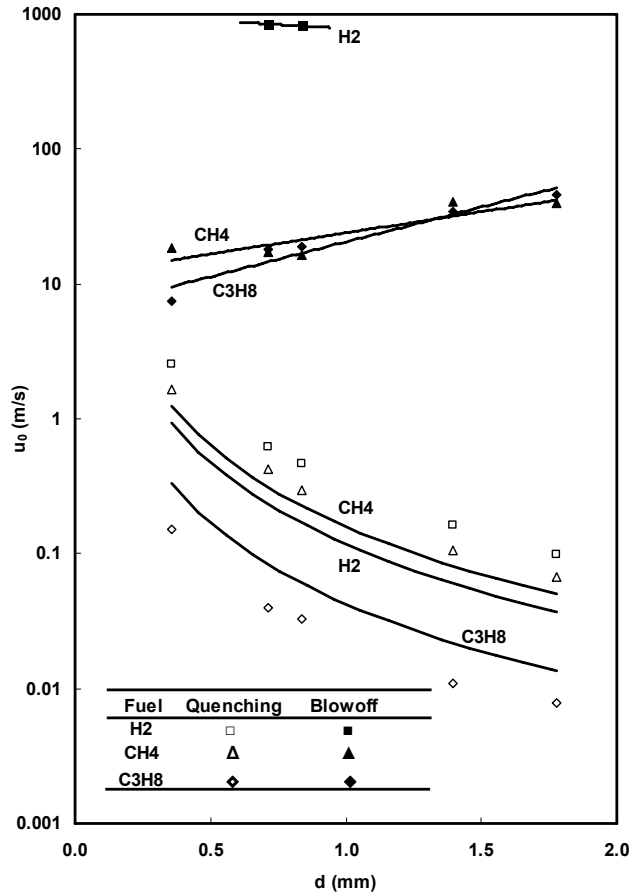


Figure 3: Measured fuel velocity at the quenching and blowoff limits versus burner diameter. The curves shown are the quenching limit theory of Eq. (3) for the fuels as shown. The lines are the best fits of the blowoff measurements for the fuels as shown.

## MATERIAL DEGRADATION

Two stainless steel burners were fabricated from 316 stainless steel. One supported a hydrogen flame and the other a methane flame, as shown in Fig. 1. Figure 4 shows the burners in their pre-test conditions.

The two flames were burned for 355 hours. The flames burned continuously except for brief periods when images were recorded. Figure 5 shows the burners after the test.

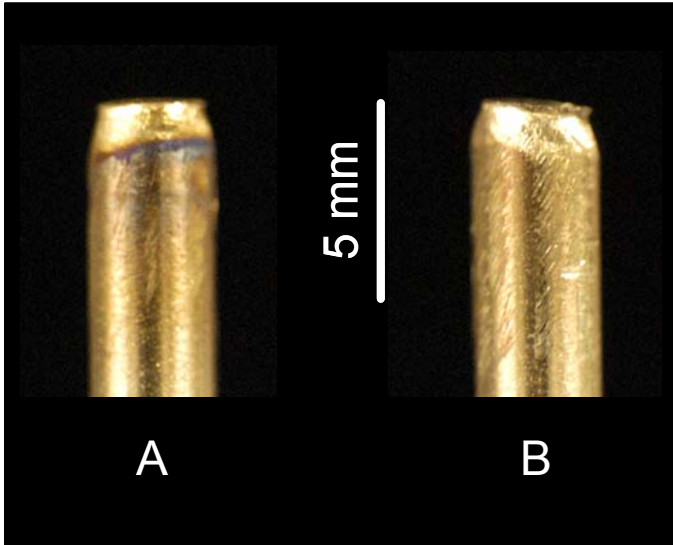


Figure 4: Color image of 316 stainless steel tube burners before the burn test. Burners A and B are for hydrogen and methane respectively.

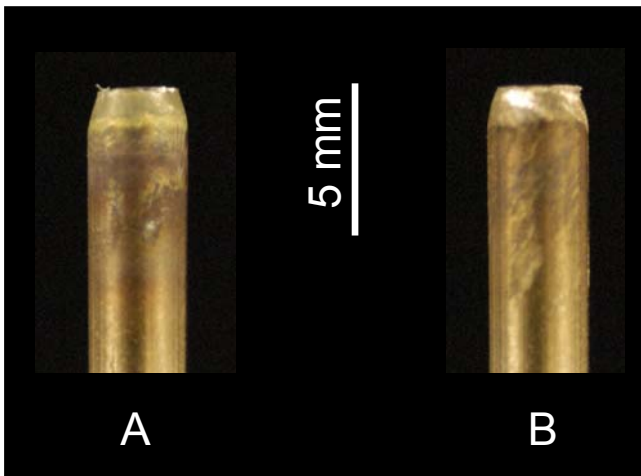


Figure 5: Color image of the burners of Fig. 4 following 355 hours of burning. Burners A and B supported hydrogen and methane flames respectively.

At the end of the test, there was noticeably more corrosion on the hydrogen burner, see Fig. 5. The

additional corrosion on the hydrogen burner is believed to arise because hydrogen flames have relatively short standoff distances and thus result in increased material temperatures.

## CONCLUSIONS

The quenching and blowoff limits for hydrogen, methane, and propane have been modeled and measured for small round burners. The fuel mass flow rate at the quenching limits was found to be independent of burner diameter. The fuel mass flow rate at blowoff was found to be considerably higher for hydrogen than for methane or propane.

Hydrogen flames were found to cause more corrosion of 316 stainless steel than methane for similar exposure conditions.

## ACKNOWLEDGMENTS

This work was supported by NIST grant 60NANB5D1209 under the technical management of J. Yang. The assistance of K.B. Lim, V. Lecoustre, and C. Moran is appreciated.

## REFERENCES

- Cadwallader, L.C. and Herring, J.S., Safety Issues with Hydrogen as a Vehicle Fuel, Report INEEL/EXT-99-00522, prepared for U.S. Department of Energy (1999).
- Kanury, A.M., *Introduction to Combustion Phenomena*. Gordon and Breach, New York, p. 131 (1975).
- Munson, B.R., Young, D.F., Okiishi, T.H., *Fundamentals of Fluid Mechanics*, Wiley, Hoboken, NJ, p. 359 (2002).
- Roper, F.G., The Prediction of Laminar Jet Diffusion Flame Sizes: Part I. Theoretical Model. *Combust. Flame* 29:219-226 (1977).
- Sunderland, P.B., Mendelson, B.J., Yuan, Z.-G., Urban, D.L., Shapes of Buoyant and Nonbuoyant Laminar Jet Diffusion Flames, *Combust. Flame* 116:376-386 (1999).
- Swain, M.R., Swain, M.N., A Comparison of H<sub>2</sub>, CH<sub>4</sub>, and C<sub>3</sub>H<sub>8</sub> Fuel Leakage in Residential Settings, *Int. J. Hydrogen Energy* 17:807-815 (1992).
- Weast, R.C., Astle, M.J., *CRC Handbook of Chemistry and Physics*, 59<sup>th</sup> edition, CRC Press, Inc. West Palm Beach, p. F-58 (1979).

## CONTACT

The corresponding author for this work is Peter B. Sunderland, pbs@umd.edu, www.enfp.umd.edu, (301) 405-3095.

## A theoretical study of spontaneous ignition of fuel jets in an oxidizing ambient with emphasis on hydrogen jets

K.B. Lim<sup>a</sup>, B.H. Chao<sup>b\*</sup>, P.B. Sunderland<sup>a</sup>, and R.L. Axelbaum<sup>c</sup>

<sup>a</sup>Department of Fire Protection Engineering, University of Maryland, College Park, MD 20742, USA;

<sup>b</sup>Department of Mechanical Engineering, University of Hawaii at Manoa, Honolulu, HI 96822, USA;

<sup>c</sup>Department of Energy, Environmental and Chemical Engineering, Washington University, St. Louis, MO 63130, USA

(Received 4 October 2007; final version received 23 April 2008)

An analysis was performed for the spontaneous ignition of a hydrogen (or other gaseous fuel) jet emanating from a slot into an oxidizing ambient (e.g., air). A similarity solution of the flow field was obtained. This was combined with the species and energy conservation equations, which were solved using activation energy asymptotics. Limits of spontaneous ignition were identified as functions of slot width, flow rate, and temperatures of the hydrogen jet and ambient gas. Two scenarios are examined: a cool jet flowing into a hot ambient and a hot jet flowing into a cool ambient. For both scenarios, ignition is favored with an increase of either the ambient temperature or the hydrogen supply temperature. Moreover, for the hot ambient scenario, a decrease in fuel Lewis number also promotes ignition. The Lewis number of the oxidizer only has a weak effect on ignition. Because spontaneous ignition is very sensitive to temperature, ignition is expected to occur near the edge of the jet if the hydrogen is cooler than the ambient gas and near the centerline if the hydrogen is hotter than the ambient gas.

**Keywords:** Spontaneous ignition; Hydrogen jets; Activation energy asymptotics; Lewis numbers; Ignition location

### Nomenclature

$a_T$	constant representing the temperature increase through reaction
$a_F$	constant representing the fuel consumption through reaction
$B$	pre-exponential factor
$c_p$	specific heat at constant pressure
$D$	mass diffusion coefficient
$Da$	Damköhler number
$\tilde{D}a$	reduced Damköhler number
$\bar{D}a$	rescaled reduced Damköhler number defined in Eq. (44)
$E$	activation temperature
$f$	nondimensional streamfunction
$h$	half width of the slot
$Le$	Lewis number
$n$	reaction order

---

\*Corresponding author. E-mail: bchao@eng.hawaii.edu

$p$	pressure
$Pr$	Prandtl number
$q_F$	heat of combustion per unit mass of fuel
$R$	ideal gas constant
$Sc$	Schmidt number
$T$	temperature
$\hat{T}$	reference temperature
$u$	flow velocity in the $x$ (streamwise) direction
$v$	flow velocity in the $y$ (transverse) direction
$W$	molecular weight
$x$	streamwise spatial coordinate
$x_0$	distance from the virtual origin of the jet to the exit of the slot
$y$	transverse spatial coordinate ( $y=0$ along the centerline)
$Y$	mass fraction
$Z$	mixture fraction

### Greek symbols

$\alpha$	parameter defined as $\alpha = (\tilde{T}_\infty - \tilde{T}_0)/\tilde{Y}_{F,0}$
$\beta$	parameter defined as $\beta = (\tilde{T}_0 - \tilde{T}_\infty)/\tilde{Y}_{O,\infty}$
$\varepsilon$	small parameter used for asymptotic expansion
$\phi$	perturbation of species concentration in the reaction region
$\theta$	perturbation of temperature in the reaction region
$\lambda$	thermal conductivity
$\mu$	viscosity
$\nu$	stoichiometric coefficient
$\rho$	gas density
$\psi$	streamfunction
$\eta$	similarity variable
$\sigma$	stoichiometric oxidizer to fuel mass ratio
$\xi$	stretched spatial coordinate in the reaction region along the streamwise direction for the hot jet scenario
$\zeta$	stretched spatial coordinate in the reaction region along the transverse direction

### Subscripts

0	value of variables at the exit of the slot
$F$	fuel
$f$	frozen solution
$I$	ignition state
$O$	oxidizer
$\infty$	ambient condition

### Superscripts

$\sim$	nondimensional quantity
$\wedge$	rescaled nondimensional quantity based on $\hat{T}$

## 1. Introduction

Concerns about the emissions of greenhouse gases and supply of oil have led to extensive consideration of hydrogen as a major fuel carrier. Nonetheless, hydrogen presents several unusual fire hazards, including high leak propensity, ease of ignition, and invisible flames. For example, heated air jets flowing into hydrogen will ignite spontaneously at an air temperature of 913 K [1]. This is cooler than for other fuels [1, 2], including gasoline and methane, and is not much higher than the autoignition temperature of stoichiometric hydrogen/air mixtures, 858 K [3]. Occasional unintended hydrogen leaks will be unavoidable, and some may involve heated hydrogen and/or air. Thus an improved understanding of limits of spontaneous ignition of hydrogen jets is sought here, with the aid of activation-energy asymptotics.

Zheng and Law [4] identified ignition limits of premixed hydrogen–air flames where ignition was by a heated counterflowing stream. The ignition limits of non-premixed hydrogen–air jets will be different from those of premixed counterflowing streams because of the non-premixed nature and the absence of strain due to counterflow heating.

Thermal ignition in subsonic [5] and supersonic [6, 7] mixing layers has been studied by activation energy asymptotics and numerically with one-step reaction as well as reduced mechanisms. Im et al. [6] employed a reduced mechanism to analyze thermal ignition in a supersonic hydrogen/air mixing layer and obtained ignition characteristics over a wide range of conditions. These findings are particularly applicable to scramjets. Lee and Chung [8] investigated the different combustion regimes in a stagnant mixing layer by employing Damköhler-number and activation-energy asymptotics, based on an eight-step reduced mechanism. Law and co-workers [9, 10] investigated the ignition of hydrogen and air in a mixing layer by using reduced reaction mechanisms that they developed.

Toro et al. [11] examined in detail the structure of laminar hydrogen jet flames both experimentally and numerically. Chaos et al. [12] examined Lewis-number effects in unsteady laminar hydrogen jet flames, which will have different effects compared to steady laminar hydrogen jet flames. Liu and Pei [13] examined autoignition and explosion limits of hydrogen–oxygen mixtures in homogeneous systems, which involved reduced mechanisms. Dryer et al. [14] examined spontaneous ignition of pressurized releases of hydrogen and natural gas into air. This investigation involved multi-dimensional transient flows with shock formation, reflection and interactions that resulted in the transition to turbulent jet nonpremixed combustion. This is a different aspect of risk, associated with rapid failures of pressure vessels, as compared to the scenario being considered here, which involves small leaks/cracks that are undetected, and that ignite spontaneously when the limits are reached.

The present study applies asymptotic analysis to investigate the spontaneous ignition of a laminar jet of hydrogen, or another gaseous fuel, leaking through a crack into an oxidizing ambient. Asymptotic flame theories can provide valuable insights into combustion reactions [15–18]. Quantitative and predictive derivations can be made using the concept of distinguished limits in activation energy asymptotics. Based largely on the concept of Zel'dovich number, asymptotic analysis enables evaluation of temperature effects on reaction rates despite the narrowness of the reaction zone relative to the transport zones of the flame structure.

The crack is taken to be straight and long, yielding a two-dimensional flow field. The ignition analysis identifies limits of spontaneous ignition. Unfortunately, comparisons with experiments are not possible because no study to date of spontaneous ignition of nonpremixed jets has measured the key phenomena analyzed here.

The objectives of this work are to: (1) develop a model of spontaneous ignition for two cases: a cool fuel jet flowing into heated ambient gas and a heated fuel jet flowing into cool ambient gas; (2) identify limits of spontaneous ignition as functions of slot width, flow rate, fuel Lewis

number, and temperatures of the fuel jet and the ambient gas; and (3) identify the location of ignition.

## 2. Formulation

The problem of interest is a steady, isobaric laminar jet of fuel (e.g. hydrogen) at temperature  $T_0$  issuing from a rectangular slot into an oxidizing environment (e.g. atmospheric air) at a temperature of  $T_\infty$ , as shown schematically in Figure 1. Spontaneous ignition occurs when either  $T_0$  or  $T_\infty$  is sufficiently high that the weak reaction between the fuel and the oxidizer transitions to a vigorous burning flame. This study analyzes the ignition state as a function of various physical properties including Lewis number,  $T_0$ ,  $T_\infty$ , the flow velocity at the slot exit,  $u_0$ , and the width of the slot. The slot is considered sufficiently long that end effects are negligible. The reaction chemistry is assumed to follow a single-step, overall, irreversible reaction with second order Arrhenius kinetics and a high activation energy.

With the above problem definition, conservation of mass and momentum are given by

$$\frac{\partial(\rho u)}{\partial x} + \frac{\partial(\rho v)}{\partial y} = 0, \quad (1)$$

$$\rho u \frac{\partial u}{\partial x} + \rho v \frac{\partial u}{\partial y} - \frac{\partial}{\partial y} \left( \mu \frac{\partial u}{\partial y} \right) = 0, \quad (2)$$

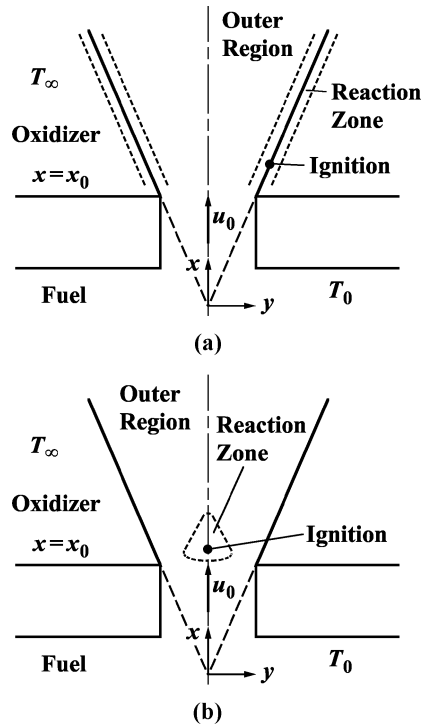


Figure 1. Schematic of slot and fuel (e.g. hydrogen) leak for the (a) hot ambient and (b) hot jet cases.

which are to be solved subject to the boundary conditions

$$y = 0, x = x_0 : u = u_0, v = 0; x > x_0 : \partial u / \partial y = 0, v = 0, \tag{3}$$

$$y \rightarrow \infty : u \rightarrow 0. \tag{4}$$

Introducing a streamfunction  $\psi$  of the form

$$\rho u = \rho_\infty u_0 (\partial \psi / \partial y), \rho v = -\rho_\infty u_0 (\partial \psi / \partial x), \tag{5}$$

such that Eq. (1) is satisfied, transforming the coordinates from  $(x, y)$  to  $(\tilde{x}, \eta)$  where

$$\tilde{x} = x/x_0, \eta = [\rho_\infty u_0 / (6 \mu_\infty x_0)]^{1/2} \tilde{x}^{-2/3} \int_0^y (\rho / \rho_\infty) dy, \tag{6}$$

and defining

$$\psi = [6 \mu_\infty x_0 / (\rho_\infty u_0)]^{1/2} \tilde{x}^{1/3} f(\eta), \tag{7}$$

Equations (2)–(4) are transformed to

$$(f''' / 2) + f f'' + f'^2 = 0, \tag{8}$$

$$\eta = 0: f = f'' = 0, f' = 1; \eta \rightarrow \infty: f' \rightarrow 0. \tag{9}$$

The notations used in this study are listed in the Nomenclature section. A similarity solution is assumed to exist so that  $f$  is a function of  $\eta$  only. Solving Equations (8)–(9) following Bickey [19] and Schlichting [20] yields  $f = \tanh \eta$ . In these equations,  $x_0$  is the value of  $x$  at the slot exit from the virtual origin of the jet, which can be determined by the conservation of the  $x$ -momentum across the slot exit, given by

$$x_0 = 3 \rho_0^2 \left[ \int_{-h}^h (u_{x=x_0^-})^2 dy \right]^2 / (32 u_0^3 \rho_\infty \mu_\infty). \tag{10}$$

Applying the coordinate transformation and the solution of the momentum equation to the energy and species conservation equations, we obtain

$$\frac{1}{Pr} \frac{\partial^2 \tilde{T}}{\partial \eta^2} + 2(\tanh \eta) \frac{\partial \tilde{T}}{\partial \eta} - 6(\operatorname{sech}^2 \eta) \tilde{x} \frac{\partial \tilde{T}}{\partial \tilde{x}} = -Da \tilde{x}^{4/3} \tilde{Y}_F \tilde{Y}_O \tilde{T}^{-1} \exp(-\tilde{E}/\tilde{T}), \tag{11}$$

$$\frac{1}{Sc_F} \frac{\partial^2 \tilde{Y}_F}{\partial \eta^2} + 2(\tanh \eta) \frac{\partial \tilde{Y}_F}{\partial \eta} - 6(\operatorname{sech}^2 \eta) \tilde{x} \frac{\partial \tilde{Y}_F}{\partial \tilde{x}} = Da \tilde{x}^{4/3} \tilde{Y}_F \tilde{Y}_O \tilde{T}^{-1} \exp(-\tilde{E}/\tilde{T}), \tag{12}$$

$$\frac{1}{Sc_O} \frac{\partial^2 \tilde{Y}_O}{\partial \eta^2} + 2(\tanh \eta) \frac{\partial \tilde{Y}_O}{\partial \eta} - 6(\operatorname{sech}^2 \eta) \tilde{x} \frac{\partial \tilde{Y}_O}{\partial \tilde{x}} = Da \tilde{x}^{4/3} \tilde{Y}_F \tilde{Y}_O \tilde{T}^{-1} \exp(-\tilde{E}/\tilde{T}), \tag{13}$$

which are to be solved subject to

$$\eta = 0, \tilde{x} = 1 : \tilde{T} = \tilde{T}_0, \tilde{Y}_F = \tilde{Y}_{F,0}, \tilde{Y}_O = 0, \tag{14}$$

$$\eta = 0, \tilde{x} > 1 : \partial \tilde{T} / \partial \eta = \partial \tilde{Y}_F / \partial \eta = \partial \tilde{Y}_O / \partial \eta = 0, \tag{15}$$

$$\eta \rightarrow \infty : \tilde{T} \rightarrow \tilde{T}_\infty, \tilde{Y}_F \rightarrow 0, \tilde{Y}_O \rightarrow \tilde{Y}_{O,\infty}. \tag{16}$$

Downloaded By: [Chao, B. H.] At: 19:40 28 November 2008

In the above,

$$\tilde{T} = \frac{c_p T}{q_F}, \tilde{Y}_F = Y_F, \tilde{Y}_O = \frac{Y_O}{\sigma}, Da = \frac{6 x_0 v_O c_p p B}{W_F q_F R u_0}, \tilde{E} = \frac{c_p E}{q_F},$$

$$Pr = \frac{\mu}{\lambda/c_p}, Sc_j = \frac{\mu}{\rho D_j}, Le_j = \frac{\lambda/c_p}{\rho D_j}, \sigma = \frac{v_O W_O}{v_F W_F}.$$

The values of  $c_p$ ,  $\rho \lambda$ ,  $\rho \mu$ , and  $\rho^2 D_j$  are considered constant. The ideal gas equation of state has been adopted in the derivation of Equations (11)–(13).

In the non-reactive limit, solving Equations (11)–(13), but without the reaction terms, subject to Equations (14)–(16) gives the frozen solutions,

$$\tilde{T}_f = \tilde{T}_\infty + (\tilde{T}_0 - \tilde{T}_\infty) (\operatorname{sech}^{2Pr} \eta) / \tilde{x}^{1/3}, \tag{17}$$

$$\tilde{Y}_{F,f} = \tilde{Y}_{F,0} (\operatorname{sech}^{2Sc_F} \eta) / \tilde{x}^{1/3}, \tag{18}$$

$$\tilde{Y}_{O,f} = \tilde{Y}_{O,\infty} [1 - (\operatorname{sech}^{2Sc_O} \eta) / \tilde{x}^{1/3}]. \tag{19}$$

**2.1. Cool jet flowing into a hot ambient ( $T_\infty > T_0$ )**

In the presence of a weak reaction, the temperature is increased from its frozen value by a small,  $O(\varepsilon)$  amount where  $\varepsilon = \tilde{T}_\infty^2 / \tilde{E}$  while the reactant concentrations are reduced from their respective frozen values by an  $O(\varepsilon)$  amount. Because of the high activation energy, ignition is primarily controlled by temperature and occurs near  $\eta \rightarrow \infty$  if successful. Away from this high temperature region, the reaction is negligible and can be considered frozen. In the outer, chemically frozen region, the solutions are similar to Equations (17)–(19) but with an  $O(\varepsilon)$  change in their values. With the application of Equations (14) and (15), the solutions of  $\tilde{T}$  and  $\tilde{Y}_F$  are given by

$$\tilde{T} = (\tilde{T}_\infty + \varepsilon a_T) - [(\tilde{T}_\infty - \tilde{T}_0) + \varepsilon a_T] (\operatorname{sech}^{2Pr} \eta) / \tilde{x}^{1/3} + O(\varepsilon^2), \tag{20}$$

$$\tilde{Y}_F = \varepsilon a_F + (\tilde{Y}_{F,0} - \varepsilon a_F) (\operatorname{sech}^{2Sc_F} \eta) / \tilde{x}^{1/3} + O(\varepsilon^2). \tag{21}$$

The solution of  $\tilde{Y}_O$  is not important to the analysis.

In the inner, reactive region, a stretched spatial inner variable is defined as

$$\zeta = \tilde{Y}_{F,0} (\operatorname{sech} \eta)^{2Pr} / (\varepsilon \tilde{x}^{1/3}), \tag{22}$$

while the solutions are expanded as

$$\tilde{T} = \tilde{T}_\infty + \varepsilon (\theta - \alpha \zeta) + O(\varepsilon^2), \tag{23}$$

$$\tilde{Y}_F = \varepsilon^{Le_F} (\tilde{Y}_{F,0} / \tilde{x}^{1/3})^{1 - Le_F} \zeta^{Le_F} + O(\varepsilon), \tag{24}$$

$$\tilde{Y}_O = \tilde{Y}_{O,\infty} + O(\varepsilon). \tag{25}$$

Equation (24) is obtained by considering  $Le_F$  to be sufficiently smaller than unity, as for hydrogen. Substitution of Equations (22)–(25) into Equation (11) and expanding in orders of  $\varepsilon$  yield

$$\zeta^2 (\partial^2 \theta / \partial \zeta^2) = - \tilde{D}a \zeta^{Le_F} \exp(\theta - \alpha \zeta), \tag{26}$$

Downloaded By: [Chao, B. H.] At: 19:40 28 November 2008

where  $\alpha = (\tilde{T}_\infty - \tilde{T}_0)/\tilde{Y}_{F,0}$  is the parameter indicating the effect of temperature difference and  $\tilde{D}a$  is the reduced Damköhler number defined as

$$\tilde{D}a = Da \tilde{Y}_{O,\infty} \tilde{x}^{4/3} [\tilde{Y}_{F,0}/(\varepsilon \tilde{x}^{1/3})]^{1-Le_F} \exp(-\tilde{E}/\tilde{T}_\infty)/(4Pr\tilde{T}_\infty). \tag{27}$$

The boundary conditions required to solve this equation can be found by applying Equations (22) and (23) to Equation (16), and matching the inner and outer solutions to yield

$$\zeta = 0: \theta = 0; \zeta \rightarrow \infty: \partial\theta/\partial\zeta \rightarrow 0, \theta \rightarrow a_T. \tag{28}$$

For the case of  $Le_F$  close to unity, as for most of gaseous fuels, Equation (24) is modified to

$$\tilde{Y}_F = \varepsilon(\phi_F + \zeta) + O(\varepsilon^2), \tag{29}$$

Substitution of Equations (22), (23), (25) and (29) into Equations (11) and (12) gives

$$\zeta^2 (\partial^2\theta/\partial\zeta^2) = -\tilde{D}a(\phi_F + \zeta) \exp(\theta - \alpha\zeta), \tag{30}$$

$$\partial^2(\theta + \phi_F)/\partial\zeta^2 = 0, \tag{31}$$

where  $\tilde{D}a$  is given by Equation (27) with  $Le_F = 1$ . Applying the boundary conditions of Equation (16) and the conditions obtained by matching the inner and outer solutions as before, we obtain Equation (28) and  $\phi_F = -\theta$ , which can be applied to Equation (30) to yield

$$\zeta^2 (\partial^2\theta/\partial\zeta^2) = -\tilde{D}a(\zeta - \theta) \exp(\theta - \alpha\zeta). \tag{32}$$

### 2.2. Hot jet flowing into a cool ambient ( $T_0 > T_\infty$ )

For the case of a hot jet issuing into a cold ambient, any ignition will occur near the jet centerline,  $\eta = 0$ . Moreover, because the jet will be cooled by the cold ambient gas along the flow, ignition is expected to occur near the slot exit. The analysis is similar to that in Section 2.1, except that  $\varepsilon = \tilde{T}_0^2/\tilde{E}$ , the inner spatial variables are defined as

$$\zeta = \eta (Pr \tilde{Y}_{O,\infty}/\varepsilon)^{1/2}, \quad \xi = \tilde{Y}_{O,\infty}(\tilde{x} - 1)/(3\varepsilon), \tag{33}$$

and the inner solutions are expanded as

$$\tilde{T} = \tilde{T}_0 + \varepsilon[\theta - \beta(\zeta^2 + \xi)] + O(\varepsilon^2), \tag{34}$$

$$\tilde{Y}_F = \tilde{Y}_{F,0} + O(\varepsilon), \tag{35}$$

$$\tilde{Y}_O = \varepsilon(\phi_O + Le_O\zeta^2 + \xi) + O(\varepsilon^2). \tag{36}$$

Substitution of Equations (33)–(36) into Equations (11) and (13) leads to

$$\frac{\partial^2\theta}{\partial\zeta^2} - 2\frac{\partial\theta}{\partial\xi} + \frac{1}{Le_O} \frac{\partial^2\phi_O}{\partial\zeta^2} - 2\frac{\partial\phi_O}{\partial\xi} = 0, \tag{37}$$

$$\frac{\partial^2\theta}{\partial\zeta^2} - 2\frac{\partial\theta}{\partial\xi} = -\tilde{D}a(\phi_O + Le_O\zeta^2 + \xi) \exp[\theta - \beta(\zeta^2 + \xi)], \tag{38}$$

with the initial and boundary conditions

$$\xi = 0: \theta = \phi_O = 0, \quad (39)$$

$$\zeta = 0 \text{ and } \zeta \rightarrow \infty, \xi > 0: \partial \theta / \partial \zeta = \partial \phi_O / \partial \zeta = 0, \quad (40)$$

where  $\beta = (\tilde{T}_0 - \tilde{T}_\infty) / \tilde{Y}_{O,\infty}$  and  $\tilde{D}a$  is

$$\tilde{D}a = \varepsilon [Da \tilde{Y}_{F,0} / (\tilde{T}_0 \tilde{Y}_{O,\infty})] \exp(-\tilde{E} / \tilde{T}_0). \quad (41)$$

Ignition is considered successful when the heat generation through reaction is sufficient to compensate for the heat loss from the jet to the ambient at any location, i.e. when the reaction is self-sustainable. The ignition criterion is then defined as

$$(\partial \theta / \partial \xi)_{\zeta=0} \geq \beta \text{ or } \partial \theta / \partial \zeta \geq 2 \beta \zeta \text{ at any } \xi. \quad (42)$$

The smallest value of  $\xi$  that satisfies either of these conditions represents the first point that thermal runaway would occur and is identified as the location of ignition.

### 3. Results and Discussion

#### 3.1. Cool jet flowing into a hot ambient ( $T_\infty > T_0$ )

For this case, Equation (26) subject to Equation (28) was solved by a fourth order Runge-Kutta method. The results are shown in Figure 2, a plot of the reaction temperature increase,  $a_T$ , versus reduced Damköhler number,  $\tilde{D}a$ , for selected values of  $\alpha = (\tilde{T}_\infty - \tilde{T}_0) / \tilde{Y}_{F,0}$  and  $Le_F = 0.6$ . This reveals the lower and middle branches of an S-shaped ignition/extinction curve [3,15,16]. In each such curve, there is a maximum value of  $\tilde{D}a$  above which a solution does not exist. For values of  $\tilde{D}a$  smaller than this critical value, there are two solutions for each  $\tilde{D}a$ . The critical value of  $\tilde{D}a$  represents the transition from weak reaction to vigorous burning, and is defined as the ignition state,  $\tilde{D}a_I$ . The lower branch, showing an increase of temperature with higher reaction rate, is the physically realistic branch. The middle branch represents conditions that are not physically possible. Spontaneous ignition is successful for any  $\tilde{D}a$  greater than  $\tilde{D}a_I$ .

Figure 2 indicates that a decrease in  $\alpha$  reduces  $\tilde{D}a_I$ , which means that ignition is favored. Such a decrease can be accomplished by increasing the jet temperature,  $\tilde{T}_0$ ,  $q_F/c_p$ . For these cases, reaction is enhanced when  $\alpha$  is reduced such that it is easier to ignite the reactants. A fuel such as hydrogen (which has  $q_F/c_p$  of roughly 78 600 K in air), is hence more ignitable as compared to fuels such as methane ( $q_F/c_p = 36 800$  K) and isooctane ( $q_F/c_p = 33 800$  K) when the flow conditions are the same. As an example, for  $Y_{F,0} = 1$ ,  $T_0 = 300$  K and  $T_\infty = 1000$  K, the values of  $\alpha$  are 0.0089, 0.019 and 0.021 for hydrogen, methane and isooctane, respectively.

Parameter  $\alpha$  also can be changed by variations in the ambient temperature,  $\tilde{T}_\infty$ , or the reactant mass fraction in the fuel supply,  $\tilde{Y}_{F,0}$ , but these changes result in a simultaneous change of  $\tilde{D}a$  as can be seen from Equation (27). To investigate the effects of  $\tilde{T}_\infty$  at fixed  $\tilde{D}a$ , a rescaling is required. The rescaling is performed by specifying a reference value of  $\tilde{T}_\infty$  as  $\hat{T}_\infty$ , defining rescaled parameters  $\hat{\varepsilon} = \tilde{T}_\infty^2 / \tilde{E}$ ,  $\hat{a}_T = (\tilde{T}_\infty / \hat{T}_\infty)^2 a_T$  and

$$\hat{D}a = Da \tilde{Y}_{O,\infty} \tilde{x}^{4/3} [\tilde{Y}_{F,0} / (\hat{\varepsilon} \tilde{x}^{1/3})]^{(1-Le_F)} \exp(-\tilde{E} / \hat{T}_\infty) / (4Pr \hat{T}_\infty). \quad (43)$$

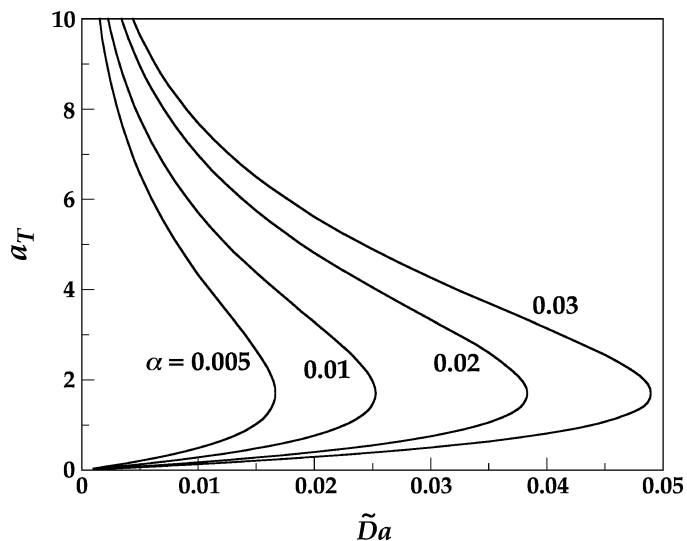


Figure 2. Reaction temperature increase  $a_T$  versus reduced Damköhler number  $\tilde{D}a$  for selected values of  $\alpha = (\tilde{T}_\infty - \tilde{T}_0)/\tilde{Y}_{F,0}$  with  $Le_F = 0.6$ . The plot is for a cool jet flowing into a hot ambient.

and plotting the results in terms of rescaled variables  $\hat{a}_T$  and  $\hat{D}a$ . In this section,  $\tilde{T}_0 = 0.00382$ ,  $\tilde{E} = 0.127$ ,  $\tilde{Y}_{F,0} = 1$  and  $\tilde{T}_\infty = 0.01382$  were used to exhibit the ignition behavior. These data correspond to  $T_0 = 300$  K,  $E = 10\,000$  K,  $T_{\infty,ref} = 1090$  K for hydrogen. The rescaled results are shown in Figure 3. Here an increase in  $\tilde{T}_\infty$ , which increases  $\alpha$  without changing  $\hat{D}a$ , is seen to favor ignition. This also is physically realistic because more heat is transferred to the cold fuel

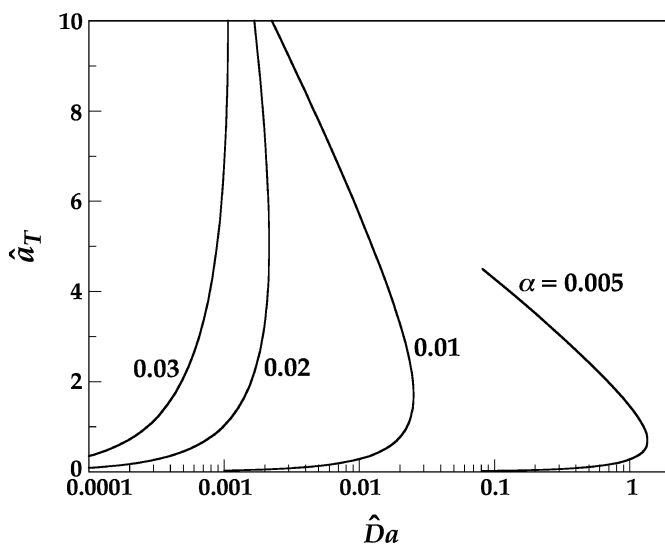


Figure 3. Rescaled plot of  $\hat{a}_T$  versus  $\hat{D}a$  from Figure 2 when changes of  $\alpha$  is caused by variations in  $\tilde{T}_\infty$ , with  $\tilde{T}_0 = 0.00382$ ,  $\tilde{E} = 0.127$ ,  $\tilde{Y}_{F,0} = 1$ , and  $\tilde{T}_\infty = 0.01382$ .

flow at a higher rate when the ambient is at a higher temperature. For the same reason, when the kinetic data are unchanged, an increased  $\tilde{T}_\infty$  yields ignition closer to the exit of the slot. Note that the reduced Damköhler number shown in Equation (27) is a function of the axial distance from the virtual origin of the jet.

When the variation of  $\alpha$  is caused by the change of  $\tilde{Y}_{F,0}$ , a similar rescaling of  $\tilde{D}a$  by defining a reference value of  $\tilde{Y}_{F,0}$  is necessary. The result is qualitatively the same as that presented in Figure 2, which is expected because an increase in  $\tilde{Y}_{F,0}$  (a decrease in  $\alpha$ ) results in a greater fuel concentration in the reaction region and a higher reaction rate.

To investigate the influence of fuel Lewis number,  $Le_F$ , on ignition, a reference fuel Lewis number is necessary. As can be seen after Equation (16),  $Le_F$  is defined as the mixture thermal diffusivity divided by the mass diffusivity of fuel into the mixture. Specifying  $Le_F = 1$  as the reference  $Le_F$ , we define a second rescaled reduced Damköhler number from Equation (43) as

$$\bar{D}a = Da \tilde{Y}_{O,\infty} \tilde{x}^{4/3} \exp(-\tilde{E}/\hat{T}_\infty)/(4 Pr \hat{T}_\infty). \tag{44}$$

The results for  $\alpha = 0.02$  are presented in Figure 4 by plotting  $a_T$  versus  $\bar{D}a$ . The curve for  $Le_F = 1$  was obtained by solving Equation (32) subject to Equation (28). For demonstration purpose, a value of  $\tilde{x} = 2$  also is specified whenever Equation (44) is used. Only quantitative differences exist when another value of  $\tilde{x}$  is adopted. Figure 4 shows that a decrease in  $Le_F$  for fixed  $\bar{D}a$  favors ignition. This occurs because a smaller  $Le_F$  implies that fuel species diffuse more quickly into the hot oxidizer. A fuel such as hydrogen, which has  $Le_F$  of 0.6 or less in mixtures of nitrogen, is hence more ignitable as compared to fuels such as isooctane and methane, which have higher  $Le_F$ , under the same conditions. Nayagam and Williams [21] found that in a one-dimensional model of steady motion of edges of reaction sheets, increasing the Lewis number decreases the propagation velocity at small Damköhler numbers. This indicates that the reaction rate is raised when  $Le_F$  is reduced, which agrees with the findings of Figure 4.

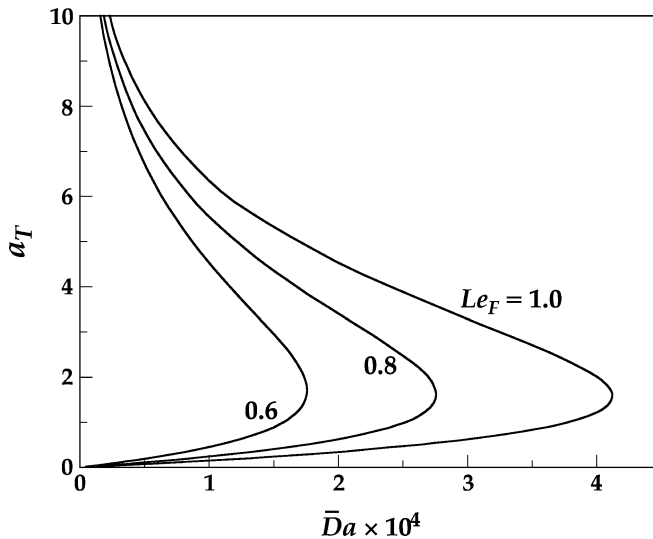


Figure 4. Reaction temperature increase  $a_T$  versus reduced Damköhler number  $\bar{D}a$  for selected values of  $Le_F$ , with  $\alpha = 0.02$ , and  $\tilde{x} = 2$ , cool jet flowing into hot ambient.

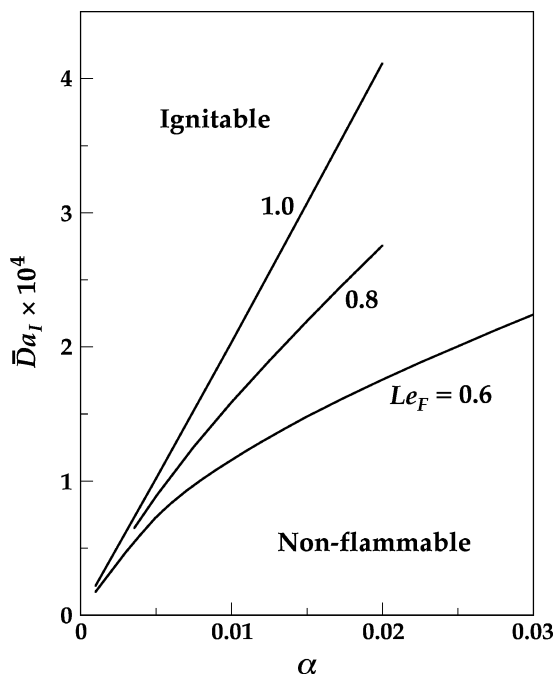


Figure 5. Variation of the ignition state,  $\bar{D}a_I$ , versus  $\alpha$  (which is changed by variations in  $\tilde{T}_0$ ) for selected values of  $Le_F$ , with  $\tilde{E} = 0.127$ ,  $\tilde{T}_\infty = 0.01382$ ,  $\tilde{x} = 2$  and  $\tilde{T}_\infty = 0.02382$ , cool jet flowing into hot ambient.

The ignition states for the three values of  $Le_F$  adopted in Figure 4 are shown in Figure 5 by plotting the reduced Damköhler number at ignition,  $\bar{D}a_I$ , versus  $\alpha$  with fixed  $\tilde{T}_\infty = 0.02382$ . Although the selection of  $\tilde{T}_\infty$  may be quantitatively unrealistic for values of  $\alpha$  greater than 0.02, the proper qualitative behavior is exhibited. The value is chosen such that Figures 4 and 5 are plotted using the same parameters. The region above the curve for any  $Le_F$  is the region in which ignition is successful and a flame can be established while the region below the curve is the region where ignition fails. The plot shows that ignition is favored when  $\alpha$  is decreased since  $\bar{D}a_I$  is reduced, as discussed earlier. Moreover, as  $Le_F$  is decreased, the ignitable region is broadened such that ignition occurs more easily. This figure again shows that hydrogen is more diffusive and, hence, more ignitable (more dangerous from a fire safety perspective) than other hydrocarbon fuels, which is consistent with the findings shown in Figure 4.

For cases where the variation of  $\alpha$  is caused by a change of  $\tilde{T}_\infty$ , the ignition state is presented in Figure 6, which shows that ignition is favored for larger  $\alpha$  and smaller  $Le_F$ , as was seen in Figures 3–5. The effect of the reaction order of the fuel, which can be obtained by replacing  $\tilde{Y}_F$  with  $\tilde{Y}_F^{n_F}$  in the reaction term of Equations (11)–(13), also has been studied. The results show that ignition is favored when the reaction order is increased because of an increased reaction rate. Its effect, however, is much weaker as compared to other effects already discussed.

### 3.2. Hot jet flowing into a cool ambient ( $T_0 > T_\infty$ )

For this scenario, ignition is expected to occur near the centerline because the fuel is hotter than the ambient gas. To obtain the ignition condition, Equations (37)–(40) were solved by the Crank-Nicholson method and the resulting matrix was inverted by LU decomposition. The solution of

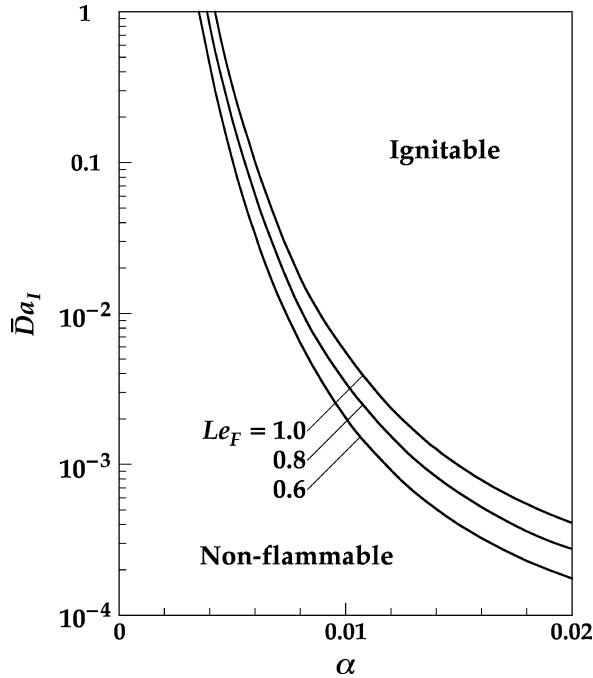


Figure 6. Variation of the ignition state,  $\bar{D}a_I$ , versus  $\alpha$  corresponding to Figure 5 when changes of  $\alpha$  is caused by variations in  $\tilde{T}_\infty$ .

$\theta$ , the temperature increase through reaction, is plotted versus  $\zeta$  in Figure 7 for selected values of  $\xi$ . Here  $\beta = 0.3$ ,  $\bar{D}a = 0.5$  and  $Le_O = 1$ , where  $\beta = (\tilde{T}_0 - \tilde{T}_\infty)/\tilde{Y}_{O,\infty}$  and  $\bar{D}a$  is given by Equation (41). At the jet exit,  $\xi = 0$ , there is no reaction so  $\theta = 0$ . With the increase of  $\xi$ , reaction takes place and  $\theta$  increases. For this case, a maximum  $\theta$  is developed away from but close to the centerline of the jet,  $\zeta = 0$ . Although the reaction is very sensitive to temperature variations, it also needs the oxidizer. When moving away from  $\zeta = 0$ , the temperature reduces while the oxidizer concentration increases. The maximum value of  $\theta$  then is located where the maximum reaction rate occurs through the competition of these two effects. At  $\xi = 1.153$ , the reaction is sufficiently strong and the heat generation is sufficiently high to overcome the heat loss to the cold ambient such that one of the conditions in Equation (42) is satisfied and ignition is successful. The value of  $\xi = 1.153$  is then identified as the ignition location  $\xi_I$  and the maximum value of  $\theta$  at  $\xi_I$  is defined as  $\theta_{\max}$ . Beyond  $\xi_I = 1.153$ ,  $\theta$  continues to increase, reaches a maximum value, and then gradually drops to 0 as  $\xi \rightarrow \infty$ . That is, the temperature continues to increase, reaches its maximum, and decreases to  $T_\infty$  as  $\xi \rightarrow \infty$ . Thermal runaway is not observed because of the strong heat loss from the reaction region to the ambient, given by the  $\exp[-\beta(\zeta^2 + \xi)]$  term of Equation (38). This part of the solution is unrealistic because once ignition is successful at  $\xi_I$ , a flame is established and the weak-reactive assumption is no longer valid. It is expected that thermal runaway would be predicted by a transient analysis of the temporal evolution of temperature at  $\xi_I = 1.153$ .

If ignition fails,  $(\partial \theta / \partial \xi)_{\zeta=0}$  first increases and then decreases such that  $(\partial \theta / \partial \xi)_{\zeta=0} \geq \beta$  can never be satisfied, because the heat generation is not high enough to overcome the heat loss to the ambient. For smaller values of  $\bar{D}a$  (but still large enough to yield ignition),  $\theta_{\max}$  is established away from  $\zeta = 0$  in the beginning, and later shifts to the centerline before ignition occurs. The

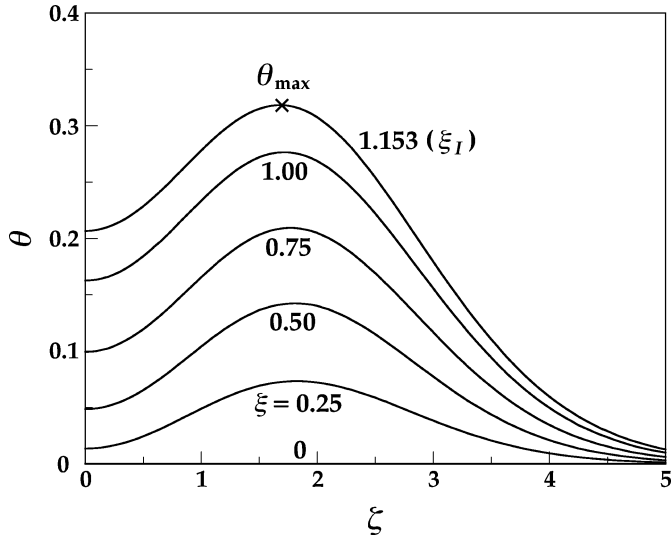


Figure 7. Evolution of the temperature increase through reaction,  $\theta$ , versus  $\zeta$  for some values of  $\xi$  until ignition. The plot is for a hot jet flowing into a cool ambient with  $\beta = 0.3$ ,  $\tilde{D}a = 0.5$  and  $Le_O = 1$ .

reason for this is that the values of  $\xi_I$  are relatively large and sufficient oxidizer is transported to the centerline such that ignition is dominated by the high temperature at the centerline.

Results of ignition conditions for three values of  $\beta$  are shown in Figures 8 and 9 by plotting  $\theta_{\max}$  and  $\xi_I$ , respectively, versus  $\tilde{D}a$  for  $Le_O = 1$ . On each curve, by increasing the reaction rate, i.e.  $\tilde{D}a$ , a smaller temperature increase and a shorter ignition location are observed before ignition. A higher value of  $\tilde{D}a$  yields an increased heat generation rate, which further compensates for heat loss from the hot jet to the cold ambient and favors ignition. The stronger reaction rate

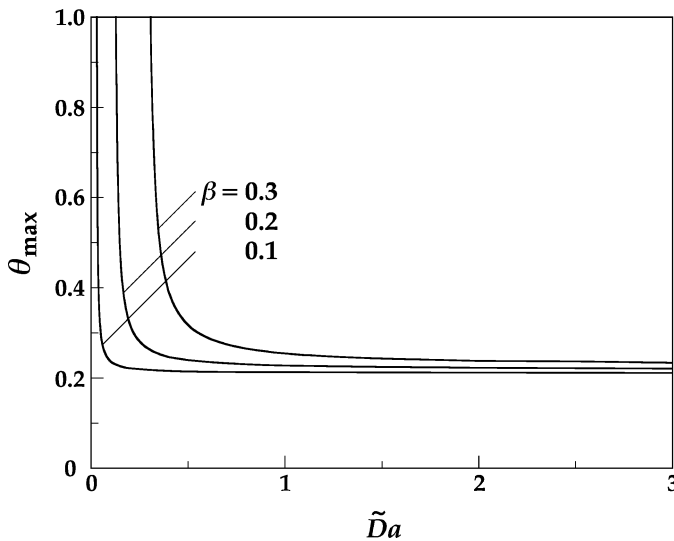


Figure 8. Reaction temperature increase before ignition,  $\theta_{\max}$ , versus reduced Damköhler number  $\tilde{D}a$  for selected values of  $\beta = (T_0 - T_\infty)/\tilde{Y}_{O,\infty}$  and  $Le_O = 1$ , hot jet flowing into cool ambient.

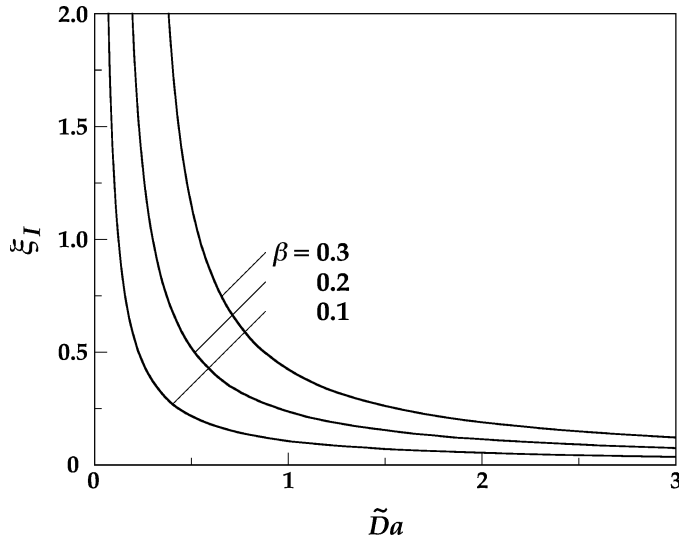


Figure 9. Ignition location  $\xi_I$  corresponding to Figure 8.

also brings the point of ignition closer to the jet exit. In contrast, a reduction in  $\tilde{D}a$  weakens the reaction and makes ignition more difficult such that both  $\theta_{\max}$  and  $\xi_I$  increase. Although an increase of  $\xi$  provides longer residence time for the reaction so that ignition can occur at a smaller  $\tilde{D}a$ , the reaction rate decreases with  $\xi$  because the jet is cooled by the cold ambient, as can be seen from the reaction term of Equation (38). A sharp increase in  $\theta_{\max}$  and  $\xi_I$  for lower values of  $\tilde{D}a$  on each  $\beta$  curve in Figures 8 and 9 means that the reduction of reaction rate dominates over the residence time increase, and defines the smallest  $\tilde{D}a$  for which ignition is possible. The

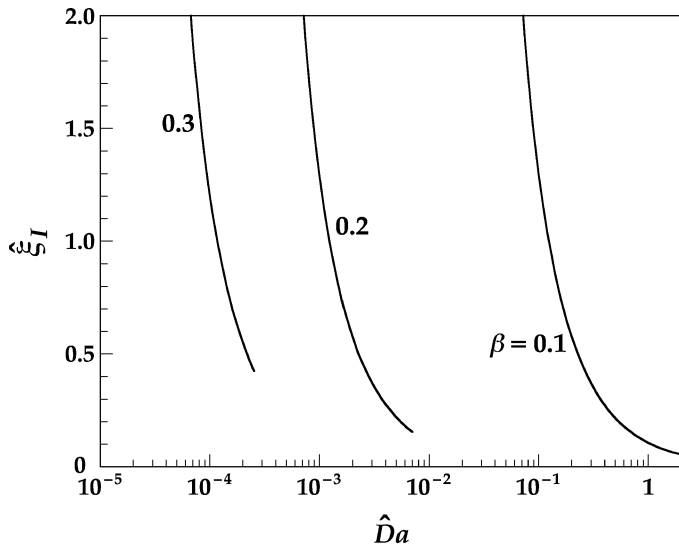


Figure 10. Rescaled plot of  $\hat{\xi}_I$  versus  $\hat{D}a$  from Figure 9 when changes of  $\beta$  is caused by variations in  $\tilde{T}_0$ , with  $\tilde{T}_\infty = 0.00382$ ,  $\tilde{E} = 0.127$ ,  $\tilde{Y}_{O,\infty} = 0.0291$ , and  $\tilde{T}_0 = 0.00673$ .

minimum value of  $\tilde{D}a$  below which ignition fails is then identified as the ignition state,  $\tilde{D}a_I$ . Ignition is successful for all  $\tilde{D}a > \tilde{D}a_I$ .

Figures 8 and 9 also indicate that a decrease in  $\beta$  for any fixed  $\tilde{D}a$  favors ignition, as ignition occurs at a lower temperature increase,  $\theta_{\max}$ , and at a shorter ignition location,  $\xi_I$ . More importantly, a decrease in  $\beta$  permits ignition at a lower value of  $\tilde{D}a$ . Such a decrease can be accomplished either by increasing the ambient temperature,  $\tilde{T}_\infty$  or  $q_F/c_p$ . Both findings are physically realistic as in the cold jet scenario.

Parameter  $\beta$  also can be changed by variations of the jet temperature,  $\tilde{T}_0$ , or the reactant mass fraction in the oxidizer supply,  $\tilde{Y}_{O,\infty}$ , but these changes result in a simultaneous change of  $\tilde{D}a$ . To investigate the effects variations in  $\tilde{T}_0$  at fixed  $\tilde{D}a$  requires a rescaling similar to that performed in Section 3.1. The rescaling is performed here by specifying a reference value of  $\tilde{T}_0$  as  $\hat{T}_0$ , defining rescaled parameters  $\hat{\varepsilon} = \tilde{T}_0^2/\tilde{E}$ ,  $\hat{\xi}_I = (\tilde{T}_0/\hat{T}_0)^2 \xi_I$  and

$$\hat{D}a = \hat{\varepsilon} [Da \tilde{Y}_{F,0}/(\hat{T}_0 \tilde{Y}_{O,\infty})] \exp(-\tilde{E}/\hat{T}_0), \tag{45}$$

and plotting the results in terms of rescaled variables  $\hat{\xi}_I$  and  $\hat{D}a$  corresponding to Figure 9. In the following discussion,  $\tilde{T}_\infty = 0.00382$ ,  $\tilde{E} = 0.127$ ,  $\tilde{Y}_{O,\infty} = 0.0291$  and  $\hat{T}_0 = 0.00673$  have been used to predict the ignition characteristics. For hydrogen, these correspond to  $T_\infty = 300$  K,  $E = 10\,000$  K,  $Y_{O,\infty} = 0.233$ , and  $T_{0,\text{ref}} = 530$  K ( $\beta_{\text{ref}} = 0.1$ ). The results are shown in Figure 10. Here an increase in  $\tilde{T}_0$ , which increases  $\beta$  without changing  $\tilde{D}a$ , is seen to favor ignition because ignition can occur at a lower reaction rate, or lower  $\tilde{D}a$ , as expected and in agreement with Figure 4. A plot corresponding to Figure 8 also can be performed but will not be included because the results are qualitatively similar to Figure 10.

As for the cold jet scenario, when the variation of  $\beta$  is caused by the change of  $\tilde{Y}_{O,\infty}$ , a rescaling of  $\tilde{D}a$  by defining a reference value of  $\tilde{Y}_{O,\infty}$ , similar to that of Equation (45), is needed. The results are qualitatively the same as those presented in Figures 8 and 9 because an increase in  $\tilde{Y}_{O,\infty}$  (a decrease in  $\beta$ ) results in a greater oxidizer concentration in the reaction region.

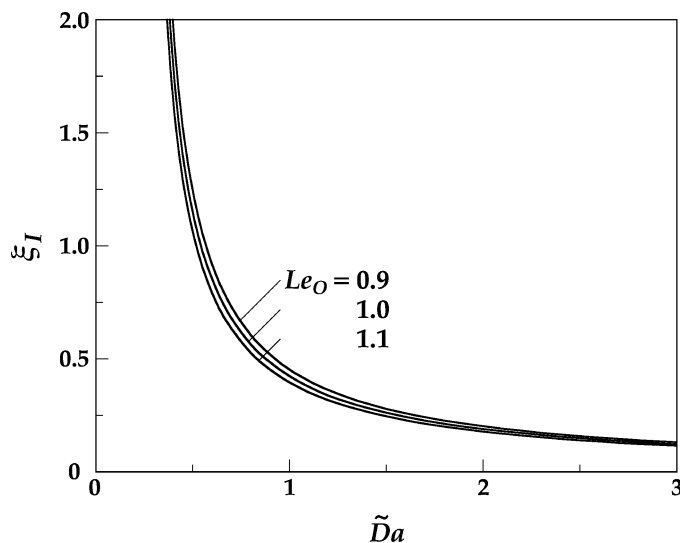


Figure 11. Effect of  $Le_O$  on ignition for a hot jet flowing into cool ambient is exhibited by plotting the ignition location  $\xi_I$  versus reduced Damköhler number  $\tilde{D}a$  with  $\beta = 0.3$ .

The effects of oxidizer Lewis number on spontaneous ignition are considered in Figure 11 by plotting  $\xi_I$  versus  $\tilde{D}a$  for various  $Le_O$ . This plot shows that a decrease in  $Le_O$  makes ignition more difficult. For an increase in the mass diffusivity of the oxidizer (or a decreased  $Le_O$ ) at a fixed value of  $\tilde{D}a$ ,  $\xi_I$  (and  $\theta_{\max}$ ) increases. In addition, the minimum  $\tilde{D}a$  for ignition increases with decreased  $Le_O$  such that a higher reaction intensity is necessary to ignite the reactants. This is contrary to the ignition behavior with respect to fuel Lewis number in the cool jet case (Figure 4). In a cool jet, there is unlimited heat transfer from the hot ambient gas to preheat the fuel so that a higher fuel diffusion rate (lower  $Le_F$ ) results in a higher fuel concentration in the reaction region, more heat generation through the reaction and, hence, easier ignition. In the hot jet, only limited heat is available from the fuel flow. An increased oxidizer mass diffusivity (lower  $Le_O$ ) increases the transport rate of oxidizer to the center of the jet, thus requiring more heat to preheat the oxidizer, decreasing the temperature in the hot zone, and making ignition more difficult. In addition, unlike the cool jet for which  $Le_F$  has a significant effect on ignition, the Lewis number of the oxidizer only has a weak effect on the ignition state (see Figure 11) because ignition occurs near the exit plane, if successful. In the reaction region, the flow velocity is high such that streamwise convection dominates over transverse diffusion. This observation, when combined with the fact that  $Le_O$  is close to unity for oxygen in air, indicates that the effect of  $Le_O$  in a hot-hydrogen cold-air system is secondary.

The ignition states for the hot jet scenario are shown in Figure 12 by plotting the reduced Damköhler number at ignition,  $\tilde{D}a_I$ , versus  $\beta$  when the variation of  $\beta$  is through the change of  $\tilde{T}_\infty$ , for  $Le_O = 1$ . Because the effect of  $Le_O$  is known from Figure 11 and is less important, it is not included in Figure 12. Instead, the effect of the oxidizer reaction order,  $n_O$ , which is obtained by replacing the  $\tilde{Y}_O$  in the reaction term of Equations (11)–(13) with  $\tilde{Y}_O^{n_O}$ , is studied.

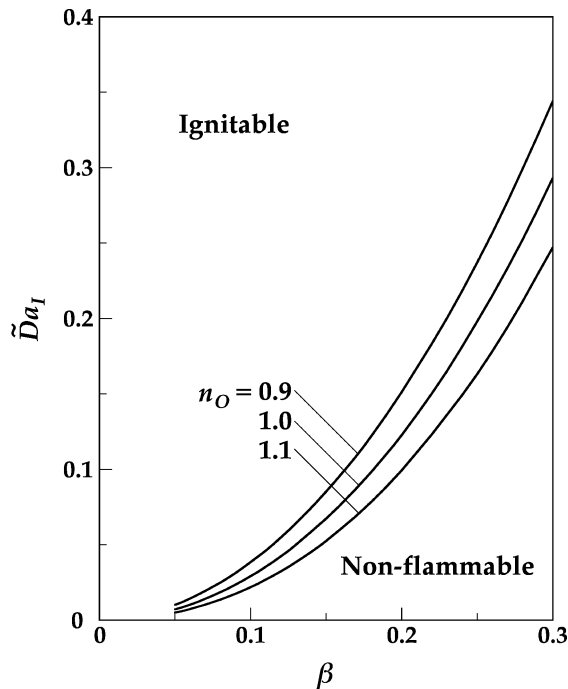


Figure 12. Variation of the ignition state,  $\tilde{D}a_I$ , versus  $\beta$  (which is changed by variations in  $\tilde{T}_\infty$ ) for selected values of the oxidizer reaction order,  $n_O$ , hot jet flowing into cool ambient.

The region above the curve for any  $n_O$  is the region in which ignition is successful, and a flame can be established, while the region below the curve is the region where ignition fails. The plot shows that ignition is favored when  $\beta$  is decreased since  $\tilde{D}a_I$  is reduced, in agreement with that discussed in Figure 5. Figure 12 also shows that ignition is favored when the oxidizer reaction order is increased, as the region that is ignitable is broadened. This is a result of increased reaction rate, or the heat generation rate. For cases when the variation of  $\beta$  is caused by the change of  $\tilde{T}_0$ , rescaling can be performed using Equation (45) as in Figure 10 and the result is qualitatively similar to Figure 6.

For both the cool and hot jet scenarios, the dependence of ignition on the slot width,  $h$ , can be identified through the  $x_0/u_0$  term given in the definition of  $Da$  after Equation (16), where  $x_0$  is given in Equation (10). Equation (10) indicates that  $x_0$  increases with  $h$ , but the exact expression requires knowledge of the flow field in the slot. It can be shown that for a choked uniform flow driven by a high pressure gradient, and a fully-developed parabolic flow induced by a lower pressure gradient,  $x_0/u_0$  (and all different forms of reduced Damköhler number) is proportional to  $h^2$ . Thus an increase in slot width favors ignition because there is more fuel in the jet.

#### 4. Conclusions

The spontaneous ignition of a fuel jet, with emphasis on a hydrogen jet, emanating from a slot into an oxidizing ambient has been considered analytically. A similarity solution of the flowfield was obtained, which was then applied to the species and energy conservation equations. Solutions of the ignition conditions were found using activation energy asymptotics. Because spontaneous ignition is very sensitive to temperature, ignition is expected to occur near the edge of the jet if the fuel is cooler than the ambient gas, and on the centerline if the fuel is hotter than the ambient gas.

For a cool jet flowing into a hot ambient, ignition is found to be a strong function of ambient temperature, initial fuel concentration and fuel Lewis number, but a weak function of the reaction order of the fuel. Ignition was favored by an increase in ambient temperature and initial fuel concentration or a decrease in Lewis number. For the hot jet scenario, ignition was significantly affected by the jet temperature, moderately affected by the reaction order of the oxidizer, but only weakly affected by the oxidizer Lewis number.

The value of the mixture fraction  $Z$  at which ignition occurs can be extracted from the solutions as  $Z = (\sigma Y_F - Y_O + Y_{O,\infty}) / (\sigma Y_{F,0} + Y_{O,\infty})$ . In the first scenario of cool jet flowing into a hot ambient, ignition occurs at  $Z \rightarrow 0$  since it occurs at the jet edge where  $Y_O \rightarrow Y_{O,\infty}$  and  $Y_F \rightarrow 0$ . In the second scenario of the hot jet, ignition occurs at the jet centerline, where  $Z \rightarrow 1$  since  $Y_O \rightarrow 0$  and  $Y_F \rightarrow Y_{F,0}$ .

The present model can be extended to studies of flame extinction and to circular jet configurations. When experimental data becomes available, parametric comparisons can be made to establish reaction rates for use in the present model.

#### Acknowledgment

This work was supported by NIST grant 60NANB5D1209 under the technical management of Dr. J. Yang.

#### References

- [1] J.M. Kuchta, *Investigation of fire and explosion accidents in the chemical, mining, and fuel-related industries—a manual*, U.S. Bureau of Mines, Bulletin 680 (1985).
- [2] J. Hord, *Is hydrogen a safe fuel?*, International Journal of Hydrogen Energy 3 (1978), 157–176.

- [3] A.M. Kanury, *Introduction to Combustion Phenomena* (Amsterdam: Gordon and Breach Publishers) (1975).
- [4] X.L. Zheng, and C.K. Law, *Ignition of premixed hydrogen/air by heated counterflow under reduced and elevated pressures*, *Combustion and Flame* 136 (2004), 168–179.
- [5] C.E. Grosch, and T.L. Jackson, *Ignition and structure of a laminar diffusion flame in a compressible mixing layer with finite rate chemistry*, *Physics of Fluids A* 3 (1991), 3087–3097.
- [6] H.G. Im, S.R. Lee, and C.K. Law, *Ignition in the supersonic hydrogen/air mixing layer with reduced reaction mechanisms*, Paper No. AIAA-1994-548, 32nd Aerospace Sciences Meeting and Exhibit, Reno, NV, (1994), 10–13 January.
- [7] H.G. Im, B.H. Chao, J.K. Bechtold, and C.K. Law, *Analysis of thermal ignition in the supersonic mixing layer*, *AIAA Journal* 32 (1994), 341–349.
- [8] S.R. Lee, and S.H. Chung, *On the structure of hydrogen diffusion flames with reduced kinetic mechanisms*, *Combustion Science and Technology* 96 (1994), 247–277.
- [9] B.T. Helenbrook, and C.K. Law, *Ignition of hydrogen and oxygen in counterflow at high pressures*, *Proceedings of Combustion Institute* 26 (1996), 815–822.
- [10] H.G. Im, B.T. Helenbrook, S.R. Lee, and C.K. Law, *Ignition in the supersonic hydrogen/air mixing layer with reduced reaction mechanisms*, *Journal of Fluid Mechanics* 322 (1996), 275–296.
- [11] V.V. Toro, A.V. Mokhov, H.B. Levinsky, and M.D. Smooke, *Combined experimental and computational study of laminar, axisymmetric hydrogen–air diffusion flames*, *Proceedings of Combustion Institute* 30 (2005), 485–492.
- [12] M. Chaos, R.-H. Chen, E.J. Welle, and W.L. Roberts, *Fuel Lewis number effects in unsteady Burke Schumann hydrogen flames*, *Combustion Science and Technology* 177 (2005), 75–88.
- [13] Y. Liu, and P. Pei, *Asymptotic analysis on autoignition and explosion limits of hydrogen–oxygen mixtures in homogeneous systems*, *International Journal of Hydrogen Energy* 31 (2006), 639–647.
- [14] F.L. Dryer, M. Chao, Z. Zhao, J.N. Stein, J.Y. Alpert, and C.J. Homer, *Spontaneous ignition of pressurized releases of hydrogen and natural gas into air*, *Combustion Science and Technology* 179 (2007), 663–694.
- [15] F.A. Williams, *Combustion Theory*, 2nd Edition (Redwood City: Addison-Wesley) (1985).
- [16] C.K. Law, *Combustion Physics* (New York: Cambridge University Press) (2006).
- [17] N. Peters, *Turbulent Combustion*, (Cambridge: Cambridge University Press) (2000).
- [18] A. Liñán, and F.A. Williams, *Fundamental Aspects of Combustion*, Vol. 34 of Oxford Engineering Science Series (New York: Oxford University Press) (1993).
- [19] W. Bickley, *The plane jet*, *Philosophical Magazine Series* 7, 23 (1939), pp. 727–731.
- [20] H. Schlichting, *Boundary-Layer Theory*, 7th Edition (New York: McGraw-Hill) (1979).
- [21] V. Nayagam, and F.A. Williams, *Lewis-number effects on edge-flame propagation*, *Journal of Fluid Mechanics* 458 (2002), 219–228.

# Flame Quenching Limits of Hydrogen Leaks

**M.S. Butler, R.L. Axelbaum**

Dept. of Energy, Environmental and Chemical Engineering, Washington Univ., St. Louis MO 63130, USA

**C.W. Moran, P.B. Sunderland**

Dept. of Fire Protection Engineering, Univ. of Maryland, College Park MD 20742, USA

Copyright © 2007 SAE International

## ABSTRACT

This study examines the types of hydrogen leaks that can support combustion. Hydrogen, methane, and propane diffusion flames on round burners and leaky compression fittings were observed. Measurements included limits of quenching and blowoff for round burners with diameters of 0.006 - 3.18 mm. The measured mass flow rates at the quenching limits were found to be generally independent of burner diameter at relatively large burner diameters. In terms of mass flow rate, hydrogen had the lowest quenching limit and the highest blowoff limit of the fuels considered, which means that there are high and low flow rates where hydrogen is able to support a flame while methane and propane are not able to. The quenching limits for hydrogen diffusion flames on round burners with thick walls were found to be higher than for thin walls. The limits were also found to be independent of burner orientation; leaks with low flow rates are able to support flames independent of their orientation. The minimum mass flow rate of hydrogen that can support combustion from a leaking compression fitting was found to be 0.028 mg/s. This flow was independent of pressure (up to 131 bar) and about an order of magnitude lower than the corresponding methane and propane flow rates. The implications for fire safety are discussed.

## INTRODUCTION

Concerns about the emissions of greenhouse gases have led to extensive consideration of hydrogen as an energy carrier. Currently, oil constitutes about 33% of the world's primary energy, and it is primarily produced in countries that are replete with political instability as viewed from a western point of view [1]. With crude oil approaching \$100/barrel, supply is not keeping up with demand and political instability makes the price even more tenuous. In addition, our society's dependence on fossil fuels possibly results in global warming, acid rain, etc. It is also predicted that crude oil supplies will run dry by 2043 [2]. Hydrogen as an energy carrier can help mitigate these issues [3]. Some benefits of hydrogen include that it can be converted to electricity with a high efficiency, its raw materials and the majority of its products are water, it can be stored as liquid, gas or

solid, and it can be transported using pipelines, tankers or rail trucks over long distances [4]. It is also projected that hydrogen production can be produced efficiently using renewable methods such as wind [5].

There are, however, several hazards associated with hydrogen. Applications for the gas will likely shift to include commercial applications; these hold more risk than the current, tightly-regulated industrial applications, thus codes and standards must be updated [6]. Experimental and numerical work has shown that there are some obvious safety risks in hydrogen explosions and high pressure gas releases [7,8]. Also, hydrogen itself presents several unusual fire hazards, including high leak propensity, high blowoff limits, ease of ignition, and invisible flames. These characteristics have been investigated in the context of micro diffusion flames.

There are three classifications for laminar jet flames: diffusion controlled flames such as the Burke-Schumann flame [9], diffusion and momentum controlled flames such as the Roper flame [10] and micro diffusion flames controlled by momentum and diffusion [11]. Extensive research has been done on the first two types, but only a limited amount has been done on micro diffusion flames. Baker et al. [12] devised a flame height expression for purely diffusion controlled flames capable of accurately predicting micro-slot diffusion flame heights. Useful parameters for characterizing dominant flame mechanisms were defined: a diffusion-buoyancy and a diffusion-momentum parameter. This work extended the investigations of Roper et al. [13] to smaller slot sizes. Ban et al. [11] investigated flames established on circular burners with inner diameters of 0.15, 0.25, and 0.40 mm. The experiments worked to verify the predicted flame shape of laminar flames ( $Re = 1 - 10$ ) for three fuels: ethane, ethylene and acetylene. The work found that buoyancy effects are negligible for small flames; nearly spherical flames were established that were unaltered by rotating the burner. An in depth analysis of a micro diffusion hydrogen flame was performed by Cheng et al. [14]; their numerical solution for species was compared with experimental data. It was found that buoyancy effects were insignificant.

Nakamura et al. [15] numerically studied methane micro diffusion flames sitting on a circular burner of a diameter less than 1 mm. They found that small flames have the same, nearly spherical structure as those in microgravity, citing weak buoyancy forces. Also, the existence of a minimum flame size necessary for combustion was predicted.

Quenching and blowoff limits bound the leak flow rates that can support combustion. Matta et al. [16] found that a flame is not able to exist when its predicted length is less than the measured standoff distance. Experiments verified this analytical method of finding the quenching flow rate by establishing a propane flame over a hypodermic, stainless steel tube and decreasing the fuel flow rate until extinction occurred. They also measured blowoff. Cheng et al. [17] performed similar quenching experiments and included a dominant mechanism similar to that of Baker et al. [12], except using methane as fuel. Kalghatgi et al. [18] measured blowoff limits for a variety of fuels including propane, methane and hydrogen on circular burners. These studies show that hydrogen blowoff limits are higher than those for methane and propane. For a given leak size, there is a range of mass flow rates where hydrogen is able to support a stable flame but methane and propane would be blown off.

In order to understand how much gas is flowing through a given leak, research has been done in evaluating leak flow rates of hydrogen, methane, and propane. Swain and Swain [19] modeled and measured leak rates for diffusion, laminar, and turbulent flow regimes. They found that combustible mixtures in an enclosed space resulted more quickly for propane and hydrogen leaks than for methane leaks. It was also found that hydrogen had significantly higher volumetric flow rates through leaks than did methane and propane. Their supply pressures were the same for all fuels.

Another risk associated with hydrogen is that it is often stored at high pressures in spite of its high propensity to leak. It is predicted that hydrogen will need to be stored at up to 40 MPa to gain the efficiency desired [22]. Hydrogen's safety hazards resulted in a Department of Energy report [23] finding that hydrogen containment was the chief safety concern associated with using hydrogen as a transportation fuel and documented several catastrophic hydrogen fires. One such accident that displays hydrogen's difficulty in storage is a pressurized hydrogen tank rupture in Hanau, Frankfurt in 1991. Heavy damage was done to the rest of the plant [20].

Other characteristics of hydrogen that make it more prone to risk are that it is also easier to ignite than most other common fuels, and, once ignited, it is difficult to detect. The minimum ignition energy for hydrogen is an order of magnitude lower than those for methane and propane [21]. This means that a small spark might be able to ignite a hydrogen leak, whereas the same spark might not be able to ignite a methane or propane leak. It

has also been noted that hydrogen flames have weak luminosity [14], hence a hydrogen leak sustaining a flame would be difficult to detect by the human eye.

Considering these properties of hydrogen, the scenario of interest in this work is that a small, easily ignitable leak in a hydrogen system might ignite, support a flame that is difficult to detect, and degrade containment materials to the point of a catastrophic failure. This study includes experiments and analysis to identify which hydrogen leaks can support flames. Thus motivated, the objectives of this work are to measure limits of sustained combustion, both at quenching and blowoff, for hydrogen on round burners and lower flaming limits for hydrogen, methane and propane on leaky compression fittings.

## FLAME QUENCH SCALING

A scaling analysis was developed to interpret measured flame quenching limits. These limits are the minimum flow rates required to support a diffusion flame.

The stoichiometric length  $L_f$  of laminar gas jet diffusion flames on round burners is:

$$L_f / d = a Re = a \rho u_0 d / \mu, \quad (1)$$

where  $d$  is the burner inside diameter,  $a$  is a dimensionless fuel-specific empirical constant,  $Re$  is Reynolds number,  $u_0$  is the average fuel velocity in the burner,  $\rho$  is fuel density, and  $\mu$  is fuel dynamic viscosity. The scaling of Eq. 1 arises from many theoretical and experimental studies, including Roper [10], Sunderland et al. [24], and references cited therein. Constant  $a$  here is assigned values measured by Sunderland et al. [24], as listed in Table 1.

The base of an attached jet diffusion flame is quenched by the burner. Its standoff distance can be approximated as one half of the quenching distance of a stoichiometric premixed flame. Such quenching distances typically are reported as the minimum tube diameter,  $L_q$ , through which a premixed flame can pass. It is assumed here that a jet flame can be supported only if its stoichiometric length is greater than half this quenching distance:

$$L_f \geq L_q / 2. \quad (2)$$

Measurements of  $L_q$ , shown in Table 1, are taken from

Table 1: Selected fuel properties of hydrogen, methane, and propane. Values for  $a$  are from Sunderland et al. [7],  $L_q$  and  $S_L$  (laminar burning velocity) are from Kanury [8], and  $\mu$  is from West and Astle [9].

Fuel	$a$	$L_q$ [mm]	$S_L$ [cm/s]	$\mu$ [g/m-s]	$m_{fuel}$ [mg/s] predicted
H <sub>2</sub>	0.236	0.51	291	8.76e-3	0.008
CH <sub>4</sub>	0.136	2.3	37.3	1.09e-2	0.085
C <sub>3</sub> H <sub>8</sub>	0.108	1.78	42.9	7.95e-3	0.063

Kanury [25]. When combined, Eqs. (1) and (2) predict the following fuel flow rate,  $m_{fuel}$ , at the quenching limit:

$$m_{fuel} = \pi \rho u_0 d^2 / 4 = \pi L_q \mu / (8 a). \quad (3)$$

Eq. (3) indicates that the fuel mass flow rate at the quenching limit is a fuel property that is independent of burner diameter. When values of  $L_q$ ,  $\mu$ , and  $a$  from Table 1 are inserted into Eq. (3), the predicted fuel mass flow rates at quenching are obtained.

## EXPERIMENTAL

Two different burner configurations are considered here: round burners and leaky compression fittings.

There is generally a limited range of flow rates for which a flame can be established on the present burners. Below this range, the flow is said to be below the quenching limit. Quenching occurs when there is too much heat loss for combustion to be sustained. Above this range, the flow is said to be above its blowoff limit. This limit occurs when the flow velocity in the flammable region of the flame becomes greater than the burning velocity of the mixture.

### Round Burners

Three different types of round burners were considered for this work: tube burners, pinhole burners, and curved-wall pinhole burners, as displayed in Fig. 1. Each had a range of flow passage diameters. All tests were performed at ambient lab pressure, and flow was delivered via a pressure regulator and a flow controlling valve.

The tube burners were made from stainless steel hypodermic tubes, oriented vertically. Tube inside diameters were 0.006, 0.016, 0.033, 0.047, and 0.087 mm. These burners resemble microinjectors that may be used in future, small scale microelectro-mechanical power generators [16]. The pinhole burners were stainless steel nozzles that are manufactured for solid-stream spray generation. The top of each burner (except the two smallest ones) is a curved surface with a hole passing through its axis, as shown in Fig. 2. The two smallest burners had holes in planar, not curved, surfaces. It is expected that the variation of quenching flow rate as a result of this slight curvature is on the order of the error associated with measurements. The hole diameters were 0.008, 0.13, 0.36, 0.53, 0.71, 0.84, 1.01, 1.40, 1.78, 2.39, and 3.18 mm. The curved-wall pinhole burners were constructed of stainless steel tubes with two outside diameters: 1.59 and 6.35 mm. A

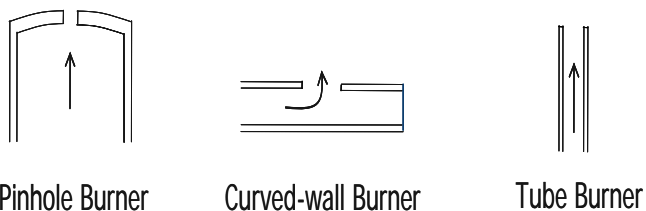


Figure 1: Burners used to find quenching limits.

radial hole was drilled in each tube. Hole sizes were 0.41, 0.53, 0.74, 0.86, and 1.02 mm (small tubes) and 0.41, 1.75, 2.46 and 3.12 mm (large tubes).

Certain complications are unique to these experiments. The present small flow rates could not be accurately measured using conventional flow meters. Instead, for tests with round burners a glass soap-bubble meter was installed upstream of the burners. Tests performed with varying air moisture content found quenching flow rate to be generally independent of air moisture content in the range of 46% to 90% relative humidity. Hydrogen flame detection was complicated by their dimness, especially at low flow rates, but this was resolved by using thermocouples to detect flames. K-type thermocouples were chosen to avoid catalysis, and were placed several flame lengths above the flames to avoid disturbances.

Quenching flow rates were measured by first establishing a small flame, decreasing the flow rate until flame extinction and then introducing a soap bubble for flow rate measurement. Each burner was allowed to warm to just above room temperature to prevent water condensation on the burner surface. This is because water condensation was found to disturb flow from the small burners, sometimes extinguishing the flames. Tests performed with different burner temperatures found quenching flow rate to be largely independent of burner temperature.

Burner temperature was not an issue during blowoff measurements because the burners remained relatively cool. The fuel flow rate at blowoff was measured in much the same way as quenching limits were. A stable, large flame was first established; the flow rate was then increased by increasing the upstream pressure via a pressure regulator until the flame first lifted and then extinguished. For these tests the flames were detected visually. Hearing protection was used for blowoff tests on larger burners.

To complete the investigation on round burners, experiments were performed to consider buoyancy effects. Quenching flow rates were found for both pinhole and tube burners in the horizontal (rotated 90°) and inverted orientations (rotated 180°). The limits were

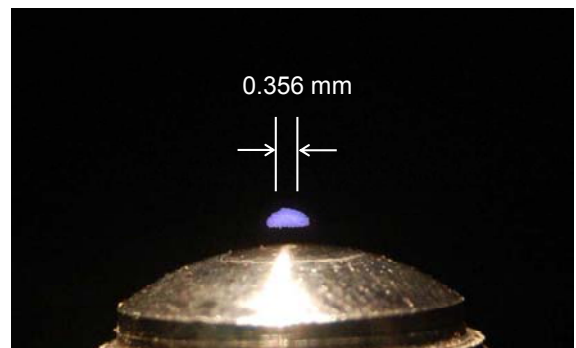


Figure 2: Contrast-enhanced image of hydrogen flame over a 0.356 mm pinhole burner (original in color).

measured in the same manner.

Leaky Fittings

Quenching limits were also measured for leaky compression fittings. Leaks were intentionally introduced. This simulates an unintended leak in a defective fuel line. Presently no regulations exist for allowable leak rates in hydrogen plumbing systems.

The leaky fittings involved 6.35 mm outside diameter stainless steel tubes. Each tube entered a Swagelok® stainless steel tube union compression fitting. The end of the union opposite the tube was sealed such that the only flowing gas was that which went through the leak. Leaks were introduced three ways into fittings that previously were made according to manufacturer instructions and found to be leak tight. The first was by reducing the torque on the threaded nut. The second was by tightening the threaded nut by an additional 0.75 turns. The third was by scratching the front ferrule sealing surface. All three types of leaks are occasionally encountered in plumbing systems. The present quenching limits results were the same for all three types of leaks, so only results from the reduced torque fittings are presented here.

Quenching limits were found by adjusting the torque on the threaded nut and the upstream pressure. For pressures above (and below) the quenching limit, an external flame impinging on the leak region did (and did not) result in a persistent flame at the leak. Upstream pressure was controlled with a pressure regulator in the range of 1.7 – 131 bar<sub>g</sub> (24 – 1900 psig). When a quenching limit was established, any flame was extinguished and a tube was installed over the fitting such that the leak flow passed into a soap bubble meter at laboratory pressure. The quenching flow rate was then measured with the bubble meter.

All tests were performed in a dim room. The burners

were cooled to room temperature prior to each test.

For hydrogen the flames generally were not visible even in dark conditions. Existence or absence of persistent flames was determined with a thermocouple about 2 cm above the burner. Unlike methane and propane, for hydrogen a pop was always heard at ignition. For a flow rate (i.e., a pressure) below the quenching limit the pop was followed by extinction when the external flame was removed. At slightly higher pressures, this pop was followed by a persistent flame.

For methane and propane, quenching limits were identified visually – tests with thermocouples confirmed these flames to be visible, even when only slightly above their quenching limits. Most tests were performed with the burner in the vertical orientation, with the leak at the top end of the 6.35 mm tube. Horizontal and inverted orientations also were considered for some tests.

**RESULTS**

Round Burners

The weak luminosity of small hydrogen flames was immediately confirmed. Figure 2 shows an image of a hydrogen flame on a 0.36 mm pinhole burner just prior to extinction. The photo was taken in a dimly lit room with an f-number of 4.2, *f*/4.2, and an exposure time of 30 s. The image was still very faint with these settings, so a digital contrast enhancement was applied. The hydrogen quenching distance of Table 1 suggests that steady hydrogen diffusion flames should be anchored about 0.25 mm above the burner surface. Figure 2 shows this is reasonable for the present flames near their quenching limits.

Figure 3 shows a summary of all the limit data for tube burners. The blowoff flow rates increase with tube burner diameter, and the quenching flow rates are relatively flat. The limits of combustion in Fig. 3 are much

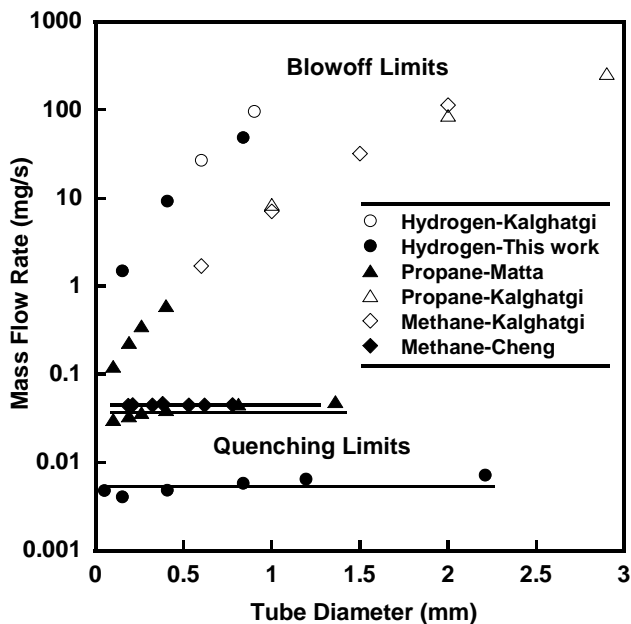


Figure 3: Quenching and blowoff limits versus tube diameter.

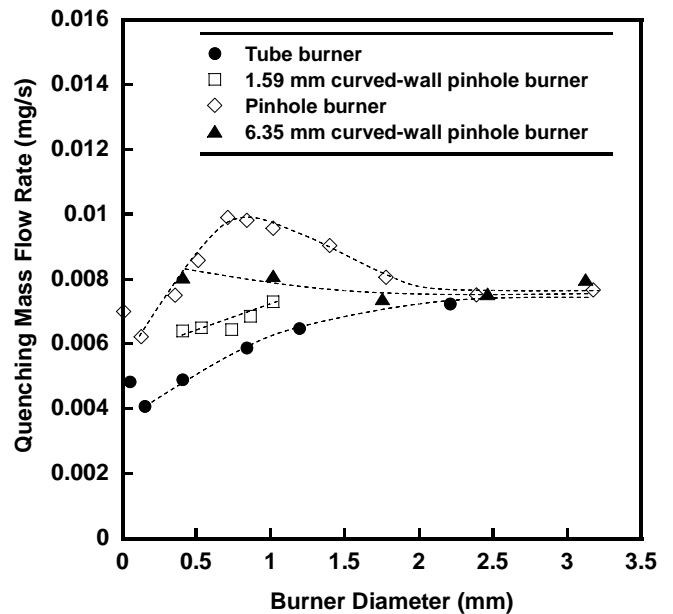


Figure 4: Quenching mass flow rates versus burner diameter for hydrogen.

wider for hydrogen than for propane or methane. The hydrogen quenching limits are about an order of magnitude lower than those for methane and propane, while hydrogen blowoff limits are about an order of magnitude higher than those of the others. For given a leak size there is a range of low and high flow rates that hydrogen would be able to support a flame while propane and methane would be either quenched or blown off. The data from Matta et al. [16], Cheng et al. [14], and Kalghatgi [18] show that the limits for methane and propane are very similar. For all fuels, the quenching limits are nearly independent of burner diameter, whereas blowoff limits increase with increasing diameter. The independence of quenching limit from burner diameter is consistent with the analysis presented above, see Eq. (3).

Figure 4 shows the present hydrogen quenching limits. Data are included for all three types of burners. The theory of Eq. (3) predicts that the quenching flow rate is independent of burner diameter. Figure 4 indicates that the scaling analysis roughly predicts the average quenching flow rate for hydrogen especially at burner diameters greater than 2 mm, although there is clearly another mechanism not accounted for in the calculation. What is clear, though, is that despite varying amounts of heat loss, all burners displayed hydrogen's ability to sustain flames at very low mass flow rates.

Heat loss is likely responsible for the differences between the types of burners. The pinhole burners show the upper limit for quenching flow rates while the tube burners bound the lower limits. This is because the pinhole burners have more heat loss than tube burners. An alternative explanation is that heat lost to the tube burners is more likely to be transferred to the fuel flow

than heat lost to the pinhole burners. This acts as a pre-heating effect which stabilizes the flame.

There also appears to be varying amounts of heat loss as a function of burner diameter. The tube burners show the same trend as the data from Matta et al. [8]; there is an increase in quenching flow rate with increasing burner size. It is reasonable to conclude that there is more heat loss to the burner with increasing burner size; with more heat loss, the quenching flow rate will increase to account for the weaker flame. The pinhole burners do not exhibit the same trend as the tube burners because approximately the same amount of heat loss occurs independent of burner size. The reason for the local maximum in Fig. 4 for pinhole burners is under investigation, however at large burner diameters, the quenching mass flow rate for both pinhole and tube burners approaches 0.008 mg/s as predicted by the scaling analysis.

The effect of curvature was investigated by using the curved-wall pinhole burners. It was expected that with increasing curvature, a flame would experience less wall heat loss. This should result in a stronger flame and a lower quenching flow rate. This is exactly what was observed in the two curved-wall burners. The 6.35 mm burners act more like pinhole burners, whereas the 1.59 mm burners act more like tube burners; the 6.35 mm curved-wall burners have higher average quenching flow rates than the 1.59 mm curved-wall burners. Although curvature did affect the quenching flow rate, the results showed that, despite the amount of curvature, a hydrogen leak can support combustion at very low mass flow rates.

Both the tube and pinhole burners have an increase in

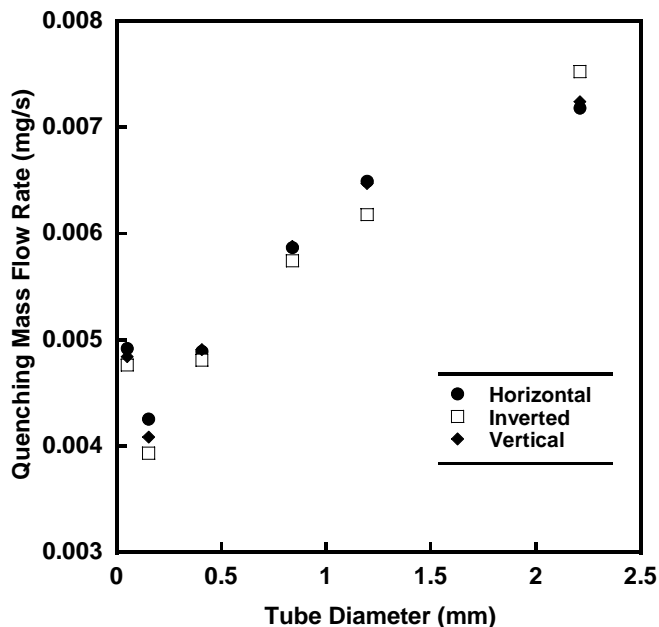


Figure 5: Quenching mass flow rates for several orientations of tube burners.

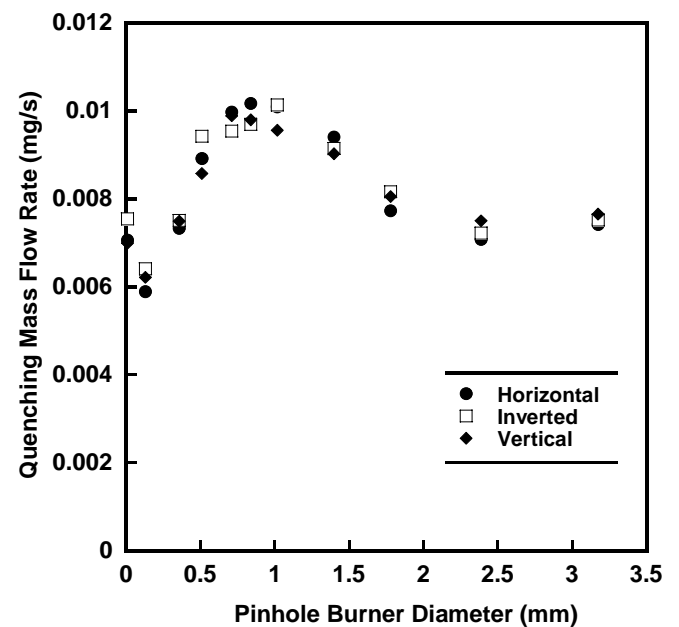


Figure 6: Quenching mass flow rates for several orientations of pinhole burners.

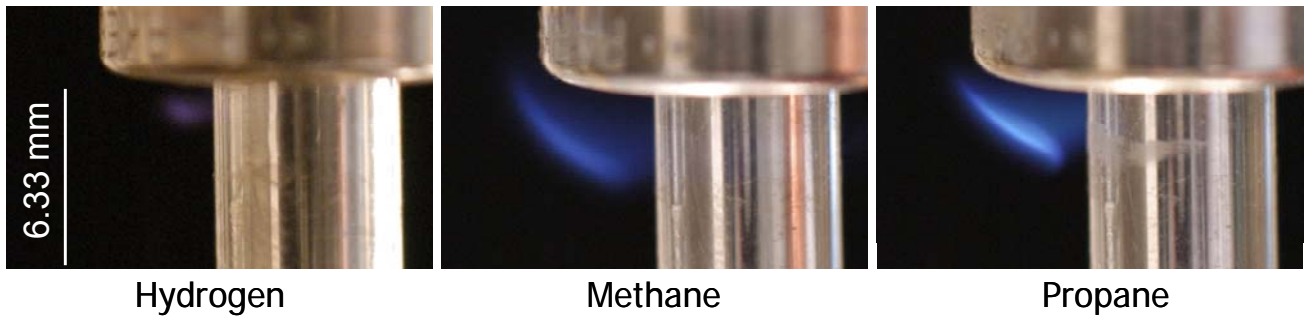


Figure 7: Flames near extinction on leaky compression fittings (original in color).

quenching flow rate for the smallest burners. This is because the velocity at the burner outlet is large enough to weaken the flame.

It was found from Figs. 5 and 6 that the quenching flow rate for pinhole and tube burners was independent of orientation indicating that the flow is not controlled by buoyancy. There are two characteristics that can affect quenching: the flow field and heat loss. Earlier tests found that quenching flow rate was independent of burner temperature. During these experiments, the burner was found to be warmer during non-vertical tests. If burner temperature does not affect quenching and it is the case that the quenching limit is not changing with orientation, then the flow field must also be constant with varying orientation. Hence, it was shown that flames near extinction are driven by mechanisms other than buoyancy. This shows that a hydrogen leak is able to support a flame at very low mass flow rates regardless of orientation. The weak effect of buoyancy in these flames is supported by a nondimensional analysis.

The Froude numbers for the present pinhole and tube burner quenching limit flames were found to be at least 0.1. Flames with these Froude numbers are within the transitional to buoyancy-controlled regime [11]. This

suggests that the flame structure should not change with varying orientation, which is consistent with the experimental results.

#### Leaky Fittings

Figure 7 includes images of flames on leaky compression fittings just above extinction. It is apparent that the hydrogen flame is significantly smaller than those for methane and propane. This seems to indicate that much less hydrogen must be escaping through the leak to sustain combustion. This was validated in the measurements.

Figure 8 shows the measured quenching limits for hydrogen, propane, and methane at a leaky compression fitting in the vertical orientation. For each fuel the data at increased pressure are associated with increased torque on the fitting. The upper limit on pressure for propane is lower than for the others because the vapor pressure of propane at 25 °C is 9.1 bar (142 psia).

Within experimental uncertainties, the data of Fig. 8 are independent of pressure for each fuel. This indicates that, as expected, at fixed fuel mass flow rate the

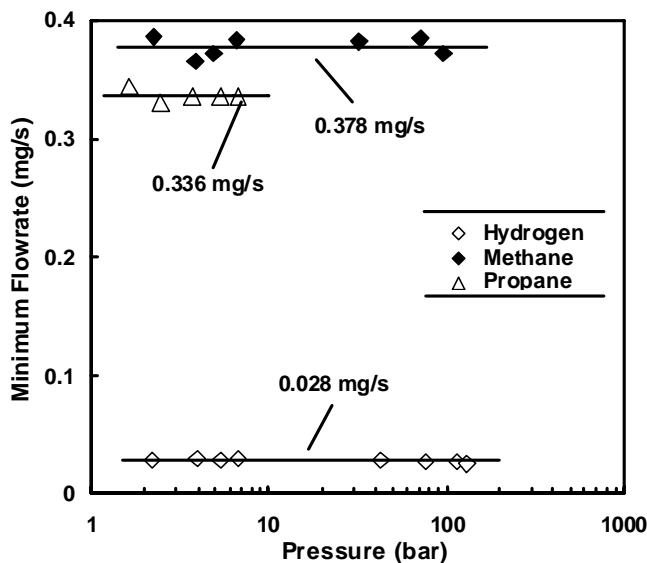


Figure 8: Quenching limit (minimum flaming flow rate) versus upstream pressure for a leaky compression fitting in the vertical orientation. The horizontal lines are means of the measured quenching limits.

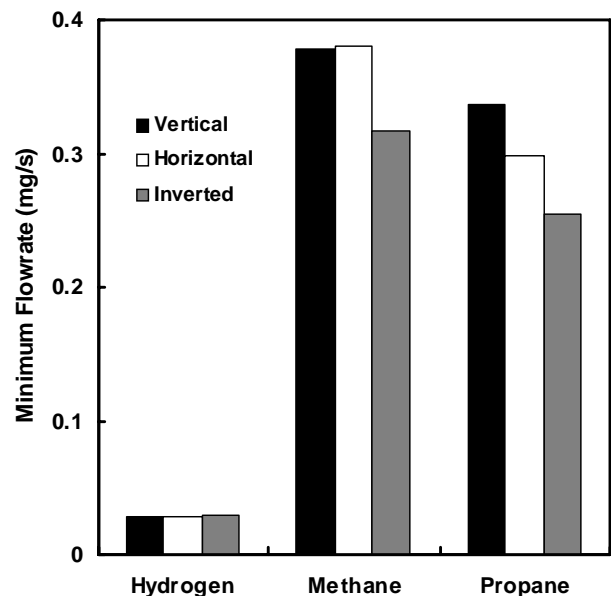


Figure 9: Minimum flaming flow rate for a leaky compression fitting in vertical, horizontal and inverted orientations. Upstream pressure was about 4 bar in all cases.

upstream pressure has little or no effect on the velocity profile of the jet entering the surrounding air. The mean hydrogen flow rate, 0.028 mg/s, is about an order of magnitude lower than for the other fuels due to its low quenching distance and low molecular weight. This behavior is similar to that seen in the round burners above, in Fig. 3. For these leaks, there is a range of pressures where hydrogen is able to support a flame while propane and methane flames would be quenched.

The minimum hydrogen flaming flow rate for round burners (Fig. 3) is about an order of magnitude lower than that for leaky fittings (Fig. 8). This is attributed to additional burner heat losses in the leaky fittings, where the flames burn near concave metal surfaces.

Figure 9 shows the effect of burner orientation on the minimum flaming flow rate. Burner orientation has little or no effect on the quenching limit of hydrogen because these flames were so small at their limits. Burner orientation did have an effect on propane and methane quenching limits, the inverted configuration requiring the lowest flow rate. The inverted orientation minimized the impingement of flames on metal surfaces.

## CONCLUSIONS

The quenching and blowoff limits for hydrogen on round burners were measured and compared with published values for other gases. Hydrogen diffusion flames on tube burners had much wider limits of combustion than propane and methane. There was a high range and a low range of flow rates where hydrogen was able to sustain a flame while propane and methane would be blown off or quenched. It has been shown that the quenching flow rates for all these gases are largely independent of burner size especially at relatively large burner diameters.

The quenching flow rate was found to depend on burner type, owing to differences in wall heat loss. Tube burners had the lowest quenching flow rates, pinhole burners had the highest, and curved wall burners fell in-between, as expected. Although the type of burner did affect the quenching mass flow rate, the results still showed that a hydrogen leak can sustain a flame at much lower flow rates than leaks of other common fuels.

Both types of burners were found to be largely independent of burner orientation. As a result, a leak in a hydrogen system would be able to sustain a flame at low flow rates independent of the orientation of the leak.

The minimum flow rate necessary for sustaining a hydrogen flame at a leaky compression fitting is 0.028 mg/s. This is about an order of magnitude lower than for propane or methane. The minimum mass flow rate for all fuels is independent of upstream pressure.

The round burner and leaky compression fitting experiments yielded similar results in that they both found that the lower limits of combustion for hydrogen were about an order of magnitude lower than those for

propane and methane. The two experiments differed in that their lower combustion limits were off by an order of magnitude owing to increased heat losses in the leaky compression fittings. In both cases, hydrogen was able to sustain flames at much lower mass flow rates than methane and propane.

## ACKNOWLEDGMENTS

This work is supported by NIST under the technical direction of J. Yang. Helpful discussions with B.H. Chao are appreciated.

## REFERENCES

1. Marban G, Valdes-Solis T. Towards the hydrogen economy? *Int. J. Hydrogen Energy* 2007;32:1625-1637.
2. Kruger P. *Alternative energy resources*. Hoboken, NJ: John Wiley & Sons, Inc., 2006.
3. Yamawaki M, Nishihara T, Inagaki Y, Minato K, Oigawa H, Onuki K, Hino R, Ogawa M. Application of nuclear energy for environmentally friendly hydrogen generation. *Int. J. Hydrogen Energy* 2007;32:2719-2725.
4. Sherif SA, Barbir F, Veziroglu TN. Wind energy and the hydrogen economy - review of the technology. *Solar Energy* 2005;78:647-660.
5. Von Jouanne A, Husain I, Wallace A, Yokochi A. Gone with the wind. *IEEE Industry Applications Magazine* July/Aug 2005:12-19.
6. MacIntyre I, Tchouvelev AV, Hay DR, Wong J, Grant J, Benard P. Canadian hydrogen safety program. *Int J Hydrogen Energy* 2007;32:2134-2143.
7. Takeno K, Okabayashi K, Kouchi A, Nonaka T, Hashiguchi K, Chitose K. Dispersion and explosion field tests for 40 MPa pressurized hydrogen. *Int J Hydrogen Energy* 2007;32:2144-2153.
8. Dorofeev SB. Evaluation of safety distances related to unconfined hydrogen explosions. *Int J Hydrogen Energy* 2007;32:2118-2124.
9. Burke SP, Schuman TEW. Diffusion flames. *Ind. Eng. Chem.* 1928;20:998-1004.
10. Roper FG. The prediction of laminar jet diffusion flame sizes: Part 1. Theoretical model. *Combust. Flame* 1977;29:219-226.
11. Ban H, Venkatesh S, Saito K. Convection-diffusion controlled laminar micro flames. *Transactions of the ASME* 1994;116:954-959.
12. Baker J, Calvert ME, Murphy DW. Structure and dynamics of laminar jet micro-slot diffusion flames. *Journal of Heat Transfer* 2002;124:783-790.
13. Roper FG, Smith C, Cunningham AC. The prediction of laminar jet diffusion flame sizes: Part II. Experimental Verification 1977;29(3):227-234.
14. Cheng TS, Chao Y-C, Wu C-Y, Li Y-H, Nakamura Y, Lee K-Y, Yuan T, Leu TS. Experimental and numerical investigation of microscale hydrogen diffusion flames. *Proceedings of the Combustion Institute* 2005;30:2489-2497.

15. Nakamura Y, Yamashita H, Saito K. A numerical study on extinction behaviour of laminar micro-diffusion flames. *Combustion Theory and Modelling* 2006;10(6):927-938.
16. Matta LM, Neumeier Y, Lemon B, Zinn BT. Characteristics of microscale diffusion flames. *Proc. Combust. Inst.* 2002; 29:933-938.
17. Cheng TS, Chen CP, Chen CS, Li YH, Wu CY, Chao YC. Characteristics of microjet methane diffusion flames. *Combust. Theory Modeling* 2006;10:861-881.
18. Kalghatgi GT. Blow-out stability of gaseous jet diffusion flames. Part I: In still air. *Combustion Science and Technology* 1981;26:5:233-239.
19. Swain MR, Swain MN. A comparison of H<sub>2</sub>, CH<sub>4</sub>, and C<sub>3</sub>H<sub>8</sub> fuel leakage in residential settings. *Int J Hydrogen Energy* 1992;17:807-815.
20. Rigas F, Sklavounos S. Evaluation of hazards associated with hydrogen storage facilities. *Int J Hydrogen Energy* 2005;30:1501-1510.
21. Babrauskas V. *Ignition handbook*, 1<sup>st</sup> edition. Issaquah, WA: Fire Science Publishers, 2003.
22. Takeno K, Okabayashi K, Kouchi A, Nonaka T, Hashiguchi K, Chitose K. Dispersion and explosion field tests for 40 MPa pressurized hydrogen. *Int J Hydrogen Energy* 2007;32(13):2144-2153.
23. Cadwallader LC, Herring JS. Safety issues with hydrogen as a vehicle fuel. Report INEEL/EXT-99-00522 prepared for U.S. Department of Energy 1999.
24. Sunderland PB, Mendelson BJ, Yuan ZG, Urban DL. Shapes of buoyant and nonbuoyant laminar jet diffusion flames. *Combust. Flame* 1999;116:376-386.
25. Kanury AM. *Introduction to combustion phenomena*. New York: Gordon and Breach, 1975. p. 131.
26. Weast RC, Astle MJ. *CRC Handbook of Chemistry and Physics*, 59<sup>th</sup> edition. West Palm Beach: CRC Press, Inc., 1979. p. F-58.
27. Munson BR, Young DF, Okiishi TJ. *Fundamentals of fluid mechanics*. Hoboken, NJ: Wiley, 2002. p. 359.
28. Morton NR, Sunderland PB, Chao BH, Axelbaum RL. Quenching limits and materials degradation of hydrogen diffusion flames. 5th U.S. Combustion Meeting, San Diego 2007.
29. Bahadori MY, Hegde U, Zhou L. Liftoff and blowoff of jet diffusion flames. Paper AIAA-2002-1078, Aerospace Sciences Meeting, Reno, Nevada, January 14-17 2002.

## CONTACT

Peter B. Sunderland, pbs@umd.edu.

WASHINGTON UNIVERSITY  
SCHOOL OF ENGINEERING AND APPLIED SCIENCE  
DEPARTMENT OF MECHANICAL, AEROSPACE, AND  
STRUCTURAL ENGINEERING

---

FLAME QUENCHING LIMITS AND MATERIALS  
DEGRADATION OF HYDROGEN LEAKS

by

Michael S. Butler, Jr.

Prepared under the direction of Professor R.L. Axelbaum

---

A thesis presented to the School of Engineering of  
Washington University in partial fulfillment of the  
requirements for the degree of  
MASTER OF SCIENCE

May 2008

Saint Louis, Missouri

WASHINGTON UNIVERSITY  
SCHOOL OF ENGINEERING AND APPLIED SCIENCE  
DEPARTMENT OF MECHANICAL, AEROSPACE, AND  
STRUCTURAL ENGINEERING

---

ABSTRACT

---

FLAME QUENCHING LIMITS AND MATERIALS  
DEGRADATION OF HYDROGEN LEAKS

by

Michael S. Butler, Jr.

---

ADVISOR: R.L. Axelbaum

---

May 2008

St. Louis, Missouri

---

This study examines the types of hydrogen leaks that can support combustion and their effects on surrounding material. Hydrogen, methane, and propane diffusion flames on round burners and leaky compression fittings were observed. Measurements included limits of quenching and blowoff for round burners with diameters of 0.006 - 3.18 mm. The measured mass flow rates at the quenching limits were found to be generally independent of burner diameter at burner diameters between 1.5 mm and 3.2 mm. In terms of mass flow rate, hydrogen had a lower quenching limit and a higher blowoff limit than either methane or propane. Hydrogen flames were the weakest flames ever recorded with mass flow rates as low as 0.0039 mg/s, which translates to a thermal power output of 0.55 W. The quenching limits for diffusion flames on round burners with thick walls were found to be higher than for thin walls. The limits were also found to be independent of burner orientation. In other words leaks with low flow rates are able to support flames independent of their orientation. The minimum mass flow rate of hydrogen that can support combustion from a leaking compression fitting was found to be 0.028 mg/s. This flow was independent of pressure (up to 131 bar) and about an order of magnitude lower than the corresponding methane and propane mass flow rates. The hydrogen embrittlement effects on 316 stainless steel and 1100 aluminum tubes with flames supported over radial holes were also investigated. Micrograph images of embrittled and as-received material were compared, and the degraded material was found to have defects that were either multi-phase material or microvoids in the material. Each of these phenomena would result in decreased fatigue resistance in a real life system. The implications for fire safety are discussed.

# Contents

List of Tables .....	iii
List of Figures .....	iv
Acknowledgements.....	vi
<b>1 Why Hydrogen? .....</b>	<b>1</b>
<b>2 Hydrogen Leak Quenching Limits .....</b>	<b>4</b>
2.1 Introduction .....	4
2.2 Flame Quench Scaling .....	7
2.3 Experimental.....	9
2.3.1 Round Burners .....	9
2.3.2 Leaky Compression Fittings.....	11
2.4 Results .....	13
2.4.1 Round Burner Results .....	13
2.4.2 Weakest Flames.....	19
2.4.3 Numerical Solution.....	21
2.4.4 Leaky Fittings Results.....	23
2.5 Conclusions .....	26
<b>3 Materials Degradation From A Sustained Leak Flame.....</b>	<b>28</b>
3.1 Introduction .....	28
3.2 Experimental.....	32
3.2.1 Burner Configuration and Temperature Measurement.....	32
3.1.3 Materials Characterization .....	33
3.2 Results .....	34
3.2.1 Temperature Measurement .....	34
3.2.2 Numerical Simulation.....	
3.2.3 Materials Characterization .....	9
3.3 Conclusion.....	10
<b>4 Future Work .....</b>	<b>7</b>
<b>References .....</b>	<b>22</b>
<b>Vita .....</b>	<b>23</b>

# List of Tables

Table 2.1: Gas Characteristics.....	8
Table 2.2: Hole diameters.....	10

# List of Figures

Figure 2.1 Burners .....	9
Figure 2.2 Contrast-enhanced hydrogen flame .....	13
Figure 2.3 Quenching and blowoff limits .....	14
Figure 2.4 Quenching mass flow rate vs. diameter .....	15
Figure 2.5 Effect of orientation on tube burners .....	17
Figure 2.6 Effect of orientation on pinhole burners .....	18
Figure 2.7 Choked flow rates through a leak .....	19
Figure 2.8 Weakest flames .....	21
Figure 2.9 Numerical grid system .....	22
Figure 2.10 OH contours compared to real flame .....	23
Figure 2.11 Flames near extinction .....	24
Figure 2.12 Quenching limits for leaky fittings .....	24
Figure 2.13 Effect of orientation on leaky fittings .....	25
Figure 2.14 Effect of burner size on leaky fittings .....	26
Figure 3.1 Flame temperature profile for pinhole burner .....	37
Figure 3.2 Flame temperature profile for tube burner .....	38
Figure 3.3 Numerical solution vs. experimental for pinhole burner .....	39
Figure 3.4 Numerical solution vs. experimental for tube burner .....	40
Figure 3.5 Experimental and numerical compared to real flame .....	41
Figure 3.6 Control aluminum specimen .....	43
Figure 3.7 Vertical flame aluminum specimen .....	43
Figure 3.8 Inverted flame aluminum specimen .....	43
Figure 3.9 Control steel specimen .....	44
Figure 3.10 Vertical flame steel specimen .....	45
Figure 3.11 Inverted flame steel specimen .....	45

# Acknowledgements

Thanks to the guidance and support of Dr. Richard Axelbaum for giving a physics student a chance to learn a new field, to my parents for teaching me that I can, to my grandma for not letting me go hungry, and to my master's thesis committee for their considerable time and effort. Considerable work was done by Chris Moran and Peter Sunderland from University of Maryland with their studies on leaky compression fittings. All of the work presented here on leaky compression fittings is theirs. Thanks to Xiaofeng Zheng for his work on the numerical simulations. This work was supported financially by the National Institute of Standards and Technology and the NASA-Missouri Space Grant Program.

Michael S. Butler, Jr.

*Washington University in St. Louis*

*May 2008*

# Chapter 1

## Why Hydrogen?

Concerns about the emissions of greenhouse gases have led to extensive consideration of hydrogen as an energy carrier. Oil supplies 33% of the world's primary energy [1], and hydrogen could help mitigate concerns about fossil fuel consumption [2]. Some benefits of hydrogen include that its products of combustion are mainly water, it can be stored as liquid, gas or solid, and it can be transported using pipelines, tankers or rail trucks over long distances [3]. It is also projected that hydrogen production can be produced efficiently using nuclear sources or renewable methods such as wind [4].

There are also many other advantages of hydrogen as an energy carrier. Hydrogen might some day be able to relieve the increasing cost of fossil fuels. It is probable that the cost of fossil fuels will continue to increase with dwindling supplies while the cost of hydrogen will decrease with advances in technology. Hydrogen can be produced from water, which is indigenous or easily accessible and relatively cheap to every nation. When the world gets to the point when avoiding carbon-containing resources is cost efficient, there will be an essentially infinite amount of raw materials for hydrogen production. Hence, this can be an opportunity to achieve wider global distribution of a sustainable energy supply. This would benefit developing nations that do not currently have access to oil fields as well as developed nations that rely on international fuel supplies. As an example, the US sacrifices about \$1 billion per week from its economy in the cost of purchasing foreign energy. Also, hydrogen has the highest specific energy of the chemical fuels adding to its potential efficiency. In regards to its environmental benefits, hydrogen can help inhibit the growth of greenhouse gas emission while stimulating economic growth in a new industry for years

to come [5]. Although many of these advantages are only foreseeable in the future, there are some current applications of hydrogen.

Hydrogen is currently economically feasible in several industries, and hydrogen production in the US has already reached 3 billion cubic feet per year. The applications that currently require this hydrogen include industrial processes that use hydrogen as a chemical feed-stock. It is used as a reducing agent in the mineral industry, as a hydrogenation agent in the petroleum industry, and as a bonding agent in the chemical industry. It is also used as a fuel in high-temperature welding and for space exploration. It can be used in future applications as a fuel for power plant fuel-cell generation of electricity, as a coolant in super-conductor technology, and as the previously noted transportation fuel to replace oil [5].

There are, however, several unusual hazards associated with hydrogen, and as applications for hydrogen shift to include the commercial sector there will be greater risk than in the current, tightly-regulated industrial sector. Thus, codes and standards must be updated [6]. Experimental and numerical results have shown that hydrogen poses significant safety risks with respect to explosions and high pressure gas release [7]. In addition, hydrogen has unique properties that lead to unusual fire safety hazards, including high leak propensity, high blowoff limits, material embrittlement tendencies, ease of ignition, and invisible flames. This combination of properties suggests that small, easily ignitable hydrogen leaks may support combustion that could go unnoticed and degrade containment materials.

To investigate this scenario, two sets of experiments were performed exposing the additional risks associated with hydrogen. First, the quenching limits and blowoff limits were found for hydrogen diffusion flames on several types of round hole burners. A quenching limit is the lowest hydrogen flow rate where a flame can still be sustained, and a blowoff limit is the maximum amount of flow where a flame can exist. Also, quenching limits were found for leaky Swagelok fittings. Next, a material degradation

study was performed to show the long-term effects of having a stable, hydrogen leak flame. A small, nearly invisible hydrogen flame was established on an aluminum and a steel tube and allowed to exist for over a month. The effects of the degradation on the metal were then examined.

## Chapter 2

# Hydrogen Leak Quenching Limits

## 2.1 Introduction

This work was done in conjunction with colleagues at the University of Maryland's Department of Fire Protection Engineering. Our goal was to evaluate the increased fire safety risks associated with hydrogen as compared to other common gaseous fuels such as propane and methane. Hydrogen has several unique characteristics that make it especially prone to safety hazards compared to other fuels; it has a high propensity for leakage, broad flammability limits, and the flame has low luminosity. One consequence of these characteristics is that a small crack in a hydrogen system can mean a large flow rate as compared to the scenario of the same sized crack in a propane or methane system. also, because of the broad flammability limits, a hydrogen and air mixture is more likely to be combustible than if it were a mixture of propane or methane in air. Once a leak is established, it will be difficult to detect because of its low luminosity, especially if the flame size is small.

These small hydrogen flames are important to analyze because they can be potentially dangerous despite their size. The "leak flame" could degrade the material around the crack and make it bigger, and they can be an ignition source in the presence of other fuels. The "leak flames" that are under consideration are very similar to flames that have already been studied, micro diffusion flames.

Only limited results are available for micro diffusion flames. The studies employed a variety of approaches including numerical techniques and varying burner sizes, burner shapes, and fuel gases to characterize micro diffusion flames. Micro-slot

burners were used by Baker et al. [9] to verify a flame height expression for purely diffusion controlled flames, and defined useful parameters for characterizing dominant flame mechanisms. Their diffusion-buoyancy and diffusion-momentum parameters were found to be in the range of flames dominated by diffusion, i.e. not buoyancy. This work extended the investigations of Roper et al. [10] to smaller slot sizes. Micro diffusion flames were also studied on circular burners. Ban et al. [11] investigated flames established on such burners with inner diameters of 0.15, 0.25, and 0.40 mm. The experimental results from these small burners verified the predicted flame shapes, which were found assuming weak gravitational effects, of laminar flames ( $Re = 1-10$ ) for three fuels: ethane, ethylene and acetylene. Weak buoyancy effects were further proven for low flow rate, nearly spherical flames that were unaltered when the burner was rotated. The numerical results conducted by Cheng et al. [12] supported these findings. Simulations for hydrogen micro diffusion flames were performed that yielded temperature contours and species profiles. The group concluded that buoyancy effects were insignificant for such flames, as indicated by their shape and a dimensionless number analysis. Nakamura et al. [13] simulated methane micro diffusion flames supported on circular burners of diameters less than 1 mm. They, too, found the nearly spherical flame structure associated with weak buoyancy forces. The group was also able to find the presence of a minimum flame size necessary for combustion.

Micro diffusion flames could be found in hydrogen plumbing systems as a result of the ignition of leaks from cracks or holes in fittings, tubing, or any other hydrogen-containing device. In order to relate the previous studies where flow rate was the independent variable to systems where hydrogen pressure is the controlling variable, Lee et al. [14] conducted leak rate experiments on micromachined orifices of different sizes and shapes. They examined the differences in flow rates among circular, square, and elliptical slit orifices as a function of pressure. In most cases, the flow was choked, which yielded flows higher than those of the helium signature test. Helium was used as a safer substitute for hydrogen. Another type of leak was investigated by Schefer et al. [15] where the flow was pressure-driven convection and permeation through metals. They obtained analytical relationships for flow rates of choked flows, subsonic laminar

flows, and turbulent flows. Hydrogen leakage in threaded pipe fittings was also considered. Ge and Sutton [16] found that a larger tightening torque is less important in leak prevention than choice and proper application of thread sealant. The tests were run up to 7000 kPa.

Swain and Swain [17] evaluated the safety risks associated with leaks of hydrogen, methane, and propane in the case where the leaks occur in an enclosed area. They modeled and measured leak rates for diffusion, laminar, and turbulent flow regimes and found that, for a given supply pressure, combustible mixtures resulted more quickly for propane and hydrogen leaks than for methane leaks. It was also found that hydrogen had significantly higher volumetric flow rates than methane or propane.

Because of the possibility of higher flow rates, blowoff limits have been studied. They were measured by Kalghatgi et al. [18] for a variety of fuels including propane, methane and hydrogen on circular burners. The limits were measured by establishing a flame over a stainless steel, hypodermic tube and increasing the fuel flow rate until the flame went out. Quenching flow rates were obtained experimentally by Matta et al. [19] for propane by establishing a flame over the same type of burner and decreasing the fuel flow rate until the flame extinguished. The same quenching limit experiments were performed by Cheng et al. [20] for methane. Both groups found that quenching mass flow rate was largely independent of burner diameter. As a result, the ability for a flame to exist at a leak is not a function of the leak size, but rather how much fuel is being emitted by the leak. Since hydrogen systems are projected to contain pressures up to 40 MPa, it is critical to be able to quantify the quenching limit of hydrogen.

Other characteristics of hydrogen that make it more prone to risk are that it is easier to ignite than most other common fuels, and, once ignited, it is difficult to detect. The minimum ignition energy for hydrogen is an order of magnitude lower than those for methane and propane [16]. This implies that a small spark discharge that would be too weak to ignite a methane or propane leak might be able to ignite a hydrogen leak.

Hydrogen flames also have minimal luminosity [12], hence a hydrogen leak sustaining a flame would be difficult to detect by the human eye.

Given that these conditions might exist, it is also a possibility that the hydrogen leak flame can degrade the surrounding material and result in a catastrophic failure. Khan et al.[21] examined the effects of raised temperatures on carbon fabric/epoxy composites, a likely material for high pressure hydrogen storage tanks. Pehr [22] discusses some of the issues associated with hydrogen containment. Utgikar and Thiesen [23] discuss the impact of hydrogen on materials, and the safety of hydrogen fuel tanks. These studies have found that hydrogen has unique degradation properties.

Considering these properties, the scenario of interest in this work is that a small leak in a hydrogen system might ignite, support a flame that is difficult to detect, and degrade containment materials to the point of a catastrophic failure. This study includes experiments and analysis to identify hydrogen leaks that can support flames. Thus motivated, the objectives of this work are to measure limits of sustained combustion, both at quenching and blowoff, for hydrogen on round burners and quenching limits for hydrogen, methane and propane on leaky compression fittings.

## 2.2 Flame Quench Scaling

A scaling analysis is presented to interpret measured flame quenching limits. These limits are the minimum flow rates required to support a diffusion flame. The stoichiometric length  $L_f$  of laminar gas jet diffusion flames on round burners is:

$$L_f / d = a Re = a \rho u_0 d / \mu , \quad (1)$$

where  $d$  is the burner inside diameter,  $a$  is a dimensionless fuel-specific empirical constant,  $Re$  is Reynolds number,  $u_0$  is the average fuel velocity in the burner,  $\rho$  is fuel density, and  $\mu$  is fuel dynamic viscosity. The scaling of Eq. (1) arises from many

theoretical and experimental studies, including Roper [10], Sunderland et al. [25], and references cited therein. The constant  $a$  is fuel specific and has been measured by Sunderland et al. [25], as listed in Table 2.1.

The base of an attached jet diffusion flame is quenched by the burner. Its standoff distance can be approximated as one half of the quenching distance of a stoichiometric premixed flame. Such quenching distances typically are reported as the minimum tube diameter,  $L_q$ , through which a premixed flame can pass. It is assumed here that a jet flame can be supported only if its stoichiometric length is greater than half this quenching distance:

$$L_f \geq L_q / 2. \quad (2)$$

**Table 2.1** Measurements of  $L_q$ , shown in Table 1, are taken from Kanury [26]. Selected fuel properties of hydrogen, methane, and propane. Values for  $a$  are from Sunderland et al. [25],  $L_a$  and  $S_L$  (laminar burning velocity) are from Kanury [26], and  $\mu$  is from Weast and Astle [27].

Fuel	$a$	$L_q$ [mm]	$S_L$ [cm/s]	$\mu$ [g/m-s]	$m_{fuel}$ [mg/s] predicted
H <sub>2</sub>	0.236	0.51	291	8.76e-3	0.008
CH <sub>4</sub>	0.136	2.3	37.3	1.09e-2	0.085
C <sub>3</sub> H <sub>8</sub>	0.108	1.78	42.9	7.95e-3	0.063

Measurements of  $L_q$ , shown in Table 2.1, are taken from Kanury [26]. When combined, Eqs. (1) and (2) predict the following fuel flow rate,  $m_{fuel}$ , at the quenching limit:

$$m_{fuel} = \pi \rho u_0 d^2 / 4 = \pi L_q \mu / (8 a). \quad (3)$$

Eq. (3) indicates that the fuel mass flow rate at the quenching limit is a fuel property that is independent of burner diameter. When values of  $L_q$ ,  $\mu$ , and  $a$  from Table 2.1 are inserted into Eq. (3), the predicted fuel mass flow rates at quenching are obtained and are listed in the table.

## 2.3 Experimental

Two different burner configurations are considered here: round hole burners and leaky compression fittings. There is generally a limited range of flow rates for which a flame can be established on the present burners. Below this range, the flow is said to be below the quenching limit. Quenching occurs when there is too much heat loss for combustion to be sustained. On the other extreme, blowoff limit occurs when the flow rate is reached beyond which the flame blows off the burner.

### 2.3.1 Round Hole Burners

Three different types of burners were considered for this work: tube burners, pinhole burners, and curved-wall pinhole burners, as displayed in Fig. 2.1. Each had a range of hole diameters. The flow was delivered via a pressure regulator and a flow control valve, and all tests were performed at ambient lab pressure.



**Figure 2.1 Burners used to find quenching limits. Inside diameters for pinhole burners were mm. Inside diameters for curved-wall burners were mm (small tubes) and mm (large tubes). Tube inside diameters were mm.**

The tube burners were made from stainless steel hypodermic tubes. Tube inside diameters ranged from 0.051 – 2.21 mm. These burners resemble microinjectors that may be used in future small-scale microelectro-mechanical power generators [14]. The pinhole burners were stainless steel nozzles that are manufactured for solid-stream spray generation. The top of each burner (except the two smallest ones) is a slightly curved

surface with a hole passing through its axis, as shown in Fig. 2.2. The two smallest burners had holes in planar, not curved, surfaces. The hole diameters ranged from 0.008 – 3.18 mm. The curved-wall pinhole burners were constructed of stainless steel tubes with two outside diameters: 1.59 and 6.35 mm. A radial hole was drilled in each tube.

**Table 2.2 Inside hole diameter on the three types of burners. Measurements are in mm. Large and small curved-wall burners denote the size of the outer diameter of the tube.**

Pinhole	Curved-wall (small)	Curved-wall (large)	Tube
0.008	0.41	0.41	0.051
0.13	0.53	1.75	0.152
0.36	0.74	2.46	0.406
0.53	0.86	3.12	0.838
0.71	1.02		1.194
0.84			2.21
1.01			
1.40			
1.78			
2.39			
3.18			

The small flow rates required special flow measurement procedures. For tests with round burners a glass soap-bubble meter was installed upstream of the burners. Quenching flow rates were measured by first establishing a small flame, decreasing the flow rate until the flame extinguished, and then introducing a soap bubble in the meter for flow rate measurement.

Each burner was allowed to warm to just above room temperature to prevent water condensation on the burner surface. This was necessary because water condensation was found to disturb flow from the small burners, sometimes extinguishing the flames. Tests performed at different burner temperatures, up to about 200 °C, found quenching flow rate to be largely independent of burner temperature.

Tests were also conducted with varying ambient humidity, and quenching flow rate was found to be generally independent of humidity in the range of 46 – 90% relative humidity. Observing the existence of a hydrogen flame was complicated by the minimal luminosity of the flames, especially at low flow rates, but this was resolved by using a downstream thermocouple to detect the flame. K-type thermocouples were chosen to avoid catalysis, and were placed several flame lengths above the flames to avoid disturbances.

Additional quenching experiments were performed to consider buoyancy effects. Quenching flow rates were found for both pinhole and tube burners in the vertical, horizontal, and inverted orientations.

Burner temperature was not an issue during blowoff measurements because the burners remained relatively cool. The fuel flow rate at blowoff was measured in much the same way as for quenching limits. A stable, large flame was first established; the flow rate was then increased by increasing the upstream pressure until the flame blew off. For these tests the flames were detected visually. Hearing protection was used for blowoff tests on larger burners.

### **2.3.2 Leaky Fittings**

Quenching limits were also measured for leaky compression fittings [31]. Leaks were intentionally introduced. This simulates an unintended leak in a defective fuel line. Presently no regulations exist for allowable leak rates in hydrogen plumbing systems.

The experiments employed Swagelok® stainless steel tube union compression fittings for 3.2, 6.4, and 12.7 mm outside diameter stainless steel tubes. The end of the union opposite the tube was capped such that the only flowing gas was that which went through the leak. Leaks were introduced three ways into fittings that previously were made according to manufacturer instructions and found to be leak tight. The first was

by reducing the torque on the threaded nut. The second was by tightening the threaded nut by an additional 0.75 turns. The third was by scratching the front ferrule sealing surface. All three types of leaks are occasionally encountered in plumbing systems.

Quenching limits were found by adjusting the torque on the threaded nut and then adjusting the upstream pressure until extinction was observed. For pressures above (and below) the quenching limit, an external flame impinging on the leak region did (and did not) result in a persistent flame at the leak. Upstream pressure was controlled with a pressure regulator in the range of 1.7 – 131 bar<sub>g</sub> (24 – 1900 psig). When a quenching limit was established, a tube was installed over the fitting such that the leak flow passed into a soap bubble meter at laboratory pressure. The quenching flow rate was then measured with the bubble meter. The burners were allowed to cool to room temperature prior to each test.

For hydrogen, the flames generally were not visible even in dark conditions. Existence or absence of persistent flames was determined with a thermocouple positioned 2 cm above the burner. Unlike for methane and propane, a pop was heard at ignition for hydrogen. For a flow rate (i.e., a pressure) below the quenching limit the pop was followed by extinction when the external flame was removed. At slightly higher pressures, this pop was followed by a persistent flame.

For methane and propane, quenching limits were identified visually – tests with thermocouples confirmed that these flames were visible, even when only slightly above their quenching limits. Most tests were performed with the burner in the vertical orientation, with the leak at the top end of the tube. Horizontal and inverted orientations also were considered for some 6.4 mm burner tests.

## 2.4 Results

The following results have been divided into those for round hole burners and those for leaky fittings.

### 2.4.1 Round Hole Burner Results

Figure 2.2 shows an image of a hydrogen flame on a 0.36 mm pinhole burner just prior to extinction. The photo was taken in a dimly lit room with  $f/4.2$  and an exposure time of 30 s. Despite the large aperture and long exposure time, the image is still very faint. The hydrogen quenching distance of Table 1 suggests that steady hydrogen diffusion flames should be anchored about 0.25 mm above the burner surface. Figure 2.2 shows this is reasonable for the present flames near their quenching limits.

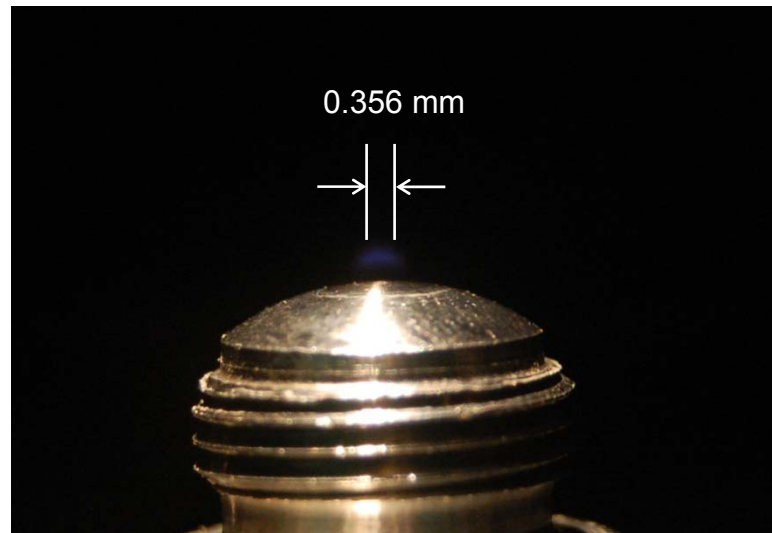


**Figure 2.2** Contrast-enhanced image of hydrogen flame over a 0.356 mm pinhole burner (original in color).

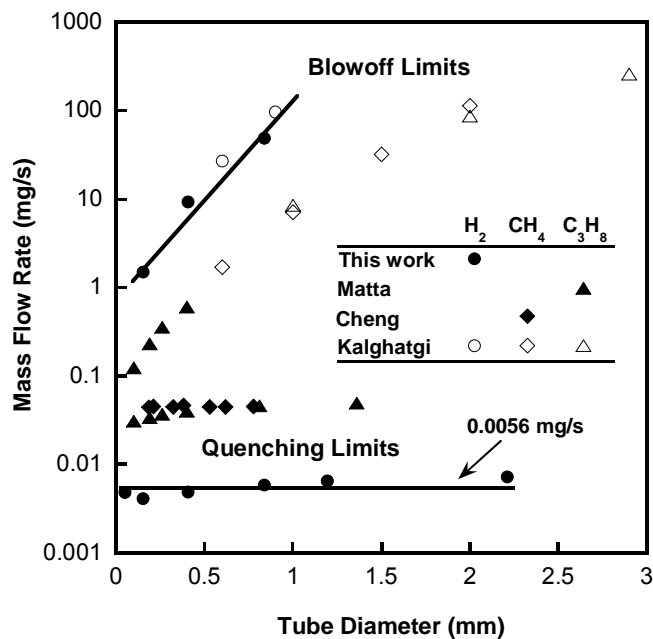


**Figure 2.3** Quenching and blowoff limits versus tube burner inner diameter. Hydrogen quenching and blowoff limits include best fit line.

Figure 2.3 shows the limit data for tube burners. The blowoff flow rates increase with tube burner diameter, and the quenching flow rates are generally independent of diameter. The limits of combustion in Fig. 2.3 are much wider for hydrogen than for propane or methane. The hydrogen quenching mass flow rate limits are about an order of magnitude lower than those for methane and propane, while hydrogen blowoff mass flow rate limits are about an order of magnitude higher than those of the others. For a given leak diameter there is a range of low and high mass flow rates that hydrogen would be able to support a flame while propane and methane would be either quenched or blown off. The data from Matta et al. [14], Cheng et al. [12], and Kalghatgi [18] show that the limits for methane and propane are very similar. For all fuels, the quenching limits are nearly independent of burner diameter, whereas blowoff limits increase with increasing diameter. The independence of quenching limit from burner diameter is consistent with the analysis presented above, see Eq. (3).

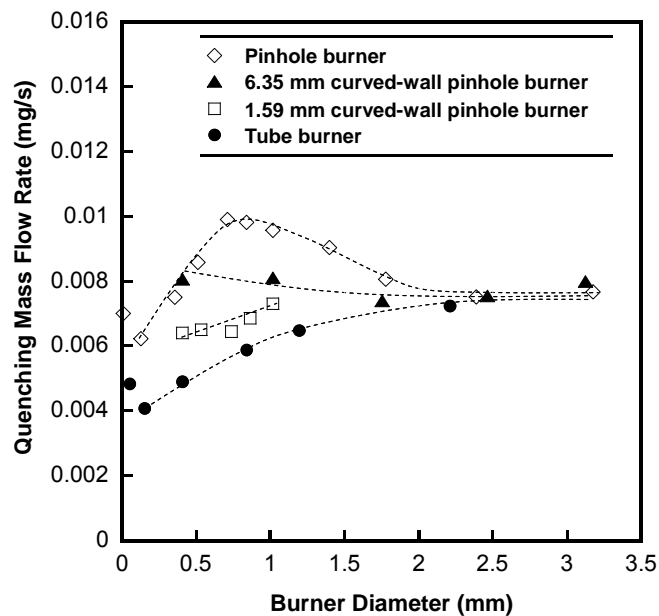


**Figure 2.4** Quenching mass flow rates versus burner diameter for hydrogen.

Figure 2.4 shows the hydrogen quenching limits for all three types of burners. The theory of Eq. (3) predicts that the quenching flow rate is independent of burner diameter. Figure 2.4 shows that the scaling analysis approximately predicts the average quenching flow rate for hydrogen, especially at burner diameters greater than 1.5 mm. For smaller burners, there are clearly other mechanisms that are affecting quenching limits that are not accounted for in the simple model.

Despite varying amounts of heat loss, the different burners display hydrogen's ability to sustain flames at very low mass flow rates. Nonetheless, heat loss contributes to the differences in limits for different round hole burners. For small burner diameters, the pinhole burners show the highest quenching flow rates, while the tube burners show the lowest. Pinhole burners have more heat loss than tube burners due to the geometry and the mass of the burner. Additionally, heat lost to the tube burners is more likely to be transferred to the incoming fuel and oxidizer flows than heat lost to the pinhole burners. This is not a loss as it acts to pre-heat the reactants, so that the primary losses are due to radiation from the tube which are small as the tube

temperature is near ambient. The results of the pinhole burners were similar to those observed by previous investigators.

The tube burners show the same trend as the data from Matta et al. [19] for propane in that there is an increase in quenching flow rate with increasing burner size. Heat loss rate increases with increasing burner diameter; with more heat loss, the quenching flow rate must increase to account for the weaker flame. The pinhole burners do not exhibit the same trend as the tube burners because approximately the same amount of heat loss occurs independent of burner hole size. The reason for the local maximum in Fig. 2.4 for pinhole burners is under investigation, however at large burner diameters, the quenching mass flow rate for both pinhole and tube burners approaches 0.008 mg/s, as predicted by the scaling analysis.

The effect of curvature on heat loss was investigated by using the curved-wall pinhole burners. It is expected that with increasing curvature, a flame will experience less wall heat loss. This should result in a stronger flame and a lower quenching flow rate. This is exactly what was observed for the two curved-wall burners. The 6.35 mm burners act more like pinhole burners, whereas the 1.59 mm burners act more like tube burners, and thus the 6.35 mm curved-wall burners have higher average quenching flow rates than the 1.59 mm curved-wall burners.

The quenching mass flow rate for hole diameters less than 0.2 mm is actually higher than that for 0.2 mm. This is true for both the pinhole and tube burners. We believe that the flow field is affecting the quenching limits at these very small sizes. In both cases, the miniscule inner diameters of the burners drastically increase the flow velocities exiting the burner. While in the larger sizes, diffusion dominates at the standoff distance, while that may not be so for the smallest diameters.

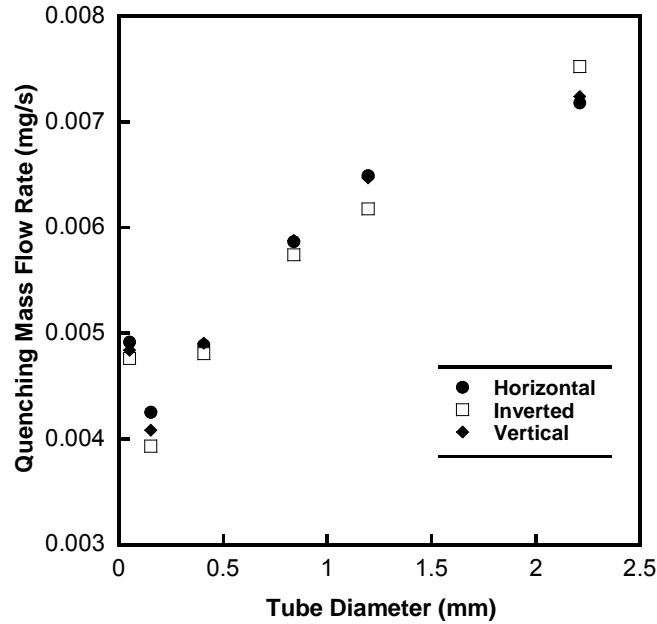


Figure 2.5 Quenching mass flow rates for several orientations of tube burners.

The effect of burner orientation was investigated in Figs. 2.5 and 2.6. The results reveal that the quenching flow rate for pinhole and tube burners is independent of orientation. Our earlier studies found that quenching flow rate was independent of burner temperature in the range of 20 °C to 200 °C. During these experiments, the burner was found to be warmer during non-vertical tests. If burner temperature does not affect temperature and it is the case that the quenching limit is not changing with orientation, then the flow field must also be constant with varying orientation. Hence, it was shown that flames near extinction are driven by mechanisms other than buoyancy. The Froude numbers were calculated from:

$$Fr = u_e^2 / gd, \quad (4)$$

where  $u_e$  is the fuel velocity at the burner port,  $g$  is the acceleration of gravity, and  $d$  is the burner diameter. The values for the present pinhole and tube burner quenching limit flames were found to be in the range of 0.17 to 3.9 E+10. Flames with the smallest Froude numbers are within the transitional to buoyancy-controlled regime [11]; typical buoyancy-controlled diffusion flames have  $Fr$  less than 0.1. This suggests that the flame structure at the quenching limits should not change with varying orientation.

Furthermore, small changes in burner temperature have been shown not to affect the quenching limits, so it is reasonable that the quenching limits are independent of orientation.

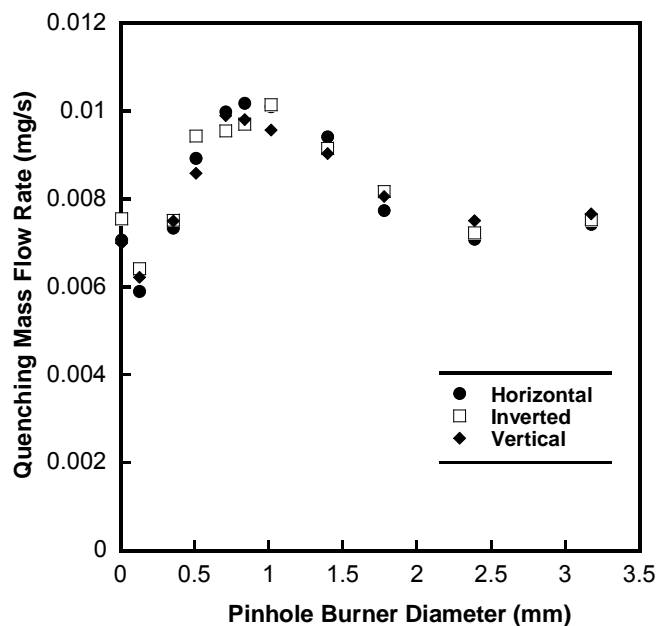
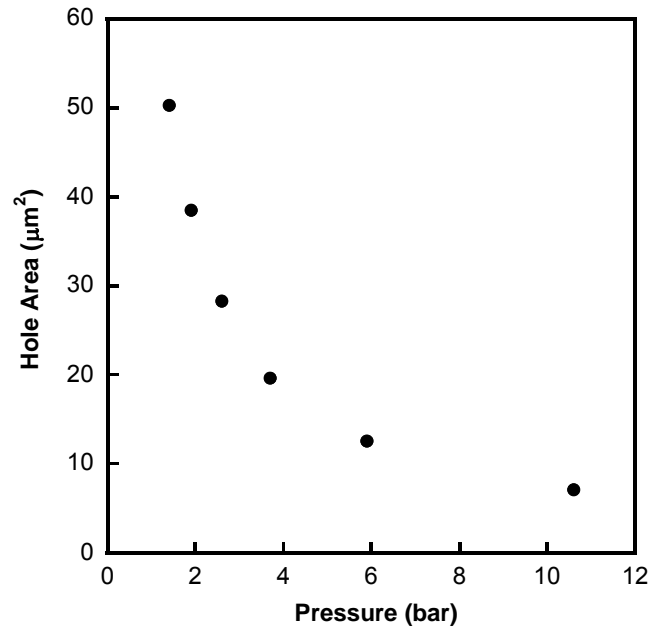


Figure 2.6 Quenching mass flow rates for several orientations of pinhole burners.

For most of the experiments the pressure drop across the burners was negligible. Nonetheless, important parameters governing the quenching limit is mass flow rate, and this can be related to the pressure drop across a small size leak. Thus the conditions that would lead to a flammable leak can be inferred from the present data. As an example, an inviscid, choked flow calculation of hydrogen mass flow rates through a hole of known cross sectional area yields a plot shown in Fig. 2.7. The plot shows data points where the mass flow rate is equal to the quenching mass flow rate and assumes that a flame would be quenched at a mass flow rate of 0.008 mg/s. By this approach the results in this work are applicable to a range of hydrogen systems after also considering viscous effects, which will be important and will vary with tubing wall thickness.



**Figure 2.7** Area and pressure given at quenching limit for an inviscid, choked flow. The region above the curve can sustain a flame, whereas the region below the curve can not sustain a flame.

## 2.4.2 Weakest Flame

The tube burners in this study had such low quenching flow rates that the flames supported over them are believed to be the weakest flames ever recorded. The smallest flame had a thermal output of 0.55 W. The thermal power output was calculated using

$$P = m\Delta H, \quad (5)$$

where  $m$  is the lowest mass flow rate (0.0039 mg/s) and  $\Delta H$  is the heat of combustion per mass (141.8 kJ/g).

Previously, Ronney et al. [32] documented flame balls produced under microgravity conditions with a power output of about 1.3 W, which were believed to be the weakest flames at that time. Flame balls were first predicted by Zeldovich [32], who proposed that a solution exists to the steady heat and mass conservation equations

corresponding to a stationary, spherical premixed flame. This solution was termed a flame ball, and the phenomena was accidentally discovered forty years after Zeldovich's work by Ronney et al. in drop tower experiments with lean hydrogen-air mixtures [34]. The microgravity environment was necessary in order to obtain the spherical symmetry and to avoid extinction brought on by buoyancy. In fact, flame balls have only been achieved in microgravity conditions with very lean hydrogen mixtures. The group's results showed that they were able to obtain flame balls that were considered the weakest flames ever recorded, at a heat release of about 1.3 W.

The hydrogen diffusion flames in this investigation were very weak, which opens up the possibility of even weaker flames. In an attempt to achieve even weaker flames, pure oxygen was used as the oxidizer. By inverting the tube, it became red hot and helped to stabilize the flame. This is shown in Fig. 2.8 where flames were able to be sustained with thermal outputs as low as 0.32 W. This shows that in the proper environment, hydrogen leaks can be established that need very little hydrogen to remain lit.

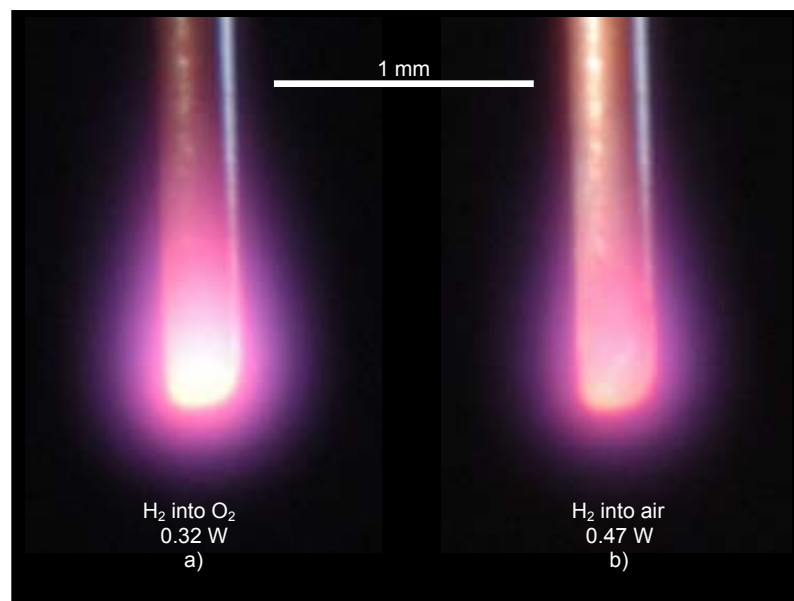


**Figure 2.8** Photos of weakest flames ever recorded; hydrogen flame in a) oxygen and b) air with a tube burner. ID=0.15 mm, OD = 0.30 mm, ISO 200, f/1.4, 1 s.

### 2.4.3 Numerical Solution

An attempt was made to numerically verifying the quenching limits. A computer code, UNICORN, was chosen that was able to model hydrogen combustion as well as other gaseous fuels. As will be shown, the code was not well suited for the limit flow situations.

First, a grid was constructed as shown in Fig. 2.9. The grid was altered for different inner diameters and outer diameters of the burner. Fig. 2.9 also shows that the domain of the region being investigated is about 10 mm in the radial direction and 20 mm in the vertical direction.

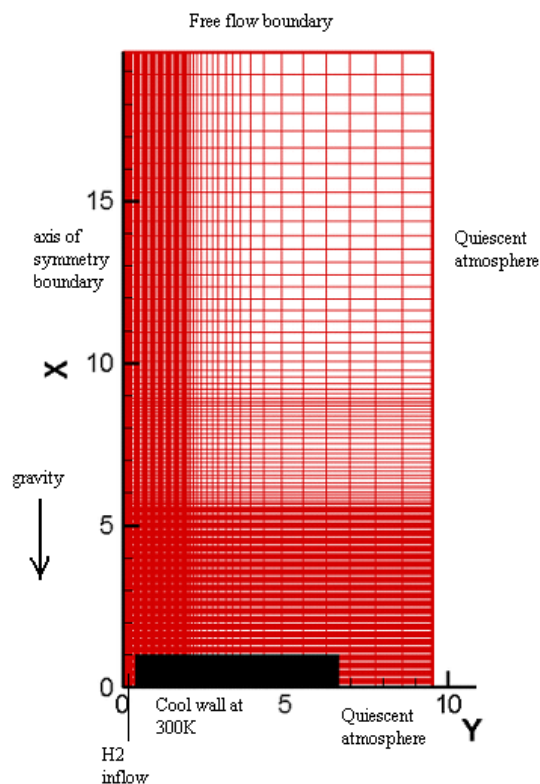


Figure 2.9 Grid system for UNICORN code.

Next, flames were modeled for a series of flow rates near the quenching limit. The numerical solutions found quenching limits that were too high at smaller pinhole

burner diameters and too low for higher diameters. At higher diameters, the flame would actually never extinguish - indicating a flaw in the code. At smaller diameters, the flame would extinguish at flow rates that could easily sustain stable flames under laboratory conditions. In order to investigate the cause of this discrepancy, photos were taken and compared to computed OH concentrations.

Figure 2.10 shows the juxtaposition of near limit photos on the left as well as computed OH concentrations on the right. It was anticipated that the flame would lie close to where the OH radicals are at their highest concentrations, and the code predicts the centerline location of the flame reasonably well, particularly at the lower flow rates. The reason that the code can not even qualitatively predict quenching limits is unknown.

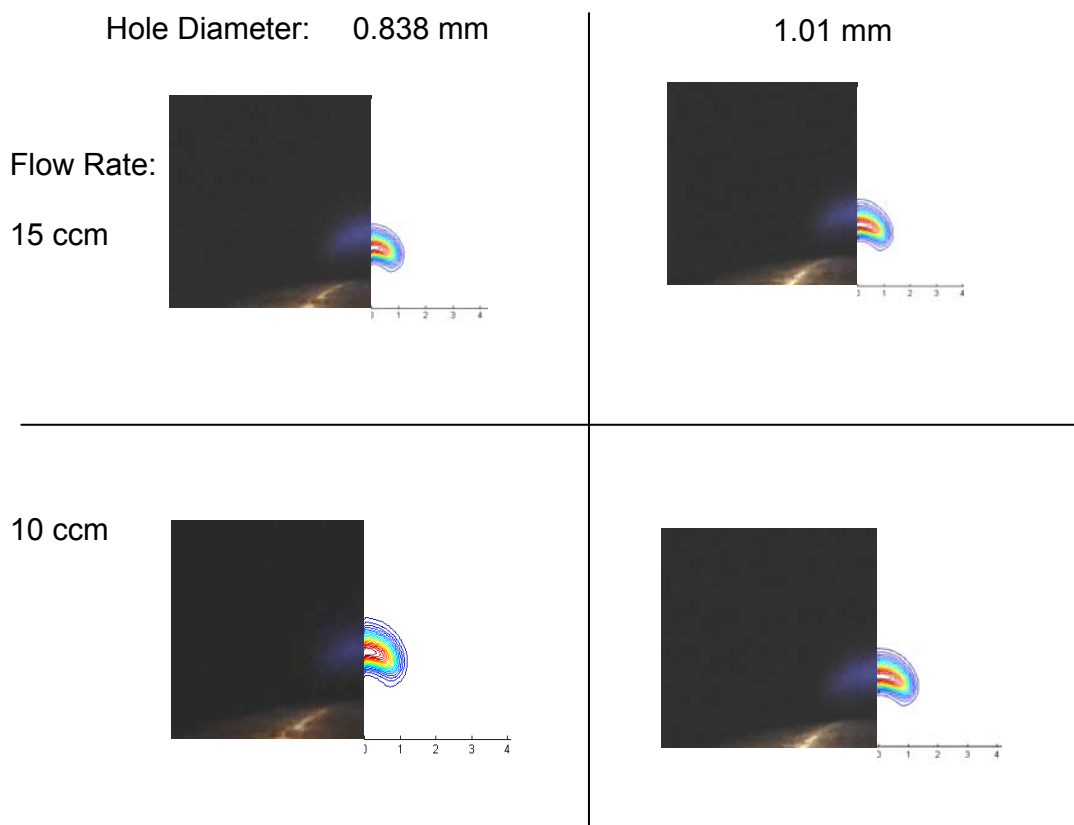
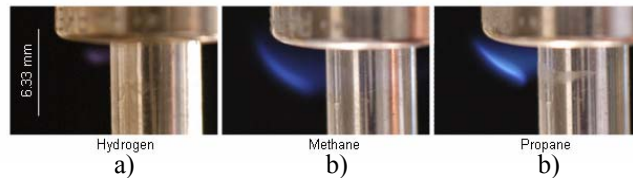


Figure 2.10 Photos compared to OH concentrations near quenching. The top row shows flames with a flow rate of 15 cm<sup>3</sup>/min and the bottom row is 10 cm<sup>3</sup>/min. The columns are split up by inner diameter.

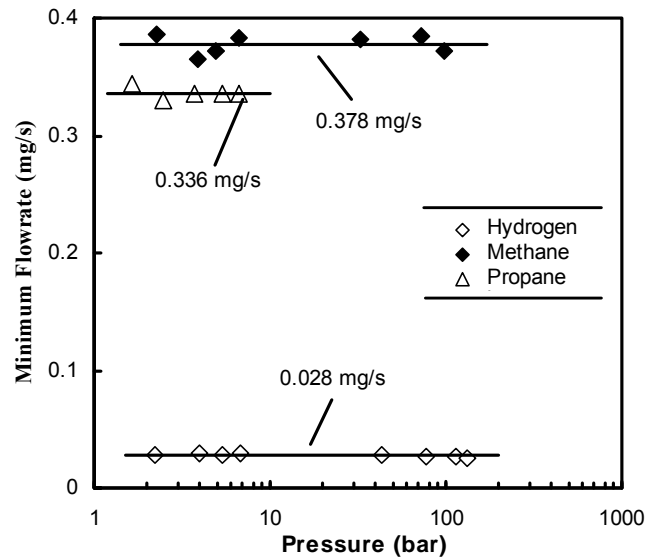
## 2.4.4 Leaky Fittings Results

Figure 2.11 shows images of hydrogen, methane, and propane flames on leaky compression fittings in the vertical orientation. These images were recorded slightly above the quenching limits. The hydrogen flame is significantly smaller than the others at the quenching limit.



**Figure 2.11** Flames near extinction on leaky compression fittings for a) hydrogen, b) methane, and c) propane (original in color).

Figure 2.12 shows the measured quenching limits for hydrogen, propane, and methane for a leaky compression fitting in the vertical orientation. A flame was established, then the pressure was decreased until the flame extinguished at the quenching limit. The present quenching limits results were the same for all three types of leaks, so only results from the reduced torque fittings are presented here. For each fuel the data at increased pressures are associated with increased torque on the fitting. The upper limit on pressure for propane is lower than for the others because the vapor pressure of propane at 25 °C is 9.1 bar (142 psia).



**Figure 2.12 Quenching limit (minimum flaming flow rate) versus upstream pressure for a leaky compression fitting in the vertical orientation. The horizontal lines represent the mean values of the measured quenching limits for a given fuel.**

Within experimental uncertainties, the data of Fig. 2.12 are independent of pressure for each fuel. This indicates that, as anticipated from the round hole burner results of Fig. 2.4, the important parameter for the quenching limit is the fuel mass flow rate and thus the upstream pressure has little or no effect on the limit. For these low flow rates and small leaks the upstream pressure is not expected to have a significant effect on the velocity profile of the jet entering the surrounding air. The mean hydrogen flow rate, 0.028 mg/s, is about an order of magnitude lower than for the other fuels owing to its low quenching distance and low molecular weight. For these leaks, there is a range of pressures where hydrogen is able to support a flame while propane and methane flames would be quenched.

The minimum flow rate to support a hydrogen flame for round burners (Fig. 2.4) is about an order of magnitude lower than that for leaky fittings (Fig. 2.12). This is attributed to additional burner heat losses in the leaky fittings, where the flames burn near large concave metal surfaces.

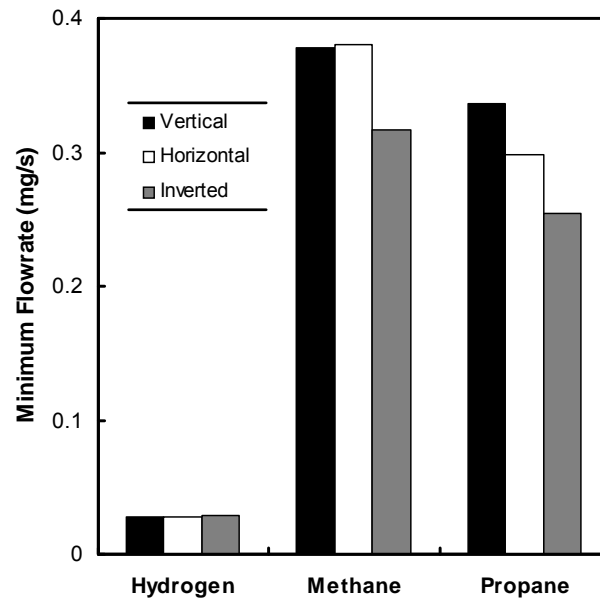


**Figure 2.13 Minimum flaming flow rate for a leaky compression fitting in vertical, horizontal and inverted orientations. Upstream pressure was about 4 bar in all cases.**

Figure 2.13 shows the effect of burner orientation on the quenching flow rate. Burner orientation has little or no effect on the quenching limit of hydrogen because these flames are so small at their limits as was shown in section 2.4.2. Burner orientation did have an effect on propane and methane quenching limits, the inverted fitting configuration requiring the lowest flow rate. The inverted configuration is such that the fitting is below the tube, opposite to what is shown in Fig. 2.11. This orientation minimized the impingement of flames on the surface of the fitting which allowed less heat to be lost to the fitting.

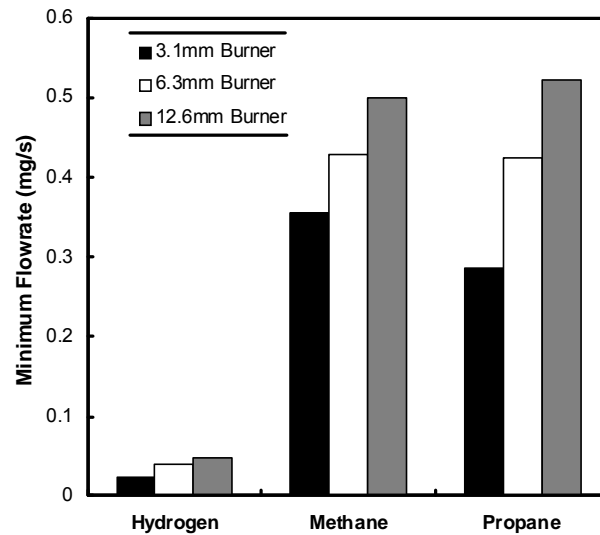


Figure 2.14 Minimum flaming flow rate for leaky compression fittings of 3.1 mm, 6.3 mm and 12.6 mm outside diameters. Upstream pressure was approximately 4 bar.

Figure 2.14 shows the effect of the tube fitting size on the minimum flaming flow rate for fitting in the vertical orientation. The tube fitting size is characterized by the tube diameter that the fitting is designed for. The tube fitting size played a large role in the minimum flaming flow rate for all fuels. There is 48% increase from the smallest to the largest burner for hydrogen, 29% increase for methane and a 45% increase for propane. This is due to the increased burner surface area that the flame loses heat to. It could also be due to the fact that the same amount of fuel is evenly distributed over a larger area hence diluting it. As the tube fitting gets larger, a larger flow is necessary to sustain combustion.

## 2.5 Conclusions

The quenching and blowoff limits for hydrogen on round hole burners were measured and compared with both our data and published values for other gases. Hydrogen diffusion flames on tube burners had significantly wider mass flow rate limits of combustion (between quenching and blowoff) than propane and methane. The

quenching flow rates for all these gases are largely independent of burner size, especially at the larger burner diameters.

The quenching flow rate was found to depend on burner type, owing to differences in wall heat loss. Tube burners had the lowest quenching flow rates, pinhole burners had the highest, and curved wall burners fell in-between. Although the type of burner did affect the quenching mass flow rate, the results showed that a hydrogen leak can sustain a flame at much lower flow rates than the other fuels for any burner type. The hydrogen flames investigated were the weakest flames in air ever documented with a thermal power output of 0.55 W.

Quenching limits for both burner types were found to be largely independent of burner orientation. As a result, a leak in a hydrogen system would be able to sustain a flame at low flow rates independent of the orientation of the leak.

The minimum flow rate necessary for sustaining a hydrogen flame on leaky 1/4" tube compression fitting is 0.028 mg/s. This is about an order of magnitude lower than for propane or methane. The minimum mass flow rate for all fuels is independent of upstream pressure.

The round burner and leaky compression fitting experiments yielded similar results in that they both found that the lower limits of combustion for hydrogen were about an order of magnitude lower than those for propane and methane. The two experiments differed in that their lower combustion limits differed by an order of magnitude owing to increased heat losses in the leaky compression fittings. In both cases, hydrogen was able to sustain flames at much lower mass flow rates than methane and propane.

## Chapter 3

# Materials Degradation from a Sustained Leak Flame

### 3.1 Introduction

Considering that hydrogen is more likely to be able to sustain a leak flame than other common gaseous fuels, the effects of a steady, hydrogen leak flame must also be considered. Furthermore, hydrogen is known to embrittle materials. This can result in decreased fatigue resistance and failure. These effects can also be increased by when a material is exposed to hydrogen at high pressures or temperatures. If a fitting or other component containing hydrogen at high pressures is exposed to a leak flame, the conditions could be present to degrade the material. Also, because of hydrogen's low luminosity, the probability of detecting a leak flame is minimal. If the material is allowed to degrade for long periods of time, this could possibly result in catastrophic failure. The scenario under investigation is material degradation due to a sustained hydrogen leak flame that is allowed to exist for a significant length of time.

Although this application of material degradation may be novel, the study of hydrogen degradation of materials is not. Nonetheless, the exact methods of hydrogen degradation are not fully understood. There are several evaluations for material degradation, but they all have common steps. Due to its low molecular weight, hydrogen is capable of being adsorbed and absorbed by the material. Marchi et al. [51] studied permeation rates of hydrogen in steels because this is the expected cause of hydrogen degradation. They found that there can be significant amounts of hydrogen

that diffuse through steels especially at high temperatures and pressures. There are many ways that hydrogen can enter a metal including electroplating, acid pickling and cathodic charging [44]. The hydrogen typically exists as atomic hydrogen once inside the metal. Minimum energy calculations show that it is advantageous for the atoms to form clusters. In addition to its localization tendencies, quantum mechanical calculations show that it is favorable for hydrogen to exist near structure defects and interfaces, due to their low electron densities. The following are possible next steps in the degradation process depending upon the type of metal:

- The atomic hydrogen can then form hard, brittle hydrides [45],
- There can be reactions between hydrogen and an impurity or alloy addition (e.g.  $2\text{H} + \text{O} \rightarrow \text{H}_2\text{O}$  in copper and  $4\text{H} + \text{C} \rightarrow \text{CH}_4$  in steel),
- A decrease in the adherence forces can result from the hydrogen clusters (decohesion),
- Molecular hydrogen can precipitate in the microcracks or microvoids creating high pressures, which can stabilize those structures [46,49].

The net result of these processes is that materials exposed to hydrogen tend to become embrittled, which includes loss of ductility and decreased stress at failure, as has been observed by Wang et al. [36].

Hydrogen embrittlement has been found in different materials including those that are potentially involved in hydrogen systems of today and those of the future. Züttel [37] notes that future pressure vessels may contain layers of carbon fiber and epoxy composites, which have been shown to degrade in a hydrogen environment at elevated temperatures. Khan et al. [21] studied a woven carbon fabric/epoxy composite material exposed to hydrogen and found that at increased temperature (tests went up to 150 °C) there was a significant decrease in the fatigue resistance of the material. Under a sinusoidal load cycling at a frequency of 20 Hz, fatigue resistance decreased by two orders of magnitude,  $2.0\text{E}+05$  to  $2.0\text{E}+03$  cycles, by increasing the temperature from

25 °C to 100 °C at a maximum stress level of 380 MPa. They also found that fatigue strength at 10E+6 cycles decreased from 400 MPa at 25 °C to 250 MPa at 150 °C. This material's strength properties are clearly negatively affected by even small increases in temperature above 25 °C.

In addition to hydrogen storage materials, there will inevitably be steels used in hydrogen systems for plumbing, which have their own risks for material degradation. It has been shown that hydrogen can have deleterious effects on many steels. Vencill et al. [37], in attempting to create a typical hydrogen environment in a fuel cell reformer, found that hydrogen can significantly embrittle some stainless steels including 304L, 310, and 253 MA along with Inconel 625, Inconel 718, and Hastelloy X nickel-based alloys, and Haynes 188 cobalt-based alloy. They showed that steel that has been subjected to an environment comparable to that of a fuel cell reformer (625 °C for up to 1500 hours) can fail at lower strains than the control specimens. A potential explanation of this was proposed by Oriani [42] in that microvoids can accumulate precipitated hydrogen at very high pressures. Panasyuk et al. [42] also performed an analysis of hydrogen systems, and they found that significant pressures within microcavities can be formed if certain conditions are present. This is one potential cause for the decrease in ductility found in tensile tests by many investigators [40,41]. The tests show a drastic decrease in area ratio for the hydrogenated material from the material not exposed to hydrogen, where area ratio is defined as the area of the specimen before stretching divided by the area afterwards.

These effects can be strongly altered by several variables, including pressure. Zheng noted that future hydrogen refueling stations may operate at pressures up to 100 MPa, so material selection must take this into consideration. Making matters worse is that there is a proportional relationship between steel susceptibility to hydrogen embrittlement and steel strength [45]. Several studies have found that this is a critical issue because stainless steels showed significant losses in ductility after being exposed to a high pressure (68.9 MPa) hydrogen environment [46,47].

Since we are considering a leak flame, the effects of elevated temperatures must be considered as well. Yokogawa et al. [48] performed tensile tests on metals exposed to elevated temperatures in a hydrogen environment. They found that, depending upon the steel type, there can be extreme reductions in ductility in samples that were found to be embrittled by hydrogen.

There is also an increased susceptibility to hydrogen attack when stress is present in steel. The reason for this is probably due to the increased hydrogen permeation rate in steel with increased stress. Beck et al. [50] found that this increase is largely dependent on the amount of stress applied over a range of 0 to 100 kg/mm<sup>2</sup>. This means that for even small stresses, say around 5 kg/mm<sup>2</sup>, the hydrogen permeation rate and hence hydrogen attack will increase. This permeation rate is probably related to the findings of Rozenak et al. [53]. They noted that stress can be responsible for crack advance, phase transformation, and localization of defects in austenitic stainless steel. Austenitic steels are those typically used in general engineering applications. It was found that the presence of atomic hydrogen in steel decreased the amount of stress required for these phenomena to occur.

There are also intrinsic hydrogen embrittlement risks associated with welds that are acknowledged by safety codes. During welding, hydrogen can be trapped in the molten metal of the weld, and the process can force hydrogen to diffuse into the heated portion of the parent material. This leads to embrittlement of both the weld and the surrounding material. Safety codes require that material testing be conducted 72 hours after the weld was performed to allow hydrogen cracking to develop [50]. Tsay et al. [52] found that steel welds containing atomic hydrogen had decreased tensile strengths compared to those welds that did not contain hydrogen. The same effect was found for the material surrounding the weld.

The scenario under consideration here is that a leak flame is established and the surrounding material, whether it be steel or a composite material, becomes degraded by the hydrogen diffusion flame and could potentially lead to catastrophic failure.

Since the application of this work is meant to be general, the exact placement of the material in the flame is not known. Therefore, varying degrees of exposure to a leak flame are considered.

## **3.2 Experimental**

### **3.2.1 Burner Configuration and Temperature Measurement**

Two experiments were run simultaneously on two different metals, 316 stainless steel and 1100 aluminum. Three holes were drilled in 3.18 mm outer diameter tubes. The holes were drilled such that one hole was issuing hydrogen in the upward, vertical direction, one was oriented horizontally and the third was oriented vertically downward. The inner diameter of the drilled holes in the steel were 1.0 mm, and 1.1 mm for the aluminum. Flames were established over each of the holes and the setup was allowed to run continuously for 44 days for the steel and 73 days for the aluminum.

For safety, the flow system only consisted of a pressure regulator and a flow restrictor to guard against failure or accidental opening of a valve. A three-sided steel barrier was constructed to guard against accidental exposure to the experiment. There were a few days throughout the experiment where the flame was extinguished due to lack of hydrogen. The experiment was set up as to allow for thermal expansion without constraint; stress was not desired as a variable in the system.

To understand the environment that material in a hydrogen system might be exposed to in the case of a leak flame, a temperature profile was measured for a hydrogen diffusion flame. The flame size was chosen such that its luminosity was undetectable by the naked eye in normal laboratory lighting and not especially bright in dim conditions. The flame represents a leak flame that could go undetected in a hydrogen system.

A B-type thermocouple was used with an inert coating to inhibit catalytic effects. A radiation correction was imposed to account for radiative losses from the finite size of the thermocouple bead. The correction assumed a sphere in forced convection. The radiation correction was as high as 180 °C at the peak temperature reading but decreased with lower temperatures. This correction is a little larger than ideal because the bead diameter was 0.2 mm. The thermocouple was translated and the voltage read using TestPoint data acquisition software. The accuracy of the readings was validated by directly comparing the voltage reading to an Omega thermocouple temperature table. The distance between temperature measurements in both the vertical and horizontal direction was 0.2 mm and was checked using a cathetometer. To minimize disturbances to the small flames due to air currents, the burner was housed in a four-sided plexiglass chamber.

### **3.2.2 Materials Characterization**

The tube specimens were cut up and placed into an epoxy that was then allowed to set. The sample was then polished beginning with a rough grade paper and ending with an alumina polish. During the experiments, it was observed that the center hole had a smaller flame size due to head losses. The flow circuit was set up so that hydrogen was being delivered to both ends of the tubes, but the flow experienced a pressure drop by the time it got to the center orifice. Thus, the degradation effects

around the center hole were largely ignored because they were not in the same conditions as their relative outer holes.

## 3.3 Results

### 3.3.1 Temperature Measurement

Figure 3.1 shows the results of the flame temperature contours for a pinhole burner. These results are most applicable to the present materials degradation experiment in that the surface of the tubes somewhat resembles the slight curvature of the pinhole burners. The fluid temperature can reach up to 1503 °C. The conditions 0.5 mm from the surface of the burner are over 1200 °C.

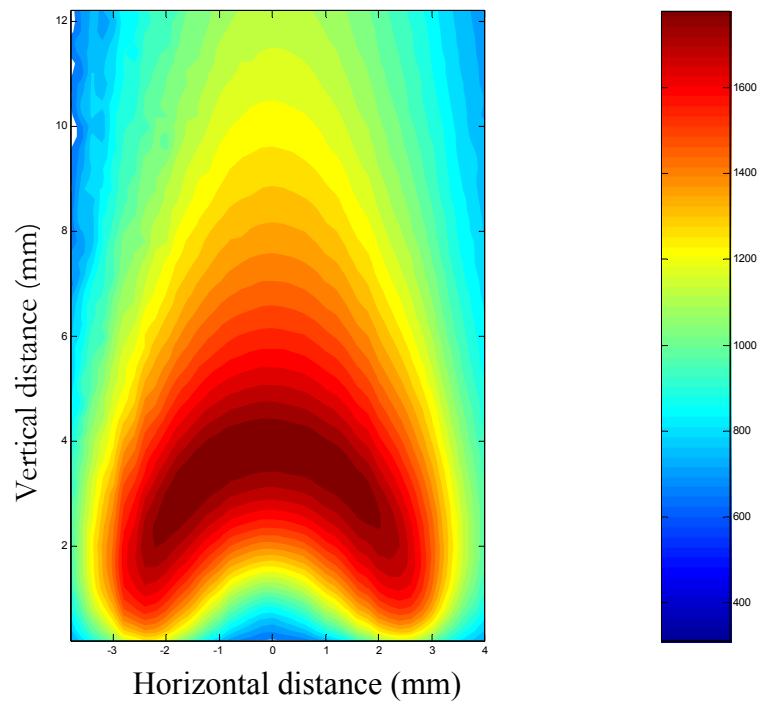


Figure 3.1 Temperature profile of a 70 cm<sup>3</sup>/min hydrogen flame. The temperature units are in K.

Temperature results were obtained for a tube burner to evaluate the effect of a burner with less material near the flame, and are shown in Fig. 3.2. The temperatures near the burner are significantly greater than for the pinhole burner. This was inferred from the high temperatures very close to the tube burner. The tube itself also glowed red indicating its high temperature. The wall temperature of the burner was found by wrapping a thermocouple around the tip of the tube. The average of the readings was around 900 °C. The roughness of the isotherms is caused by random ambient fluctuations of the air within the chamber. Precautions were taken as to minimize these, but they were difficult to completely eliminate.

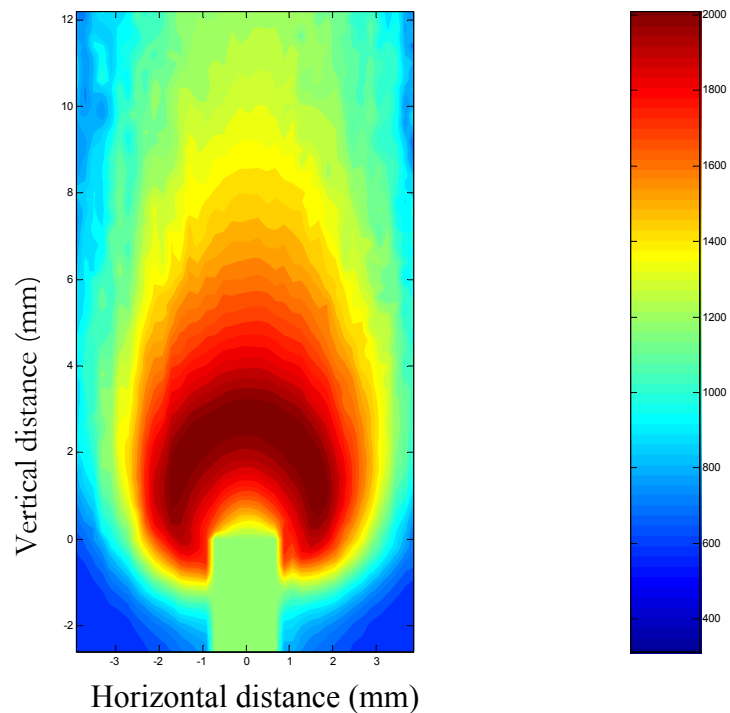


Figure 3.2 Temperature profile of 70 cm<sup>3</sup>/min hydrogen diffusion flame issuing from a tube burner.

### 2.3.2 Numerical Solution

Similar to the quenching limit numerical survey, numerical results were sought that would verify the experimental temperature profile. The code was used to model pinhole burners, which are geometrically similar to the tubes in the present experiment. There is some curvature of the pinhole burners, but there is also some curvature involved in the aluminum and steel tube specimens. Figure 3.3 exposes some first glance issues with the numerical solution. It is immediately apparent that the flame width, height, and standoff distance are dissimilar. This comparison corroborates the issues experienced with finding quenching limits numerically. Clearly, if the computer code is not able to accurately model the flame, then it can not accurately model the quenching limit. The same problem exists with the tube burners shown in Fig. 3.4. They are on the same temperature scale, which indicates that the flame temperatures are different.

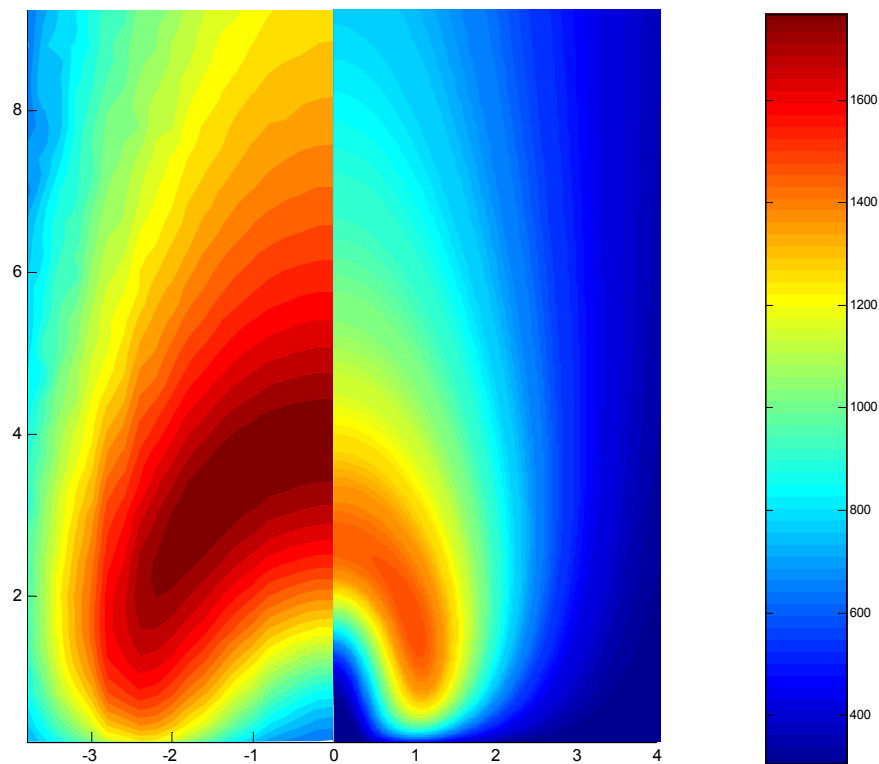
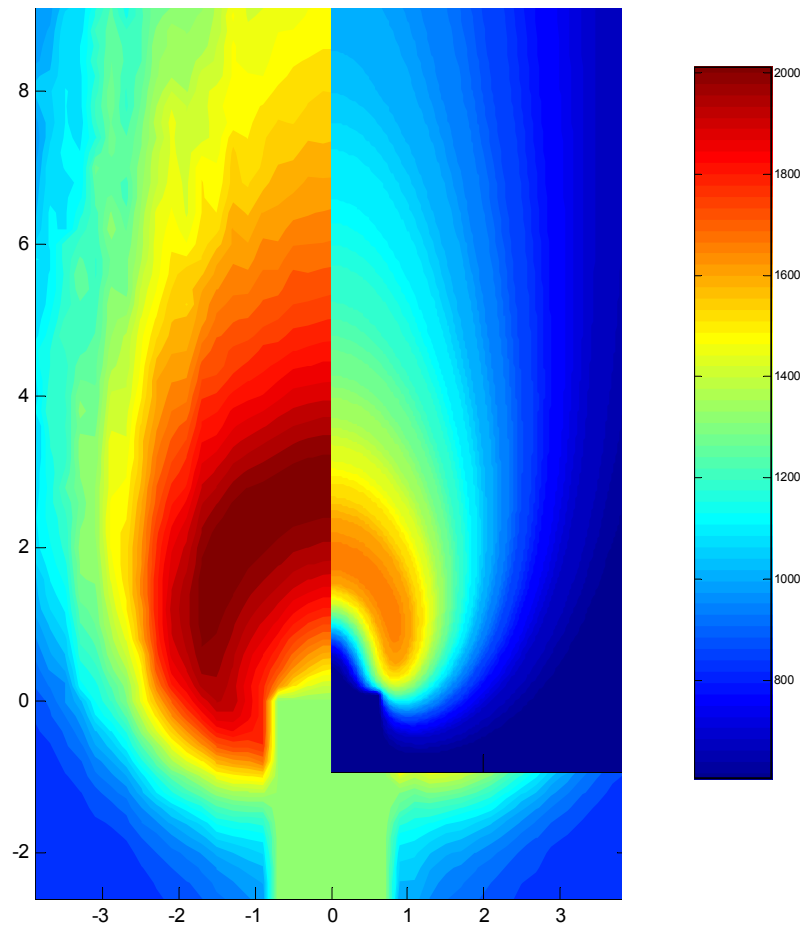


Figure 3.3 Experimental profile of 70 cm<sup>3</sup>/min hydrogen flame on left with numerical solution on right over pinhole burner.



**Figure 3.4** Experimental profile of 70 cm<sup>3</sup>/min hydrogen flame on left with numerical solution on right over tube burner.

Photographs of flames were taken and compared to the temperature profiles. Unlike the numerical results, the experimental temperature measurements accurately represented the basic flame shapes. The numerical flame is significantly smaller than the actual flame.

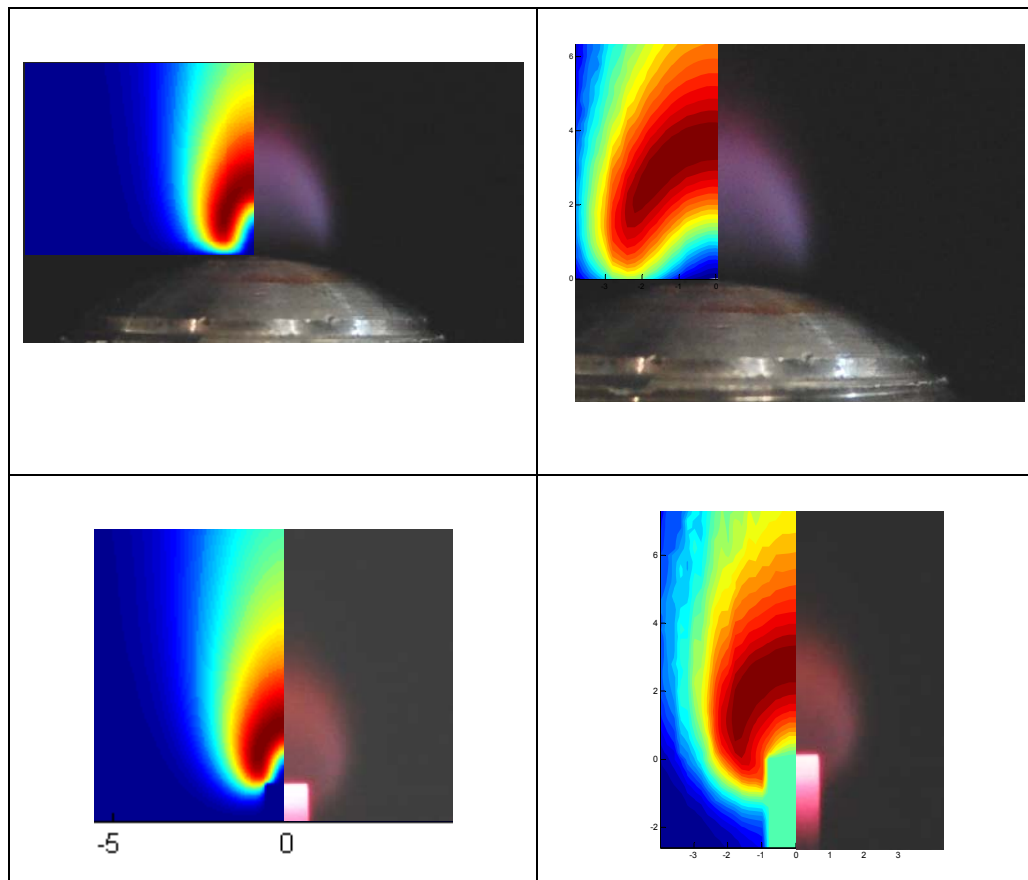


Figure 3.5 Numerical temperature solution on left and experimental temperature measurements on right compared to photo. The first row is pinhole burners, and the second is tube burners.

### 3.3.3 Materials Characterization

The parts of the tube that were studied were several millimeters away from the hole where the material was at the highest temperatures. Figure 3.6 includes the photos taken of the aluminum control specimen. In Figs. 3.7 and 3.8, which are for aluminum in the vertical and downward flame orientation, it is clear that there are dark spots that don't exist in the control specimen.

Temperature readings of the material were 490 °C and 640 °C of the vertical flame and inverted flame specimen, respectively. The temperature readings have limited accuracy due to the difficulty of the measurements, but it is clear that the temperatures approach the melting point of aluminum, 660 °C. 1100 aluminum contains .35 wt. %

iron and 0.25 wt. % silicon. By examining aluminum phase diagrams, it was found that the dark spots are most likely second phase material. Aluminum and iron form  $\text{Fe}_3\text{Al}$  and aluminum and silicon form Si particles within the material at the present temperatures [55].

To evaluate the effect on the mechanical properties of the material, the hardness of the samples was measured. The dimensions of a micro depression made with a known load were found. The control aluminum specimen yielded a hardness of 175 HV while the specimen with the inverted flame had a hardness of 62 HV. Both of these values are average values over six trials excluding the maximum and minimum data points because each set had a few outliers. This decrease in hardness is consistent with the transition from a metal that is in the worked condition to a metal in the annealed condition. The result is the annealing of the deformation substructure and a coarsened microstructure. Although, the effects are most likely due to the temperatures, it can not be ruled out that the effects of hydrogen embrittlement have not played a role in the degradation. Also, within a hydrogen flame, there are highly reactive radicals that may also have had an effect.

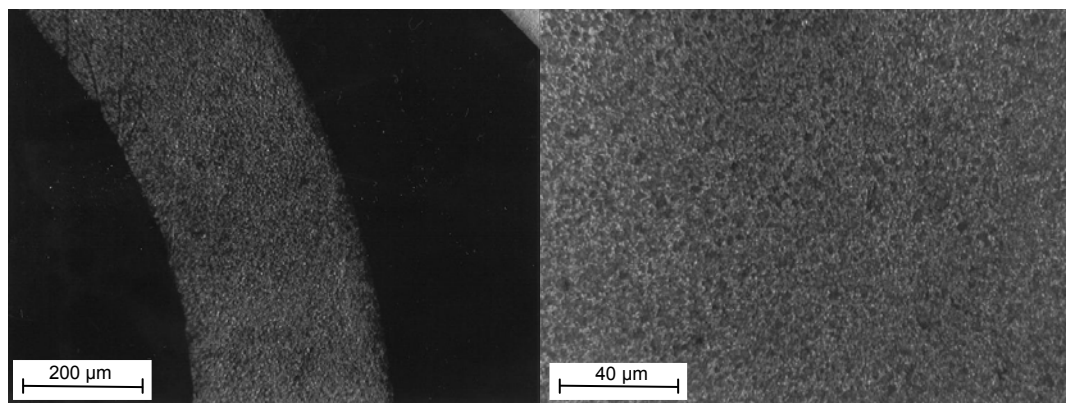
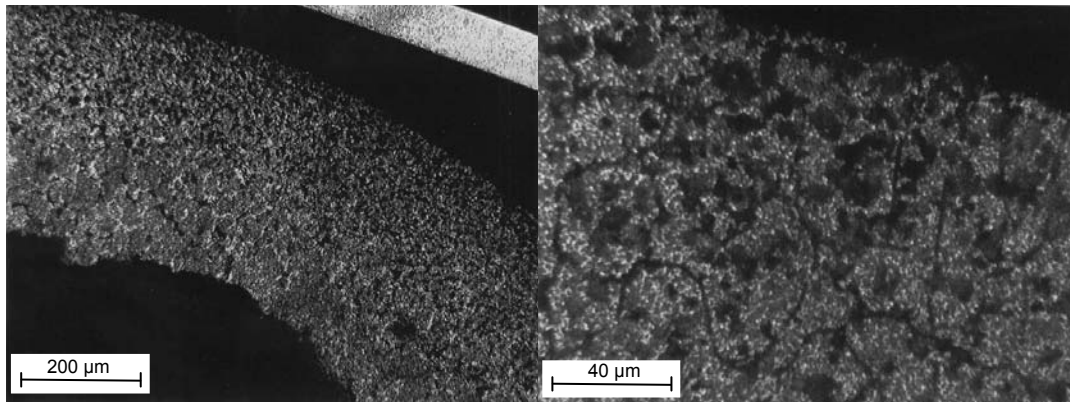
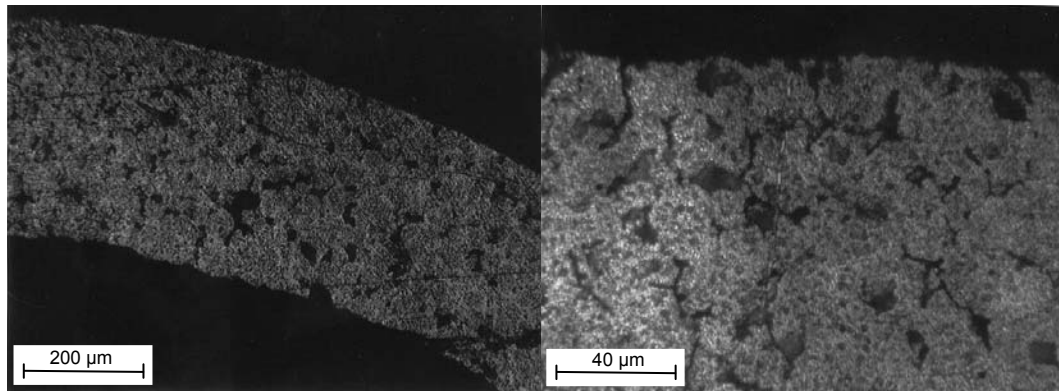


Figure 3.6 Microscopic images of the aluminum control specimen.



**Figure 3.7** Microscopic images of an aluminum specimen exposed to a hydrogen, vertical flame.



**Figure 3.8** Microscopic images of an aluminum specimen after being exposed to a hydrogen, inverted flame.

Figures 3.9-3.11 show micrographs of the stainless steel specimens. As seen from Fig. 3.10, which is for the vertical upwards orientation, the steel does not show significant degradation as compared to the aluminum. Nonetheless, Figs. 3.10 and 3.11, which is for the vertical flame and inverted flame on the steel, show signs of material degradation. Considering that the temperature readings were 640 °C and 490 °C, both cases are likely to have the formation of carbides due to the chromium content [56]. This is most likely what the dark spots are. The same argument applies for the steel in that the effects are most likely due to temperature, but this experiment allows for the interaction of metal and radicals in the flame.

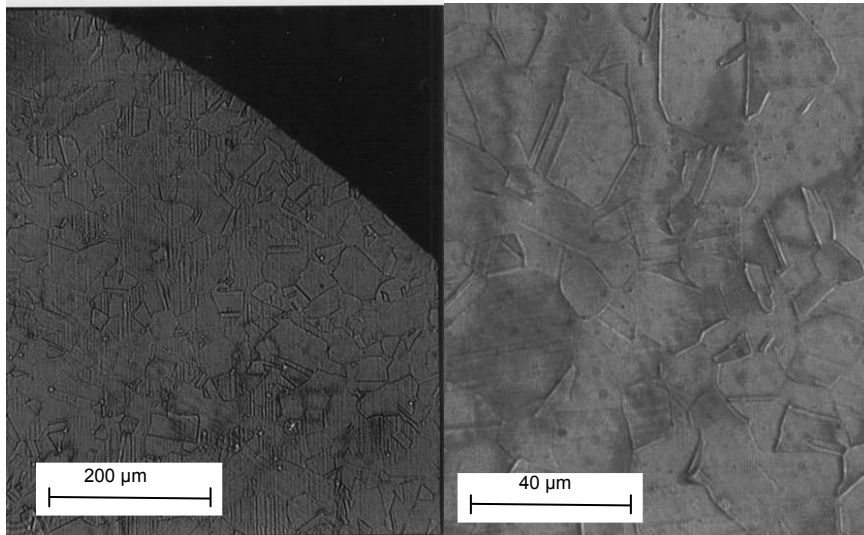


Figure 3.9 Microscopic images of the control, steel specimen.

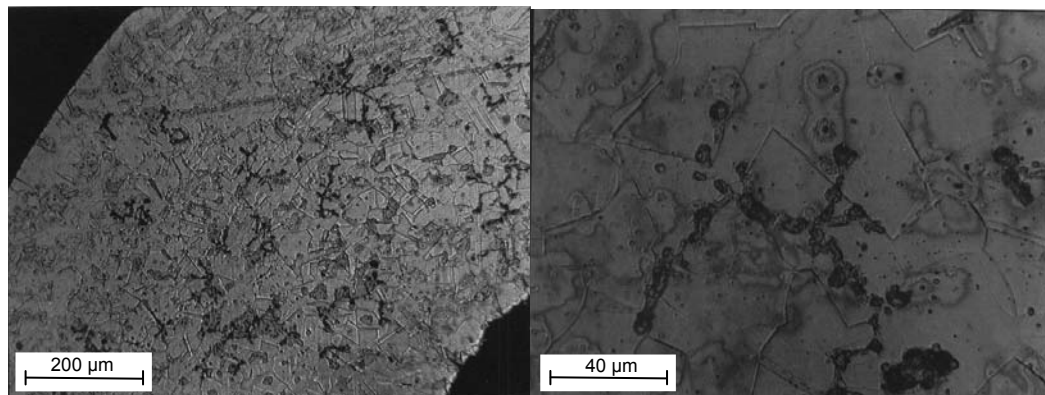


Figure 3.10 Microscopic images of the steel specimen exposed to a vertical flame.

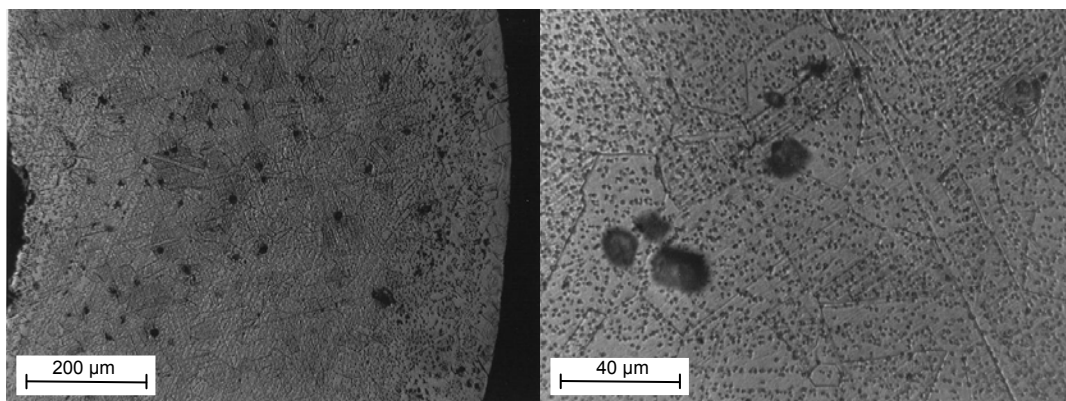


Figure 3.11 Microscopic images of the steel specimen exposed to an inverted hydrogen flame.

Hardness tests were performed to investigate the effects of the material degradation. The hardness was tested as a function of distance from the surface where the flame was anchored. The results were all within a normal standard deviation.

## **3.5 Conclusions**

The results show that there is significant degradation in 1100 aluminum specimens' hardness results. The stainless steel showed a slight amount of degradation in that second phase material developed. The hardness tests performed on the stainless steel showed insignificant effects from the experiment while the aluminum showed a significant reduction in hardness.

While the results of this study may not be conclusive, it is readily apparent that a hydrogen leak flame can degrade metals. Aluminum was used as a control experiment, and while this material may not be used in hydrogen systems, it shows that metals can be degraded by a hydrogen leak flame. The stainless steel experiment showed visual signs of degradation but negligible changes in hardness, but it is anticipated that greater degradation would occur with time.

# **Chapter 4**

## **Future Work**

In regards to the quenching limit investigation, several more issues have been produced in addition to the ones answered. The study considered only round burners and leaky Swagelok fittings; there are many other types of burners and leaks that could represent real world hydrogen leaks. For instance, slot burners could better represent a leak from a crack considering that a crack will likely have a high aspect ratio. This study

showed that there are different amounts of heat loss depending upon the geometry of the burner, so different geometries are critical to quenching limits.

The materials degradation study emphasized the significance of the type of material used in hydrogen systems. Further work is needed to fully investigate the types of materials that are used in current hydrogen systems and those that are predicted to be used in the future. Similar experiments can be run using an array of different materials to show the optimal material for hydrogen systems considering its corrosive properties. There are several different methods of hydrogen storage that have safety issues that have not been investigated. In the future, hydrogen sorption techniques could be used to store hydrogen. Also, if fuel cell vehicles become popular, then fittings within them have to be gas tight as well as protected in the case of a crash. The time frame of this experiment was just a few months, but the situation could exist where a leak goes undetected for years. Thus, questions arise as to the effects of a leak flame over long periods of time. Additionally, the effects of temperature were lumped with the effects of hydrogen attack. More experiments are needed to distinguish the two variables.

## References

- 1 Gregorio Marban and Teresa Valdes-Solis. Towards the hydrogen economy? *Int J Hydrogen Energy*, 32:1625-1637, February 2007.
- 2 Michio Yamawaki, Tetsuo Nishihara, Yoshiyuki Inagaki, Kazuo Minato, Hiroyuki Oigawa, Kaoru Onuki, Ryutaro Hino, Masuro Ogawa. Application of nuclear energy for environmentally friendly hydrogen generation. *Int J Hydrogen Energy*, 32:2719-2725, November 2006.
- 3 S.A. Sherif, F. Barbir, T.N. Veziroglu. Wind energy and the hydrogen economy - review of the technology. *Solar Energy*, 78:647-660, March 2005.
- 4 Annette Von Jouanne, Iqbal Husain, Alan Wallace, Alex Yokochi. Gone with the wind. *IEEE Industry Applications Magazine*, 12-19, July/August 2005.
- 5 Paul Kruger. Alternative energy resources: the quest for sustainable energy. John Wiley and Sons, Inc., Hoboken, NJ, 2006, 174-175.
- 6 I. MacIntyre, A.V. Tchouvelev, D.R. Hay, J. Wong, J. Grant, P. Benard. Canadian hydrogen safety program. *Int J Hydrogen Energy*, 32:2134-2143, May 2007.
- 7 K. Takeno, K. Okabayashi, A. Kouchi, T. Nonaka, K. Hashiguchi, K. Chitose. Dispersion and explosion field tests for 40 MPa pressurized hydrogen. *Int J Hydrogen Energy*, 32;13:2144-2153, June 2007.
- 8 S.B. Dorofeev. Evaluation of safety distances related to unconfined hydrogen explosions. *Int J Hydrogen Energy*, 32:2118-2124, May 2007.
- 9 John Baker, Mark E. Calvert, David W. Murphy. Structure and dynamics of laminar jet micro-slot diffusion flames. *Journal of Heat Transfer*, 124:783-790, August 2002.
- 10 F.G. Roper. The prediction of laminar jet diffusion flame sizes: Part 1. Theoretical model. *Combust. Flame*, 29:219-226, January 1977.
- 11 H. Ban, S. Venkatesh, K. Saito. Convection-diffusion controlled laminar micro flames. *Transactions of the ASME*, 116:954-959, November 1994.
- 12 T.S. Cheng, Y.-C. Chao, C.-Y. Wu, Y.-H. Li, Y. Nakamura, K.-Y. Lee, T. Yuan, T.S. Leu. Experimental and numerical investigation of microscale hydrogen diffusion flames. *Proceedings of the Combustion Institute*, 30:2489-2497, 2005.

- 13 Y. Nakamura, H. Yamashita, K. Saito. A numerical study on extinction behaviour of laminar micro-diffusion flames. *Combustion Theory and Modelling*, 10;6:927-938, December 2006.
- 14 I.D. Lee, O.I. Smith, A.R. Karagozian. Hydrogen and helium leak rates from micromachined orifices. *AIAA Journal*, 41;3:457-463, March 2003.
- 15 R.W. Schefer, W.G. Houf, C. San Marchi, W.P. Chernicoff, L. Englom. Characterization of leaks from compressed hydrogen dispensing systems and related components. *Int J Hydrogen Energy*, 31:1247-1260, August 2006.
- 16 Xinyu Ge, William H. Sutton. Analysis and test of compressed hydrogen interface leakage by commercial stainless steel (NPT) fittings. *SAE International*, 35-47, 2006.
- 17 M.R. Swain, M.N. Swain. A comparison of H<sub>2</sub>, CH<sub>4</sub>, and C<sub>3</sub>H<sub>8</sub> fuel leakage in residential settings. *Int J Hydrogen Energy*, 17:807-815, May 1992.
- 18 Gautam T. Kalghatgi. Blow-out stability of gaseous jet diffusion flames. Part I: In still air. *Combustion Science and Technology*, 26;5:233-239, April 1981.
- 19 L.M. Matta, Y. Neumeier, B. Lemon, B.T. Zinn. Characteristics of microscale diffusion flames. *Proc. Combust. Inst.*, 29:933-938, 2002.
- 20 T.S. Cheng, C.-P. Chen, C.-S. Chen, Y.-H. Li, C.-Y. Wu, Y.-C. Chao. Characteristics of microjet methane diffusion flames. *Combust. Theory Modeling*, 10:861-881, October 2006.
- 21 Rehan Khan, Z. Kan, F. Al-Sulaiman, N. Merah. Fatigue life estimates in woven carbon fabric/epoxy composites at non-ambient temperatures. *Journal of Composite Materials*, 36;22:2517-2535, April 2002.
- 22 K. Pehr. Aspects of safety and acceptance of LH<sub>2</sub> tank systems in passenger cars. *Int J Hydrogen Energy*, 21;5:387-395, August 1995.
- 23 Vivek Utgikar, Todd Thiesen. Safety of compressed hydrogen fuel tanks: Leakage from stationary vehicles. *Technology in Society*, 27:315-320, 2005.
- 24 L.C. Cadwallader, J.S. Herring. Safety issues with hydrogen as a vehicle fuel. *Report INEEL/EXT-99-00522 prepared for U.S. Department of Energy*, September 1999.
- 25 P.B. Sunderland, B.J. Mendelson, Z.G. Yuan, D.L. Urban. Shapes of buoyant and nonbuoyant laminar jet diffusion flames. *Combust. Flame*, 116:376-386, 1999.

- 26 A.M. Kanury. *Introduction to combustion phenomena*. Gordon and Breach, New York, 1975, p. 131.
- 27 R.C. Weast, M.J. Astle. *CRC Handbook of Chemistry and Physics*, CRC Press, Inc., West Palm Beach, 59<sup>th</sup> edition, 1979, P. F-58.
- 28 B.R. Munson, D.F. Young, T.J. Okiishi. *Fundamentals of fluid mechanics*. Wiley, Hoboken, 2002, p. 359.
- 29 N.R. Morton, P.B. Sunderland, B.H. Chao, R.L. Axelbaum. Quenching limits and materials degradation of hydrogen diffusion flames. *5th U.S. Combustion Meeting held in San Diego March 25-28 2007*, Paper #25.
- 30 M.Y. Bahadori, U. Hegde, L. Zhou. Liftoff and blowoff of jet diffusion flames. *Paper ALAA-2002-1078, Aerospace Sciences Meeting held in Reno, Nevada January 14-17 2002*.
- 31 Chris Moran, Flame quenching limits of hydrogen leaks. *M.S. Thesis*, University of Maryland., May 2008.
- 32 Paul D. Ronney, Ming-Shin Wu, Howard G. Pearlman. Experimental study of flame balls in space: preliminary results from STS-83. *ALAA Journal*, 36;8:1361-1368, August 1998.
- 33 Ya Zeldovich. *Theory of Combustion and Detonation of Gases*. *Academy of Science (USSR)*, Moscow, 1994.
- 34 P.D. Ronney. Near-limit flame structures at low Lewis Number. *Combustion and Flame*, 82:1-14, 1990.
- 35 P.D. Ronney, K.N. Whaling, A. Abbud-Madrid, J.L. Gatto, and V.L. Pisowicz. Stationary premixed flames in spherical and cylindrical geometries. *ALAA Journal*, 32;3:569-577, 1994.
- 36 Maoquiu Wang, Eiji Akiyama, Kaneaki Tsuzaki. Effect of hydrogen on the fracture behavior of high strength steel during slow strain rate test. *Corrosion Science*, 49: 4081-4097.
- 37 Thomas R. Vencill, Walter H. Moy, Yu-Lin Shen, Shailendra B. Rathod. Thermal embrittlement characterization of metallic alloys in high temperature hydrogen environments. *Materials Science and Technology*, 1:189-197, 2006.
- 38 Andreas Züttel. Hydrogen storage methods. *Naturwissenschaften*, 91:157-172, March 2004.

- 39 John L. Cox. What steel to use at high pressures and temperatures. *Chemical and Metallurgical Engineering*, 405-409, August 1933
- 40 E. Minkovitz, D. Eliezer. Hydrogen-assisted cracking of sensitized 316L stainless steel. *Journal of Materials Science*, 16:2507-2511, 1981.
- 41 Anthony W. Thompson. Hydrogen embrittlement of stainless steels by lithium hydride. *Metallurgical Transactions*, 4:2819-2825, December 1973.
- 42 R.A. Oriani. Hydrogen embrittlement of steels. *Annual Reviews in Material Science*, 8:327-357, 1978.
- 43 V.V. Pansyuk, O.Y. Andreykiv, O.V. Gembara. Hydrogen degradation of materials under long-term operation of technological equipment. *International Journal of Hydrogen Energy*, 25:67-74, 2000.
- 44 T.J. Carter, L.A. Cornish. Hydrogen in Metal. *Engineering Failure Analysis*, 8:113-121, October 1999.
- 45 Jinyang Zheng, Lei Li, Rui Chen, Ping Xu, Fangming Kai. High pressure steel storage vessels used in hydrogen refueling station. *Journal of Pressure Vessel Technology*, vol. 130, February 2008.
- 46 M.R. Louthan, G.R. Caskey, J.A. Donovan, D.E. Rawl. Hydrogen embrittlement of metals. *Materials Science and Engineering*, 10:357-368, June 1972.
- 47 D.D. Perlmutter, B.F. Dodge. Effects of hydrogen on properties of metals. *Industrial and Engineering Chemistry*, 885-893, May 1956.
- 48 K. Yokogawa, S. Fukuyama, G. Han and J. He. Hydrogen environment embrittlement of materials for hydrogen energy service. *Hydrogen Energy Progress*, 3:2291-2295, 1996.
- 49 V.I. Tkachov. Effect of hydrogen on the properties of structural steels. *Materials Science*, 41;4:107-110, July-August 2005.
- 50 W. Beck, J. O'M. Bockris, J. McBreen, L. Nanis. Hydrogen permeation in metals as a function of stress, temperature and dissolved hydrogen Concentration. *Proceedings of the Society of London. Series A, Mathematical and Physical Sciences*, 1;1421:220-235, February 1966.
- 51 C. San Marchi, B.P. Somerday, S.L. Robinson. Permeability, solubility and diffusivity of hydrogen isotopes in stainless steels at high gas pressures. *International Journal of Hydrogen Energy*, 32:100-116, May 2006.

- 52 L.W. Tsay, S.C. Yu, San-Der Chyou, D.-Y. Lin. A comparison of hydrogen embrittlement susceptibility of two austenitic stainless steel welds. *Corrosion Science*, 49:4028-4039, April 2007.
- 53 P. Rozenak, I.M. Robertson, and H.K. Birnbaum. HVEM studies of the effects of hydrogen on the deformation and fracture of AISI type 316 austenitic stainless steel. *Israel Journal of Technology: Proc. Of the 4<sup>th</sup> Israel Materials Engineering Conference*, 24:231-236, 1988.
- 54 M.R. Louthan, Jr. and A.H. Dexter. Hydrogen embrittlement of 1100 aluminum. *Metallurgical Transactions A*, 6A:1655-1657, August 1975.
- 55 *Metals Handbook, vol. 8: Metallography, Structures and Phase Diagrams*, USA, 1973.
- 56 William F. Smith. *Foundations of Materials Science and Engineering*, McGraw-Hill, New York, 2004, p. 497.

# Vita

## Michael S. Butler, Jr.

**Date of Birth** December 25, 1983

**Place of Birth** St. Louis, MO

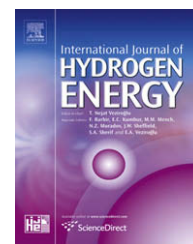
**Degrees** B.A. Cum Laude, Physics, May 2006  
M.S. Mechanical Engineering, May 2008

**Publications** M.S. Butler, C.W. Moran, P.B. Sunderland, R.L. Axelbaum, *Flame Quenching Limits of Hydrogen Leaks*, SAE World Congress, Detroit, SAE Paper 2008-01-0726 (2008) 8 pp.

M.S. Butler, C.W. Moran, P.B. Sunderland, R.L. Axelbaum, *Quenching Limits of Hydrogen Diffusion Flames*, Eastern States Section of the Combustion Institute, Charlottesville, October 21-24 (2007).

May 2008

**Short Title: Flame Quenching Limits and Materials Degradation of Hydrogen Leaks**

Available at [www.sciencedirect.com](http://www.sciencedirect.com)journal homepage: [www.elsevier.com/locate/he](http://www.elsevier.com/locate/he)

## Limits for hydrogen leaks that can support stable flames

M.S. Butler<sup>a</sup>, C.W. Moran<sup>b</sup>, P.B. Sunderland<sup>b,\*</sup>, R.L. Axelbaum<sup>a</sup>

<sup>a</sup>Department of Energy, Environmental and Chemical Engineering, Washington University, St. Louis, MO 63130, USA

<sup>b</sup>Department of Fire Protection Engineering, University of Maryland, College Park, MD 20742, USA

### ARTICLE INFO

#### Article history:

Received 31 January 2009

Received in revised form

4 April 2009

Accepted 5 April 2009

Available online 9 May 2009

#### Keywords:

Compression fittings

Fire safety

Laminar flames

Leakage

Quenching limits

Microcombustion

Microflames

### ABSTRACT

Quenching and blowoff limits of hydrogen diffusion flames on small burners were observed. Four burner types, with diameters as small as 8  $\mu\text{m}$ , were considered: pinhole burners, curved-wall burners, tube burners, and leaky fittings. In terms of mass flow rate, hydrogen had a lower quenching limit and a higher blowoff limit than either methane or propane. Hydrogen flames at their quenching limits were the weakest flames recorded to date, with mass flow rates and heat release rates as low as 3.9  $\mu\text{g/s}$  and 0.46 W. The quenching limit for a hydrogen flame at a 6 mm leaky compression fitting was found to be 28  $\mu\text{g/s}$ . This limit was independent of supply pressure (up to 131 bar) and about an order of magnitude lower than the corresponding limits for methane and propane.

© 2009 International Association for Hydrogen Energy. Published by Elsevier Ltd. All rights reserved.

## 1. Introduction

Hydrogen is attractive as an energy carrier for highway vehicles. It can power fuel cells or engines with only water vapor as exhaust. With oil supplying 33% of the world's primary energy, hydrogen could help mitigate concerns over fossil fuel consumption if it is produced from renewable energy sources or nuclear energy [1,2]. Hydrogen can be stored as a gas, liquid, or a solid (in metal hydrides), and can be transported using pipelines, tankers or rail trucks [3].

Hydrogen is an unusual fuel. It has a high leak propensity and wide flammability limits, 4–75% by volume [4]. Among all fuels, hydrogen has the lowest molecular weight, the lowest quenching distance (0.51 mm), the smallest ignition energy in air (28  $\mu\text{J}$ ), the lowest auto-ignition temperature by a heated air jet (640 °C), the highest laminar burning velocity

in air (2.91 m/s), and the highest heat of combustion (119.9 kJ/g) [4]. Hydrogen flames are the dimmest of any fuel. Hydrogen embrittles and attacks metals more than any other fuel.

Hydrogen may ultimately prove to be no more hazardous from a fire safety standpoint than gasoline or diesel. However, gasoline and diesel have undergone over a century of widespread vehicle use, and this has resulted in codes and standards that have yielded an acceptable fire safety record. Further research is necessary if hydrogen is to be rapidly introduced with a similar safety record. It is expected that existing codes and standards will require updating to ensure safe use of hydrogen in highway vehicles [5].

The goal of this study is to investigate small hydrogen flames—flames that can be characterized as “leak flames,” i.e., small flames that could exist as a result of hydrogen leaking

\* Corresponding author. Tel.: +1 301 405 3095; fax: +1 301 405 9383.

E-mail address: [pbs@umd.edu](mailto:pbs@umd.edu) (P.B. Sunderland).

from a containment vessel. The scenario of concern is that a small leak in a hydrogen system could ignite, burn undetected for a long time, and potentially degrade surrounding materials or ignite secondary fires.

Several studies have been conducted to evaluate the characteristics of hydrogen leaks without combustion. Lee et al. [6] conducted hydrogen and helium leak rate experiments on micromachined orifices of different sizes and shapes. They examined the differences in flow rates among circular, square, and elliptical slit orifices as a function of pressure, and in most cases the flow was choked. Schefer et al. [7] investigated leaks where the flow was due to pressure-driven convection and permeation through metals. They obtained analytical relationships for flow rates of choked flows, subsonic laminar flows, and turbulent flows. Hydrogen leakage in stainless steel threaded pipe fittings was considered by Ge and Sutton [8]. They found that a larger tightening torque is less important in leak prevention than choice and proper application of thread sealant. The tests were run at up to 70 bar and typical hydrogen leak rates through these fittings were found to be 1  $\mu\text{g/s}$ .

Studies have also evaluated the risks of hydrogen leaks with respect to accumulation and explosion of hydrogen [9–11]. Swain and Swain [12] examined risks associated with leaks of hydrogen, methane, and propane from leaky fittings into an enclosure. Their measured leak rates showed that for a given supply pressure (except at the lowest supply pressures), hydrogen had a significantly higher volumetric flow rate than methane or propane. This behavior is expected for choked flows, owing to the high speed of sound of hydrogen gas.

Leak flames resemble the micro diffusion flames that have been observed in other laboratories and, while only one previous study specifically evaluated leak flames [13], there have been many studies of micro diffusion flames [14–19]. Micro diffusion flames are typically associated with an application, e.g., a microcombustor for power generation. Nonetheless, it is possible that they could arise unexpectedly. For example, if a fuel leak from a crack or hole in a fitting, tube or storage vessel of a plumbing system were ignited, this could be characterized as a micro diffusion flame.

Ban et al. [14] investigated micro diffusion flames that were 2–3 mm long on round burners with inner diameters of 0.15–0.4 mm. Three fuels were considered: ethane, ethylene and acetylene. The experiments agreed with predictions of flame shapes in the absence of buoyancy. The flames were nearly spherical and their shapes were unaltered when burner orientation was changed with respect to gravity. Cheng et al. [17] performed detailed measurements and computations on small hydrogen flames burning on similar burners. Buoyancy was found to be insignificant for these flames. Nakamura et al. [19] simulated methane micro diffusion flames supported on circular burners with diameters less than 1 mm. They, too, found nearly spherical flames, as a result of the weak buoyancy forces. They also considered quenching limits of the methane flames. Baker et al. [15] studied micro-slot burners (with port widths of 0.1–0.76 mm) and developed a flame height expression for purely diffusion-controlled propane/air nonpremixed flames.

Quenching and blowoff limits refer to flames with the smallest and highest fuel flow rates for sustained burning. Matta et al. [16] measured quenching limits for propane on small round burners. Similar experiments were performed by

Cheng et al. [18] for methane. Both studies found that quenching mass flow rate was largely independent of burner diameter. Prior to the present work, quenching flow rates had not been measured for hydrogen. Blowoff limits for diffusion flames on small burners have been measured for a variety of fuels [16,20].

Thus motivated, this study includes experiments and analysis to identify which hydrogen leaks can support flames. A scaling analysis is presented to estimate the fuel mass flow rate at the quenching limit. Measured mass flow rates, both at the quenching and blowoff limits, are presented for hydrogen, methane and propane on round-hole burners. Flame quenching limits for leaky compression fittings are also presented. Further details are available in Butler [21] and Moran [22].

## 2. Scaling for flame quenching limits

A scaling analysis is presented here for flame quenching limits. This is similar to past work of Matta et al. [16]. The stoichiometric length  $L_f$  of laminar gas jet diffusion flames on round-hole burners is given by:

$$L_f/d = a \text{Re} = 4m_{\text{fuel}}a/(\pi \mu d) \quad (1)$$

where  $d$  is the burner inside diameter,  $a$  is a fuel-specific coefficient,  $\text{Re}$  is fuel port Reynolds number,  $m_{\text{fuel}}$  is the fuel mass flow rate, and  $\mu$  is fuel dynamic viscosity. The scaling of Eq. (1) arises from many theoretical and experimental studies, including Roper [23], Sunderland et al. [24], and references cited therein.

The base of an attached jet diffusion flame is quenched by the burner and is premixed. The flame's standoff distance can be approximated as the standoff distance (i.e., 50% of the quenching distance) of the corresponding stoichiometric premixed flame. The 50% modification arises here because premixed flame quenching distances typically are reported as the minimum tube diameter or plate separation distance,  $L_q$ , through which a premixed flame can pass [4]. It is assumed here that a jet flame is above its quenching limit if its stoichiometric length exceeds its standoff distance:

$$L_f > L_q/2. \quad (2)$$

Combining Eqs. (1) and (2) yields the fuel mass flow rate at the quenching limit:

$$m_{\text{fuel}} = \pi L_q \mu / (8a) \quad (3)$$

Eq. (3) predicts that the fuel mass flow rate at the quenching limit is a fuel property that is independent of burner diameter, which was similarly predicted by Matta et al. [16]. When measured values of  $L_q$ ,  $\mu$ , and  $a$  (see Table 1) are inserted into Eq. (3), predicted fuel mass flow rates at the quenching limit are obtained, as listed in Table 1.

## 3. Experimental

### 3.1. Round-hole burners

Three types of round-hole burners were considered: pinhole burners, curved-wall burners, and tube burners, as illustrated in Fig. 1. Each type included various hole diameters, as

**Table 1 – Selected properties of hydrogen, methane, and propane and predicted quenching mass flow rates.**

Fuel	$a$	$L_q$ (mm)	$S_L$ (cm/s)	$\mu$ (g/m-s)	$m_{fuel}$ ( $\mu$ g/s)
H <sub>2</sub>	0.236	0.51	291	8.76E-3	8
CH <sub>4</sub>	0.136	2.3	37.3	1.09E-2	85
C <sub>3</sub> H <sub>8</sub>	0.108	1.78	42.9	7.95E-3	63

Values for  $a$  are from [24],  $L_q$  and  $S_L$  (laminar burning velocity) are from [4], and  $\mu$  is from [25]. The quantity  $m_{fuel}$  is predicted from Eq. (3).

tabulated in Table 2. The pinhole burners (such as the one in Fig. 2) were stainless steel nozzles that were manufactured for solid-stream spray generation. The top surface of each burner (except the two smallest ones, which were planar) is a curved surface (radius of curvature of 9.6 mm) with a hole passing through its axis, as depicted in Fig. 1. The pinhole burners represent pinhole leaks in pressure vessels where the radius of curvature of the wall is large or infinite.

The curved-wall burners were constructed from stainless steel tubes with two outside diameters: 1.6 and 6.4 mm. A radial hole was drilled in the wall of each tube. These burners represent pinhole leaks that might occur in fuel supply tubing.

The tube burners were made from stainless steel hypodermic tubes. Although they do not represent practical leak flames, they are a fundamental configuration that leads to a flame from a wall where the radius of curvature approaches zero. Their observation should lead to an improved understanding of microinjectors in small-scale microelectromechanical power generators [16].

Fuel was delivered via a pressure regulator and a needle valve, and all tests were performed at normal lab pressure and temperature. Measuring the small flow rates at the quenching limits required special procedures. A glass soap-bubble meter was installed upstream of the burners. Quenching flow rates were measured by establishing a small flame near the quenching limit and gradually decreasing the flow rate until the flame extinguished. The fuel flow rate was then measured using the soap-bubble meter.

Determining the existence of hydrogen flames near their quenching limits was complicated by their small size and low luminosity. The flames were detected with a K-type thermocouple positioned 10 mm above the burner, yielding detection that is believed to be more sensitive than available camera technology could provide.

Burners were allowed to warm slightly above room temperature to prevent water condensation. This was necessary because condensation was found to disturb the flows from the small burners, sometimes extinguishing the flames.

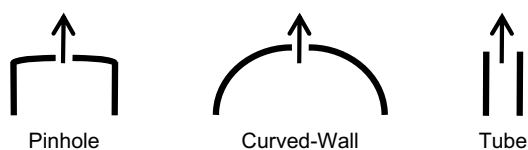


**Fig. 1 – Schematics of the round-hole burners. Arrows show the fuel flow direction. Burner dimensions are shown in Table 2.**

**Table 2 – Hole diameters (mm) for the round-hole burners.**

Pinhole	Curved wall <sup>a</sup>	Curved wall <sup>b</sup>	Tube
0.008	0.41	0.41	0.051
0.13	0.53	1.75	0.152
0.36	0.74	2.46	0.406
0.53	0.86	3.12	0.838
0.71	1.02		1.194
0.84			2.21
1.01			
1.40			
1.78			
2.39			
3.18			

<sup>a</sup> Tube diameter of 1.6 mm.

<sup>b</sup> Tube diameter of 6.4 mm.

Using similar burners, Takahashi et al. [13] also reported complications of water condensation. Tests performed here at different burner temperatures, up to about 200 °C, found quenching flow rate to be largely independent of burner temperature provided condensation was avoided. Tests were also conducted with varying ambient humidity, and quenching limits were found to be generally independent of the relative humidity of the air in the range of 46–90%.

Hydrogen flow rate at blowoff was measured with a soap bubble meter. A stable flame was established and then the flow rate was increased until the flame first lifted and then extinguished. For blowoff tests the flames were detected visually. Hearing protection was required for the blowoff tests for the larger burners.

Additional tests were performed to consider buoyancy effects. To this end quenching flow rates were found for pinhole and tube burners in the vertical, horizontal, and inverted orientations.

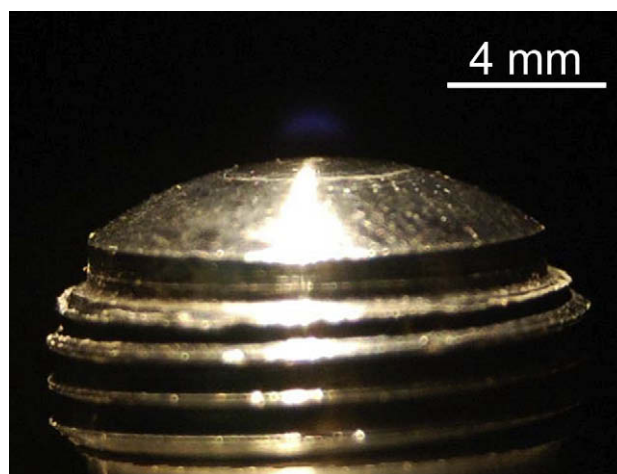


**Fig. 2 – Image of a hydrogen flame slightly above its quenching limit of 7.5  $\mu$ g/s (original in color). The burner is a 0.36 mm pinhole burner, with a surface radius of curvature of 9.6 mm, and is oriented vertically. The image was recorded in a dim room at  $f/4.2$  with an exposure time of 30 s.**

### 3.2. Leaky fittings

Quenching limits were also measured for leaky compression fittings. The tests involved leaks between Swagelok® stainless steel tube union compression fittings and stainless steel tubes. Tube diameters were 3.2, 6.4, and 12.7 mm. The end of each union opposite the tube was sealed. New tubes and fittings were assembled according to manufacturer instructions and were rejected if bubbles appeared in an applied soap water solution when pressurized with hydrogen to 8 bar absolute. Leaks were then introduced in one of three ways: by reducing the torque on the threaded nut, by over tightening the nut, or by scratching the front ferrule sealing surface. These types of leaks are occasionally encountered in plumbing systems. The three leak types were found to yield the same flame quenching limits, so only results for reduced torque fittings are presented here. Reduced torque fittings allow quenching limits to be measured for different upstream pressures by adjusting the torque, i.e., an increased torque requires an increased upstream pressure at the quenching limit. Most tests were performed with the fitting in the vertical orientation, with the leaky fitting at the top end of the tube, but several horizontal and inverted orientations also were considered.

Quenching limits were found by igniting the fuel (with an external flame) and then reducing fuel flow rate until extinction. Fuel flow rate was controlled with upstream pressure, primarily, and with torque on the threaded nut. Upstream pressure was set with a pressure regulator. When a quenching limit was established, a plastic tube was installed over the fitting such that the leak flow was measured with a downstream soap bubble meter at laboratory pressure. The quenching limits were obtained with fittings at nearly laboratory temperature.

The hydrogen flames generally were not visible even in dark conditions. As with the round-hole burners, the presence of hydrogen flames was determined with a thermocouple positioned 10 mm above the flame position. Quenching limits for methane and propane were identified visually because thermocouples confirmed these flames to be visible in all cases.

Uncertainties for the round-hole and leaky fitting tests are estimated at  $\pm 5\%$  for hole diameter, fuel flow rate, and upstream pressure.

## 4. Results

### 4.1. Round-hole burners

Fig. 2 shows an image of a hydrogen flame burning slightly above its quenching limit on a 0.36 mm pinhole burner. The flame appearance is similar to that of all the quenching limit hydrogen flames on round-hole burners. The hydrogen quenching distance of Table 1 suggests steady hydrogen diffusion flames should be anchored about 0.26 mm from the burner surface. Fig. 2 indicates that this is reasonable for the hydrogen flames near their quenching limits. Because the maximum flame dimension is comparable to its standoff distance, this flame closely resembles a flat premixed flame [16].

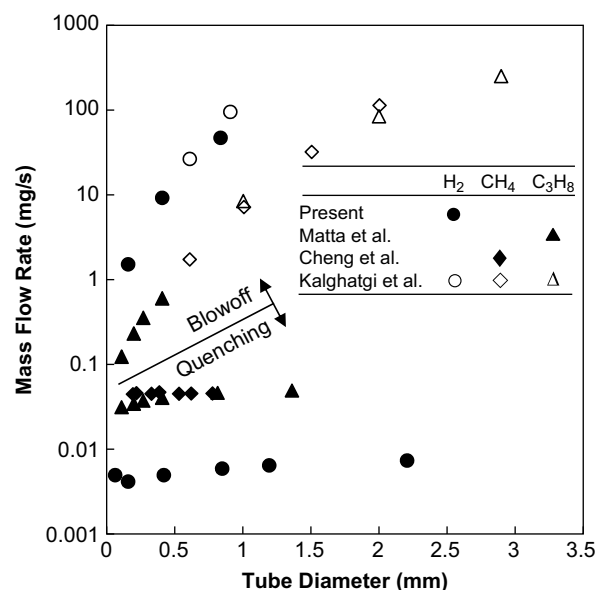


Fig. 3 – Quenching and blowoff limits for tube burners. Past measurements shown are from Refs. [16,18,20].

Measured quenching and blowoff limits for hydrogen, methane, and propane on tube burners are shown in Fig. 3. Measurements shown for methane and propane come from past work, and were confirmed in our laboratory for representative conditions. Consistent with the prediction of Eq. (3), the mass flow rate at quenching is not strongly dependent on burner diameter. The mean quenching limit flow rates are in reasonable agreement with the predictions of Table 1. The mean quenching limits for hydrogen are about an order of magnitude lower than those of the other fuels. Table 1 and Eq. (3) indicate this arises from hydrogen's short quenching distance (primarily) and from its large flame length relative to its mass flow rate (i.e., large coefficient  $a$ ).

The mass flow rate at blowoff, see Fig. 3, increases with tube diameter because for these flames blowoff occurs when local velocities exceed local flame speeds. The blowoff limits for hydrogen are about an order of magnitude larger than those of the other fuels, largely owing to the high burning velocity of hydrogen. Regardless of tube diameter, the limits of stable combustion of hydrogen are much wider than those for propane or methane. The limits narrow with decreasing tube diameter, as was shown for propane in Matta et al. [16], but they never meet.

Various existing codes and standards require leak rates below 20 scc/h (0.46  $\mu\text{g/s}$ ) for hydrogen and below 200 scc/h (36  $\mu\text{g/s}$ ) for natural gas [13]. For hydrogen this leak rate is well below the measured flame quenching limits, whereas for methane this leak rate is only slightly below the quenching limits. Referring to the hydrogen measurements in Fig. 3, SAE J2579 [26] now limits localized hydrogen leaks in highway vehicles to a maximum of 5  $\mu\text{g/s}$ .

Fig. 4 shows the hydrogen quenching limits for the three types of round burners. Fig. 4 indicates that quenching limits are affected by burner type and diameter for the smaller burner diameters. Where the limits are affected by burner type, the differences can largely be attributed to varying

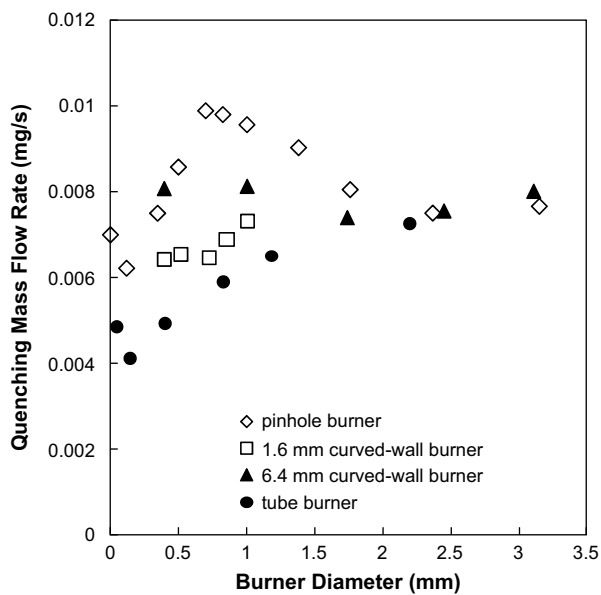


**Fig. 4 – Quenching mass flow rates for hydrogen for various burner types and diameters. See Fig. 1 for burner schematics.**

amounts of heat loss, as discussed next. An increase in heat loss requires a higher quenching flow rate to sustain the flame.

For burner diameters below 1.5 mm, pinhole burners have the highest quenching flow rates, while tube burners have the lowest. Pinhole burners have greater heat losses owing to their shape and mass. Heat conducted to the pinhole burners is mostly transferred to the ambient and constitutes a loss of enthalpy from the system. On the other hand, much of the heat conducted to the tube burners is transferred to the fuel and oxidizer and thus is not intrinsically lost from the system. For tube burners the primary mechanism of heat loss is expected to be radiation from the tube.

The effects of burner curvature on heat loss were investigated by observing quenching limits on curved-wall burners. An increase in curvature is expected to reduce wall heat loss. Indeed the 1.6 mm curved-wall burners yield quenching limits approaching those of the tube burners, whereas the 6.4 mm burners have quenching limits closer to those of the pinhole burners.

The dependence of quenching limits on burner diameter is complicated for small hole diameters, as shown in Fig. 4. For tube burners the quenching flow rate generally increases with increasing burner diameter. This also was observed for propane by Matta et al. [16], as shown in Fig. 3. This is attributed to increasing heat loss with increasing burner diameter. In contrast pinhole burners do not exhibit this trend because their heat loss is nearly independent of burner hole size. The reason for the local maximum in Fig. 4 for pinhole burners is unknown. For burner diameters above 1.5 mm, the quenching flow rates for both pinhole and tube burners agree reasonably well with the 8 μg/s prediction of Eq. (3), shown in Table 1.

Quenching mass flow rate increases slightly when hole diameters are decreased below 0.1 mm for both pinhole and tube burners (see Fig. 4). It is likely that the flow field is

affecting the quenching limits at these very small sizes. In particular, the measured quenching flow rates for these two burners indicate sonic velocities and Reynolds numbers of 14–130. For all other hole sizes, velocities are well below sonic and Reynolds numbers are small (with a range of 0.4–7).

While the results above are for vertical burner orientation (upward flowing fuel), hydrogen quenching limits also were measured for inverted and horizontal orientations. The results, shown in Fig. 5, reveal that quenching limits for the pinhole and tube burners are not dependent on orientation, indicating that these limit flames are not affected significantly by buoyancy. This can be elucidated by considering their Froude numbers, given by

$$Fr = u^2 / (gd) \tag{4}$$

where  $u$  is the fuel velocity at the burner port and  $g$  is the acceleration of gravity. For the present quenching limit flames on pinhole and tube burners, the  $Fr$  range is 0.17–39. These are generally in the nonbuoyant regime for microflames of  $Fr > 1$  [14]. Thus, flame structure at the quenching limits should not vary with orientation. Furthermore, as mentioned in the experimental section, small changes in burner temperature do not affect the quenching limits, so any effects of orientation on burner heating should not affect these limits.

The above results demonstrate that flame quenching limits depend on fuel type, with burner type, diameter, and orientation having far less significant effects. For a given fuel the mass flow rate from the leak is a function of the leak geometry and the upstream pressure. This relationship depends on whether the leak regime is diffusional, subsonic laminar, subsonic turbulent, isentropic choked, supersonic, etc., as considered by Schefer et al. [7]. While the leaks considered here would not be considered isentropic, insight into the quenching limits can be obtained by considering isentropic

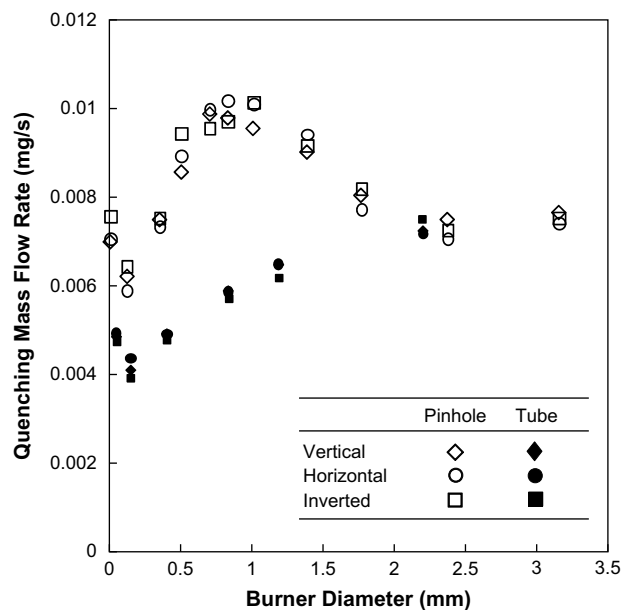


**Fig. 5 – Quenching mass flow rates for hydrogen for pinhole and tube burners in horizontal, inverted, and vertical orientations.**

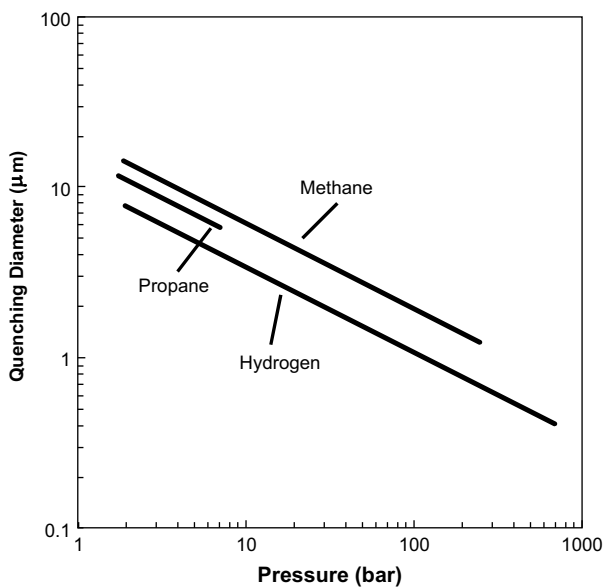


**Fig. 6 – Minimum diameter of a circular port for a leak flame as a function of upstream absolute pressure assuming isentropic choked flow.**

choked flows through round holes at the quenching limits. This could, for example, be relevant to a pinhole leak in a thin wall tube. Under these conditions the fuel flow rate is linear with respect to leak area  $A$  and upstream absolute pressure  $p_0$  as follows [7]:

$$m_{\text{fuel}} = Ap_0 \left( \frac{kMW}{T_0 R_u} \right)^{1/2} \left( \frac{2}{k+1} \right)^{k+1/2(k-1)} \quad (5)$$

where  $k$  is fuel specific heat ratio,  $MW$  is fuel molecular weight,  $T_0$  is upstream stagnation pressure, and  $R_u$  is the universal gas constant.

For a given fuel and upstream pressure, Eq. (5) can predict the hole diameter associated with the quenching limit. The results of these predictions are shown in Fig. 6 for hydrogen, methane, and propane. For this plot the quenching limit flow rates were taken as the average values for tube burners in Fig. 3. Each line in Fig. 6 starts at the minimum upstream pressure for choked flow and ends at the maximum pressure anticipated in alternative fuel vehicles. This plot predicts that for a given storage pressure, hydrogen is susceptible to leak flames for hole diameters that are smaller than those for

methane or propane. Furthermore, at hydrogen’s maximum anticipated storage pressure of 690 bar (10,000 psi), a hole diameter of just 0.4  $\mu\text{m}$  is predicted to support a flame.

The limit flames in this study are believed to be among the weakest steady flames ever recorded. The weakest of these had a hydrogen flow rate of 3.9  $\mu\text{g/s}$  (see Fig. 5), which corresponds to a heat release rate of 0.46 W based on hydrogen’s lower heating value of 119.9 kJ/g. Previously, Ronney et al. [27] documented hydrogen flame balls produced under microgravity conditions with a power output of about 1 W. In subsequent tests they achieved flames as weak as 0.5 W. It is believed these were the weakest flames recorded until the present work.

Flame balls were first predicted by Zeldovich [28], who proposed that a solution exists to the steady heat and mass conservation equations corresponding to a stationary, spherical premixed flame. The phenomenon was discovered 40 years after Zeldovich’s work by Ronney et al. [29] in drop tower experiments with lean hydrogen–air mixtures. The microgravity environment was necessary to obtain the spherical symmetry and to avoid extinction brought on by buoyancy. Flame balls have only been achieved in microgravity conditions with very lean hydrogen mixtures. With no mechanism other than radiative heat loss, and this being low for hydrogen flames, it was reasonable to assume that these flames were the weakest possible flames. The present results indicate that, despite the possibility of heat loss to the tube, the present diffusion flame geometry is actually slightly more resistant to extinction than a flame ball. As noted earlier, heat transfer to the hypodermic tube does not intrinsically imply a significant loss of enthalpy as much of this heat preheats the reactants.

#### 4.2. Leaky fittings

Fig. 7 shows images of hydrogen, methane, and propane flames on 6.3 mm leaky compression fittings in the vertical orientation. These images were recorded slightly above the quenching limits. The hydrogen flame is significantly smaller and dimmer than the others. Near their quenching limits the flames do not burn along the entire fitting annulus. For all three flames the shortest distance between the flame and the metal material is approximately 50% of the quenching distances given in Table 1. No yellow soot luminosity was visible in any of the flames near their quenching limits. The leaks associated with the images of Fig. 7 produced readily visible bubbles when soap water solution was applied.

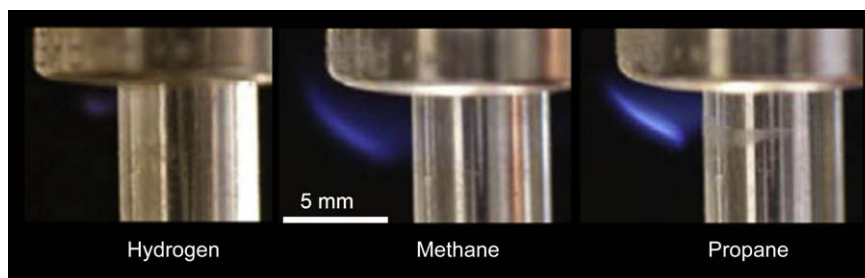


**Fig. 7 – Flames near extinction on leaky compression fittings for hydrogen, methane, and propane (original in color). Also visible is the 6.3 mm tube and the threaded nut. The fitting was vertically oriented and the upstream absolute pressure was 4 bar.**

An audible pop occurred upon hydrogen ignition, but not upon ignition of methane or propane. When the external flame was removed, ignition was quickly followed by extinction for fuel flow rates below the quenching limit. For fuel flow rates above the quenching limit, ignition was followed by a stable flame.

Fig. 8 shows measured quenching limits for hydrogen, propane, and methane for 6.3 mm fittings in the vertical orientation. The data at the higher line pressures were obtained by increasing the torque on the fitting, thus reducing the leak size. The upper limit on line pressure for propane is lower than that of the others because the vapor pressure of propane is only 9.1 bar absolute (142 psia) at 25 °C.

Within experimental uncertainties, the quenching limits of Fig. 8 are independent of line pressure for each fuel. This suggests that, as anticipated from the round-hole burner results of Fig. 4, the key parameter controlling quenching limits is the fuel mass flow rate. For these low flow rates and small leak sizes the line pressure does not significantly affect the velocity field in the flame region.

The mean hydrogen flow rate at the quenching limit is about an order of magnitude lower than for the other fuels, which is consistent with the results of Fig. 3. For leaky fittings, the quenching flow rates for hydrogen, methane, and propane are about an order of magnitude higher than the corresponding flows for tube burners (see Fig. 3). This is attributed to additional heat loss in the leaky fittings, where the flames burn near thick concave metal surfaces.

The effects of fitting orientation are shown in Fig. 9, and reveal that orientation has little or no effect on the quenching limits of the hydrogen flames. This is anticipated as these flames are small at their limits and the results are consistent with the tube and pinhole burner hydrogen measurements of Fig. 5. Nonetheless, fitting orientation did affect the quenching

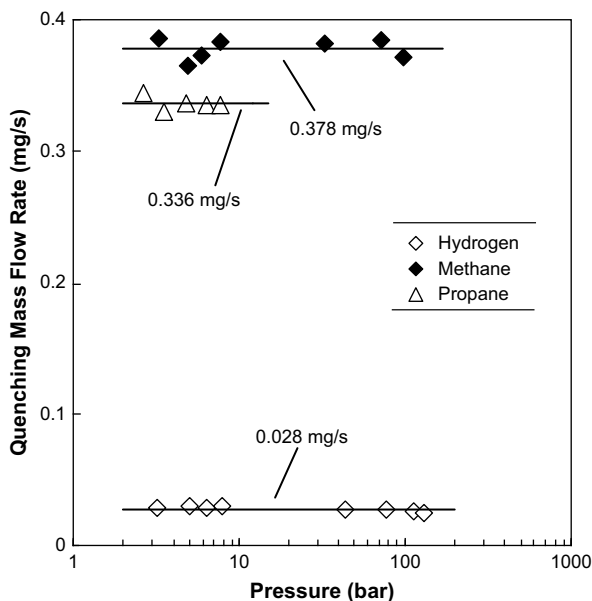


Fig. 8 – Quenching limit (minimum flaming flow rate) versus upstream absolute pressure for a 6.3 mm leaky compression fitting in the vertical orientation. The line fits represent mean values of the measured quenching limits.

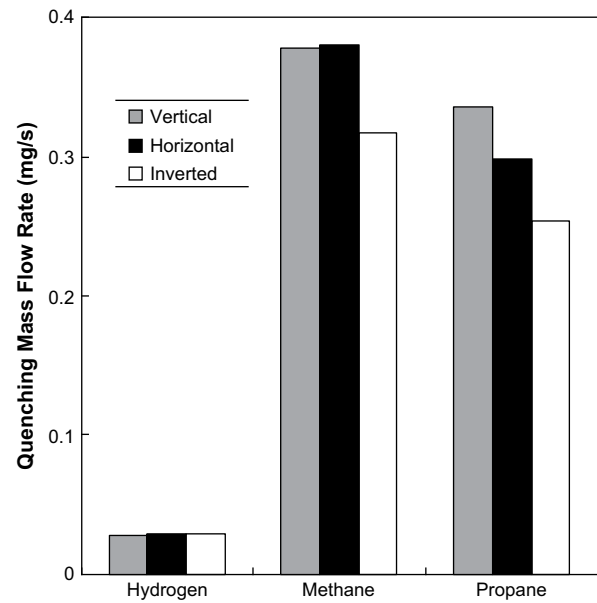


Fig. 9 – Hydrogen quenching limits for a 6.3 mm leaky compression fitting in vertical, horizontal and inverted orientations. The upstream absolute pressure was 4 bar.

limits of propane and methane flames, with the inverted orientation yielding limits about 20% lower than the vertical orientation. These flames are larger than the corresponding hydrogen flames such that buoyancy begins to have a significant effect on the flow field. The inverted orientation has the fitting below the tube, and this minimizes the surface area of the flame impingement, leading to a reduced heat loss and thus lower quenching limits.

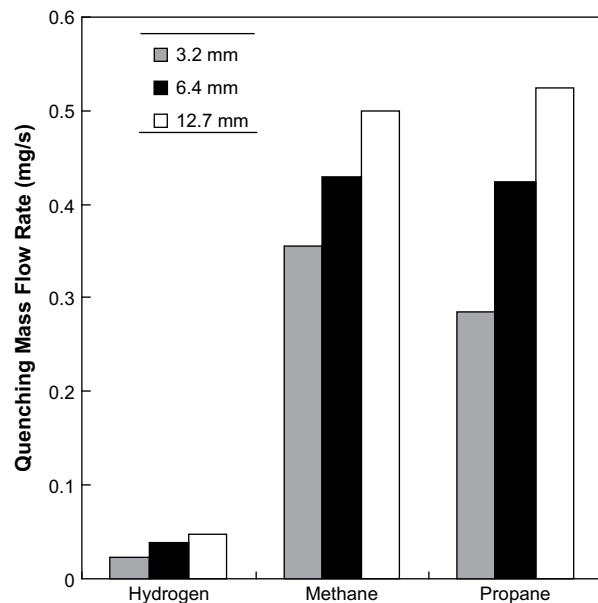


Fig. 10 – Hydrogen quenching limits for leaky compression fittings for tube diameters of 3.1, 6.3, and 12.6 mm. The fittings were vertically oriented and the upstream absolute pressure was 4 bar.

The effects of fitting diameter on quenching limits are examined in Fig. 10. Diameter had a significant impact on the quenching limits in all cases; on average as tube diameter doubles, the fuel mass flow rate at quenching increases 30%. This is attributed to increased heat losses associated with larger fittings.

This study has identified new questions that warrant further study. For example, what corrosive effects do leak flames have on containment materials? Can permeation leaks support flames? Can surface coatings, e.g., intumescent paints, be applied that will increase the quenching fuel flow rate? An improved understanding of hydrogen leaks is necessary to ensure safe use of hydrogen in the public sector.

## 5. Conclusions

Flame quenching and blowoff limits were measured for diffusion flames resulting from fuel issuing from small burners. Hydrogen fuel was emphasized, and was compared with methane and propane for a variety of burner types that characterized a range of heat losses. The key findings are as follows.

1. Flame quenching limits for round-hole burners were measured for hydrogen, methane, and propane. For hydrogen these are in the range of 4–10  $\mu\text{g/s}$  depending on burner diameter, shape, and orientation. The limits for methane and propane are about 10 times as high. The measurements indicate that many existing safety codes and standards should revisit their allowable fuel leak rates in consideration of these quenching limits.
2. Flame blowoff limits increase with burner diameter and for hydrogen are about 10 times as high as the corresponding limits for methane and propane. Thus the limits of stable combustion are much wider for hydrogen than for the other fuels considered.
3. For an isentropic choked leak, hydrogen is susceptible to leak flames for hole diameters that are smaller than those for methane or propane. This suggests that for hydrogen stored at 690 bar, a pinhole leak as small as 0.4  $\mu\text{m}$  could support a stable flame.
4. The weakest hydrogen flame found in this study, which was generated with a hypodermic needle with an inner diameter of 0.152 mm, is believed to be the weakest flame ever observed, with a fuel flow rate of 3.9  $\mu\text{g/s}$  and a heat release rate of 0.46 W.
5. The minimum flow rate necessary for sustaining a hydrogen flame on a leaky 6.3 mm tube compression fitting is 28  $\mu\text{g/s}$ . This is about an order of magnitude lower than for propane or methane. The minimum mass flow rate for all fuels is independent of upstream (line) pressure, and is sufficient to produce bubbles when a soap-water solution is applied.
6. Fitting orientation had about a 20% effect on the quenching limits of the leaky compression fittings considered here, while a doubling of tube size on average results in a 30% increase in quenching flow rate.

This work was undertaken because hydrogen is such an unusual fuel and its quenching limits had not previously been

measured. Hydrogen's low quenching limits, combined with its high leak propensity, could present unusual risks in a hydrogen economy. These risks should be explored in further research and should be incorporated into the many relevant safety codes and standards.

## Acknowledgments

This work was supported by NIST under the technical direction of J. Yang. The assistance of B.H. Chao and N.R. Morton is appreciated.

## REFERENCES

- [1] Marban G, Valdes-Solis T. Towards the hydrogen economy? *Int J Hydrogen Energy* 2007;32:1625–37.
- [2] Yamawaki M, Nishihara T, Inagaki Y, Minato K, Oigawa H, Onuki K, et al. Application of nuclear energy for environmentally friendly hydrogen generation. *Int J Hydrogen Energy* 2007;32:2719–25.
- [3] Sherif SA, Barbir F, Veziroglu TN. Wind energy and the hydrogen economy—review of the technology. *Solar Energy* 2005;78:647–60.
- [4] Kanury AM. Introduction to combustion phenomena. New York: Gordon and Breach; 1975. p. 131.
- [5] MacIntyre I, Tchouvelev AV, Hay DR, Wong J, Grant J, Benard P. Canadian hydrogen safety program. *Int J Hydrogen Energy* 2007;32:2134–43.
- [6] Lee ID, Smith OI, Karagozian AR. Hydrogen and helium leak rates from micromachined orifices. *AIAA J* 2003;41(3):457–63.
- [7] Schefer RW, Houf WG, San Marchi C, Chernicoff WP, Englom L. Characterization of leaks from compressed hydrogen dispensing systems and related components. *Int J Hydrogen Energy* 2006;31:1247–60.
- [8] Ge X, Sutton WH. Analysis and test of compressed hydrogen interface leakage by commercial stainless steel (NPT) fittings. *SAE Int* 2006:35–47.
- [9] Dorofeev SB. Evaluation of safety distances related to unconfined hydrogen explosions. *Int J Hydrogen Energy* 2007;32:2118–24.
- [10] Takeno K, Okabayashi K, Kouchi A, Nonaka T, Hashiguchi K, Chitose K. Dispersion and explosion field tests for 40 MPa pressurized hydrogen. *Int J Hydrogen Energy* 2007;32(13):2144–53.
- [11] Zbikowski M, Makarov D, Molkov V. LES model of large scale hydrogen-air planar detonations: verification by the ZND theory. *Int J Hydrogen Energy* 2008;33:4884–92.
- [12] Swain MR, Swain MN. A comparison of  $\text{H}_2$ ,  $\text{CH}_4$ , and  $\text{C}_3\text{H}_8$  fuel leakage in residential settings. *Int J Hydrogen Energy* 1992;17:807–15.
- [13] Takahashi M, Tamura Y, Suzuki J, Watanabe S. Investigation of the allowable flow rate of hydrogen leakage on receptacle. Detroit: SAE International; April 2008. Paper 2008-01-724.
- [14] Ban H, Venkatesh S, Saito K. Convection-diffusion controlled laminar micro flames. *Trans ASME* 1994;116:954–9.
- [15] Baker J, Calvert ME, Murphy DW. Structure and dynamics of laminar jet micro-slot diffusion flames. *J Heat Transfer* 2002;124:783–90.
- [16] Matta LM, Neumeier Y, Lemon B, Zinn BT. Characteristics of microscale diffusion flames. *Proc Combust Inst* 2002;29:933–8.
- [17] Cheng TS, Chao Y-C, Wu C-Y, Li Y-H, Nakamura Y, Lee K-Y, et al. Experimental and numerical investigation of

- microscale hydrogen diffusion flames. *Proc Combust Inst* 2005;30:2489–97.
- [18] Cheng TS, Chen CP, Chen CS, Li YH, Wu CY, Chao YC. Characteristics of microjet methane diffusion flames. *Combust Theory Modeling* 2006;10:861–81.
- [19] Nakamura Y, Yamashita H, Saito K. A numerical study on extinction behaviour of laminar micro-diffusion flames. *Combust Theory Modeling* 2006;10(6):927–38.
- [20] Kalghatgi GT. Blow-out stability of gaseous jet diffusion flames. Part I: In still air. *Combust Sci Technol* 1981;26(5):233–9.
- [21] Butler MS. Flame quenching and materials degradation of hydrogen leaks. M.S. Thesis. St. Louis: Washington University; May 2008. 50 pp.
- [22] Moran CW. Flame quenching limits of hydrogen leaks. M.S. Thesis. University of Maryland; May 2008. 48 pp.
- [23] Roper FG. The prediction of laminar jet diffusion flame sizes: Part 1. Theoretical model. *Combust. Flame* 1977;29:219–26.
- [24] Sunderland PB, Mendelson BJ, Yuan ZG, Urban DL. Shapes of buoyant and nonbuoyant laminar jet diffusion flames. *Combust Flame* 1999;116:376–86.
- [25] Weast RC, Astle MJ. *CRC Handbook of chemistry and physics*. 59th ed. West Palm Beach: CRC Press Inc; 1979. p. F-58.
- [26] SAEJ2579. Recommended practice for general fuel cell vehicle safety, a surface vehicle recommended practice. Detroit, MI: SAE International; January, 2009.
- [27] Ronney PD, Wu MS, Pearlman HG. Structure of flame balls at low Lewis-number (SOFBALL): preliminary results from the STS-83 and STS-94 space flight experiments. Paper AIAA-1998-463. Reno, Nevada: Aerospace Sciences Meeting; January 1998.
- [28] Zeldovich Y. *Theory of combustion and detonation of gases*. Moscow, Russia: Academy of Science; 1994.
- [29] Ronney PD, Wu MS, Pearlman HG. Experimental study of flame balls in space: preliminary results from STS-83. *AIAA J* 1998;36(8):1361–8.

# Fire Safety of Hydrogen Leaks

M.S. Butler<sup>1</sup>, C.W. Moran<sup>2</sup>, P.B. Sunderland<sup>2</sup>, R.L. Axelbaum<sup>1</sup>

<sup>1</sup>Dept. of Energy, Environmental and Chemical Eng., Washington Univ., St. Louis MO 63130, USA

<sup>2</sup>Dept. of Fire Protection Eng., Univ. of Maryland, College Park MD 20742, USA

*email: pbs@umd.edu*

## Abstract

Quenching limits of hydrogen diffusion flames on small burners were observed. Four burner types, with diameters as small as 8  $\mu\text{m}$ , were considered: pinhole burners, curved-wall pinhole burners, tube burners, and leaky fittings. In terms of mass flow rate, hydrogen had a lower quenching limit and a higher blowoff limit than either methane or propane. Hydrogen flames at their quenching limits were the weakest flames recorded to date, with mass flow rates and heat release rates as low as 3.9  $\mu\text{g/s}$  and 0.46 W. The quenching limits were generally independent of hole diameter and burner orientation, and generally decreased with increased surface curvature. The quenching limit for a hydrogen flame at a 6 mm leaky compression fitting was found to be 28  $\mu\text{g/s}$ . This limit was independent of supply pressure (up to 131 bar) and about an order of magnitude lower than the corresponding limits for methane and propane.

## 1. Introduction

Hydrogen is attractive as an energy carrier for highway vehicles. It can power fuel cells or engines with only water vapor as exhaust. Hydrogen could help mitigate concerns over fossil fuel consumption [1,2]. Hydrogen can be stored as a gas, liquid, or a solid (in metal hydrides), and can be transported using pipelines, tankers or rail trucks [3]. It is anticipated that hydrogen could be produced efficiently using nuclear sources or renewable sources such as wind [4].

Hydrogen is an unusual fuel. It has a high leak propensity and wide flammability limits, 4 – 75% by volume [5]. Hydrogen is the lightest fuel and has the lowest quenching distance (0.51 mm) and smallest ignition energy of any fuel in air (28  $\mu\text{J}$ ), the lowest auto-ignition temperature of any fuel ignited by a heated air jet (640  $^{\circ}\text{C}$ ), the highest laminar burning velocity of any fuel in air (2.91 m/s), and the highest heat of combustion (119.9 kJ/g) [5]. Hydrogen flames are the dimmest of any fuel. Hydrogen embrittles metals more than any other fuel does.

Hydrogen may ultimately prove to be no more hazardous from a fire safety standpoint than gasoline or diesel. However, gasoline and diesel underwent over a century of widespread vehicle use, and this has resulted in codes and standards that have yielded an acceptable fire safety record. Further research is necessary if hydrogen is to be rapidly introduced with a similar safety record. It is expected that existing codes and standards will need to be updated [6] to ensure safe use of hydrogen in vehicles.

The goal of present study is to investigate small hydrogen flames that could be characterized as “leak flames,” i.e., small flames that could result from hydrogen leaking from a containment vessel. The scenario of concern is that a small leak in a hydrogen system could ignite, burn undetected for a long period of time, and potentially degrade surrounding materials, or ignite secondary fires.

Several studies have been conducted to evaluate the characteristics the hydrogen leak itself. Lee et al. [15] conducted leak rate experiments on micromachined orifices of different sizes and shapes. They examined the differences in flow rates among circular, square, and elliptical slit orifices as a function of pressure, and in most cases the flow was choked. Helium was used as a substitute for hydrogen for safety reasons. Schefer et al. [16] investigated leaks where the flow was due to pressure-driven convection and permeation through metals. They obtained analytical relationships for flow rates of choked flows, subsonic laminar flows, and turbulent flows. Hydrogen leakage in stainless steel threaded pipe fittings was considered by Ge and Sutton [17]. They found that a larger tightening torque is less important in leak prevention than choice and proper application of thread sealant. The tests were run up to 70 bar and typical hydrogen leak rates through these fittings were found to be 1  $\mu\text{g/s}$ .

Studies have also evaluated the risks of hydrogen leaks with respect to accumulation and explosion of hydrogen [7,8]. Swain and Swain [18] evaluated the safety risks associated with leaks of hydrogen, methane, and propane into an enclosed area. They modeled and measured leak rates for diffusion, laminar, and turbulent flow regimes and found that, for a given supply pressure, hydrogen had a significantly higher volumetric flow rate than methane or propane. They also found that combustible mixtures resulted more quickly for propane and hydrogen leaks than for methane leaks.

Leak flames resemble the micro diffusion flames that have been observed in other laboratories and while only one previous study specifically evaluated leak flames [20], there have been many studies of micro diffusion flames [9-14]. Micro diffusion flames are typically associated with an application, e.g., a microcombustor for power generation. Nonetheless, it is possible that they could arise unexpectedly. For example, if a leak from a crack or hole in a fitting, tube or storage vessel of a plumbing system were ignited, this could be characterized as a micro diffusion flame.

Ban et al. [10] investigated micro diffusion flames that were 2 – 3 mm long on round burners with inner diameters of 0.15 – 0.4 mm. Three fuels were considered: ethane, ethylene and acetylene. The experiments agreed with predictions of flame shapes in the absence of buoyancy. The flames were nearly spherical and their shapes were unaltered when burner orientation was changed with respect to gravity. Cheng et al. [11] performed detailed measurements and computations on small hydrogen flames burning on similar burners. Buoyancy was found to be insignificant for these flames. Nakamura et al. [12] simulated methane micro diffusion flames supported on circular burners with diameters less than 1 mm. They, too, found nearly spherical flames, associated with weak buoyancy forces. They also considered quenching limits of the flames. Baker et al. [9] studied micro-slot burners (with port widths of 0.1 – 0.76 mm) and developed a flame height expression for purely diffusion-controlled propane/air nonpremixed flames.

Quenching and blowoff limits refer to flames with the smallest and highest fuel flow rates for sustained burning. Matta et al. [13] measured quenching limits for propane on small round burners. Similar experiments were performed by Cheng et al. [14] for methane. Both studies found that quenching mass flow rate was largely independent of burner diameter. Prior to the present work, quenching flow rates had not been measured for hydrogen. Blowoff limits for micro diffusion flames have been measured for a variety of fuels by several researchers [13,19].

Thus motivated, this study includes experiments and analysis to identify which hydrogen leaks can support flames. A scaling analysis is presented to estimate the fuel mass flow rate at the quenching limit. Measured mass flow rates, both at the quenching and blowoff limits, are presented for hydrogen, methane and propane on round-hole burners. Flame quenching limits for leaky compression fittings are also presented.

## 2. Scaling for Flame Quenching Limits

A scaling analysis is presented here for flame quenching limits. This is similar to past work of Matta et al. [13]. The stoichiometric length  $L_f$  of laminar gas jet diffusion flames on round-hole burners is given by:

$$L_f/d = a \text{Re} = 4 m_{fuel} a / (\pi \mu d), \quad (1)$$

where  $d$  is the burner inside diameter,  $a$  is a fuel-specific coefficient,  $\text{Re}$  is fuel port Reynolds number,  $m_{fuel}$  is the fuel mass flow rate, and  $\mu$  is fuel dynamic viscosity. The scaling of Eq. (1) arises from many theoretical and experimental studies, including Roper [21], Sunderland et al. [22], and references cited therein.

The base of an attached jet diffusion flame is quenched by the burner and is premixed. Its standoff distance can be approximated as one half of the quenching distance of a stoichiometric premixed flame. Quenching distances typically are reported as the minimum tube diameter or plate separation distance,  $L_q$ , through which a premixed flame can pass. It is assumed here that a jet flame is above its quenching limit if its stoichiometric length exceeds half this quenching distance:

$$L_f > L_q / 2. \quad (2)$$

Combining Eqs. (1) and (2), yields the fuel mass flow rate at the quenching limit:

$$m_{fuel} = \pi L_q \mu / (8 a). \quad (3)$$

Eq. (3) predicts that the fuel mass flow rate at the quenching limit is a fuel property that is independent of burner diameter, which was similarly predicted by Ref. [13]. When measured values of  $L_q$ ,  $\mu$ , and  $a$  (see Table 1) are inserted into Eq. (3), the predicted fuel mass flow rates at the quenching limit are obtained and are listed in Table 1.

## 3. Experimental

Two different burner configurations are considered in this study: round-hole burners and leaky compression fittings.

Table 1

Selected properties of hydrogen, methane, and propane and predicted quenching mass flow rates. Values for  $a$  are from [22],  $L_a$  and  $S_L$  (laminar burning velocity) are from [5], and  $\mu$  is from [23]. The quantity  $m_{fuel}$  is predicted from Eq. (3).

Fuel	$A$	$L_q$ (mm)	$S_L$ (cm/s)	$\mu$ (g/m-s)	$m_{fuel}$ ( $\mu\text{g/s}$ )
H <sub>2</sub>	0.236	0.51	291	8.76E-3	8
CH <sub>4</sub>	0.136	2.3	37.3	1.09E-2	85
C <sub>3</sub> H <sub>8</sub>	0.108	1.78	42.9	7.95E-3	63

### 3.1 Round-Hole Burners

Three types of round-hole burners were considered: pinholes, and curved-wall pinholes, and tubes, as illustrated in Fig. 1. Each type included various hole diameters, given in Table 2. The pinhole burners were stainless steel nozzles that were manufactured for solid-stream spray generation. The top surface of each burner (except for the two smallest ones) is a curved surface (radius of curvature of 4.3 mm) with a hole passing through its axis, as shown in Fig. 1. The top surfaces of the two smallest pinhole burners were planar, not curved, surfaces. The pinhole burners represent pinhole leaks in pressure vessels where the radius of curvature of the wall is large or infinite.

The curved-wall pinhole burners were constructed from stainless steel tubes with two outside diameters: 1.6 and 6.4 mm. A radial hole was drilled in each tube. These burners represent pinhole leaks that might occur in fuel supply tubing.

The tube burners were made from stainless steel hypodermic tubes. Although they do not represent practical leak flames, they are a fundamental configuration that leads to a flame from a wall where the radius of curvature approaches zero. Their observation should also lead to an improved understanding of microinjectors in small-scale microelectro-mechanical power generators [13].

Fuel was delivered via a pressure regulator and a needle valve, and all tests were performed at normal lab pressure and temperature. Measuring the small flow rates at the quenching limits required special procedures. A glass soap-bubble meter was installed upstream of the burners. Quenching flow rates were measured by establishing a small flame near the quenching limit and gradually decreasing the flow rate until the flame extinguished. The fuel flow rate was then measured using the soap-bubble meter.

Determining the existence of hydrogen flames near their quenching limits was complicated by their small size and low luminosity. These flames were detected with a K-type thermocouple positioned 10 mm above each burner.

Burners were allowed to warm slightly above room temperature to prevent water condensation. This was necessary because water condensation was found to disturb the flows from the small burners, sometimes extinguishing the flames. Using similar burners, Takahashi et al. [20] also reported complications of water condensation. Tests performed at different burner temperatures, up to about 200 °C, found quenching flow rate to be largely independent of burner temperature provided condensation was avoided. Tests were also conducted with varying ambient humidity, and quenching limits were found to be generally independent of the relative humidity of the air in the range of 46 – 90%.

Hydrogen flow rate at blowoff was measured with a soap bubble meter. A stable flame was established and then the flow rate was increased until the flame first lifted and then extinguished. For blowoff tests the flames were detected visually. Hearing protection was required for the blowoff tests for the larger burners.

Additional tests were performed to consider buoyancy effects. To this end, quenching flow rates were found for pinhole and tube burners in the vertical, horizontal, and inverted orientations.

### 3.2 Leaky Fittings

Quenching limits were also measured for leaky compression fittings. The tests involved leaks between Swagelok® stainless steel tube union compression fittings and stainless steel tubes. Tube diameters were 3.2, 6.4, and 12.7 mm. The end of each union opposite the tube was sealed. New tubes and fittings were assembled according to manufacturer instructions and were rejected if bubbles appeared in an applied soap water solution when pressurized with hydrogen to 8 bar absolute. Leaks were then introduced in one of three ways: by reducing the torque on the threaded



Fig. 1. Schematics of the present round-hole burners. Arrows show the fuel flow direction. Burner dimensions are given in Table 2.

Table 2  
Hole diameters (mm) for the present round-hole burners.

Pinhole	Curved wall <sup>a</sup>	Curved wall <sup>b</sup>	Tube
0.008	0.41	0.41	0.051
0.13	0.53	1.75	0.152
0.36	0.74	2.46	0.406
0.53	0.86	3.12	0.838
0.71	1.02		1.194
0.84			2.21
1.01			
1.40			
1.78			
2.39			
3.18			

<sup>a</sup>For tube diameter of 1.6 mm.

<sup>b</sup>For tube diameter of 6.4 mm.

nut, by over tightening the nut, or by scratching the front ferrule sealing surface. These types of leaks are occasionally encountered in plumbing systems. The three leak types were found to yield the same flame quenching limits, so only results for reduced torque fittings are presented here. Reduced torque fittings allow quenching limits to be measured for different upstream pressures by adjusting the torque, i.e., an increased torque requires an increased upstream pressure at the quenching limit. Most tests were performed with the burner in the vertical orientation, with the leaky fitting at the top end of the tube. Horizontal and inverted orientations also were considered for some tests.

Quenching limits were found by igniting the fuel (with an external flame) and then reducing fuel flow rate until extinction. Fuel flow rate was controlled with upstream pressure, primarily, and with torque on the threaded nut. Upstream absolute pressure was set with a pressure regulator. When a quenching limit was established, any flame was extinguished and a plastic tube was installed over the fitting such that the leak flow was measured with a downstream soap bubble meter at laboratory pressure. The quenching limits were obtained with burners at nearly laboratory temperature.

The hydrogen flames generally were not visible even in dark conditions. As with the round-hole burners, the presence of hydrogen flames was determined with a thermocouple positioned 10 mm above the flame position. Quenching limits for methane and propane were identified visually because thermocouples confirmed these flames to be visible in all cases.

Uncertainties for the present round-hole and leaky fitting tests are estimated at  $\pm 5\%$  for hole diameter, fuel flow rate, and upstream pressure.

## 4. Results

### 4.1 Round-Hole Burners

Figure 2 shows an image of a hydrogen flame burning slightly above its quenching limit on a 0.36 mm pinhole burner. The flame appearance is similar to that of all the quenching limit hydrogen flames on round-hole burners. The hydrogen quenching distance of Table 1 suggests steady hydrogen diffusion flames should be anchored about 0.26 mm from the burner surface. Figure 2 indicates this is reasonable for the present hydrogen flames near their quenching limits. Because the maximum flame dimension is comparable to its standoff distance, this flame closely resembles a flat premixed flame [13].

Measured quenching limits for hydrogen, methane, and propane on tube burners are shown in Fig. 3. Consistent with Eq. (3), for each fuel the mass flow rate at quenching is nearly independent of burner diameter. The mean quenching limit flow rates are shown and are in reasonable agreement

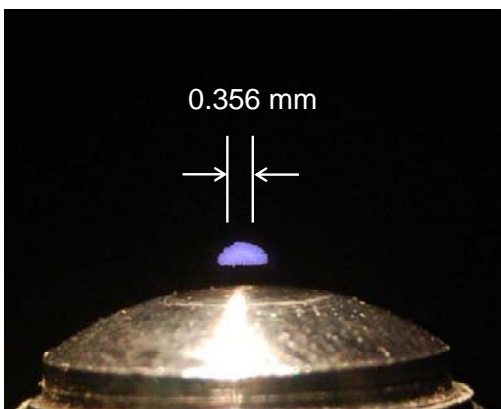


Fig. 2. Color image of a hydrogen flame slightly above its quenching limit of  $7.5 \mu\text{g/s}$ . The burner is a 0.36 mm pinhole burner and is oriented vertically. The image was recorded in a dimly lit room at  $f/4.2$  with an exposure time of 30 s.

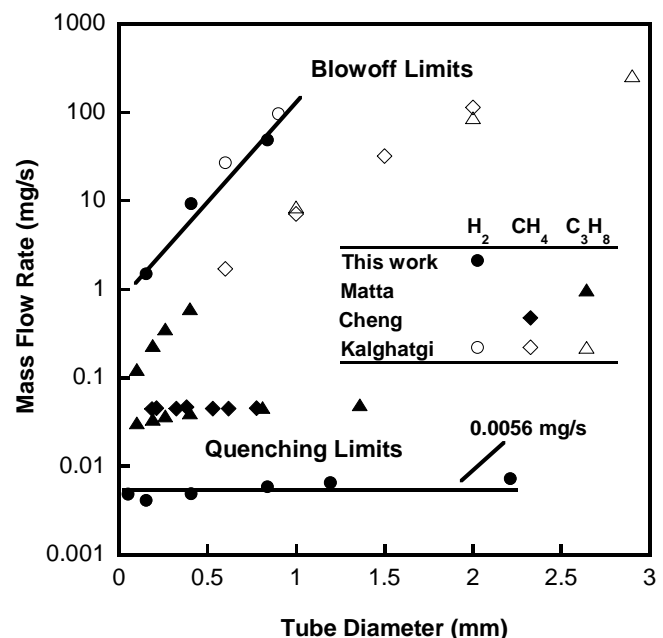


Fig. 3. Quenching and blowoff limits for tube burners. Hydrogen quenching and blowoff limits include best fit lines. Past measurements shown are from Refs. [13,14,19].

with the predictions of Table 1. The mean quenching limits for hydrogen are about an order of magnitude lower than those of the other fuels. Table 1 and Eq. (3) indicate this arises from hydrogen's short quenching distance (primarily) and from its large flame length relative to its mass flow rate (i.e., large coefficient  $a$ ).

Figure 3 also shows measured blowoff limits. The mass flow rate at blowoff increases with tube diameter because for these flames blowoff occurs when the local velocity exceeds the local premixed flame speed. The blowoff limits for hydrogen are about an order of magnitude larger than those of the other fuels, largely owing to the high burning velocity of hydrogen. Regardless of tube diameter, the limits of stable combustion of hydrogen are much wider than those for propane or methane. The limits narrow with decreasing tube diameter, as was shown for propane in Ref. [13], but they never meet.

Figure 4 shows the hydrogen quenching limits for the three types of round burners. Figure 4 indicates that, in general, quenching limits are somewhat affected by burner type and diameter for the smaller burner diameters. Where the limits are affected by burner type, the differences can largely be attributed to varying amounts of heat loss, as discussed next. An increase in heat loss requires a higher quenching flow rate to sustain the flame.

For burner diameters below 1.5 mm, pinhole burners have the highest quenching flow rates, while tube burners have the lowest. Pinhole burners have greater heat losses owing to their shape and mass. Heat conducted to the pinhole burners is mostly transferred to the ambient and constitutes a loss of enthalpy from the system. On the other hand, much of the heat conducted to the tube burners is transferred to the fuel and oxidizer and thus is not intrinsically lost from the system. For tube burners the primary heat losses are expected to be radiation from the tube.

The effects of burner curvature on heat loss were investigated by observing curved-wall pinhole burners. An increase in curvature is expected to reduce wall heat loss. Indeed the 1.59 mm curved-wall pinhole burners yield quenching limits approaching those of the tube burners, whereas the 6.35 mm burners have quenching limits closer to those of the pinhole burners.

Burner diameter has interesting effects on the quenching limits of Fig. 4. For tube burners quenching flow rate generally increases with increasing burner diameter. This also was observed for propane by Matta et al. [13], as shown in Fig. 3. This is attributed to increasing heat loss with increasing burner diameter. In contrast pinhole burners do not exhibit this trend because their heat loss is nearly independent of burner hole size. The reason for the local maximum in Fig. 4 for pinhole burners is unknown. For burner diameters above 1.5 mm, the quenching flow rates for both pinhole and tube burners agree with the  $8 \mu\text{g/s}$  prediction of Table 1.

Quenching mass flow rates show a small increase for hole diameters less than 0.2 mm for both pinhole and tube burners. It is likely that the flow field is affecting the quenching limits at these very small sizes. In particular, the measured quenching flow rates for these two burners indicate sonic velocities. For the next larger hole sizes velocities are well below sonic. While exit velocities are high, the hole size is sufficiently small that the Reynolds numbers are all small and less than 10.

While the results above are for vertical burner orientation (upward flowing fuel), hydrogen quenching limits also were measured for inverted and horizontal orientations. The results, shown in Figs. 5 and 6, reveal that quenching limits for the pinhole and tube burners are not dependent on orientation. Thus these limit flames are not affected significantly by buoyancy. This can be elucidated by considering their Froude numbers, given by

$$\text{Fr} = u^2 / (g d), \quad (4)$$

where  $u$  is the fuel velocity at the burner port and  $g$  is the acceleration of gravity. For the present quenching limit flames on pinhole and tube burners, the Fr range is 0.17 – 39. These are not in the buoyancy-controlled regime of  $\text{Fr} \leq 0.1$  [10]. Thus flame structure at the quenching limits should not vary with orientation. Furthermore, as mentioned in the experimental section, small changes in burner temperature do not affect the quenching limits, so any effects of orientation on burner heating should

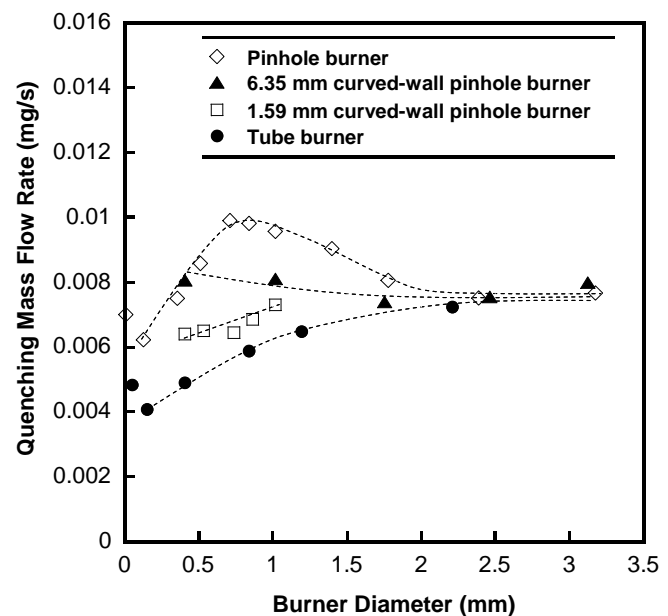


Fig. 4. Quenching mass flow rates for hydrogen for various burner types and diameters.

not affect these limits.

The above results demonstrate that flame quenching limits depend on fuel type and mass flow rate, with burner type, diameter, and orientation having far less significant effects. For a given fuel the mass flow rate out of the leak is a function of the leak geometry and the upstream pressure. This relationship depends whether the leak regime is diffusional, subsonic laminar, subsonic turbulent, isentropic choked, supersonic, etc., as considered by Schefer et al. [16]. While the leaks considered here would not be considered isentropic, insight into the present quenching limits can be obtained by considering isentropic choked flows through round holes at the quenching limits. This could, for example, be relevant to a pinhole leak in a thin wall tube. Under these conditions the fuel flow rate is linear with respect to leak area  $A$  and upstream absolute pressure  $p_0$  as follows [16]:

$$m_{fuel} = A p_0 \left( \frac{k MW}{T_0 R_u} \right)^{1/2} \left( \frac{2}{k+1} \right)^{\frac{k+1}{2(k-1)}} \quad (5)$$

where  $k$  is fuel specific heat ratio,  $MW$  is fuel molecular weight,  $T_0$  is upstream stagnation pressure, and  $R_u$  is the universal gas constant.

Insight into the present quenching limits is obtained by considering isentropic choked flows through round holes at the quenching limits. For a given fuel and upstream pressure, Eq. (5) can predict the hole diameter (the quenching diameter) associated with the quenching limit. The results of these predictions are shown in Fig. 7. For this plot the quenching limit flow rates were taken as the average values for tube burners in Fig. 3. Each line in Fig. 7 starts at the minimum upstream pressure for choked flow and ends at the maximum pressure anticipated in alternative fuel vehicles. This plot predicts that for a given storage pressure, hydrogen is susceptible to flaming leaks for hole diameters that are smaller than those for methane or propane. Furthermore, at hydrogen's maximum anticipated storage pressure of 690 bar (10,000 psi), a hole diameter of just 0.4  $\mu\text{m}$  is predicted to support a flame.

The limit flames in this study are believed to be among the weakest steady flames ever recorded. The weakest of these had a hydrogen flow rate of 3.9  $\mu\text{g/s}$  (see Fig. 5), or a heat release rate of 0.46 W based on hydrogen's lower heating value of 119.9 kJ/g. Previously, Ronney et al. [24] documented hydrogen flame balls produced under microgravity conditions with a power output of about 1 W. In subsequent tests they achieved flames as weak as 0.5 W. These were believed to be the weakest flames ever recorded.

Flame balls were first predicted by Zeldovich [25], who proposed that a solution exists to the steady heat and mass conservation equations corresponding to a stationary, spherical premixed flame. This solution was termed a flame ball, and the phenomena was discovered forty years after Zeldovich's work by Ronney et al. [26] in drop tower experiments with lean hydrogen-air mixtures. The microgravity environment was necessary to obtain the

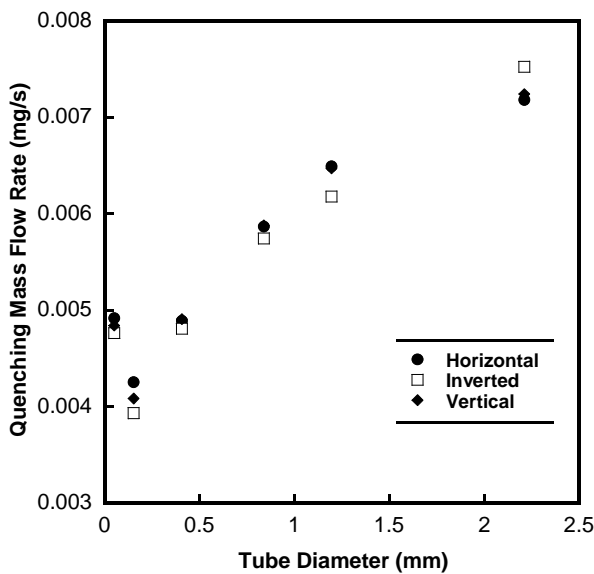


Fig. 5. Quenching mass flow rates for tube burners in horizontal, inverted, and vertical orientations.

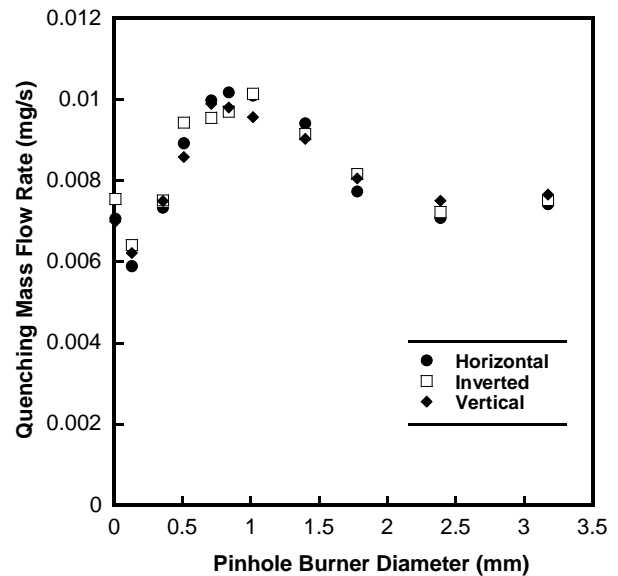


Fig. 6. Quenching mass flow rates for pinhole burners in horizontal, inverted, and vertical orientations.

spherical symmetry and to avoid extinction brought on by buoyancy. Flame balls have only been achieved in microgravity conditions with very lean hydrogen mixtures. With no mechanism other than radiative heat loss, and this being low for hydrogen flames, it was reasonable to assume that these flames were the weakest possible flames. The present results indicate that, despite the possibility of heat loss to the tube, the present diffusion flame geometry is actually slightly more resistant to extinction than a flame ball. As noted earlier, heat transfer to the hypodermic tube does not intrinsically imply a significant loss of enthalpy as most of this heat preheats the reactants.

#### 4.2 Leaky fittings

Figure 8 shows photographs of hydrogen, methane, and propane flames on 6.3 mm leaky compression fittings in the vertical orientation. These images were recorded slightly above the quenching limits. Near their quenching limits the flames did not burn along the entire fitting annulus. The hydrogen flame is significantly smaller and dimmer than the others. For all three flames the shortest distance between the flame and the metal material is approximately 50% of the quenching distance given in Table 1. No yellow soot luminosity was visible in any of the present flames near their quenching limits. The leaks associated with the images of Fig. 8 produced readily visible bubbles when soap water solution was applied.

An audible pop occurred upon hydrogen ignition, but not upon ignition of methane or propane. When the external flame was removed, ignition was quickly followed by extinction for fuel flow rates below the quenching limit. For fuel flow rates above the quenching limit, ignition was followed by a stable flame.

Figure 9 shows measured quenching limits for hydrogen, propane, and methane for 6.3 mm fittings in the vertical orientation. The data at the higher line pressures were obtained by increasing the torque on the fitting, and thus reducing the leak size. The upper limit on line pressure for propane is lower than that of the others because the vapor pressure of propane is only 9.1 bar (142 psia) at 25 °C.

Within experimental uncertainties, the quenching limits of Fig. 9 are independent of line pressure for each fuel. This suggests that, as

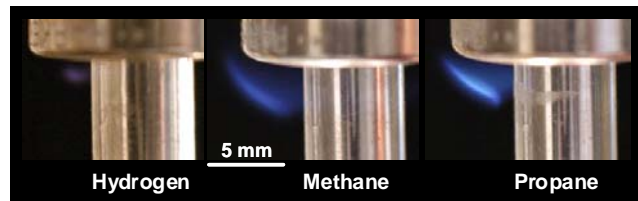


Fig. 8. Flames near extinction on leaky compression fittings for hydrogen, methane, and propane (original in color). Also visible here is the 6.3 mm tube and the threaded nut. The fitting was vertically oriented and the upstream absolute pressure was 4 bar.

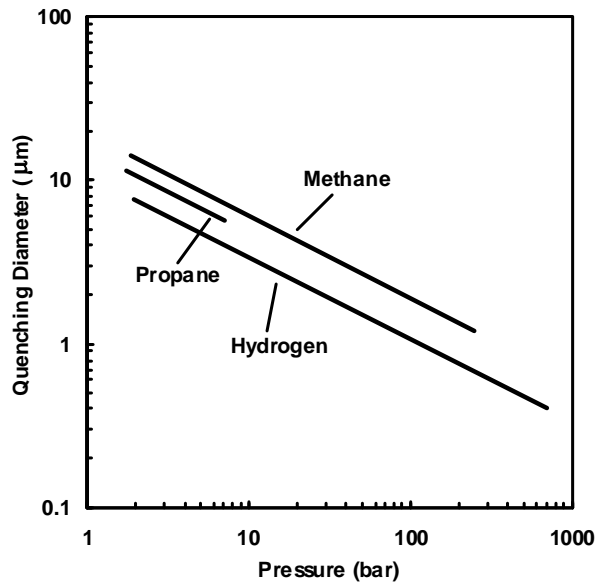


Fig. 7. Minimum diameter of a circular port for flaming (quenching diameter) as a function of upstream absolute pressure assuming isentropic choked flow.

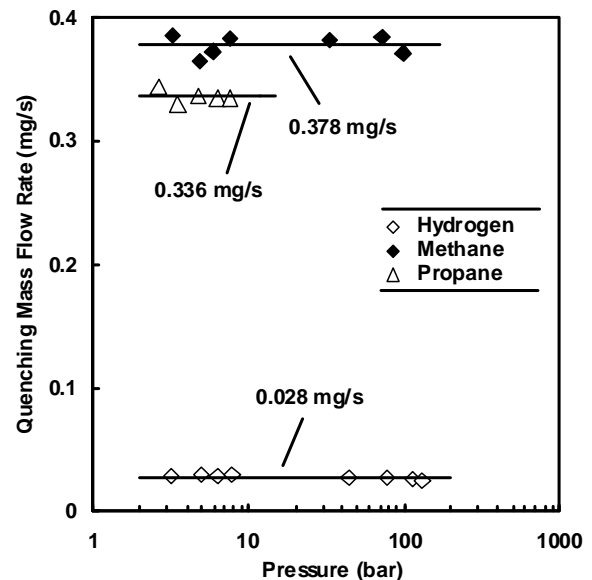


Fig. 9. Quenching limit (minimum flaming flow rate) versus upstream absolute pressure for a 6.3 mm leaky compression fitting in the vertical orientation. The line fits represent mean values of the measured quenching limits.

anticipated from the round-hole burner results of Fig. 4, the key parameter controlling quenching limits is the fuel mass flow rate. For these low flow rates and small leak sizes the line pressure does not have a significant effect on the velocity field in the flame region.

The mean hydrogen flow rate at the quenching limit is about an order of magnitude lower than for the other fuels, which is consistent with the results of Fig. 3. For leaky fittings, the quenching flow rates for hydrogen, methane, and propane are about an order of magnitude higher than the corresponding flows for round-hole burners (Fig. 4). This is attributed to additional burner heat losses in the leaky fittings, where the flames burn near concave metal surfaces.

The effects of orientation of leaky fittings are investigated in Fig. 10. Fitting orientation had little or no effect on the quenching limits of hydrogen flames. This is anticipated as these flames are small at their limits and the results are consistent with the round-hole hydrogen measurements of Figs. 5 and 6. Nonetheless, burner orientation did have an effect on the quenching limits of propane and methane flames, with the inverted limits averaging 20% lower than the vertical limits. These flames are larger than the corresponding hydrogen flames such that buoyancy is beginning to have a significant effect on the flow field. The inverted orientation has the fitting below the tube, and this minimizes the surface area of the flame impingement, leading to a reduced heat loss and thus lower quenching limits.

The effects of fitting diameter on quenching limits are examined in Fig. 11. Diameter had a significant impact on the quenching limits in all cases; on average as tube diameter doubles, the fuel mass flow rate at quenching increases 30%. This is attributed to increased heat losses associated with larger fittings.

This study has identified new questions that warrant further study. For example, what corrosive effects do leak flames have on containment materials? Can permeation leaks support flames? Can surface coatings, e.g., intumescent paints, be applied that will increase the fuel flow rate at quenching? An improved understanding of hydrogen leaks is necessary to ensure safe use of hydrogen in the commercial sector.

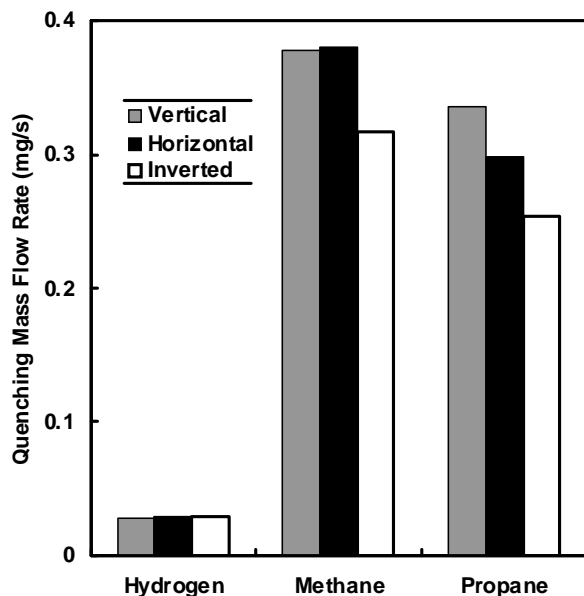


Fig. 10. Quenching limits for a 6.3 mm leaky compression fitting in vertical, horizontal and inverted orientations. The upstream absolute pressure was 4 bar.

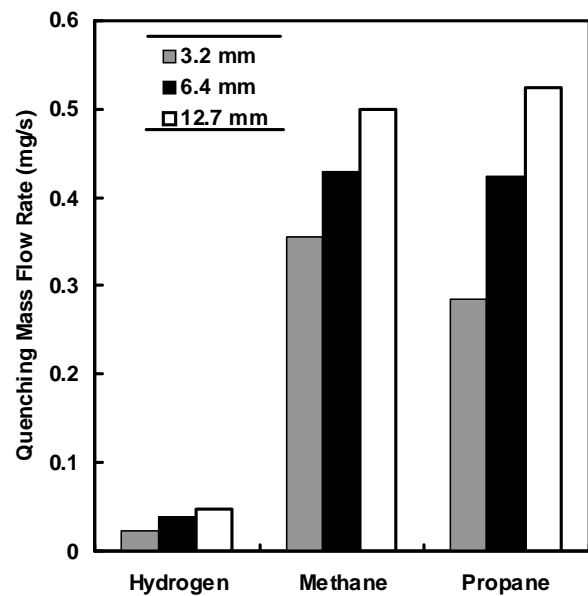


Fig. 11. Quenching limits for leaky compression fittings for tube diameters of 3.1 mm, 6.3 mm and 12.6 mm. The fittings were vertically oriented and upstream absolute pressure was 4 bar.

## 5. Conclusions

Flame quenching and blowoff limits were measured for diffusion flames results from fuel issuing out of small burners. Hydrogen fuel was emphasized, and was compared with methane and propane for a variety of burner types that characterized a range of heat losses. The key findings are as follows:

1. Flame quenching limits for round-hole burners are nearly independent of burner diameter. These limits are reasonably predicted by a simple model presented here. The quenching limit mass flow rate of hydrogen, 5.6  $\mu\text{g/s}$ , which is only is about one-tenth of that of methane and propane.

2. Existing codes and standards require leak rates below 200 mL/h (36  $\mu\text{g/s}$ ) for natural gas and 20 mL/h (0.46  $\mu\text{g/s}$ ) for hydrogen [20]. The measurements show that these flow rates are well below the associated quenching limits.
3. The mass flow rate at blowoff increases with burner diameter, and for hydrogen is about 10 times that for methane and propane for the same diameter burner. Thus the limits of stable combustion are much wider for hydrogen than for the other fuels.
4. For round-hole burners, the quenching flow rate was found to depend weakly on burner type, and to be independent of burner orientation. These observations are consistent with known wall heat loss and buoyancy effects.
5. For an isentropic choked leak, hydrogen is susceptible to flaming leaks for hole diameters that are smaller than those for methane or propane. This suggests that for hydrogen stored at 690 bar, a pinhole leak as small as 0.4  $\mu\text{m}$  could support a stable flame.
6. The weakest hydrogen flame found in this study, which was generated with a hypodermic needle with an inner diameter of 0.152 mm, is believed to be the weakest flame ever observed, with a fuel flow rate of 3.9  $\mu\text{g/s}$  and a heat release rate of 0.46 W.
7. The minimum flow rate necessary for sustaining a hydrogen flame on a leaky 6.3 mm tube compression fitting is 28  $\mu\text{g/s}$ . This is about an order of magnitude lower than for propane or methane. The minimum mass flow rate for all fuels is independent of upstream (line) pressure, and is sufficient to produce bubbles when a soap-water solution is applied.
8. Fitting orientation had about a 20% effect on the quenching limits of the leaky compression fittings considered here, while a doubling of tube size on average results in a 30% increase in quenching flow rate.

#### Acknowledgments

This work is supported by NIST under the technical direction of J. Yang. The assistance of B.H. Chao and N.R. Morton is appreciated.

#### References

- [1] Marban G, Valdes-Solis T. Towards the hydrogen economy? *Int J Hydrogen Energy* 2007;32:1625-1637.
- [2] Yamawaki M, Nishihara T, Inagaki Y, Minato K, Oigawa H, Onuki K, Hino R, Ogawa M. Application of nuclear energy for environmentally friendly hydrogen generation. *Int J Hydrogen Energy* 2007;32:2719-2725.
- [3] Sherif SA, Barbir F, Veziroglu TN. Wind energy and the hydrogen economy - review of the technology. *Solar Energy* 2005;78:647-660.
- [4] Von Jouanne A, Husain I, Wallace A, Yokochi A. Gone with the wind. *IEEE Industry Applications Magazine* July/Aug 2005:12-19.
- [5] Kanury AM. Introduction to combustion phenomena. New York: Gordon and Breach, 1975. p. 131.
- [6] MacIntyre I, Tchouvelev AV, Hay DR, Wong J, Grant J, Benard P. Canadian hydrogen safety program. *Int J Hydrogen Energy* 2007;32:2134-2143.
- [7] Takeno K, Okabayashi K, Kouchi A, Nonaka T, Hashiguchi K, Chitose K. Dispersion and explosion field tests for 40 MPa pressurized hydrogen. *Int J Hydrogen Energy* 2007;32(13):2144-2153.
- [8] Dorofeev SB. Evaluation of safety distances related to unconfined hydrogen explosions. *Int J Hydrogen Energy* 2007;32:2118-2124.
- [9] Baker J, Calvert ME, Murphy DW. Structure and dynamics of laminar jet micro-slot diffusion flames. *Journal of Heat Transfer* 2002;124:783-790.
- [10] Ban H, Venkatesh S, Saito K. Convection-diffusion controlled laminar micro flames. *Transactions of the ASME* 1994;116:954-959.
- [11] Cheng TS, Chao Y-C, Wu C-Y, Li Y-H, Nakamura Y, Lee K-Y, Yuan T, Leu TS. Experimental and numerical investigation of microscale hydrogen diffusion flames. *Proceedings of the Combustion Institute* 2005;30:2489-2497.
- [12] Nakamura Y, Yamashita H, Saito K. A numerical study on extinction behaviour of laminar micro-diffusion flames. *Combustion Theory and Modelling* 2006;10(6):927-938.
- [13] Matta LM, Neumeier Y, Lemon B, Zinn BT. Characteristics of microscale diffusion flames. *Proc. Combust. Inst.* 2002; 29:933-938.
- [14] Cheng TS, Chen CP, Chen CS, Li YH, Wu CY, Chao YC. Characteristics of microjet methane diffusion flames. *Combust. Theory Modeling* 2006;10:861-881.

- [15] Lee ID, Smith OI, Karagozian AR. Hydrogen and helium leak rates from micromachined orifices. *AIAA Journal* 2003;41(3):457-463.
- [16] Schefer RW, Houf WG, San Marchi C, Chernicoff WP, Englom L. Characterization of leaks from compressed hydrogen dispensing systems and related components. *Int J Hydrogen Energy* 2006;31:1247-1260.
- [17] Ge X, Sutton WH. Analysis and test of compressed hydrogen interface leakage by commercial stainless steel (NPT) fittings. *SAE International* 2006:35-47.
- [18] Swain MR, Swain MN. A comparison of H<sub>2</sub>, CH<sub>4</sub>, and C<sub>3</sub>H<sub>8</sub> fuel leakage in residential settings. *Int J Hydrogen Energy* 1992;17:807-815.
- [19] Kalghatgi GT. Blow-out stability of gaseous jet diffusion flames. Part I: In still air. *Combustion Science and Technology* 1981;26:5:233-239.
- [20] Takahashi M, Tamura Y., Suzuki J, Watanabe S, Investigation of the allowable flow rate of hydrogen leakage on receptacle. Paper 2008-01-724, SAE International, Detroit, April 2008.
- [21] Roper FG. The prediction of laminar jet diffusion flame sizes: Part 1. Theoretical model. *Combust. Flame* 1977;29:219-226.
- [22] Sunderland PB, Mendelson BJ, Yuan ZG, Urban DL. Shapes of buoyant and nonbuoyant laminar jet diffusion flames. *Combust. Flame* 1999;116:376-386.
- [23] Weast RC, Astle MJ. *CRC Handbook of Chemistry and Physics*, 59<sup>th</sup> edition. West Palm Beach: CRC Press, Inc., 1979. p. F-58.
- [24] Ronney PD, Wu MS, Pearlman HG. Structure of flame balls at low lewis-number (SOFBALL): preliminary results from the STS-83 and STS-94 space flight experiments. Paper AIAA-1998-463, Aerospace Sciences Meeting, Reno, Nevada, January, 1998.
- [25] Zeldovich Y. *Theory of Combustion and Detonation of Gases*. Moscow, Russia: Academy of Science, 1994.
- [26] Ronney PD, Wu MS, Pearlman HG. Experimental study of flame balls in space: preliminary results from STS-83. *AIAA Journal* 1998;36(8):1361-1368.

# Experimental and Numerical Investigation of Extremely Weak Hydrogen Diffusion Flames

V.R. Lecoustre<sup>1</sup>, C.W Moran<sup>1</sup>, P.B. Sunderland<sup>1,\*</sup>, B.H. Chao<sup>2</sup>, R.L. Axelbaum<sup>3</sup>

<sup>1</sup>Dept. of Fire Protection Engineering  
University of Maryland  
College Park MD 20742

<sup>2</sup>Dept. of Mechanical Engineering  
University of Hawaii,  
Honolulu HI 96822

<sup>3</sup>Dept. of Energy, Environmental  
and Chemical Engineering  
Washington University  
St. Louis MO 63130

## Abstract

Hydrogen micro diffusion flames were studied experimentally and numerically. The experiments involved gas jets of hydrogen flowing downward from stainless steel tube burners with inside diameters of 0.15 mm. At their quenching limits, these flames had heat release rates of 0.46 and 0.25 W in air and in oxygen, respectively. The corresponding hydrogen flow rates were 3.9 and 2.1 mg/s. These are the weakest flames ever observed, and are even weaker than microgravity flame balls. The flames were modeled numerically as spherical diffusion flames with detailed chemistry and transport. The modeling results confirmed the quenching limits and revealed high rates of reactant leakage near the limits. The model predicted double peaked heat release rate profiles for some flames. The results may be of use in future microcombustor designs.

## Introduction

The use of microcombustion processes for electric power generation has potential advantages over conventional electrochemical batteries, in terms of power generation per unit volume and energy storage per unit mass [1]. The increasing needs and demand for smaller scale and higher density power sources motivates the development of micropower devices.

Recent developments in silicon technologies and development of new materials have led to opportunities of creating highly effective small thermoelectric and photovoltaic power generators [2]. Their use opens new prospects in creation of micro scale energy supply devices. Recent developments Micro-Electro-Mechanical Systems (MEMS) [3] have enabled new microcombustor designs. Microcombustors can be defined as reactors with characteristic length scales on the order of millimeters or less.

Laminar diffusion flames can be classified in three categories. The first one corresponds to diffusion controlled flames, which can be accurately modeled using Burke-Schumann theory [4]. The second category comprises flames that are controlled by momentum or buoyancy, such as the Roper flame [5]. The third category corresponds to micro diffusion flames, where momentum and diffusion effects are comparable.

Recent attention has been dedicated to microflames. Ban et al. [6] observed flame shapes of small hydrocarbon laminar diffusion flames issuing from small fuel jets and

compared them to the shapes predicted analytically. They found that buoyancy effects are negligible for small flames and their shapes tend to be spherical. At this size, the effects of diffusion are comparable to the effects of convection. Matta et al. [7] reached the same conclusion considering a preheated weak propane flame issued at a rate of 0.31 cc/min from a 101  $\mu\text{m}$  tube and equivalent to 0.49 W.

Cheng et al. [8] characterized microjet methane diffusion flames issuing from burners with inner diameters ranging from 186 – 778  $\mu\text{m}$ . They compared the measured flame shapes with those predicted using a 2-D code with detailed chemistry model based on GRI-Mech 3.0. They observed that near extinction, the flame burns in a diffusion mode. Hydrogen microscale flames were also studied both experimentally and numerically [9]. Those flames were produced from small tubes (0.2 and 0.48 mm) and were spherical, with a radius of 1 mm. This work observed that the increased diffusivity of  $\text{H}_2$  leads to lean-burn conditions for the flame.

Nakamura et al. [10] numerically studied methane micro diffusion flames on circular burners of diameter less than 1 mm. They found that small flames have the same, nearly spherical, structure as those in microgravity, with similar species and temperature distributions. The spherical shape occurs when the Peclet number,  $Pe$ , of the flame is lower than 5. The Peclet is defined as the ratio of the mean exit velocity  $U_e$  to the diffusion velocity  $U_D$ . This number is defined as:

---

\* Corresponding author: pbs@umd.edu

$$Pe = \frac{U_e l_D}{D}, \quad (1)$$

with  $l_D$  and  $D$  being the characteristic diffusion length and the mass diffusivity coefficient, respectively.

Nakurama et al. [10] predicted a near quenching methane-air micro-flame releasing 0.5 W. The existence of a minimum flame size below which no flame exists was predicted, the minimum flame height being comparable to the reaction layer thickness. This is confirmed by Matta et al [7], who concluded that a micro-flame must be longer than its quenching distance to exist.

The ability to burn weak but stable flames is important in the design of microcombustors. In some microcombustors, weak flames may be suitable as permanent pilots, thus replacing electrical ignitors. Weak flames also can increase the turndown ratios of microcombustors.

Ronney et al. [11] observed the burning of spherical flame balls in microgravity during the STS-83/MSL-1 Space Shuttle mission. Heat released by those flames was as low as 1 W. Subsequently they achieved flames as weak as 0.5 W. It is believed these were the weakest flames recorded until the present work.

Butler et al. [12] examined quenching limits associated with various fuels and burner configurations. Their weakest flames involved hydrogen issuing downward into air from a hypodermic tube with an inside diameter of 0.15 mm. These flames, and a related flame burning in oxygen, are the subject of this study.

This work aims to experimentally observe weak hydrogen micro-flames at their quenching limits. This work also investigates these and related flames numerically to study their structure in detail. Special attention on the effects of the burner on the flame structure is carried. The numerical code used here is a one-dimensional, time accurate spherical diffusion flame code with detailed hydrogen/air combustion model and transport properties.

## Experimental

The experiments involved hydrogen non-premixed flames burning in quiescent air and weakly counterflowing oxygen. Experimental details are reported in Butler et al. [12]. The burners used were made of stainless steel with inside and outside diameters of 0.15 and 0.30 mm and with downward orientation. Hydrogen flow rates were measured with a soap bubble meter. The hydrogen flames were not visible but were detected with a thermocouple 1 cm above the burner tip. Following ignition, the hydrogen flow rate was slowly reduced until each flame extinguished at its quenching limit.

Images of the two hydrogen flames at their quenching limits are shown in Fig. 1. The test conditions for these flames are given in Table 1. The images were recorded with a Nikon D100 camera at ISO 200, f/1.4, and 30 s. The word “WE” is included at flame scale to show that



Fig. 1. Color images of hydrogen flames at their quenching limits burning in air (left) and oxygen (right).

the flames are smaller than the smallest letters on a U.S. dime. The flames are hazy, suggesting distributed reaction zones rather than thin flame sheets.

The heat release rates associated with the mass flow rates are provided in Table 1, assuming complete combustion and a heat of combustion of 120 kJ/g. Also presented in Table 1 are the Reynolds numbers,  $Re$ , at the burner exit based on hydrogen properties at laboratory conditions. At these low Reynolds numbers, the hydrogen flow in the hypodermic tube has similar conditions to those experienced in a Stokes flow, where viscous forces

Table 1. Summary of the hydrogen flames at their quenching limits.

Oxidizer	Flow rate $\mu\text{g/s}$	$U_e$ m/s	$Re$ -	$Fr$ -	$Pe$ -	Power W
air	3.9	2.5	3.96	65	5.3	0.46
O <sub>2</sub>	2.1	1.4	2.13	36	3.0	0.25

are very important. The velocities of the issued hydrogen are 2.5 m/s and 1.4 m/s for H<sub>2</sub>/air and H<sub>2</sub>/O<sub>2</sub>, respectively.

Froude number is defined here as  $Fr = U_e / (g d)^{1/2}$ , with  $U_e$  the mean exit velocity,  $g = 9.81 \text{ m/s}^2$  and  $d$  the burner inside diameter. The relatively high Froude numbers in Table 1 reveal the flames to be minimally affected by gravity. Examination of the Peclet number,  $Pe$ , assesses the dominance of diffusion over momentum. From Eq. (1), it can be derived:

$$Pe = Re_D \left( \frac{l_D}{D} \right) Sc, \quad (2)$$

with  $Re$  the Reynolds number associated with the conditions at the burner outlet,  $l_D$  the characteristic diffusion length,  $D$  the burner diameter and  $Sc$  the Schmidt number of the fuel, taken here as 0.204 for H<sub>2</sub>/air and 0.22 for H<sub>2</sub>/O<sub>2</sub> [13]. If the characteristic diffusion length is taken as the same order of magnitude as the flame size, 1 mm, the Peclet numbers are 5.3 and 3 for the H<sub>2</sub>/air and H<sub>2</sub>/O<sub>2</sub> flames, respectively. According to Han [6], flames with such small Peclet numbers are spherical (or hemispherical here).

## Numerical Methods

Laminar spherical hydrogen flames at various flow rates and issuing from different burners were numerically modeled using a one-dimensional solver, allowing the modeling of steady state and transient laminar spherical diffusion flames. The use of spherical coordinates is motivated by the low values of the Peclet number for the experimental flames, see Table 1.

The solver was modified from the PREMIX [14] code, which was originally developed for the study of one-dimensional freely propagating and burner-stabilized premixed laminar flames and which is a part of Sandia's CHEMKIN package [15]. The code features include the use of detailed chemistry and detailed transport properties using CHEMKIN II format. The equations numerically solved are:

$$A(r) \frac{\partial \rho}{\partial t} + \frac{\partial}{\partial r}(\dot{m}) = 0, \quad (3)$$

$$\rho A(r) \frac{\partial T}{\partial t} + \dot{m} \frac{\partial T}{\partial r} - \frac{1}{c_p} \frac{\partial}{\partial r} \left( A(r) \lambda \frac{\partial T}{\partial r} \right) + \quad (4)$$

$$\frac{A(r)}{c_p} \sum_{k=1}^K (\rho c_{p,k} Y_k V_k \frac{\partial T}{\partial r} + h_k \dot{\omega}_k) + Ra = 0,$$

$$\rho A(r) \frac{\partial Y_k}{\partial t} + \dot{m} \frac{\partial Y_k}{\partial r} + \frac{\partial}{\partial r} (A(r) \rho Y_k V_k) \quad (5)$$

$$- A(r) M_k \dot{\omega}_k = 0, \quad k = 1, 2, \dots, K,$$

where  $A(r)$  is the surface area of the sphere of radius  $r$ ,  $T$  is the local temperature,  $Y_k$  is the mass fraction of the  $k^{\text{th}}$  species,  $W_k$  is the molecular weight of the  $k^{\text{th}}$  species,  $t$  is time,  $r$  is the radial spatial coordinate,  $U$  is the radial flow

velocity,  $\rho$  is the gas density,  $c_p$  is the averaged specific heat at constant pressure,  $\lambda$  is the heat conductivity of the mixture,  $h_k$  is the specific enthalpy of the  $k^{\text{th}}$  species,  $c_{p,k}$  is the specific heat of the  $k^{\text{th}}$  species,  $V_k$  is the diffusion velocity of  $k^{\text{th}}$  species,  $\dot{\omega}_k$  is the production rate of the  $k^{\text{th}}$  species,  $K$  is the total number of species considered in the reaction mechanism, and  $Ra$  is a term expressing the local radiative heat loss rate.

Conventional finite difference techniques with non-uniform mesh spacing were adopted for the discretization of the differential equations. The transient terms were expressed by a forward difference formula, the diffusive terms by a central difference formula, and the convective terms by an upwind difference formula. The discretized equations were solved using Sandia's Twopoint package [16], which uses a modified damped Newton's method to solve transient and steady-state boundary value problems.

The chemical reaction rates, the thermodynamic properties, and the transport properties were evaluated by CHEMKIN and the Transport library [15,17]. The net chemical production rate of each species,  $\dot{\omega}_k$ , results from a competition between all the chemical reactions involving that species and is calculated using the modified Arrhenius form:

$$k_f = B T^b \exp\left(-\frac{E_a}{RT}\right), \quad (6)$$

where  $B$  is the pre-exponential factor,  $R$  is the ideal gas constant and  $E_a$  is the activation energy of the reaction.  $B$ ,  $R$ , and  $E_a$  were given by the reaction mechanism and written into an input file read by the code. The gas phase chemistry model used was based on GRI 3.0 mechanism [18]. Reactions considered are reported in Table 2 along with the corresponding parameters for Eq. (6). Mixture-average diffusion was considered.

Modified transport properties were introduced to improve agreement with observed flame sizes. Using the same code, Santa et al. [19] have shown that increasing the diffusivities of all species and heat by 30% yields higher peak temperatures and smaller flames. This strategy was maintained in the present simulations.

Local scalar dissipation rate was computed using the following definition:

$$\chi(r) = 2\alpha_{\text{mix}}(r) \left( \frac{dZ(r)}{dr} \Big|_{r=r} \right)^2, \quad (7)$$

The diffusivity coefficient  $\alpha_{\text{mix}}$  in Eq. (7) is the local thermal diffusivity of the mixture. The mixture fraction was computed from the local mass fractions of oxygen and hydrogen atoms. The mixture fraction is expressed as:

$$Z(r) = \frac{Y_H(r) + 2(Y_{O,\infty} - Y_O(r))}{1 + 2Y_{O,\infty}}. \quad (8)$$

The burner surface was defined as the inner boundary of the computational domain. At this location, an adiabatic boundary condition was considered, allowing the burner temperature to increase. Cheng [9] estimated burner temperatures of about 1010 K based on the burner glowing. Moreover, this condition frees the study from effects of heat losses to the burner and emphasizes the effects due to the burner presence. Cheng et al. [20] showed that for small flames with low Reynolds numbers, variable wall temperature conditions yield better agreement between computed and measured data.

The mass flux allowed backward species diffusion into the burner, conditions that were adopted by Chang et al. [9]. Under these conditions, the mass fraction of the  $k^{\text{th}}$  species at the burner surface was expressed by:

$$Y_k = \frac{\varepsilon_k}{1 + \frac{\rho V_k A}{\dot{m}_b}} \quad (9)$$

with  $\varepsilon_k$  as the input mass fraction of the  $k^{\text{th}}$  species of the initial mixture.

At the outer boundary, temperature was assigned a constant value. Species mass fractions at this boundary were set to as either air or oxygen. For all the simulations, special attention was dedicated to the position of the outer

boundary such that it did not interfere with the flame, simulating an infinite boundary. The gradients at the outer boundary were negligible. The pressure was held constant over the domain at 0.98 bar. For all the simulations performed, heat losses by radiation were neglected. Cheng et al. [20] showed that the effects of radiation on flame structure are small for low Reynolds number flames. The flames modeled were purely adiabatic.

The computational domain for the predictions of diffusion hydrogen micro-flames ranged from the burner exit (1  $\mu\text{m}$ , 75  $\mu\text{m}$ , 300  $\mu\text{m}$  or 3.175 mm) to 150 cm. For all cases considered, the position of the outer boundary was far enough from the flame that the temperature gradient there was negligible. Non-uniform grids were generated, with clustered mesh points near the reacting zone and coarse points near the outer boundary. Adaptive mesh point addition was used to reduce the gradients and curvature, improving accuracy. New grid points were automatically added until values of gradients and curvature fell below user specified limits. Further addition of grid points did not affect the solution. Typically the computational domain consisted of 300 points.

Steady state solutions of  $\text{H}_2/\text{air}$  and  $\text{H}_2/\text{O}_2$  were considered. For the study of quenching limits, the following process was observed. A first solution based on the characteristic of the flame studied was generated by the code with a moderate mass flow. Then this solution was used as the starting condition for a new simulation using the same parameters but with a lower mass flow rate. The process was reiterated until extinction was defined. Extinction was defined as a solution of the flame where no reaction was observed and with the absence of a significant raise of temperature.

## Numerical Results

Numerical predictions of steady state hydrogen flame were performed considering four different burner radii, 1  $\mu\text{m}$ , 75  $\mu\text{m}$ , 300  $\mu\text{m}$  or 3.175 mm and two different oxidizers, quiescent air and quiescent oxygen. Predictions of flames were realized using the 1-D spherical code considering adiabatic conditions in temperature at the burner surface and neglecting radiation.

Numerical investigations of quenching limits were performed first to characterize the lowest hydrogen mass flow sustaining a flame and to compare it with the experimental results. The radius of the burner was taken at 75  $\mu\text{m}$  for the cases  $\text{H}_2/\text{air}$  and  $\text{H}_2/\text{O}_2$ , matching the dimension of the hypodermic tube used in both experiments. Numerically, the lowest mass flow rate was achieved by decreasing hydrogen flow rate and reusing the former steady-state solution as initial guess for the solver. This sped convergence.

The lowest hydrogen mass flow rates sustaining flames were numerically predicted to be 3.65 and 2.67  $\mu\text{g}/\text{s}$  for the  $\text{H}_2/\text{air}$  and  $\text{H}_2/\text{O}_2$  flames, respectively. The heat release rates associated with those mass flow

Table 2.  $\text{H}_2\text{-O}_2$  reactions mechanisms considered for the simulations. From GRI Mech. 3.0 [18].

Name	Reaction	$\mathcal{B}$ ( $\text{gmol.cm}^{-3}\text{s}^{-1}$ )	$b$	$E_a$ ( $\text{cal.gmol}^{-1}$ )
R1	$2\text{O}+\text{M} \rightarrow \text{O}_2+\text{M}$	1.20E+17	-1.0	0
R2	$\text{O}+\text{H}+\text{M} \rightarrow \text{OH}+\text{M}$	5.00E+17	-1.0	0.0
R3	$\text{O}+\text{H}_2 \rightarrow \text{H}+\text{OH}$	3.87E+04	2.7	6260
R4	$\text{O}+\text{HO}_2 \rightarrow \text{OH}+\text{O}_2$	2.00E+13	0.0	0
R5	$\text{O}+\text{H}_2\text{O}_2 \rightarrow \text{OH}+\text{HO}_2$	9.63E+06	2.0	4000
R33	$\text{H}+\text{O}_2+\text{M} \rightarrow \text{HO}_2+\text{M}$	2.80E+18	-0.86	0
R34	$\text{H}+2\text{O}_2 \rightarrow \text{HO}_2+\text{O}_2$	2.08E+19	-1.24	0
R35	$\text{H}+\text{O}_2+\text{H}_2\text{O} \rightarrow \text{HO}_2+\text{H}_2\text{O}$	1.13E+19	-0.76	0
R36	$\text{H}+\text{O}_2+\text{N}_2 \rightarrow \text{HO}_2+\text{N}_2$	2.60E+19	-1.24	0
R37	$\text{H}+\text{O}_2+\text{Ar} \rightarrow \text{HO}_2+\text{Ar}$	7.00E+17	-0.8	0
R38	$\text{H}+\text{O}_2 \rightarrow \text{O}+\text{OH}$	2.65E+16	-0.67	17041
R39	$2\text{H}+\text{M} \rightarrow \text{H}_2+\text{M}$	1.00E+18	-1.0	0
R40	$2\text{H}+\text{H}_2 \rightarrow 2\text{H}_2$	9.00E+16	-0.60	0
R41	$2\text{H}+\text{H}_2\text{O} \rightarrow \text{H}_2+\text{H}_2\text{O}$	6.00E+19	-1.25	0
R43	$\text{H}+\text{OH}+\text{M} \rightarrow \text{H}_2\text{O}+\text{M}$	2.20E+22	-2.00	0
R44	$\text{H}+\text{HO}_2 \rightarrow \text{O}+\text{H}_2\text{O}$	3.97E+12	0.0	671
R45	$\text{H}+\text{HO}_2 \rightarrow \text{O}_2+\text{H}_2$	4.48E+13	0.0	1068
R46	$\text{H}+\text{HO}_2 \rightarrow 2\text{OH}$	8.40E+13	0.0	635
R47	$\text{H}+\text{H}_2\text{O}_2 \rightarrow \text{HO}_2+\text{H}_2$	1.21E+07	2.0	5200
R48	$\text{H}+\text{H}_2\text{O}_2 \rightarrow \text{OH}+\text{H}_2\text{O}$	1.00E+13	0.0	3600
R84	$\text{OH}+\text{H}_2 \rightarrow \text{H}+\text{H}_2\text{O}$	2.16E+08	1.51	3430
R85	$2\text{OH}+\text{M} \rightarrow \text{H}_2\text{O}_2+\text{M}$	7.40E+13	-0.37	0
R86	$2\text{OH} \rightarrow \text{O}+\text{H}_2\text{O}$	3.57E+04	2.4	-2110
R87	$\text{OH}+\text{HO}_2 \rightarrow \text{O}_2+\text{H}_2\text{O}$	1.45E+13	0.0	-500
R88	$\text{OH}+\text{H}_2\text{O}_2 \rightarrow \text{HO}_2+\text{H}_2\text{O}$	2.00E+12	0.0	427
R89	$\text{OH}+\text{H}_2\text{O}_2 \rightarrow \text{HO}_2+\text{H}_2\text{O}$	1.70E+18	0.0	29410
R115	$2\text{HO}_2 \rightarrow \text{O}_2+\text{H}_2\text{O}_2$	1.30E+11	0.0	-1630
R116	$2\text{HO}_2 \rightarrow \text{O}_2+\text{H}_2\text{O}_2$	4.20E+14	0.0	12000

rates are 0.41 and 0.31 W. These heat release rates were obtained by numerical integration of the local heat release rate computed by the code using CHEMKIN library. These values are in reasonable agreement with the measured mass flow rates and heat release rates of Table 1.

In Fig. 2, predicted  $H_2$ /air flame structure issued prior extinction and from a 75  $\mu\text{m}$  radius is plotted and compared with the structure of a  $H_2$ /air flame issuing from a 1  $\mu\text{m}$  radius burner, at a mass flow rate of 3.49  $\mu\text{g/s}$ . This mass flow rate corresponds to the lowest mass flow rate sustaining a flame issuing from a spherical burner with a radius of 1  $\mu\text{m}$ . For this configuration, the smallest heat released rate predicted is 0.4 W.

Superimposing the two data set shows similarities shared by the two flames. A common region is located beyond 75  $\mu\text{m}$ , corresponding to the radius of the burner. Figure 2 shows the flame truncation induced by the physical presence of the burner. Both flames present the same peak temperature of 1290 K. Scalar dissipation rates at the flame location are  $0.98 \text{ s}^{-1}$  for the 75  $\mu\text{m}$  radius

burner and  $1.18 \text{ s}^{-1}$  for the 1  $\mu\text{m}$  radius burner. Due to the small flame radius, about 200  $\mu\text{m}$  for both, the heat release rate density is very high, peaking at 3800 and 8000  $\text{W/cm}^3$ , respectively.

The smaller burner considered presents the highest scalar dissipation rate value prior extinction. Its predicted surface temperature is 300 K, which implies that the burner does not remove any heat from the system. Moreover, at the burner surface, the mass fraction of  $H_2$  is nearly unity, which is not the case for the 75  $\mu\text{m}$  radius burner.

The oxidizer presence is important near the burner for the 75  $\mu\text{m}$  burner. The oxygen and intermediate species mass fractions at the burner surface are high. The mass fraction of  $H_2$  drops considerably outside the burner. For the 75  $\mu\text{m}$  radius burner,  $H_2$  mass fraction at the burner surface is lower than 1%. The reaction zone exists under lean conditions. This was also observed by Chang et al. [9].

The main reactions contributing to the heat release rate for the 75  $\mu\text{m}$  radius burner are:

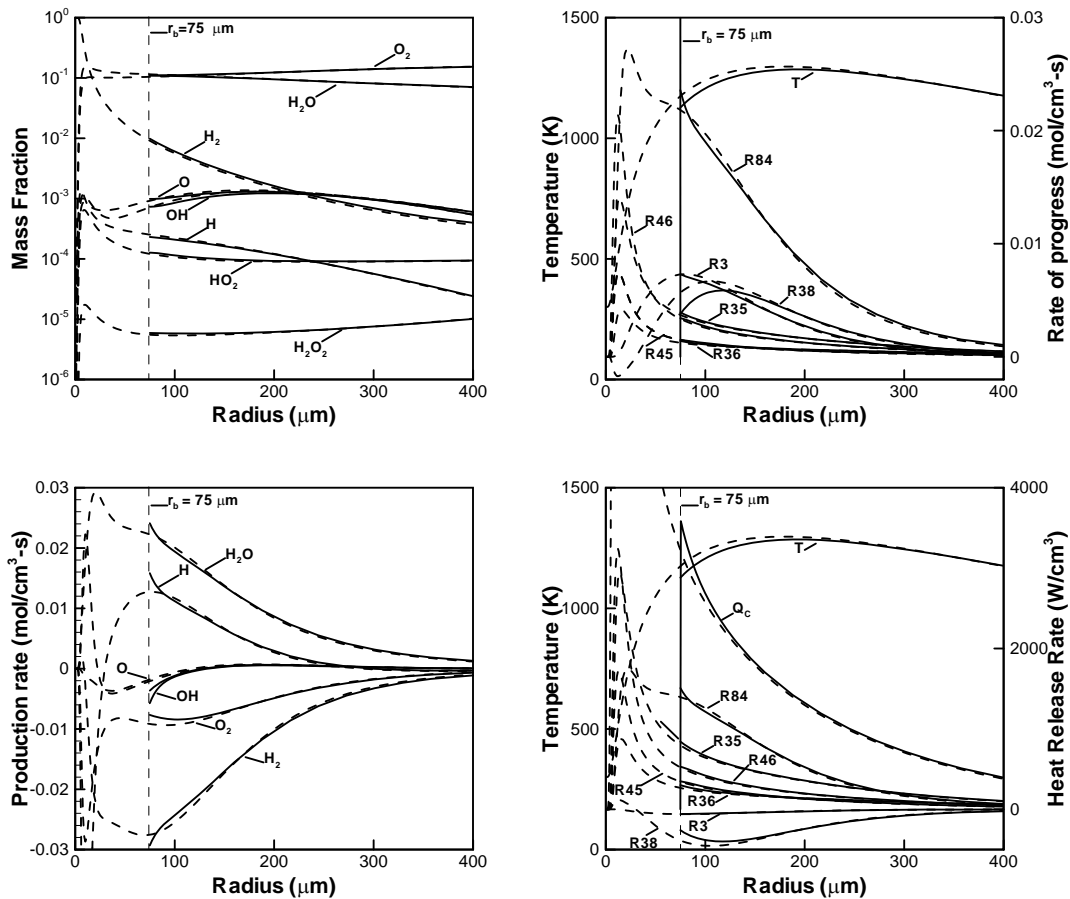
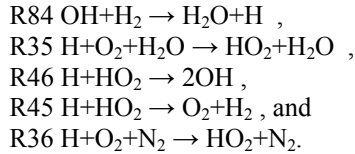
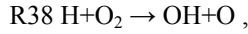


Fig. 2. From top left, clockwise, plot of the species mass fraction, elementary reactions rate of progress, elementary reactions heat release rate and species production rate for  $H_2$ /Air flames at the onset of kinetic extinction. Burner radii are 75  $\mu\text{m}$  plain line (1  $\mu\text{m}$  dashed), supplied mass flow rate is set at 3.65  $\mu\text{g/s}$  (3.49  $\mu\text{g/s}$ ),  $Q_c$  is 0.41 W (0.40 W).

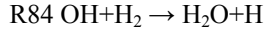


There is a significant endothermic reaction, the chain branching reaction

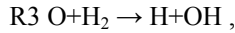


which consumes part of the energy release.

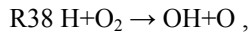
The major contributors to the heat release rate are not necessarily the reactions with the highest rates of progress. Indeed, although reaction



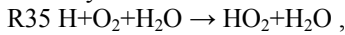
shows the highest rate of progress and the highest heat release rate, reaction



which does not contribute to the heat release rate, has the second highest rate of progress. The third highest belongs to reaction



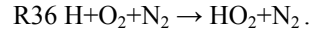
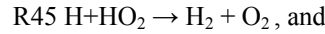
followed by chain termination reaction



chain branching



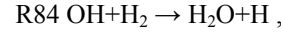
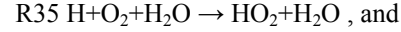
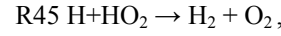
and to a lesser measure,



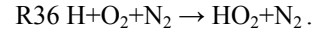
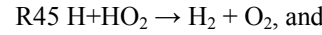
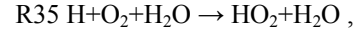
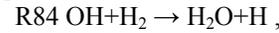
The main reactions predicted for the 1  $\mu\text{m}$  radius burner flame are the same, except their order of importance are different. The main reaction, in terms of heat release rate is



followed by



all are reactions involving the consumption of H radical except for reaction R84. In terms of rate of progress, the important reactions are



Note that reactions

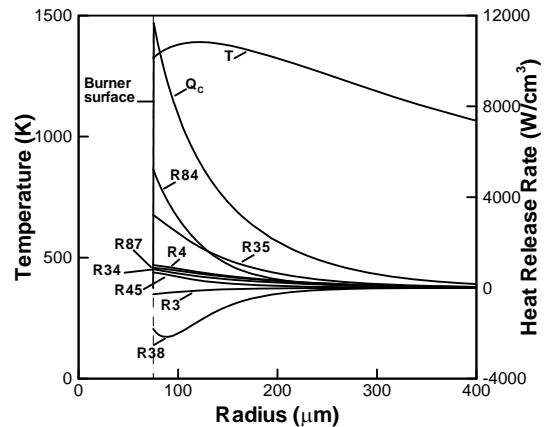
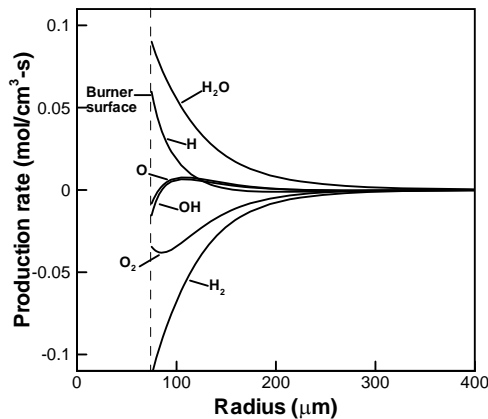
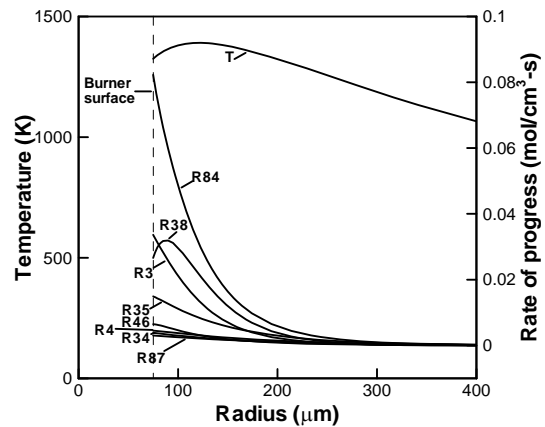
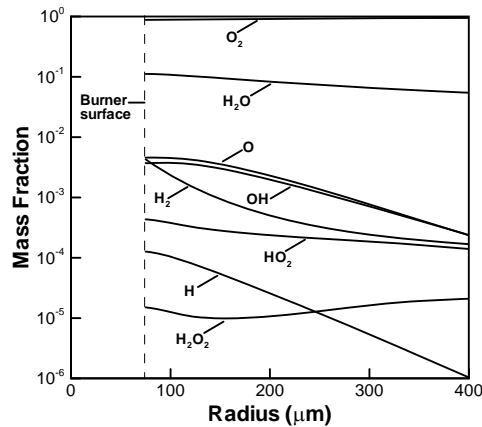
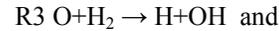
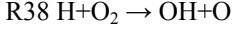


Fig. 3. From top left, clockwise, plot of the species mass fraction, elementary reactions rate of progress, elementary reactions heat release rate and species production rate for  $\text{H}_2/\text{O}_2$  flame at the onset of kinetic extinction. Burner radius is 75  $\mu\text{m}$ , hydrogen mass flow rate is 2.67  $\mu\text{g/s}$ , and  $Q_c$  is 0.31 W.

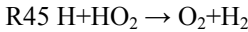
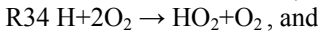
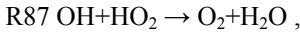
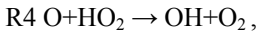
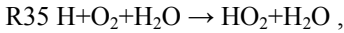
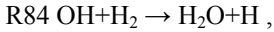


have negative rates of progress close to the burner.

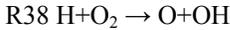
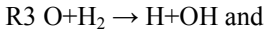
The structure of a weak hydrogen flame burning in oxygen at the onset of extinction was numerically investigated and is shown in Fig. 3. The lowest possible flow rate sustaining a steady state flame is found to be 2.67  $\mu\text{g/s}$ . At this flow rate, the peak temperature is 1400 K and the heat generated is 0.31 W. The scalar dissipation rate at the peak temperature is 2.43  $\text{s}^{-1}$ . This value is twice the scalar dissipation rate of the extinction limit  $\text{H}_2/\text{air}$  flame generated by the 1  $\mu\text{m}$  radius burner.

For the same burner size, higher oxygen and OH radical leakage at the flame location is observed for the system  $\text{H}_2/\text{O}_2$  than for the  $\text{H}_2/\text{air}$  system. However  $\text{H}_2/\text{O}_2$  flames present faster chemistry, with peak values of species production rate 5 times higher than those predicted for the  $\text{H}_2/\text{air}$  flame. This is due to an increase of reaction rates of progress.

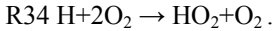
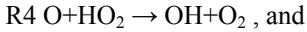
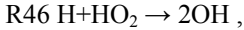
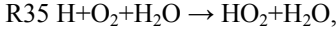
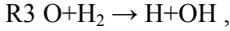
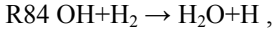
The main chemical reactions contributing to the heat release rate for  $\text{H}_2/\text{O}_2$  flames at the onset of extinction are:



for the exothermic reactions, and



for the endothermic ones. The important reactions by decreasing rate of progress, are



The  $\text{H}_2/\text{O}_2$  flame has a slightly higher temperature at the onset of extinction (1400 versus 1290 K) than the  $\text{H}_2/\text{air}$  flame. However, its flame extent is smaller than that of the  $\text{H}_2/\text{air}$  flame. The location of the peak temperature is located at a radius of 130  $\mu\text{m}$  for the  $\text{H}_2/\text{O}_2$  flame and at almost 200  $\mu\text{m}$  for the  $\text{H}_2/\text{air}$  flame.

The impacts of the mass flow rate and of the burner size were studied for the  $\text{H}_2/\text{air}$  flame. Their effects on flame temperature, flame position, scalar dissipation rate were investigated and plotted in Fig. 4. Four different burner radii were considered: 3.175 mm, 300  $\mu\text{m}$ , 75  $\mu\text{m}$  and 1  $\mu\text{m}$ .

At high mass flow rates, flame temperature and radius are independent of the burner radius. The flame temperature plateaus at about 2300 K for mass flow rates higher than 0.3 mg/s. Decreasing the mass flow rate reduces the flame radius, the flame moving closer to the burner. As the flow rate diminishes, the flame moves

closer to the burner to eventually being so close that any further decrease in mass flow rate does not change the flame position, the burner preventing the flame from moving inward. This is observed in Fig. 2 for the burner radius of 3.175 mm for mass flow rate lower than 0.1 mg/s. This has for effect to truncate the flame and to accelerate flame extinction.

Extinction is observed for a peak temperature of about 1300 K. This value is common for the four burner radii considered. Reducing the mass flow rate below 0.1 mg/s leads to a similar drop in peak temperature for burner radii of 1, 75 and 300  $\mu\text{m}$ . The 1  $\mu\text{m}$  radius burner does not affect the flame, as observed in Fig. 2, and thus can be taken as reference. Therefore, the mass flow rate of 3.49  $\mu\text{g/s}$  is the lowest mass flow rate possible regardless of burner size. The flame produced generates a heat release rate of 0.4 W, which is the weakest flame predicted numerically.

We aim to investigate the structure differences as the regime change from a well developed flame with a mass flow rate high enough to be free from the burner effects to a flame to a flame at the onset of extinction. Figure 2 represents the latter.

Figure 5 plots the temperature, local heat release rate and rate of progress, of main reactions, species net production rate and species distributions for a spherical diffusion flame of hydrogen issuing from a 3.175 mm radius burner at a rate of 10 mg/s into quiescent air. This flame is typical of a large and strong diffusion flame. This flow rate produces a relatively large diffusion flame, with a peak temperature of 2303 K located 22 cm from the burner center. The predicted heat release rate is 1275 W. The scalar dissipation rate at the peak temperature is 5.2e-6  $\text{s}^{-1}$ , characterizing a very low mixing rate, corresponding to a large Damköhler number. The high

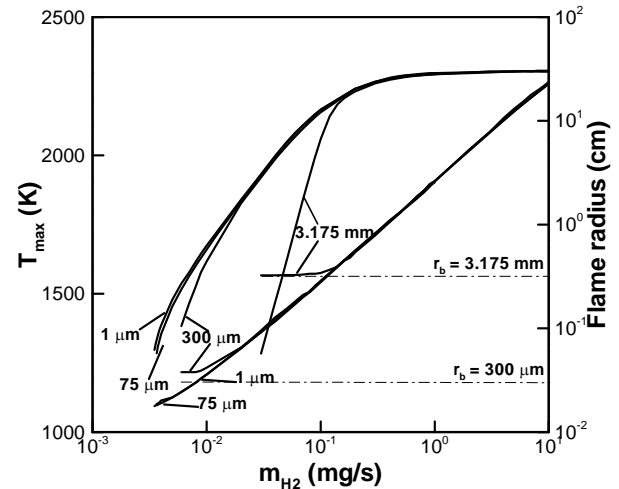


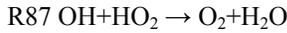
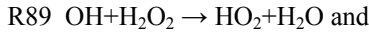
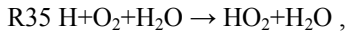
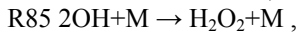
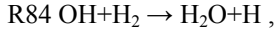
Fig. 4. Evolution of predicted  $\text{H}_2/\text{Air}$  flame temperature and flame radius with supplied mass flow rate issued from 3.175 mm, 300  $\mu\text{m}$ , 75  $\mu\text{m}$  and 1  $\mu\text{m}$  radius burners.

flow rate prevents the burner temperature from rising, keeping it constant at 300 K. The  $H_2$  and  $O_2$  concentrations near the reaction zone are very low, indicating negligible leakage of fuel or oxidizer.

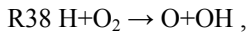
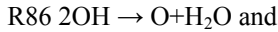
The overall heat release rate presents two peaks, instead of one as seen in Figs. 2 and 3. The bigger peak is near the location of peak temperature, while the smaller peak is close to the burner. The first peak corresponds to the location of water formation, with the reaction



as the major contributor. Other less important reactions at this location are the exothermic reactions

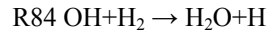


and the endothermic reactions

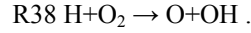


which is one of the most important branching reactions of

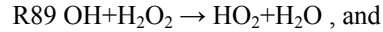
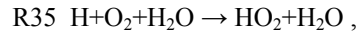
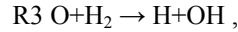
hydrogen-oxygen combustion. In terms of rate of progress, the importance of the reactions varies. Exothermic reaction



is the reaction having the highest rate of progress, followed by



The rate of progress of these two reactions is 4 times higher than the rate of progress of other reactions, namely



Molecular oxygen is consumed by reactions R35 and R38. Molecular hydrogen is consumed by reaction R84. The radical OH is consumed within the inner part of the flame and is produced in the outer part of the flame.

The smaller peak of heat release rate corresponds to the contributions of the reactions

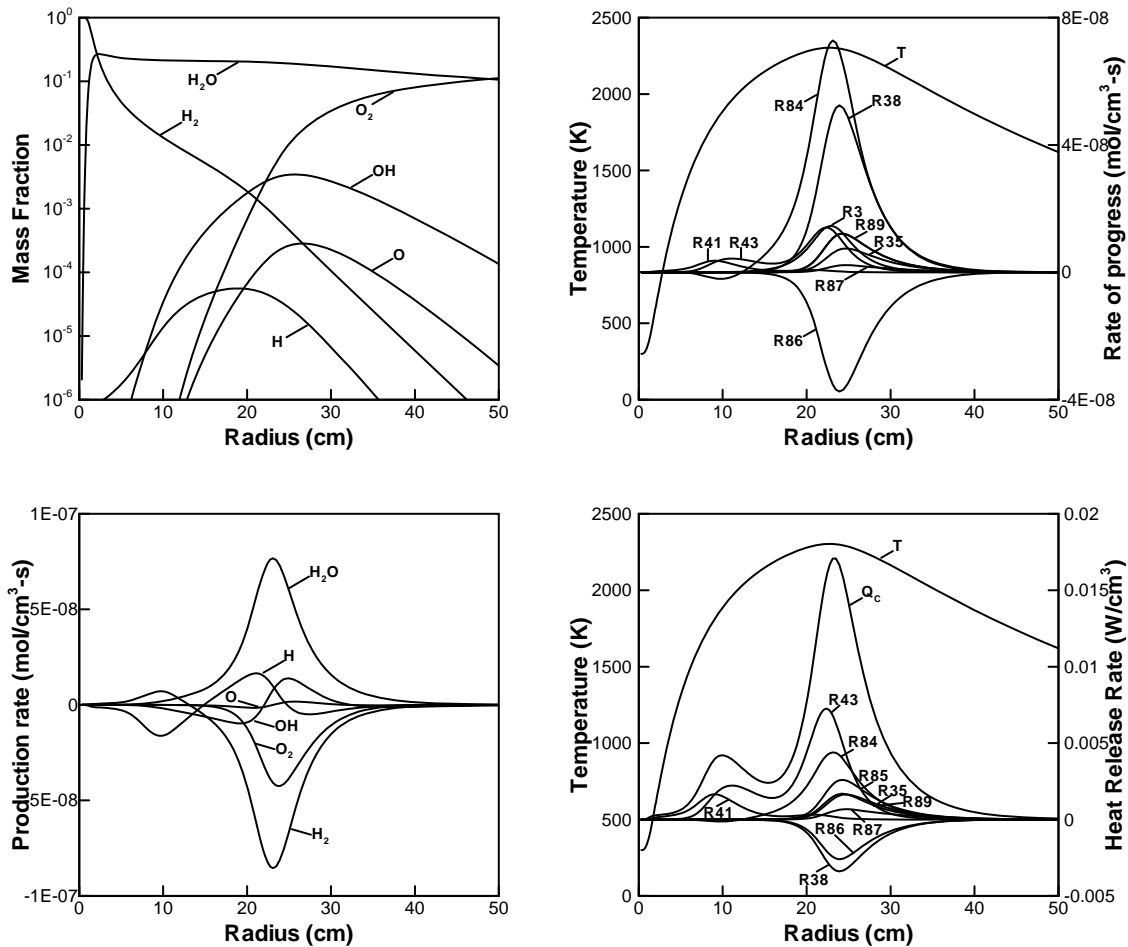
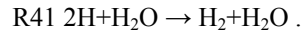
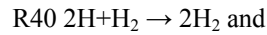


Fig. 5. From top left, clockwise, plot of the species mass fraction, elementary reactions rate of progress, elementary reactions heat release rate and species production rate for  $H_2$ /Air flame. Burner radius is 3.175 mm, supplied mass flow rate is set at 10 mg/s,  $Q_c$  is 1275 W.

At this location H radicals recombine into  $H_2$ . Hydrogen atom radical is mostly produced in the zone of high temperatures, with its production peaking near the flame location, located at a reasonable distance from its consumption location, implying that H radicals diffuse upstream before being recombined into  $H_2$ .

Figure 6 plots the temperatures, local heat release rates, rates of progress, species net production rates, and species distributions for a spherical diffusion flame of hydrogen issuing from a 3.175 mm radius burner at a rate of 0.1 mg/s into quiescent air. This flame is at the turning point of the burning regime and corresponds to the dramatic change of slope evident in Fig. 4.

This flame shows a different structure than the large and strong diffusion flame of Fig. 5. The flame in Fig. 6 has a peak temperature of 2059 K, which is far from the temperature observed at kinetic extinction, typically 1300 K for  $H_2$ /air. The predicted heat release rate is 12.52 W, which is still significant, compare to the flames of Figs. 2 and 3. The scalar dissipation rate at the peak temperature is  $1.6 \times 10^{-2} \text{ s}^{-1}$ , which is about four orders of

magnitude larger than the scalar dissipation rate observed at the reaction zone in Fig. 5.

The low flow rates of the flame in Fig. 6 induce profound changes on the flame structure. The flame is very close to the, the peak temperature being found about 400  $\mu\text{m}$  from the burner surface. The temperature profile of the flame is relatively flat, compared to the profiles exhibited by flames at the onset of kinetic extinction. Burner surface temperature is close to 2000 K.

Significant oxygen leakage is observed for this flame. The mass fraction of hydrogen is very low, less than 0.1%. This is less than the hydrogen mass fraction observed in Fig. 2, which is about 1%. The mass fraction of OH radical is high, about 10 times those of the  $H_2$ /air flames at the onset of kinetic extinction.

The heat release rate curve presents only 1 peak, which is located very close to the burner. This corresponds to the production of water and H radical. The main heat release rate exothermic contributors are reactions

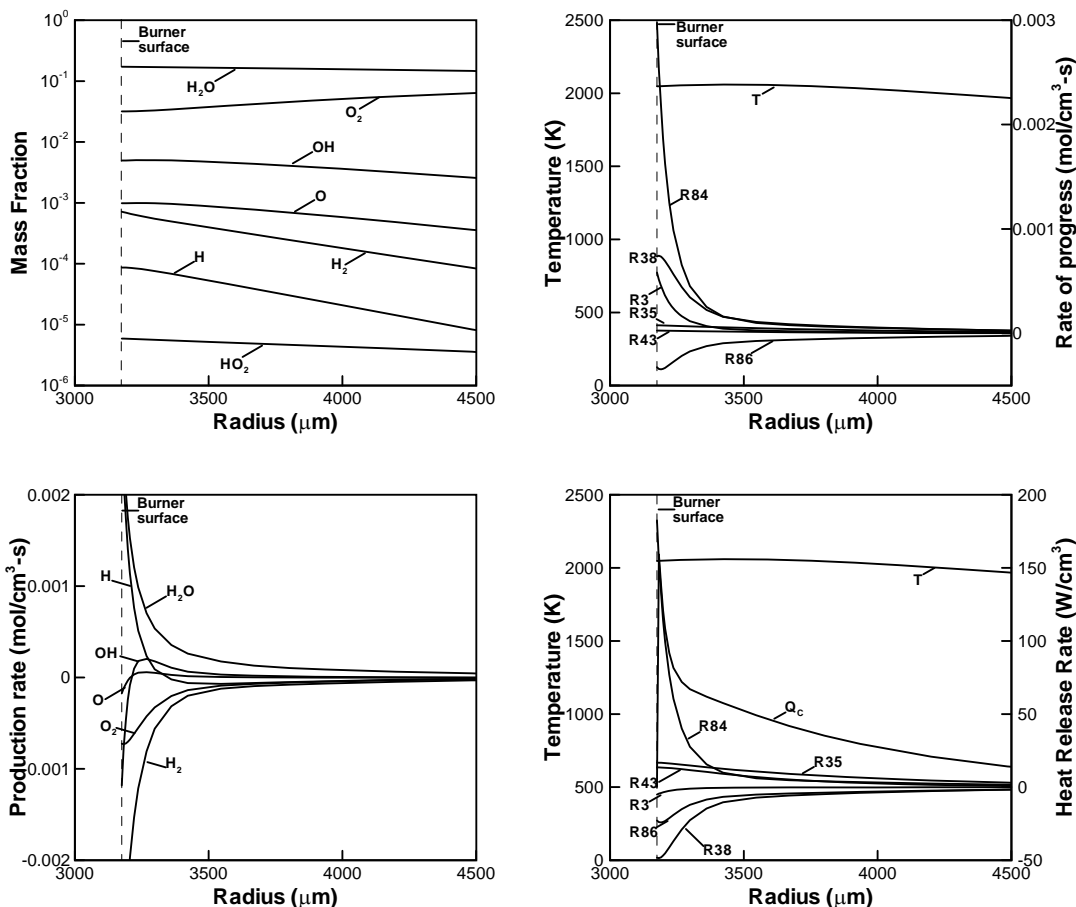
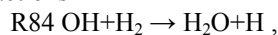


Fig. 6. From top left, clockwise, plot of the species mass fraction, elementary reactions rate of progress, elementary reactions heat release rate and species production rate for  $H_2$ /Air flame presenting important leakage. Burner radius is 3.175 mm, supplied mass flow rate is 100  $\mu\text{g/s}$ , and  $Q_c$  is 12.52 W.

R35  $\text{H}+\text{O}_2+\text{H}_2\text{O} \rightarrow \text{HO}_2+\text{H}_2\text{O}$  , and  
R43  $\text{H}+\text{OH}+\text{M} \rightarrow \text{H}_2\text{O}+\text{M}$  .

The main endothermic reactions are

R38  $\text{H}+\text{O}_2 \rightarrow \text{O}+\text{OH}$  ,  
R86  $2\text{OH} \rightarrow \text{O}+\text{H}_2\text{O}$  and  
R3  $\text{O}+\text{H}_2 \rightarrow \text{H}+\text{OH}$  .

Note that R86 has a negative rate of progress, while reaction R84 has the highest rate of progress. The dominant reactions remain the same as those for the strong diffusion flame shown in Fig. 5, although their rates are lower because the flame is truncated by the burner.

Kinetic extinction is achieved as the mass flow rate is gradually decreased. This diminishes the flame temperature and the flame radius, as seen in Fig. 4. This also increases the scalar dissipation rate at the flame location. The evolution of scalar dissipation rate with the mass flow rate can be observed in Fig. 7. The scalar dissipation rate is increased by a factor of  $10^6$  as the flow is decreased by a factor  $10^3$ .

Mills and Matalon [21] have shown that the reduced Damköhler number  $D_a$  for adiabatic spherical diffusion flame scales with the mass flow rate to the power two:

$$D_a \propto \dot{m}^2 \quad (10)$$

Therefore a decrease of mass flow rate leads to a decrease in Damköhler number, meaning that the characteristic time of transport is reduced to eventually be of the same order of magnitude as the chemistry time scale, leading to kinetic extinction.

Scalar dissipation rate scales as the inverse of a characteristic transport time. If one models the reaction rate with the Arrhenius law, the Damköhler number can be expressed by:

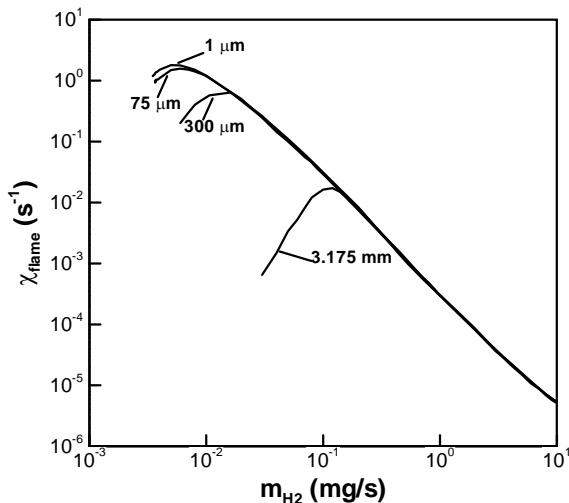


Fig. 7. Evolution of predicted scalar dissipation rate of  $\text{H}_2/\text{Air}$  flame with supplied mass flow rate issued from 3.175 mm, 300  $\mu\text{m}$ , 75  $\mu\text{m}$  and 1  $\mu\text{m}$  radius burners.

$$D_a \propto \chi_{st}^{-1} \exp\left(-\frac{E_a}{RT_{ad}}\right) , \quad (11)$$

where  $E_a$  is energy of activation,  $T_{ad}$  is the adiabatic flame temperature and  $R$  the universal gas constant.

Because reducing the mass flow affects only the scalar dissipation rate, we can write:

$$\chi_{st} \propto \dot{m}^{-2} , \quad (12)$$

This is the trend observed in Fig. 7.

Plotting the peak temperature against the scalar dissipation rate yields a S-curve as illustrated in Fig. 8. At low scalar dissipation rates, the peak temperature remains constant and nearly equal to the adiabatic  $\text{H}_2/\text{air}$  flame temperature. At this point, there is no reactant leakage across the flame.

Reducing the mass flow rate leads to an increase of scalar dissipation rate and hence to a decrease of the Damköhler number. When the scalar dissipation rate is greater than  $10^{-3} \text{ s}^{-1}$ , the flame peak temperature starts to diminish. Increasing the scalar dissipation rate leads to flame size reductions.

At some point the flame cannot move closer to the burner even when the mass flow decreases. When this occurs, the flame position is not affected by diminishing the mass flow rate. However this decreases the velocity at the flame location, decreasing the strength of the mixing and thus the value of the scalar dissipation rate. This creates this backward branch, which can be taken as the middle branch of the S-curve. This part of the curve corresponds to a flame structure with an important oxidizer leakage, as seen in Fig. 6. The smaller burners present oxidizer leakage, but in lesser rates. For the smallest burner considered, quenching occurs at the turning point of the S-curve, presenting the highest scalar dissipation rate, characteristic of kinetic extinction.

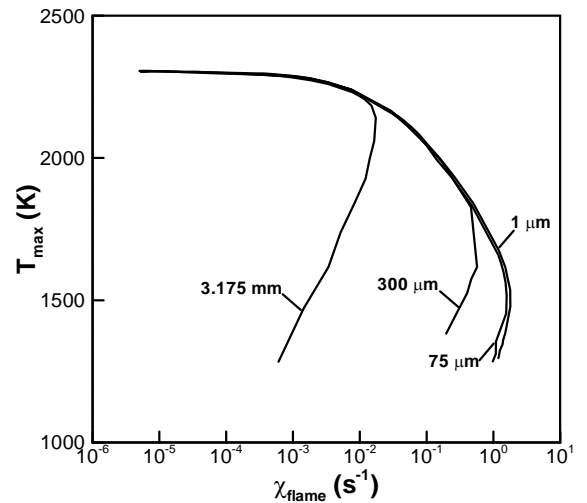


Fig. 8. Evolution of predicted peak temperature of  $\text{H}_2/\text{Air}$  flame with scalar dissipation rate at flame location for 3.175 mm, 300  $\mu\text{m}$ , 75  $\mu\text{m}$  and 1  $\mu\text{m}$  burner radii.

## Conclusions

Hydrogen micro flames were studied both experimentally and numerically based on a spherical model. The weakest flames observed experimentally have mass flow rates as low as 3.9  $\mu\text{g/s}$  for the  $\text{H}_2/\text{air}$  flames and 2.1  $\mu\text{g/s}$  for the  $\text{H}_2/\text{O}_2$  flames, corresponding to heat release rates of 0.46 and 0.25 W, respectively.

The weakest flames observed numerically, with a burner radius matching the experimental dimension, have mass flow rates of 3.65  $\mu\text{g/s}$  for the  $\text{H}_2/\text{air}$  flame and 2.67  $\mu\text{g/s}$  for the  $\text{H}_2/\text{O}_2$  flame, corresponding to heat release rates of 0.4 and 0.31 W, respectively. They are in reasonable agreement with the measured quenching limits.

Kinetic extinction, arising from hydrogen flow rate reduction, was numerically observed for adiabatic flames. For the larger burners, the presence of the burner prevents the flames from moving inward when flow rate is reduced, resulting in truncated flames. This yields extinction at higher flow rates even under adiabatic conditions and high rates of oxidizer leakage across the flame.

The flames are predicted to extinguish at high level of scalar dissipation rate, of about  $1 \text{ s}^{-1}$  for  $\text{H}_2/\text{air}$  flames and  $2 \text{ s}^{-1}$  for  $\text{H}_2/\text{O}_2$  flames, which is a factor of  $10^6$  higher than for the  $\text{H}_2/\text{air}$  diffusion flame at highest flow rate considered. Because heat losses are neglected in this study, the flames predicted are at the onset of kinetic extinction.

The main reactions contributing to the flame heat release rate differ with the Damköhler number. Flames with high Damköhler number present a double peaked heat release rate profile. The main exothermic reactions are, in order of contribution to the heat release rate: the chain terminating reaction  $\text{H}+\text{OH}+\text{M} \rightarrow \text{H}_2\text{O}+\text{M}$  and the chain propagating reaction  $\text{OH}+\text{H}_2 \rightarrow \text{H}_2\text{O}+\text{H}$  for the bigger peak and the chain-terminating reaction  $2\text{H}+\text{H}_2\text{O} \rightarrow \text{H}_2+\text{H}_2\text{O}$  and the chain propagating reaction  $\text{OH}+\text{H}_2 \rightarrow \text{H}_2\text{O}+\text{H}$  for the smaller peak.

Flames with low Damköhler number do not present a double peaked heat release rate profile but a single peak profile, with the maximum heat release rate close to the burner. The main exothermic reactions are, in order of contribution to the heat release rate: the chain propagating reactions  $\text{H}+\text{O}_2+\text{H}_2\text{O} \rightarrow \text{HO}_2+\text{H}_2\text{O}$  and  $\text{OH}+\text{H}_2 \rightarrow \text{H}_2\text{O}+\text{H}$ , and the chain-branching reaction  $\text{H}+\text{HO}_2 \rightarrow 2\text{OH}$ . The hydroperoxy radical ( $\text{HO}_2$ ) plays an important role in those flames.

The main endothermic reaction, which absorbs a part of the heat released by exothermic reactions, is the chain-branching reaction  $\text{H}+\text{O}_2 \rightarrow \text{O}+\text{OH}$ . Its contribution remains the same regardless of the Damköhler number.

## Acknowledgments

This work was co-funded by the National Aeronautics and Space Administration (D.P. Stocker, technical contact) and by the National Institute of Standards and Technology (J. Yang, technical contact). The authors thank M.S. Butler for his help with the experiments.

## References

- [1] P.D. Ronney, <http://carambola.usc.edu/Research/MicroFIRE/>.
- [2] A. Carlos Fernandez-Pello, *Micropower generation using combustion: issued and approaches*. Proceedings of the Combustion Institute 29 (2002) pp. 883-899.
- [3] S.A. Jacobson, A.H. Epstein, *An informal survey of power MEMS*. The International Symposium on Micro-mechanical Engineering (2003)
- [4] Burke SP, Schuman. *Diffusion flames*. Ind. Eng. Chem. 20 (1928) 998-1004.
- [5] Roper FG. *The prediction of laminar jet diffusion flame sizes: Part 1. Theoretical model*. Combust. Flame 29 (1977) 219-226.
- [6] H. Han, S. Venkatesh and K. Saito, *Convection-Diffusion Controlled Laminar Micro Flames*, Journal of Heat Transfer 954 (1994) pp. 954-959.
- [7] L.M. Matta, Y. Neumeir, B. Lemon and B.T. Zinn, *Characteristic of microscale diffusion flames*. Proceedings of the Combustion Institute 29 (2002) pp. 933-939.
- [8] T.S. Cheng, C.-P. Chen, C.-S. Chen, Y.-H. Li, C.-Y. Wu and Y.C. Chao, *Characteristics of Microjet methane diffusion flames*. Combust. Sci. and Tech. 10 (2006) 861-881.
- [9] T.S. Cheng, Y.-C. Chao, C.-Y. Wu, Y.-H. Li, Y. Nakamura, K.-Y. Lee, T. Yuan, T.S. Leu, *Experimental and numerical investigation of microscale hydrogen diffusion flames*. Proceedings of the Combustion Institute 30 (2005) pp. 2489-2497.
- [10] Nakamura Y, Yamashita H, Saito K. *A numerical study on extinction behaviour of laminar microdiffusion flames*. Combustion Theory and Modeling 10 (2006) 927-938.
- [11] P.D. Ronney, M.S. Wu, K.J. Weiland and H.G. Pearlman, *Flame Ball Experiments in Space: Preliminary Results from STS-83*. AIAA Journal 36 (1998) 1361-1368.
- [12] M.S. Butler, C.W. Moran, P.B. Sunderland, R.L. Axelbaum, *Flame Quenching Limits of Hydrogen Leaks*, Int. J. Hydrogen Energy, submitted.
- [13] B.J. Lee, S.H. Chung, *Stabilization of Lifted Tribrachial Flames in Nonpremixed Jet*. Combust. Flame 109 (1997) 163-172.
- [14] R.J. Kee, J.F. Gear, M.D. Smooke, J.A. Miller, E. Meeks, *A program for modeling steady, laminar,*

- one-dimensional premixed flames*, Sandia National Laboratories Report No. SAND85-8240 1987.
- [15] R.J. Kee, F.M. Rupley, J.A. Miller, E. Meeks, *CHEMKIN-III: A Fortran Chemical Kinetics Package for the analysis of Gasphase Chemical and Plasma Kinetics*, Sandia National Laboratories Report No.SAND96-8216.
- [16] J.F. Grcar, *The twopoint program for boundary value problems*. SAND91- 8230, Sandia National Laboratories (1996).
- [17] R.J. Kee, G. Dixon-Lewis, J. Warnatz, M.E. Coltrin, J.A. Miller, *A Fortran Computer Code Package for the Evaluation of Gas Phase Multicomponent Transport Properties*. Report SAND86-8246, Sandia National Laboratories (1988).
- [18] Gregory P. Smith, David M. Golden, Michael Frenklach, Nigel W. Moriarty, Boris Eiteneer, Mikhail Goldenberg, C. Thomas Bowman, Ronald K. Hanson, Soonho Song, William C. Gardiner, Jr., Vitali V. Lissianski, and Zhiwei Qin [http://www.me.berkeley.edu/gri\\_mech/](http://www.me.berkeley.edu/gri_mech/)
- [19] K.J. Santa, Z. Sun, B.H. Chao, P.B. Sunderland, R.L. Axelbaum, D.L. Urban, D.P. Stocker, *Numerical and experimental observations of spherical diffusion flames*, Combust. Theory and Modelling 11 (2007) 639-652.
- [20] T.S. Cheng, C.-Y. Wu, C.-P. Chen, Y.-H. Li, Y.-C. Chao, T. Yuan, T.S. Leu, *Detailed measurements and assessment of laminar hydrogen jet diffusion flames*. Combust. Flame 146 (2006) 268.
- [21] K. Mills, M. Mantalon, *Burner Generated Spherical Diffusion Flames*. Combust. Sci. and Tech. 129 (1997) 295-319.

## ABSTRACT

Title of Document: AN ASYMPTOTIC ANALYSIS OF  
SPONTANEOUS IGNITION OF HYDROGEN  
JETS

Kian Boon Lim, M.S., 2007

Directed By: Assistant Professor Peter B. Sunderland,  
Department Of Fire Protection Engineering

Analytical work is presented for the spontaneous ignition of a hydrogen jet emanating from a slot into air. A similarity solution of the flowfield was obtained. This was combined with the species and energy conservation equations, which were solved using activation energy asymptotics. Limits of spontaneous ignition were identified as functions of slot width, flow rate, and temperatures of the hydrogen jet and ambient air. Two scenarios are examined: a cool jet flowing into a hot ambient and a hot jet flowing into a cool ambient. For both scenarios, ignition is favored with an increase of either the ambient temperature or the hydrogen supply temperature. Moreover, for the hot ambient scenario, a decrease in local fuel Lewis number also promotes ignition. The Lewis number of the oxidizer only has a weak effect on ignition. Because spontaneous ignition is very sensitive to temperature, ignition is predicted to occur near the edge of the jet if the hydrogen is cooler than the air and on the centerline if the hydrogen is hotter than the air.

AN ASYMPTOTIC ANALYSIS OF SPONTANEOUS IGNITION  
OF HYDROGEN JETS

By

KIAN BOON LIM

Thesis submitted to the Faculty of the Graduate School of the  
University of Maryland, College Park, in partial fulfillment  
of the requirements for the degree of  
Master of Science  
2007

Advisory Committee:  
Peter B. Sunderland, Chair  
André W. Marshall  
Arnaud C. Trouvé

© Copyright by  
Kian Boon Lim  
2007

## Dedication

To my dearest wife Jolene and precious son Zaccaeus. And to God, for His grace and providence, and for watching over me every step of the way.

## Acknowledgements

This work was supported by NIST under grant 60NANB5D1209, the Fulbright Fellowship program under grant number 15052695, and the sponsorship of the Singapore Civil Defense Force.

First and foremost, I would like to express my heartfelt gratitude to Professor Peter Sunderland, my advisor, for his guidance, encouragement and genuine concern throughout my stay in UMD. His progressive thinking and openness has certainly made things so much easier. He is certainly the coolest Professor that I have the privilege of working with. Special thanks also to Professor Beei-Huan Chao, from the University of Hawaii, for his patience and guidance for the research work. I cannot imagine getting through the mind-boggling and complex mathematics and derivations without his great help. It is indeed an honor to learn from the Master himself. Also thanks to Professor Richard Axelbaum, from Washington University in Missouri, for his insights and comments on my work, which helped in refining and enhancing this thesis.

I would also like to thank my advisory committee, Professor Arnaud Trouvé and Professor André Marshall for their valuable time and suggestions.

My sincere thanks to Vivien Lecoustre “The French Meister” for the help he had given for my research, the French that he taught me (*quelle belle langue*), and the friendship we have forged.

# Table of Contents

Dedication .....	iv
Acknowledgements .....	v
Table of Contents .....	vi
List of Tables .....	vii
List of Figures .....	viii
Nomenclature .....	xi
Chapter 1: Introduction .....	1
1.1 Motivation for Project .....	1
1.2 Literature Review .....	1
1.3 Combustion S-curve .....	3
1.4 Activation Energy Asymptotics .....	4
1.5 Project Objectives .....	7
Chapter 2: Formulation .....	8
2.1 Introduction .....	8
2.2 Assumptions .....	9
2.2 Assumptions .....	10
2.3 Slot Flowfield .....	10
2.4 Conservation Equations and Boundary Conditions in the Jet .....	13
2.5 Coordinate Transformation and the Solution of Momentum Equation .....	14
2.6 Nondimensionalizing the Energy and Species Equations .....	19
2.7 Frozen Solution .....	22
2.8 Summary of Formulation .....	24
Chapter 3: Ignition Analysis .....	25
3.1 Description of Analysis .....	25
3.2 Ignition Analysis I : $T_\infty > T_0$ , $Le_F < 1$ .....	25
3.3 Ignition Analysis II : $T_\infty > T_0$ , $Le_F \approx 1$ .....	34
3.4 Ignition Analysis III : $T_0 > T_\infty$ , $\tilde{x} \approx 1$ , Thicker Reaction Region .....	38
3.5 Analysis Scenarios .....	43
Chapter 4: Results and Discussions .....	47
4.1 Recapitulation .....	47
4.2 Cool jet flowing into a hot ambient ( $T_\infty > T_0$ ) .....	47
4.2.1 Ignition states that separate the ignitable and non-flammable regions ....	51
4.3 Hot jet flowing into a cool ambient ( $T_0 > T_\infty$ ) .....	54
4.3.1 Ignition states that separate the ignitable and non-flammable regions ....	60
Chapter 5: Conclusions .....	61
Chapter 5: Conclusions .....	62
5.1 Conclusions .....	62
Bibliography .....	64

## List of Tables

Table 1	Values of $\alpha$ and specific heat of combustion ( $q_F$ ) from [4].	49
---------	--	----

## List of Figures

Fig. 1.1	Combustion S-Curve reproduced from [18]	4
Fig. 2.1	Schematic of slot and hydrogen leak for the hot ambient case	9
Fig. 2.2	Schematic of slot and hydrogen leak for the hot jet case	9
Fig. 3.1	Schematic of inner and outer regions for the hot ambient case	43
Fig. 3.2	Schematic of inner and outer regions for the hot jet case	45
Fig. 4.1	$a_T$ versus $\tilde{D}a$ for varying $\alpha$ (which is changed by variations in $\tilde{T}_0$ or $\tilde{Y}_{F,0}$ ), with $Le_F = 0.6$ and constant $\tilde{T}_\infty = 0.0123$ , hot ambient.	48
Fig. 4.2	Rescaled plot of $\hat{a}_T$ versus $\hat{D}a$ (rescaled $\tilde{D}a$ values due to changes in $\tilde{T}_\infty$ ) for varying $\alpha$ (which is changed by variations in $\tilde{T}_\infty$ ), with $Le_F = 0.6$ , $\tilde{T}_0 = 0.00226$ , $\tilde{E} = 1.79$ , $\tilde{Y}_{F,0} = 1$ , and $\alpha = 0.01$ as reference value, hot ambient.	50
Fig. 4.3	$a_T$ versus $\hat{D}a$ (rescaled $\tilde{D}a$ values due to changes in $Le_F$ ) for varying $Le_F$ , with $\alpha = 0.02$ , $\tilde{T}_0 = 0.00226$ , and $\tilde{E} = 1.79$ , hot ambient.	51
Fig. 4.4	$\alpha$ (which is changed by variations in $\tilde{T}_0$ or $\tilde{Y}_{F,0}$ ) versus $\hat{D}a$ (rescaled $\tilde{D}a$ values due to changes in $Le_F$ ) for varying $Le_F$ , with $Le_F = 1$ as reference and constant $\tilde{T}_\infty = 0.0123$ , hot ambient.	52
Fig. 4.5	$\alpha$ (which is changed by variations in $\tilde{T}_\infty$ ) versus $\hat{D}a$ (rescaled $\tilde{D}a$ values due to changes in $\tilde{T}_\infty$ ) for varying $Le_F$ , and $\tilde{T}_0$	

	= 0.00226, hot ambient.	53
Fig. 4.6	$\alpha$ (which is changed by variations in $\tilde{T}_\infty$ ) versus $\hat{D}\tilde{a}$ (rescaled $\tilde{D}a$ values due to changes in $\tilde{T}_\infty$ ) for varying $n_o$ at $Le_F = 1$ and $\tilde{T}_0 = 0.00226$ , hot ambient.	53
Fig. 4.7	$\theta_{\max}$ versus $\tilde{D}\tilde{a}$ for varying $\beta$ (which is changed by variations in $\tilde{T}_\infty$ or $\tilde{Y}_{O,\infty}$ ) at $Le_o = 1$ and constant $\tilde{T}_0 = 0.0388$ , hot jet.	54
Fig. 4.8	$X$ versus $\tilde{D}\tilde{a}$ for varying $\beta$ (which is changed by variations in $\tilde{T}_\infty$ or $\tilde{Y}_{O,\infty}$ ), with $Le_o = 1$ and constant $\tilde{T}_0 = 0.0388$ , hot jet.	55
Fig. 4.9	Rescaled plot of $\hat{\theta}_{\max}$ versus $\hat{D}\tilde{a}$ (rescaled $\tilde{D}a$ values due to changes in $\tilde{T}_0$ ) for varying $\beta$ (which is changed by variations in $\tilde{T}_0$ ), with $Le_o = 1$ , $\tilde{T}_\infty = 0.0358$ , $\tilde{E} = 1.79$ , $\tilde{Y}_{O,\infty} = 0.029$ , and $\beta = 0.1$ as reference value, hot jet.	57
Fig. 4.10	$X$ versus $\hat{D}\tilde{a}$ (rescaled $\tilde{D}a$ values due to changes in $\tilde{T}_0$ ) for varying $\beta$ (which is changed by variations in $\tilde{T}_0$ ), with $Le_o = 1$ , $\tilde{T}_\infty = 0.0358$ , $\tilde{E} = 1.79$ , $\tilde{Y}_{O,\infty} = 0.029$ , and $\beta = 0.1$ as reference value, hot jet.	58
Fig. 4.11	$\theta_{\max}$ versus $\tilde{D}\tilde{a}$ for varying $Le_o$ , with $\beta = 0.3$ , and constant $\tilde{T}_0 = 0.0388$ , hot jet.	59
Fig. 4.12	$X$ versus $\tilde{D}\tilde{a}$ for varying $Le_o$ , with $\beta = 0.3$ , and constant $\tilde{T}_0 = 0.0388$ , hot jet.	60
Fig. 4.13	$\beta$ (which is changed by variations in $\tilde{T}_\infty$ or $\tilde{Y}_{O,\infty}$ ) versus $\tilde{D}\tilde{a}$ for varying $n_o$ , and constant $\tilde{T}_0 = 0.0388$ , hot jet.	61

Fig. 4.14  $\beta$  (which is changed by variations in  $\tilde{T}_0$ ) versus  $\hat{Da}$  (rescaled  $\tilde{Da}$  values due to changes in  $\tilde{T}_0$ ) for varying  $n_o$ , with  $Le_o = 1$ ,  $\tilde{T}_\infty = 0.0358$ ,  $\tilde{E} = 1.79$ ,  $\tilde{Y}_{O_\infty} = 0.029$ , and  $\beta = 0.1$  as reference value, hot jet.

61

## Nomenclature

$a_T$	constant representing the temperature increase through reaction
$B$	pre-exponential factor
$c_j$	molar concentration of species $j$
$c_p$	specific heat at constant pressure
$c_v$	specific heat at constant volume
$Da$	Damköhler number
$\tilde{Da}$	reduced Damköhler number; flow time divided by chemical time
$Da_E$	Damköhler number at extinction
$Da_I$	Damköhler number at ignition
$D_j$	mass diffusion coefficient of species $j$
$E$	extinction state (when used in Fig.1)
$E$	activation temperature
$F$	fuel
$f$	nondimensional stream function
$h$	half width of the slot
$I$	ignition state
$Le_j$	local Lewis number of species $j$ ; thermal diffusivity of mixture divided by mass diffusivity of species $j$ into mixture
$\ell_F$	perturbation of the fuel Lewis number from unity

$M$	linear momentum per unit depth of the slot
$O$	oxidizer
$p$	pressure
$p_a$	atmospheric pressure
$P$	combustion products
$Pr$	local Prandtl number; mixture viscosity divided by mixture thermal diffusivity
$q_F$	heat of combustion per unit mass of the fuel
$R$	ideal gas constant ( $R^\circ/W^*$ )
$R^\circ$	universal gas constant
$Sc_j$	local Schmidt number of species $j$ ; mixture viscosity divided by mass diffusivity of species $j$ into mixture
$T$	temperature
$u$	flow velocity in the $x$ (streamwise) direction
$v$	flow velocity in the $y$ (transverse) direction
$w$	thickness of the wall
$W^*$	average molecular weight
$W_j$	molecular weight of species $j$
$x$	streamwise spatial coordinate
$x_0$	distance between the virtual origin of the jet to the exit of the slot
$y$	transverse spatial coordinate ( $y = 0$ on the plane of symmetry)
$Y_j$	mass fraction of species $j$

## Greek Symbols

- $\alpha$  parameter defined as  $\alpha = (\tilde{T}_\infty - \tilde{T}_0) / \tilde{Y}_{F0}$
- $\beta$  parameter defined as  $\beta = (\tilde{T}_0 - \tilde{T}_\infty) / \tilde{Y}_{O,\infty}$
- $\varepsilon$  small parameter, defined as  $\varepsilon = \tilde{T}_\infty^2 / \tilde{E}$ , used for asymptotic expansion
- $\phi_F$  perturbation of fuel concentration in the inner, reaction region (because of the weak reaction)
- $\Phi_F$  perturbation of fuel concentration in the outer, chemically inert region (because of the weak reaction)
- $\phi_O$  perturbation of oxidizer concentration in the inner, reaction region
- $\Phi_O$  perturbation of oxidizer concentration in the outer, chemically inert region (because of the weak reaction)
- $\gamma$  specific heat ratio ( $c_p/c_v$ )
- $\eta$  similarity variable
- $\lambda$  thermal conductivity
- $\mu$  dynamic viscosity
- $\nu_j$  stoichiometric coefficient of species  $j$
- $\theta$  perturbation of temperature in the inner, reaction region (because of the weak reaction)
- $\Theta$  perturbation of temperature in the outer, chemically inert region (because of the weak reaction)

$\rho$	gas density
$\sigma$	parameter defined as $\sigma = \tilde{Y}_{F,0} / \tilde{x}^{1/3}$
$\omega$	reaction rate function
$\xi$	spatial coordinate defined as $\xi = \text{sech}^2 \eta$
$\psi$	streamfunction
$\zeta$	stretched spatial coordinate in the inner, reaction region (inner variable)
$\bar{\zeta}$	rescaled inner spatial coordinate defined as $\bar{\zeta} = \sigma \zeta$

### Subscripts

$0$	value of variables at the exit of the slot
$f$	frozen solution
$F$	fuel
$i$	value of variables in the fuel supply
$O$	oxidizer
$P$	combustion products
$T$	temperature
$\infty$	value of variables at the ambient

### Superscripts

$n_j$	reaction order of species $j$
$\sim$	nondimensional quantity
$\wedge$	rescaled nondimensional quantity

# Chapter 1: Introduction

## 1.1 Motivation for Project

Concerns about the emissions of greenhouse gases have led to extensive consideration of hydrogen as a major fuel carrier. Hydrogen presents several unusual fire hazards, including high leak propensity, ease of ignition, and invisible flames. Heated air jets flowing into hydrogen ignite spontaneously at an air temperature of 943 K [1]. This is cooler than for most other fuels [2,3], including gasoline and methane, and is not much higher than the autoignition temperature of stoichiometric hydrogen/air mixtures, 858 K [4]. Occasional unintended hydrogen leaks will be unavoidable, and some may involve heated hydrogen and/or air. Thus an improved understanding of limits of spontaneous ignition of hydrogen jets is sought here, with the aid of activation-energy asymptotics.

## 1.2 Literature Review

Asymptotic flame theories can provide valuable insights into combustion reactions [5-7]. Quantitative and predictive derivations can be made using the concept of distinguished limits in activation energy asymptotics. Based largely on the concept of Zel'dovich number, asymptotic analysis enables derivation and establishing of temperature effects on reaction rates despite the narrowness of the reaction zone relative to the preheat zone of the laminar flame structure.

Im et al. [8,9] analyzed thermal ignition in supersonic hydrogen/air mixing layers and obtained ignition characteristics over a wide range of conditions. The findings were however based on reduced mechanisms and supersonic flows, which are more

applicable for scramjets. An investigation of different combustion regimes by Damköhler-number and activation-energy asymptotics in a stagnant mixing layer, based on an eight-step reduced mechanisms was performed by Lee and Chung [10]. Helenbrook and Law investigated the ignition of hydrogen/air mixing layer with reduced reaction mechanisms which they developed [11,12]. However, no single-step reaction mechanism was developed. Compared to a single-step, overall, irreversible reaction with second order Arrhenius kinetics and a high activation energy (which was used in the research), the reduced mechanism has different assumptions in length scales in determining the reaction rates, which will yield different results with emphasis on temperature dependence for thermal runaway. This is because the emphasis for reduced mechanisms is on the role of chemical kinetic mechanisms, involving chain-branching and termination reactions, in effecting a non-linear feedback in the concentrations of certain radicals and consequently, thermal runaway.

Zheng and Law [13] identified ignition limits of premixed hydrogen-air flames where ignition was by heated counterflow. Ignition limits of non-premixed hydrogen-air flames from jets will be different because of the non-premixed combustion mode and the absence of strain due to counterflow heating. Toro et al. [14] examined in detail the structure of laminar hydrogen jet flames both experimentally and numerically. For completeness, analytical results should be obtained to enable comparison with experimental and numerical results, under the same conditions and scenarios. Chaos et al. [15] examined Lewis-number effects in unsteady laminar hydrogen jet flames, which will have different effects compared to a steady laminar hydrogen jet flame. Liu and Pei [16] examined autoignition and explosion limits of

hydrogen-oxygen mixtures in homogenous systems, which involved reduced mechanisms. Dryer et al. [17] examined spontaneous ignition of pressurized releases of hydrogen and natural gas into air, which investigated multi-dimensional transient flows involving shock formation, reflection and interactions which resulted in the transition to turbulent jet diffusive combustion. This is a different aspect of risk associated with rapid failures of compressed storages, as compared to the scenario being considered here, involving small leaks/cracks that are undetected, and that ignite spontaneously when the limits are reached.

### 1.3 Combustion S-curve

In understanding and analyzing the limits of spontaneous ignition of hydrogen jets, it is important to appreciate the fundamentals of flame ignition and extinction, which can be characterized and explained by the famous combustion S-curve [5,7,18]. The S-curve, as shown in Fig. 1.1, comprises 3 branches, the lower, middle and upper branches. The y-axis represents the reaction temperature, and the x-axis represents the Damköhler-number ( $Da$ ). Starting with the left end of the lower branch, at  $Da = 0$ , we have the chemically frozen flow limit. By increasing  $Da$  along this branch, every possible weakly reacting state that the system can have was covered.  $Da_I$  represents the ignition  $Da$ , at which weak reactions transition to vigorous burning with a sudden jump to the upper branch. Anywhere beyond this  $Da$  will result in spontaneous combustion. We define this point as the ignition state. Conversely, as we decrease the  $Da$  for an intense burning flame on the upper branch to the point  $Da_E$ , there will be another jump of the temperature down to the lower branch. This point is defined as the extinction  $Da$ .

Physically, the existence of turning points implies that there exist states for which the chemical reaction rate cannot balance the heat transport rate in steady state. Thus for the lower branch, beyond  $Da_I$ , the chemical heat is generated so fast in the reaction zone that it cannot be transported away in steady manner. The middle branch is never observed because it has a negative slope which implies that reaction temperature decreases as  $Da$  increases, which is physically unrealistic.

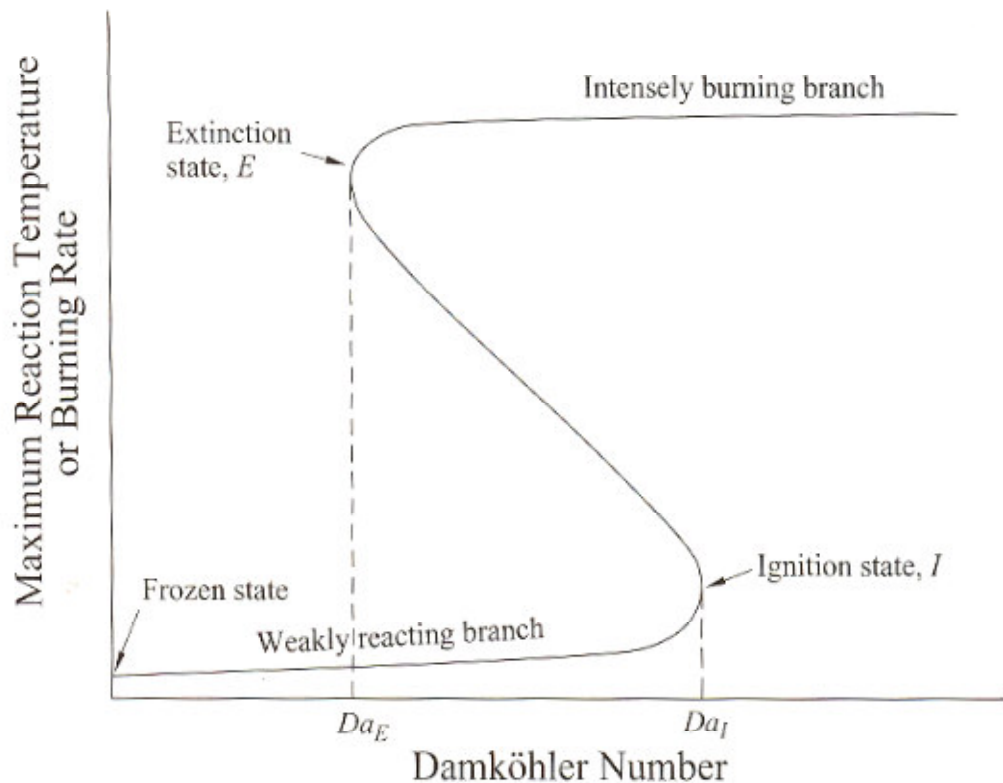


**Fig. 1.1: Combustion S-Curve reproduced from [18].**

#### 1.4 Activation Energy Asymptotics

There are a number of possible approaches to modeling the influences of finite-rate chemistry on diffusion flames. Known rates of elementary reaction steps may be employed in the full set of conservation equations, with solutions sought by

numerical integration and computational fluid dynamics (CFD). While CFD is like an experiment, with only one condition considered at a time, other modeling such as activation-energy asymptotics (AEA) can quickly identify trends and give additional physical insights. Complexities of diffusion flame problems motivates searches for simplifications of the chemical kinetics [19]. With simplified chemical kinetics, perturbation methods [20] are attractive for improving understanding and also for seeking quantitative comparison with experiment results. Two types of perturbation approaches have been developed, Damköhler-number asymptotics and AEA. In the former, the ratio of a flow time to reaction time, one of the dimensionless groups introduced by Damköhler [21] is treated as a large parameter. And in the latter, the ratio of the activation energy to the thermal energy, emphasized as important by Frank-Kamenetskii [22], is taken to be large. Damköhler-number asymptotics can provide estimates of reaction zone broadening in near-equilibrium situations [23,24], and also affords possibilities of investigating other regimes [25].

Analyses of phenomena such as sharp ignition and extinction events cannot be performed on the basis of Damköhler-number asymptotics, but they can be treated by activation-energy asymptotics. Moreover, activation-energy asymptotics may lead to results valid for all Damköhler numbers, and therefore results of Damköhler-number asymptotics may be extracted from those of activation-energy asymptotics. Activation-energy asymptotics is the more general of the two types of perturbation approaches. As compared to CFD, AEA was selected for our study as it provides the complete physics of the problem instead of just providing exact solutions for

individual points, and provides a good representation of trends and limit behavior, which is sought here.

In the research, the AEA approach which was adopted to derive the exact solutions to the Navier-Stokes Equations can be summarized as:

- 1) Solutions of the flowfield for the scenario of hydrogen jet emanating from a rectangular slot were derived. A similarity solution of the non-reacting flowfield is obtained, and then used in the energy and species conservation equations. Coordinate transformation is necessary to investigate the effects of perturbations because the reaction zone of concern is a very small thin one.
- 2) Frozen solutions were then obtained. These represent the solutions in very low  $Da$  regime whereby there are no reactions.
- 3) Outer solutions were derived. These solutions deviate from the frozen solution by a small amount due to perturbation, and are present in outer regions where there is no reaction due to the low temperature. Before ignition, there are only weak reactions.
- 4) Inner solutions were derived for the reaction zone where weak chemical reactions occur.
- 5) Matching of inner and outer solutions is then performed to determine the conditions whereby ignition can occur. Ignition can occur when the heat generated from the chemical reaction is sufficient to overcome heat losses. The results are presented in terms of  $Da$ ,  $T_o$ ,  $T_\infty$ ,  $Le_F$ , and  $Le_o$ .

### 1.5 Project Objectives

The present analysis considers the spontaneous ignition of a jet of hydrogen or other gaseous fuel leaking through a slot into air. The slot is taken to be straight and long, yielding a two-dimensional flow field. The ignition analysis identifies limits of spontaneous ignition.

The objectives of this work are to:

- 1) develop a model of spontaneous ignition for two cases: a cool fuel jet flowing into heated air and a heated fuel jet flowing into cool air,
- 2) identify limits of spontaneous ignition as functions of slot width, flow rate, fuel Lewis number, and temperatures of the fuel jet and the ambient air, and
- 3) identify the location of ignition.

## Chapter 2: Formulation

### 2.1 Introduction

The problem of interest is a steady, isobaric laminar jet of fuel (e.g. hydrogen) at temperature  $T_0$  issuing from a rectangular slot into an oxidizing environment (e.g. atmospheric air) at a temperature of  $T_\infty$ , as shown schematically in Figs. 2.1 and 2.2 for the two scenarios. Spontaneous ignition occurs when either  $T_0$  or  $T_\infty$  is sufficiently high that the weak reaction between the fuel and the oxidizer transitions to a vigorous burning flame. This study analyzes the ignition state as a function of various physical properties including Lewis number,  $T_0$ ,  $T_\infty$ , the flow velocity at the slot exit,  $u_0$ , and the width of the slot. The slot is considered sufficiently long that end effects are negligible. The reaction chemistry is simulated by a single-step, overall, irreversible reaction with second order Arrhenius kinetics and a high activation energy.

The formulation that follows is an exact solution of the conservation of mass, momentum, energy and species. The key assumptions are boundary layer behavior ( $\frac{\partial}{\partial y} \gg \frac{\partial}{\partial x}$ ) and single-step chemistry. A similarity solution of the non-reacting flowfield is obtained. This is then used in the conservation of energy and species equations.

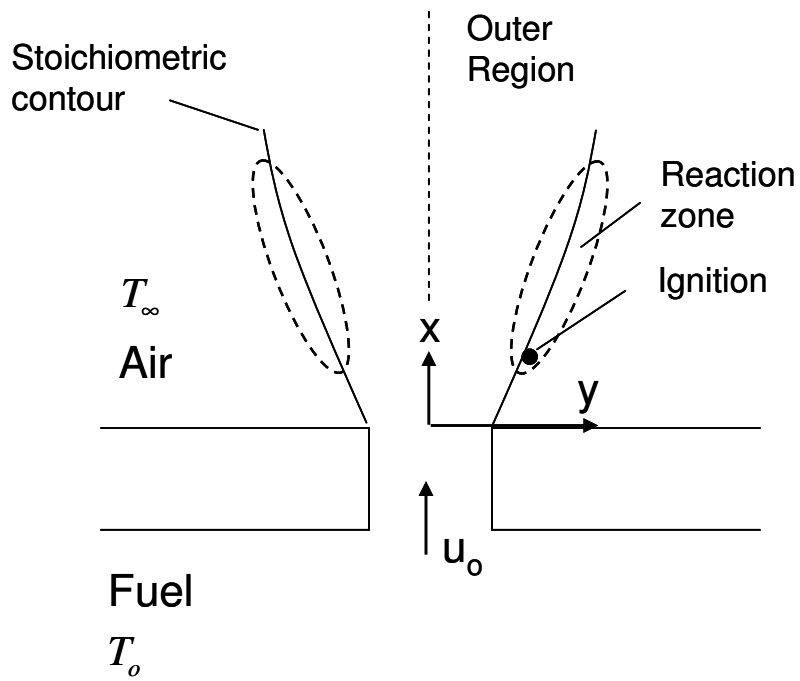


**Fig. 2.1: Schematic of slot and hydrogen leak for hot ambient case**

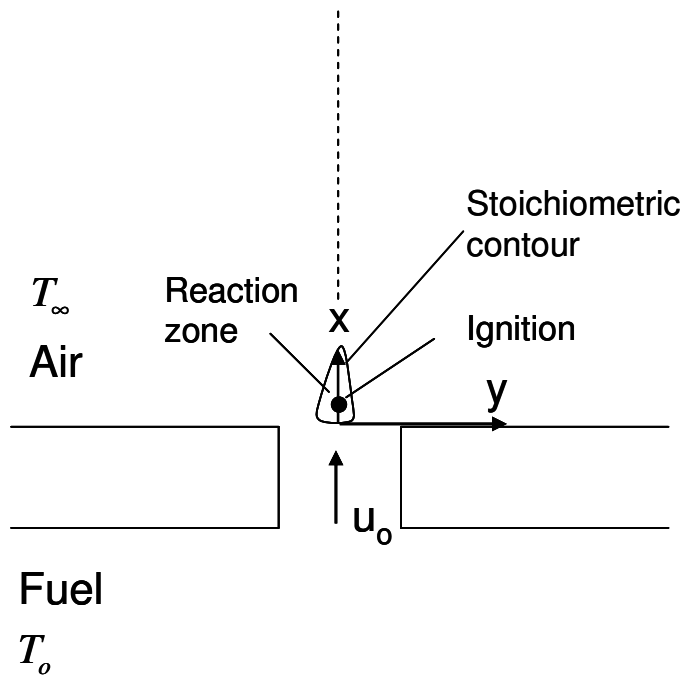


**Fig. 2.2: Schematic of slot and hydrogen leak for hot jet case**

## 2.2 Assumptions

The assumptions are as follow:

- (1) steady, 2D flow, negligible body force
- (2) reaction follows Arrhenius kinetics
- (3) high activation energy reaction
- (4) isobaric flow
- (5) symmetric with respect to the plane of symmetry
- (6)  $c_p$ ,  $\rho \lambda$ ,  $\rho \mu$ , and  $\rho^2 D_i$  do not vary with position

These assumptions are reasonable in light of the mathematical simplicity they introduce. Similar assumptions are commonly invoked in this type of analysis.

[11,12]

## 2.3 Slot Flowfield

The reaction is



The flowfield is described by conservation of mass,

$$\frac{\partial(\rho u)}{\partial x} + \frac{\partial(\rho v)}{\partial y} = 0 \quad (2.2)$$

conservation of momentum, x-direction

$$\rho u \frac{\partial u}{\partial x} + \rho v \frac{\partial u}{\partial y} - \frac{\partial}{\partial x} \left\{ \mu \left[ 2 \frac{\partial u}{\partial x} - \frac{2}{3} \left( \frac{\partial u}{\partial x} + \frac{\partial v}{\partial y} \right) \right] \right\} - \frac{\partial}{\partial y} \left[ \mu \left( \frac{\partial u}{\partial y} + \frac{\partial v}{\partial x} \right) \right] = - \frac{\partial p}{\partial x} \quad (2.3)$$

and conservation of momentum, y-direction

$$\rho u \frac{\partial v}{\partial x} + \rho v \frac{\partial v}{\partial y} - \frac{\partial}{\partial x} \left[ \mu \left( \frac{\partial v}{\partial x} + \frac{\partial u}{\partial y} \right) \right] - \frac{\partial}{\partial y} \left\{ \mu \left[ 2 \frac{\partial v}{\partial y} - \frac{2}{3} \left( \frac{\partial u}{\partial x} + \frac{\partial v}{\partial y} \right) \right] \right\} = - \frac{\partial p}{\partial y} \quad (2.4)$$

Within the slot, the only velocity component is  $u$  along the  $x$  direction :  $v = 0$

$$\frac{\partial(\rho u)}{\partial x} = 0 \quad \text{Therefore, } \rho u \text{ is independent of } x_0 \quad (2.5)$$

Conservation of momentum becomes

$$\rho u \frac{\partial u}{\partial x} - \frac{4}{3} \frac{\partial}{\partial x} \left( \mu \frac{\partial u}{\partial x} \right) - \frac{\partial}{\partial y} \left( \mu \frac{\partial u}{\partial y} \right) = -\frac{\partial p}{\partial x} \quad (2.6)$$

$$\frac{\partial}{\partial x} \left( \mu \frac{\partial u}{\partial y} \right) - \frac{2}{3} \frac{\partial}{\partial y} \left( \mu \frac{\partial u}{\partial x} \right) = \frac{\partial p}{\partial y} \quad (2.7)$$

$$y = 0 : \quad \partial u / \partial x = 0$$

*Case I Uniform flow*

A uniform flow is possible when the effect of viscosity is negligible ( $\mu \approx 0$ ).

At any  $x$ ,  $u$  is uniform for all  $y$

$$\frac{\partial p}{\partial y} = 0 \quad \text{leading to} \quad p = p(x)$$

$$\rho u \frac{du}{dx} = -\frac{dp}{dx} \quad \text{leading to} \quad \rho u^2 = c - p \quad (\text{Bernoulli Equation})$$

In the tank :  $u = 0$  ,  $p = p_i$  , therefore  $c = p_i$

At the exit :  $u = u_0$  ,  $p = p_0$  ,  $\rho = \rho_0$  therefore,  $\rho_0 u_0^2 = p_i - p_0$  or

$$u_0 = \sqrt{(p_i - p_0) / \rho_0} \quad (2.8)$$

$$M = \int_{-h}^h \rho_0 u_0^2 dy = \int_{-h}^h (p_i - p_0) dy = (p_i - p_0) \int_{-h}^h dy = 2h(p_i - p_0) \quad (2.9)$$

For this case, there is no friction. The flow is supported by the expansion caused by the pressure reduction so  $\rho$  cannot be considered constant. If the pressure difference is large, the flow is choked ( $Ma = 1$  at the exit).

If there is no heat addition or generation during the expansion, the gas temperature density and velocity at the exit ( $T_0$ ,  $\rho_0$  and  $u_0$ ) are (isentropic compressible flow)

$$T_0/T_i = 2/(\gamma + 1) \quad , \quad \gamma = c_p/c_v \quad (2.10)$$

$$p_0/p_i = [2/(\gamma + 1)]^{\gamma/(\gamma - 1)} \quad (2.11)$$

$$\rho_0/\rho_i = [2/(\gamma + 1)]^{1/(\gamma - 1)} \quad (2.12)$$

An expansion wave exists if  $p_a < p_0$ .

*Case II Fully developed flow in a channel :  $u = u(y)$*

The flow velocity is relatively low so the flow can be considered incompressible and isothermal

$$\frac{\partial p}{\partial y} = 0 \quad \text{leading to} \quad p = p(x) \quad (\mu = \mu_i = \mu_0 = \text{constant when } \rho = \text{constant})$$

$$\frac{d}{dy} \left( \mu_0 \frac{du}{dy} \right) = \frac{dp}{dx} \quad (2.13)$$

since lefthand side is a function of  $y$  only and righthand side is a function of  $x$  only,

$$\frac{d}{dx} p = \text{constant.}$$

$$dp/dx = -(p_i - p_0)/w \quad w \text{ is the thickness of the wall, } p_0 = p_a \quad (2.14)$$

$$\frac{du}{dy} = \frac{1}{\mu_0} \frac{dp}{dx} y + c_1 = -\frac{p_i - p_0}{\mu_0 w} y + c_1 \quad \text{and} \quad u = -\frac{p_i - p_0}{2\mu_0 w} y^2 + c_1 y + c_2 \quad (2.15)$$

$$\text{At } y = 0 \text{ (centerline)} : \frac{du}{dy} = 0$$

$$\text{therefore } c_1 = 0 \quad \text{leading to} \quad u = -\frac{p_i - p_0}{2\mu_0 w} y^2 + c_2 \quad (2.16)$$

$$\text{At } y = h \text{ (channel wall)} : u = 0$$

$$\text{therefore } c_2 = \frac{p_i - p_0}{2\mu_0 w} h^2 \quad \text{leading to} \quad u = \frac{p_i - p_0}{2\mu_0 w} (h^2 - y^2) \quad (2.17)$$

$$\begin{aligned}
M &= \int_{-h}^h \rho_0 u^2 dy = \int_{-h}^h \rho_0 \left[ \frac{p_i - p_0}{2\mu_0 w} (h^2 - y^2) \right]^2 dy = \rho_0 \left( \frac{p_i - p_0}{2\mu_0 w} \right)^2 \int_{-h}^h (h^4 - 2h^2 y^2 + y^4) dy \quad (2.18) \\
&= \rho_0 \left( \frac{p_i - p_0}{2\mu_0 w} \right)^2 \left( h^4 y - \frac{2}{3} h^2 y^3 + \frac{1}{5} y^5 \right) \Big|_{-h}^h = \rho_0 \left( \frac{p_i - p_0}{2\mu_0 w} \right)^2 \left[ h^4 (2h) - \frac{2}{3} h^2 (2h^3) + \frac{1}{5} (2h^5) \right] = \frac{4}{15} \rho_0 h^5 \left( \frac{p_i - p_0}{\mu_0 w} \right)^2
\end{aligned}$$

$$\text{At } y = 0 : u = u_0 \quad \therefore \quad u_0 = \frac{p_i - p_0}{2\mu_0 w} h^2$$

#### 2.4 Conservation Equations and Boundary Conditions in the Jet

(a) Conservation equations

$p = \rho RT$  or  $\rho = p/(RT)$  ;  $R =$  ideal gas constant ,  $p =$  constant (isobaric flow)

$$\frac{\partial(\rho u)}{\partial x} + \frac{\partial(\rho v)}{\partial y} = 0 \quad (2.19)$$

$$\frac{\partial p}{\partial y} = 0 \quad \text{leading to} \quad p = p(x)$$

$$\rho u \frac{\partial u}{\partial x} + \rho v \frac{\partial u}{\partial y} - \frac{\partial}{\partial y} \left( \mu \frac{\partial u}{\partial y} \right) = - \frac{\partial p}{\partial x} = - \frac{dp}{dx} = 0 \quad (\text{At any } x, \text{ as } y \rightarrow \pm\infty, u \rightarrow 0 \text{ therefore}$$

$$\frac{dp}{dx} = 0)$$

Conservation of energy is,

$$\rho u c_p \frac{\partial T}{\partial x} + \rho v c_p \frac{\partial T}{\partial y} - \frac{\partial}{\partial y} \left( \lambda \frac{\partial T}{\partial y} \right) = v_F W_F q_F \omega \quad (2.20)$$

Conservation of fuel is,

$$\rho u \frac{\partial Y_F}{\partial x} + \rho v \frac{\partial Y_F}{\partial y} - \frac{\partial}{\partial y} \left( \rho D_F \frac{\partial Y_F}{\partial y} \right) = -v_F W_F \omega \quad (2.21)$$

Conservation of oxidizer is,

$$\rho u \frac{\partial Y_O}{\partial x} + \rho v \frac{\partial Y_O}{\partial y} - \frac{\partial}{\partial y} \left( \rho D_O \frac{\partial Y_O}{\partial y} \right) = -\nu_O W_O \omega \quad (2.22)$$

Conservation of oxidizer is,

$$\begin{aligned} \omega &= B c_F^{n_F} c_O^{n_O} T^{n_T} \exp(-E/T) = B (\rho Y_F / W_F)^{n_F} (\rho Y_O / W_O)^{n_O} T^{n_T} \exp(-E/T) \\ &= (B / W_F^{n_F} W_O^{n_O}) \rho^{n_F+n_O} Y_F^{n_F} Y_O^{n_O} T^{n_T} \exp(-E/T) \end{aligned} \quad (2.23)$$

(b) Boundary and interface conditions

Let  $x = 0$  be the virtual origin of the jet and  $x = x_0$  be the exit of the jet.

$$\begin{aligned} x = x_0^- , -h < y < h : \quad T &= T_0 , \quad Y_F = Y_{F,0} , \quad Y_O = 0 , \quad u = u_0 , \quad v = 0 \\ y = 0 , x = x_0^+ : \quad T &= T_0 , \quad Y_F = Y_{F,0} , \quad Y_O = 0 , \quad u = u_0 , y = 0 , x > x_0 : \\ \partial T / \partial y = \partial Y_F / \partial y = \partial Y_O / \partial y = \partial u / \partial y = 0 , \quad v &= 0 \\ y \rightarrow \infty : \quad T &\rightarrow T_\infty , \quad Y_F \rightarrow 0 , \quad Y_O \rightarrow Y_{O,\infty} , \quad u \rightarrow 0 \end{aligned}$$

### 2.5 Coordinate Transformation and the Solution of Momentum Equation

A stream function  $\psi$  is defined such that the continuity equation is satisfied :

$$\frac{\rho u}{\rho_\infty u_0} = \frac{\partial \psi}{\partial y} , \quad \frac{\rho v}{\rho_\infty u_0} = -\frac{\partial \psi}{\partial x} \quad (2.24)$$

A new coordinate system is defined using similarity variables [26,27].

$$\eta = \frac{\alpha_1}{x^{2/3}} \int_0^y \frac{\rho}{\rho_\infty} dy' , \quad \psi = \alpha_2 x^{1/3} f(\eta) , \quad \tilde{x} = x / x_0 \quad (2.25)$$

( $\alpha_1$  and  $\alpha_2$  are constants that are defined later to simplify the expression)

It is assumed that a similarity solution exists so that  $f$  is a function of  $\eta$  only.

Coordinate transformation from  $(x, y)$  to  $(x, \eta)$  yields

$$\begin{aligned}\frac{\partial}{\partial x} &= \frac{\partial}{\partial x} \frac{\partial x}{\partial x} + \frac{\partial}{\partial \eta} \frac{\partial \eta}{\partial x} = \frac{\partial}{\partial x} + \left[ -\frac{2}{3} \frac{\alpha_1}{x^{5/3}} \int_0^y \frac{\rho}{\rho_\infty} dy' + \frac{\alpha_1}{x^{2/3}} \frac{\partial}{\partial x} \left( \int_0^y \frac{\rho}{\rho_\infty} dy' \right) \right] \frac{\partial}{\partial \eta} \\ &= \frac{\partial}{\partial x} - \frac{2\eta}{3x} \frac{\partial}{\partial \eta} + \frac{\alpha_1}{x^{2/3}} \left( \frac{\partial}{\partial x} \int_0^y \frac{\rho}{\rho_\infty} dy' \right) \frac{\partial}{\partial \eta}\end{aligned}\quad (2.26)$$

$$\frac{\partial}{\partial y} = \frac{\partial}{\partial x} \frac{\partial x}{\partial y} + \frac{\partial}{\partial \eta} \frac{\partial \eta}{\partial y} = \frac{\partial}{\partial \eta} \left[ \frac{\alpha_1}{x^{2/3}} \frac{\partial}{\partial y} \left( \int_0^y \frac{\rho}{\rho_\infty} dy' \right) \right] = \frac{\alpha_1}{x^{2/3}} \frac{\rho}{\rho_\infty} \frac{\partial}{\partial \eta}\quad (2.27)$$

$$\frac{\rho u}{\rho_\infty u_0} = \frac{\partial \psi}{\partial y} = \frac{\alpha_1}{x^{2/3}} \frac{\rho}{\rho_\infty} \frac{\partial}{\partial \eta} \left[ \alpha_2 x^{1/3} f(\eta) \right] = \frac{\alpha_1 \alpha_2}{x^{1/3}} \frac{\rho}{\rho_\infty} \frac{df}{d\eta}\quad (2.28)$$

We define  $\alpha_1 \alpha_2 = x_0^{1/3}$  or  $\alpha_2 = x_0^{1/3} / \alpha_1$  such that  $\frac{u}{u_0} = \frac{x_0^{1/3}}{x^{1/3}} \frac{df}{d\eta}$  or  $u = \frac{u_0}{x^{1/3}} \frac{df}{d\eta}$

$$\begin{aligned}\frac{\rho v}{\rho_\infty u_0} &= -\frac{\partial \psi}{\partial x} = -\frac{\partial}{\partial x} \left[ \frac{x_0^{1/3}}{\alpha_1} x^{1/3} f(\eta) \right] + \frac{2}{3x} \eta \frac{\partial}{\partial \eta} \left[ \frac{x_0^{1/3}}{\alpha_1} x^{1/3} f(\eta) \right] \\ &\quad - \alpha_1 x^{-2/3} \left( \frac{\partial}{\partial x} \int_0^y \frac{\rho}{\rho_\infty} dy' \right) \frac{\partial}{\partial \eta} \left[ \frac{x_0^{1/3}}{\alpha_1} x^{1/3} f(\eta) \right] \\ &= -\frac{x_0^{1/3}}{3\alpha_1 x^{2/3}} \left( f - 2\eta \frac{df}{d\eta} \right) - \frac{x_0^{1/3}}{x^{1/3}} \left( \frac{\partial}{\partial x} \int_0^y \frac{\rho}{\rho_\infty} dy' \right) \frac{df}{d\eta}\end{aligned}\quad (2.29)$$

$$\begin{aligned}\frac{\partial u}{\partial x} &= \frac{\partial}{\partial x} \left( \frac{x_0^{1/3} u_0}{x^{1/3}} \frac{df}{d\eta} \right) - \frac{2\eta}{3x} \frac{\partial}{\partial \eta} \left( \frac{x_0^{1/3} u_0}{x^{1/3}} \frac{df}{d\eta} \right) + \frac{\alpha_1}{x^{2/3}} \left( \frac{\partial}{\partial x} \int_0^y \frac{\rho}{\rho_\infty} dy' \right) \frac{\partial}{\partial \eta} \left( \frac{x_0^{1/3} u_0}{x^{1/3}} \frac{df}{d\eta} \right) \\ &= -\frac{x_0^{1/3} u_0}{3x^{4/3}} \left( \frac{df}{d\eta} + 2\eta \frac{d^2 f}{d\eta^2} \right) + \frac{\alpha_1 x_0^{1/3} u_0}{x} \left( \frac{\partial}{\partial x} \int_0^y \frac{\rho}{\rho_\infty} dy' \right) \frac{d^2 f}{d\eta^2}\end{aligned}\quad (2.30)$$

$$\frac{\partial u}{\partial y} = \frac{\alpha_1}{x^{2/3}} \frac{\rho}{\rho_\infty} \frac{\partial}{\partial \eta} \left( \frac{x_0^{1/3} u_0}{x^{1/3}} \frac{df}{d\eta} \right) = \frac{\alpha_1 x_0^{1/3} u_0}{x} \frac{\rho}{\rho_\infty} \frac{d^2 f}{d\eta^2}\quad (2.31)$$

$$\begin{aligned}\frac{\partial}{\partial y} \left( \mu \frac{\partial u}{\partial y} \right) &= \frac{\alpha_1}{x^{2/3}} \frac{\rho}{\rho_\infty} \frac{\partial}{\partial \eta} \left[ \frac{\alpha_1 x_0^{1/3} u_0}{x} \frac{\rho \mu}{\rho_\infty} \frac{d^2 f}{d\eta^2} \right] = \frac{\alpha_1^2 x_0^{1/3} u_0}{x^{5/3}} \frac{\rho^2 \mu}{\rho_\infty^2} \frac{d^3 f}{d\eta^3} \\ &= \frac{\alpha_1^2 x_0^{1/3} u_0}{x^{5/3}} \frac{\rho \rho_\infty \mu_\infty}{\rho_\infty^2} \frac{d^3 f}{d\eta^3} = \frac{\alpha_1^2 x_0^{1/3} u_0}{x^{5/3}} \frac{\rho \mu_\infty}{\rho_\infty} \frac{d^3 f}{d\eta^3}\end{aligned}\quad (2.32)$$

(It is assumed that  $\rho\mu = \rho_\infty\mu_\infty = \text{constant}$ )

Momentum equation is given by,

$$\rho u \frac{\partial u}{\partial x} + \rho v \frac{\partial u}{\partial y} - \frac{\partial}{\partial y} \left( \mu \frac{\partial u}{\partial y} \right) = 0 \quad (2.33)$$

$$\begin{aligned} & \frac{\rho x_0^{1/3} u_0}{x^{1/3}} \frac{df}{d\eta} \left[ -\frac{x_0^{1/3} u_0}{3x^{4/3}} \left( \frac{df}{d\eta} + 2\eta \frac{d^2 f}{d\eta^2} \right) + \frac{\alpha_1 x_0^{1/3} u_0}{x} \left( \frac{\partial}{\partial x} \int_0^y \frac{\rho}{\rho_\infty} dy' \right) \frac{d^2 f}{d\eta^2} \right] \\ & + \left[ -\frac{\rho_\infty u_0 x_0^{1/3}}{3\alpha_1 x^{2/3}} \left( f - 2\eta \frac{df}{d\eta} \right) - \frac{\rho_\infty u_0 x_0^{1/3}}{x^{1/3}} \left( \frac{\partial}{\partial x} \int_0^y \frac{\rho}{\rho_\infty} dy' \right) \frac{df}{d\eta} \right] \frac{\alpha_1 x_0^{1/3} u_0}{x} \frac{\rho}{\rho_\infty} \frac{d^2 f}{d\eta^2} \\ & - \frac{\alpha_1^2 x_0^{1/3} u_0}{x^{5/3}} \frac{\rho \mu_\infty}{\rho_\infty} \frac{d^3 f}{d\eta^3} - \frac{\rho u_0^2 x_0^{2/3}}{3x^{5/3}} \left[ \left( \frac{df}{d\eta} \right)^2 + f \frac{d^2 f}{d\eta^2} + \alpha_1^2 \frac{3\mu_\infty}{\rho_\infty u_0 x_0^{1/3}} \frac{d^3 f}{d\eta^3} \right] = 0 \end{aligned} \quad (2.34)$$

We define  $\alpha_1^2 \frac{3\mu_\infty}{\rho_\infty u_0 x_0^{1/3}} = \frac{1}{2}$  such that it leads to  $\alpha_1 = \sqrt{\frac{\rho_\infty u_0 x_0^{1/3}}{6\mu_\infty}}$  and

$$\frac{1}{2} \frac{d^3 f}{d\eta^3} + f \frac{d^2 f}{d\eta^2} + \left( \frac{df}{d\eta} \right)^2 = 0 \quad (2.35)$$

$$\eta = \frac{\alpha_1}{x^{2/3}} \int_0^y \frac{\rho}{\rho_\infty} dy' = \sqrt{\frac{\rho_\infty u_0 x_0^{1/3}}{6\mu_\infty}} \frac{1}{x^{2/3}} \int_0^y \frac{\rho}{\rho_\infty} dy' = \sqrt{\frac{\rho_\infty u_0}{6\mu_\infty x_0}} \frac{1}{\tilde{x}^{2/3}} \int_0^y \frac{\rho}{\rho_\infty} dy' \quad (2.36)$$

$$\psi = \alpha_2 x^{1/3} f(\eta) = \frac{x_0^{1/3}}{\alpha_1} x^{1/3} f(\eta) = x_0^{1/3} \sqrt{\frac{6\mu_\infty}{\rho_\infty u_0 x_0^{1/3}}} x^{1/3} f(\eta) = \sqrt{\frac{6\mu_\infty x_0}{\rho_\infty u_0}} \tilde{x}^{1/3} f(\eta) \quad (2.37)$$

$$\begin{aligned} \frac{\partial}{\partial x} &= \frac{\partial}{\partial x} - \frac{2\eta}{3x} \frac{\partial}{\partial \eta} + \frac{\alpha_1}{x^{2/3}} \left( \frac{\partial}{\partial x} \int_0^y \frac{\rho}{\rho_\infty} dy' \right) \frac{\partial}{\partial \eta} = \frac{\partial}{\partial(x_0 \tilde{x})} - \frac{2\eta}{3x_0 \tilde{x}} \frac{\partial}{\partial \eta} \\ &+ \sqrt{\frac{\rho_\infty u_0 x_0^{1/3}}{6\mu_\infty}} \frac{1}{x_0^{2/3} \tilde{x}^{2/3}} \left( \frac{\partial}{\partial x} \int_0^y \frac{\rho}{\rho_\infty} dy' \right) \frac{\partial}{\partial \eta} \\ &= \frac{1}{x_0} \frac{\partial}{\partial \tilde{x}} - \frac{1}{x_0} \frac{2\eta}{3\tilde{x}} \frac{\partial}{\partial \eta} + \sqrt{\frac{\rho_\infty u_0}{6\mu_\infty x_0}} \frac{1}{\tilde{x}^{2/3}} \left( \frac{\partial}{\partial x} \int_0^y \frac{\rho}{\rho_\infty} dy' \right) \frac{\partial}{\partial \eta} \end{aligned} \quad (2.38)$$

$$\frac{\partial}{\partial y} = \frac{\alpha_1}{x^{2/3}} \frac{\rho}{\rho_\infty} \frac{\partial}{\partial \eta} = \sqrt{\frac{\rho_\infty u_0 x_0^{1/3}}{6\mu_\infty}} \frac{1}{x_0^{2/3} \tilde{x}^{2/3}} \frac{\rho}{\rho_\infty} \frac{\partial}{\partial \eta} = \sqrt{\frac{\rho_\infty u_0}{6\mu_\infty x_0}} \frac{1}{\tilde{x}^{2/3}} \frac{\rho}{\rho_\infty} \frac{\partial}{\partial \eta} \quad (2.39)$$

Boundary conditions

$$y = 0, x = x_0^+ : u = u_0 \Rightarrow \eta = 0 : df/d\eta = 1 \text{ (} f \text{ is independent of } x\text{)}$$

$$y = 0, x > x_0 : \partial u / \partial y = v = 0 \Rightarrow \eta = 0, x > x_0 : f = d^2 f / d\eta^2 = 0$$

$$y \rightarrow \infty : u \rightarrow 0 \Rightarrow \eta \rightarrow \infty : df/d\eta \rightarrow 0$$

Solution in the jet ( $x > x_0$  or  $\tilde{x} > 1$ )

$$0 = \frac{1}{2} \frac{d^3 f}{d\eta^3} + f \frac{d^2 f}{d\eta^2} + \left( \frac{df}{d\eta} \right)^2 = \frac{1}{2} \frac{d^3 f}{d\eta^3} + \frac{d}{d\eta} \left( f \frac{df}{d\eta} \right) = \frac{d}{d\eta} \left( \frac{1}{2} \frac{d^2 f}{d\eta^2} + f \frac{df}{d\eta} \right) \text{ therefore} \quad (2.40)$$

$$\frac{1}{2} \frac{d^2 f}{d\eta^2} + f \frac{df}{d\eta} = c$$

$$\eta = 0 : f = d^2 f / d\eta^2 = 0 \text{ therefore } c = 0 \text{ leading to } \frac{1}{2} \frac{d^2 f}{d\eta^2} + f \frac{df}{d\eta} = 0$$

$$0 = \frac{1}{2} \frac{d^2 f}{d\eta^2} + f \frac{df}{d\eta} = \frac{1}{2} \frac{d^2 f}{d\eta^2} + \frac{1}{2} \frac{df^2}{d\eta} = \frac{1}{2} \frac{d}{d\eta} \left( \frac{df}{d\eta} + f^2 \right) \text{ therefore } \frac{df}{d\eta} + f^2 = c \quad (2.41)$$

$$\text{Let } z = a\eta, f = aF(z), c = a^2 \text{ then } \frac{df}{d\eta} = \frac{d(aF)}{dz} \frac{dz}{d\eta} = a \frac{dF}{dz} a = a^2 \frac{dF}{dz}$$

$$a^2 \frac{dF}{dz} + \frac{(aF)^2}{2} = a^2 \text{ or } \frac{dF}{dz} + F^2 = 1 \Rightarrow \frac{dF}{dz} = 1 - F^2 \text{ or } \frac{dF}{1 - F^2} = dz$$

$$\tanh^{-1} F = z + c \text{ or } F = \tanh(z + c) \text{ or } \frac{f}{a} = \tanh(a\eta + c) \text{ or } f = a \tanh(a\eta + c)$$

$$\eta = 0 : f = 0, df/d\eta = 1$$

$$\tanh c = 0 \text{ or } c = 0 \Rightarrow f = a \tanh(a\eta) \text{ and } df/d\eta = a^2 \operatorname{sech}^2(a\eta)$$

$$a^2 \operatorname{sech}^2(0) = 1 \text{ therefore } a^2 = 1 \text{ or } a = 1$$

$$\text{Thus : } f = \tanh \eta, df/d\eta = \operatorname{sech}^2 \eta,$$

$$u = (u_0 / \tilde{x}^{1/3}) (df/d\eta) = u_0 (\operatorname{sech}^2 \eta) \tilde{x}^{1/3} \quad (2.42)$$

$$\rho v = \rho_\infty u_0 \left[ -\frac{x_0^{1/3}}{3\alpha_1 x^{2/3}} \left( f - 2\eta \frac{df}{d\eta} \right) - \frac{x_0^{1/3}}{x^{1/3}} \left( \frac{\partial}{\partial x} \int_0^y \frac{\rho}{\rho_\infty} dy' \right) \frac{df}{d\eta} \right] \quad (2.43)$$

$$= -\rho_\infty u_0 \left[ \sqrt{\frac{6\mu_\infty}{\rho_\infty u_0 x_0}} \frac{x_0^{1/3}}{3x_0^{2/3} \tilde{x}^{2/3}} \left( f - 2\eta \frac{df}{d\eta} \right) + \frac{1}{\tilde{x}^{1/3}} \left( \frac{\partial}{\partial x} \int_0^y \frac{\rho}{\rho_\infty} dy' \right) \frac{df}{d\eta} \right] \quad (2.44)$$

$$= -\rho_\infty u_0 \left\{ \sqrt{\frac{6\mu_\infty}{\rho_\infty u_0 x_0}} \frac{(\tanh \eta) - 2\eta(\operatorname{sech}^2 \eta)}{3\tilde{x}^{2/3}} + \frac{\operatorname{sech}^2 \eta}{\tilde{x}^{1/3}} \left( \frac{\partial}{\partial x} \int_0^y \frac{\rho}{\rho_\infty} dy' \right) \right\} \quad (2.45)$$

Determination of  $x_0$  by momentum conservation

$$\int_{-\infty}^{\infty} \rho u^2 dy = \int_{-h}^h \rho_0 u_0^2 dy = M$$

$$\begin{aligned} M &= \int_{-\infty}^{\infty} \rho u^2 dy = \int_{-\infty}^{\infty} \rho \left( \frac{u_0}{\tilde{x}^{1/3}} \operatorname{sech}^2 \eta \right)^2 \left( \sqrt{\frac{6\mu_\infty x_0}{\rho_\infty u_0}} \tilde{x}^{2/3} \frac{\rho_\infty}{\rho} d\eta \right) \\ &= u_0 \sqrt{6x_0 u_0 \rho_\infty \mu_\infty} \int_{-\infty}^{\infty} (\operatorname{sech}^4 \eta) d\eta \end{aligned} \quad (2.46)$$

$$\begin{aligned} &= u_0 \sqrt{6x_0 u_0 \rho_\infty \mu_\infty} \left[ \frac{(\operatorname{sech}^2 \eta)(\tanh \eta)}{3} \Big|_{-\infty}^{\infty} + \frac{2}{3} \int_{-\infty}^{\infty} (\operatorname{sech}^2 \eta) d\eta \right] \\ &= u_0 \sqrt{6x_0 u_0 \rho_\infty \mu_\infty} \left[ 0 + \frac{2}{3} \tanh \eta \Big|_{-\infty}^{\infty} \right] = \frac{4}{3} u_0 \sqrt{6x_0 u_0 \rho_\infty \mu_\infty} \end{aligned} \quad (2.47)$$

$$\text{Therefore } \frac{32}{3} u_0^3 x_0 \rho_\infty \mu_\infty = M^2 \quad \text{or} \quad x_0 = \frac{3M^2}{32u_0^3 \rho_\infty \mu_\infty} \quad (2.48)$$

In summary, the flowfield solution is :

$$\eta = \sqrt{\frac{\rho_\infty u_0}{6\mu_\infty x_0}} \frac{1}{\tilde{x}^{2/3}} \int_0^y \frac{\rho}{\rho_\infty} dy' \quad (2.36), \quad \psi = \sqrt{\frac{6\mu_\infty x_0}{\rho_\infty u_0}} \tilde{x}^{1/3} f(\eta) \quad (2.37), \quad x_0 = \frac{3M^2}{32u_0^3 \rho_\infty \mu_\infty} \quad (2.48)$$

$$f = \tanh \eta \quad , \quad df/d\eta = \operatorname{sech}^2 \eta \quad , \quad u = u_0 (\operatorname{sech}^2 \eta) \tilde{x}^{1/3} \quad (2.42)$$

$$\frac{\partial}{\partial x} = \frac{1}{x_0} \frac{\partial}{\partial \tilde{x}} - \frac{1}{x_0} \frac{2\eta}{3\tilde{x}} \frac{\partial}{\partial \eta} + \sqrt{\frac{\rho_\infty u_0}{6\mu_\infty x_0}} \frac{1}{\tilde{x}^{2/3}} \left( \frac{\partial}{\partial x} \int_0^y \frac{\rho}{\rho_\infty} dy' \right) \frac{\partial}{\partial \eta} \quad (2.38)$$

$$\frac{\partial}{\partial y} = \sqrt{\frac{\rho_\infty u_0}{6\mu_\infty x_0}} \frac{1}{\tilde{x}^{2/3}} \frac{\rho}{\rho_\infty} \frac{\partial}{\partial \eta} \quad (2.39)$$

$$\rho v = -\rho_\infty u_0 \left\{ \sqrt{\frac{6\mu_\infty}{\rho_\infty u_0 x_0}} \frac{(\tanh \eta) - 2\eta(\operatorname{sech}^2 \eta)}{3\tilde{x}^{2/3}} + \frac{\operatorname{sech}^2 \eta}{\tilde{x}^{1/3}} \left( \frac{\partial}{\partial x} \int_0^y \frac{\rho}{\rho_\infty} dy' \right) \right\} \quad (2.45)$$

## 2.6 Nondimensionalizing the Energy and Species Equations

The following nondimensional quantities are defined as :

$$\tilde{T} = \frac{c_p T}{q_F} \quad , \quad \tilde{Y}_F = Y_F \quad , \quad \tilde{Y}_O = \frac{v_F W_F}{v_O W_O} Y_O \quad , \quad \tilde{E} = \frac{c_p E}{q_F} \quad (2.49)$$

$$\text{Damköhler number: } Da = \frac{6x_0 v_O^{n_O} B}{v_F^{n_O-1} W_F^{n_O+n_F-1} u_0} \left( \frac{q_F}{c_p} \right)^{n_T - n_F - n_O + 1} \left( \frac{p}{R} \right)^{n_F + n_O - 1} \quad (2.50)$$

$$\text{Prandtl number : } Pr = \frac{\mu}{\lambda l c_p} = \frac{\rho \mu}{\rho \lambda l c_p} = \text{constant} \quad (2.51)$$

$$\text{Schmidt number of species } j : Sc_j = \frac{\mu}{\rho D_j} = \frac{\rho \mu}{\rho^2 D_j} = \text{constant} \quad (2.52)$$

$$\text{Lewis number of species } j : Le_j = \frac{\lambda c_p}{\rho D_j} = \frac{Sc_j}{Pr} = \text{constant} \quad (2.53)$$

Nondimensionalizing the energy equation:

$$(1) \quad \rho = p / (RT) = (p / R) (c_p / q_F) / \tilde{T} \quad (2.54)$$

$$(2) \quad \rho u c_p \frac{\partial \tilde{T}}{\partial x} + \rho v c_p \frac{\partial \tilde{T}}{\partial y} - \frac{\partial}{\partial y} \left( \lambda \frac{\partial \tilde{T}}{\partial y} \right) = \frac{v_F W_F B}{W_F^{n_F} W_O^{n_O}} q_F \rho^{n_F + n_O} Y_F^{n_F} Y_O^{n_O} T^{n_T} \exp(-E / T)$$

$$\begin{aligned} & \frac{q_F}{c_p} \left[ \rho u c_p \frac{\partial \tilde{T}}{\partial x} + \rho v c_p \frac{\partial \tilde{T}}{\partial y} - \frac{1}{Pr} \frac{\partial}{\partial y} \left( \mu c_p \frac{\partial \tilde{T}}{\partial y} \right) \right] \\ & = \frac{v_F W_F B}{W_F^{n_F} W_O^{n_O}} q_F \rho^{n_F + n_O} Y_F^{n_F} \left( \frac{v_O W_O}{v_F W_F} \tilde{Y}_O \right)^{n_O} \left( \frac{q_F}{c_p} \tilde{T} \right)^{n_T} \exp(-\tilde{E} / \tilde{T}) \end{aligned} \quad (2.55)$$

$$\begin{aligned} & \rho u \frac{\partial \tilde{T}}{\partial x} + \rho v \frac{\partial \tilde{T}}{\partial y} - \frac{1}{Pr} \frac{\partial}{\partial y} \left( \mu \frac{\partial \tilde{T}}{\partial y} \right) \\ & = \frac{v_O^{n_O} B}{v_F^{n_O-1} W_F^{n_O+n_F-1}} (q_F / c_p)^{n_T} \rho^{n_F + n_O} \tilde{Y}_F^{n_F} \tilde{Y}_O^{n_O} \tilde{T}^{n_T} \exp(-\tilde{E} / \tilde{T}) \end{aligned} \quad (2.56)$$

$$\frac{\partial \tilde{T}}{\partial x} = \frac{1}{x_0} \frac{\partial \tilde{T}}{\partial \tilde{x}} - \frac{1}{x_0} \frac{2\eta}{3\tilde{x}} \frac{\partial \tilde{T}}{\partial \eta} + \sqrt{\frac{\rho_\infty u_0}{6\mu_\infty x_0}} \frac{1}{\tilde{x}^{2/3}} \left( \frac{\partial}{\partial x} \int_0^y \frac{\rho}{\rho_\infty} dy' \right) \frac{\partial \tilde{T}}{\partial \eta} \quad ; \quad \frac{\partial \tilde{T}}{\partial y} = \sqrt{\frac{\rho_\infty u_0}{6\mu_\infty x_0}} \frac{1}{\tilde{x}^{2/3}} \frac{\rho}{\rho_\infty} \frac{\partial \tilde{T}}{\partial \eta}$$

$$\frac{\partial}{\partial y} \left( \mu \frac{\partial \tilde{T}}{\partial y} \right) = \sqrt{\frac{\rho_\infty u_0}{6\mu_\infty x_0}} \frac{1}{\tilde{x}^{2/3}} \frac{\rho}{\rho_\infty} \frac{\partial}{\partial \eta} \left( \mu \sqrt{\frac{\rho_\infty u_0}{6\mu_\infty x_0}} \frac{1}{\tilde{x}^{2/3}} \frac{\rho}{\rho_\infty} \frac{\partial \tilde{T}}{\partial \eta} \right) = \frac{\rho u_0}{6x_0} \frac{1}{\tilde{x}^{4/3}} \frac{\partial^2 \tilde{T}}{\partial \eta^2} \quad (2.57)$$

( $\rho \mu = \rho_\infty \mu_\infty = \text{constant}$ )

$$\begin{aligned}
& \rho u \frac{\partial \tilde{T}}{\partial x} + \rho v \frac{\partial \tilde{T}}{\partial y} - \frac{1}{Pr} \frac{\partial}{\partial y} \left( \mu \frac{\partial \tilde{T}}{\partial y} \right) = \\
& \rho u_0 \frac{\text{sech}^2 \eta}{\tilde{x}^{1/3}} \left[ \frac{1}{x_0} \frac{\partial \tilde{T}}{\partial \tilde{x}} - \frac{1}{x_0} \frac{2\eta}{3\tilde{x}} \frac{\partial \tilde{T}}{\partial \eta} + \sqrt{\frac{\rho_\infty u_0}{6\mu_\infty x_0}} \frac{1}{\tilde{x}^{2/3}} \left( \frac{\partial}{\partial x} \int_0^y \frac{\rho}{\rho_\infty} d y' \right) \frac{\partial \tilde{T}}{\partial \eta} \right] \\
& - \frac{1}{Pr} \frac{\rho u_0}{6x_0} \frac{1}{\tilde{x}^{4/3}} \frac{\partial^2 \tilde{T}}{\partial \eta^2} - \rho_\infty u_0 \left\{ \sqrt{\frac{6\mu_\infty}{\rho_\infty u_0 x_0}} \frac{(\tanh \eta) - 2\eta(\text{sech}^2 \eta)}{3\tilde{x}^{2/3}} + \frac{\text{sech}^2 \eta}{\tilde{x}^{1/3}} \left( \frac{\partial}{\partial x} \int_0^y \frac{\rho}{\rho_\infty} d y' \right) \right\} \\
& \left( \sqrt{\frac{\rho_\infty u_0}{6\mu_\infty x_0}} \frac{1}{\tilde{x}^{2/3}} \frac{\rho}{\rho_\infty} \frac{\partial \tilde{T}}{\partial \eta} \right) \\
& = \frac{\rho u_0 (\text{sech}^2 \eta)}{x_0} \frac{\partial \tilde{T}}{\partial \tilde{x}} - \frac{\rho u_0 (\tanh \eta)}{x_0} \frac{\partial \tilde{T}}{3\tilde{x}^{4/3} \partial \eta} - \frac{1}{Pr} \frac{\rho u_0}{6x_0} \frac{1}{\tilde{x}^{4/3}} \frac{\partial^2 \tilde{T}}{\partial \eta^2} \\
& = -\frac{\rho u_0}{6x_0 \tilde{x}^{4/3}} \left[ \frac{1}{Pr} \frac{\partial^2 \tilde{T}}{\partial \eta^2} + 2(\tanh \eta) \frac{\partial \tilde{T}}{\partial \eta} - 6(\text{sech}^2 \eta) \tilde{x} \frac{\partial \tilde{T}}{\partial \tilde{x}} \right] \tag{2.58}
\end{aligned}$$

$$\begin{aligned}
& \frac{1}{Pr} \frac{\partial^2 \tilde{T}}{\partial \eta^2} + 2(\tanh \eta) \frac{\partial \tilde{T}}{\partial \eta} - 6(\text{sech}^2 \eta) \tilde{x} \frac{\partial \tilde{T}}{\partial \tilde{x}} \\
& = -\frac{6x_0 \tilde{x}^{4/3}}{\rho u_0} \frac{\nu_0^{n_o} B}{\nu_F^{n_o-1} W_F^{n_o+n_F-1}} \left( \frac{q_F}{c_p} \right)^{n_T} \rho^{n_F+n_o} \tilde{Y}_F^{n_F} \tilde{Y}_O^{n_o} \tilde{T}^{n_T} \exp(-\tilde{E}/\tilde{T}) \\
& = -Da \tilde{x}^{4/3} \tilde{Y}_F^{n_F} \tilde{Y}_O^{n_o} \tilde{T}^{n_T-n_F-n_o+1} \exp(-\tilde{E}/\tilde{T}) \tag{2.59}
\end{aligned}$$

$$\begin{aligned}
(3) \quad & \rho u \frac{\partial Y_F}{\partial x} + \rho v \frac{\partial Y_F}{\partial y} - \frac{\partial}{\partial y} \left( \rho D_F \frac{\partial Y_F}{\partial y} \right) = -\frac{\nu_F W_F B}{W_F^{n_F} W_O^{n_o}} \rho^{n_F+n_o} Y_F^{n_F} Y_O^{n_o} T^{n_T} \exp(-E/T) \\
& \rho u \frac{\partial \tilde{Y}_F}{\partial x} + \rho v \frac{\partial \tilde{Y}_F}{\partial y} - \frac{\partial}{\partial y} \left( \frac{\rho D_F}{\mu} \mu \frac{\partial \tilde{Y}_F}{\partial y} \right) \\
& = -\frac{\nu_F W_F B}{W_F^{n_F} W_O^{n_o}} \rho^{n_F+n_o} Y_F^{n_F} \left( \frac{\nu_O W_O}{\nu_F W_F} \tilde{Y}_O \right)^{n_o} \left( \frac{q_F \tilde{T}}{c_p} \right)^{n_T} \exp(-\tilde{E}/\tilde{T}) \rho u \frac{\partial \tilde{Y}_F}{\partial x} + \rho v \frac{\partial \tilde{Y}_F}{\partial y} - \frac{1}{Sc_F} \frac{\partial}{\partial y} \left( \mu \frac{\partial \tilde{Y}_F}{\partial y} \right) \\
& = -\frac{\nu_0^{n_o} B}{\nu_F^{n_o-1} W_F^{n_o+n_F-1}} (q_F / c_p)^{n_T} \rho^{n_F+n_o} \tilde{Y}_F^{n_F} \tilde{Y}_O^{n_o} \tilde{T}^{n_T} \exp(-\tilde{E}/\tilde{T}) \tag{2.60}
\end{aligned}$$

By the same analysis as that of (2), we have (change  $Pr$  to  $Sc_F$  and the sign of the righthand side)

$$\frac{1}{Sc_F} \frac{\partial^2 \tilde{Y}_F}{\partial \eta^2} + 2(\tanh \eta) \frac{\partial \tilde{Y}_F}{\partial \eta} - 6(\text{sech}^2 \eta) \tilde{x} \frac{\partial \tilde{Y}_F}{\partial \tilde{x}} = Da \tilde{x}^{4/3} \tilde{Y}_F^{n_F} \tilde{Y}_O^{n_o} \tilde{T}^{n_T-n_F-n_o+1} \exp(-\tilde{E}/\tilde{T}) \tag{2.61}$$

$$\begin{aligned}
(4) \quad & \rho u \frac{\partial Y_O}{\partial x} + \rho v \frac{\partial Y_O}{\partial y} - \frac{\partial}{\partial y} \left( \rho D_O \frac{\partial Y_O}{\partial y} \right) = - \frac{v_O W_O B}{W_F^{n_F} W_O^{n_O}} \rho^{n_F+n_O} Y_F^{n_F} Y_O^{n_O} T^{n_T} \exp(-E/T) \\
& \frac{v_O W_O}{v_F W_F} \left[ \rho u \frac{\partial \tilde{Y}_O}{\partial x} + \rho v \frac{\partial \tilde{Y}_O}{\partial y} - \frac{\partial}{\partial y} \left( \frac{\rho D_O}{\mu} \mu \frac{\partial \tilde{Y}_O}{\partial y} \right) \right] \\
& = - \frac{v_O W_O B}{W_F^{n_F} W_O^{n_O}} q_F \rho^{n_F+n_O} Y_F^{n_F} \left( \frac{v_O W_O}{v_F W_F} \tilde{Y}_O \right)^{n_O} \left( \frac{q_F \tilde{T}}{c_p} \right)^{n_T} \exp(-\tilde{E}/\tilde{T}) \\
& \rho u \frac{\partial \tilde{Y}_O}{\partial x} + \rho v \frac{\partial \tilde{Y}_O}{\partial y} - \frac{1}{S c_O} \frac{\partial}{\partial y} \left( \mu \frac{\partial \tilde{Y}_O}{\partial y} \right) \\
& = - \frac{v_O^{n_O} B}{v_F^{n_O-1} W_F^{n_O+n_F-1}} (q_F / c_p)^{n_T} \rho^{n_F+n_O} \tilde{Y}_F^{n_F} \tilde{Y}_O^{n_O} \tilde{T}^{n_T} \exp(-\tilde{E}/\tilde{T}) \tag{2.62}
\end{aligned}$$

Similar to (3), we have

$$\frac{1}{S c_O} \frac{\partial^2 \tilde{Y}_O}{\partial \eta^2} + 2(\tanh \eta) \frac{\partial \tilde{Y}_O}{\partial \eta} - 6(\operatorname{sech}^2 \eta) \tilde{x} \frac{\partial \tilde{Y}_O}{\partial \tilde{x}} = D a \tilde{x}^{4/3} \tilde{Y}_F^{n_F} \tilde{Y}_O^{n_O} \tilde{T}^{n_T-n_F-n_O+1} \exp(-\tilde{E}/\tilde{T}) \tag{2.63}$$

$$(5) \quad y = 0, \quad x = x_0^+ : \quad T = T_0, \quad Y_F = Y_{F,0}, \quad Y_O = 0$$

$$\text{leading to } \eta = 0, \quad \tilde{x} = 1^+ : \quad \tilde{T} = \tilde{T}_0 = \frac{c_p T_0}{q_F}, \quad \tilde{Y}_F = \tilde{Y}_{F,0} = Y_{F,0}, \quad \tilde{Y}_O = 0$$

$$y = 0, \quad x > x_0 : \quad \partial T / \partial y = \partial Y_F / \partial y = \partial Y_O / \partial y = 0$$

$$\text{leading to } \eta = 0, \quad \tilde{x} > 1 : \quad \partial \tilde{T} / \partial \eta = \partial \tilde{Y}_F / \partial \eta = \partial \tilde{Y}_O / \partial \eta = 0$$

$$y \rightarrow \infty : \quad T \rightarrow T_\infty, \quad Y_F \rightarrow 0, \quad Y_O \rightarrow Y_{O,\infty}, \quad u \rightarrow 0$$

$$\text{leading to } \eta \rightarrow \infty : \quad \tilde{T} \rightarrow \tilde{T}_\infty = \frac{c_p T_\infty}{q_F}, \quad \tilde{Y}_F \rightarrow 0, \quad \tilde{Y}_O \rightarrow \tilde{Y}_{O,\infty} = \frac{v_F W_F}{v_O W_O} Y_{O,\infty}$$

(6) In summary

$$\frac{1}{P r} \frac{\partial^2 \tilde{T}}{\partial \eta^2} + 2(\tanh \eta) \frac{\partial \tilde{T}}{\partial \eta} - 6(\operatorname{sech}^2 \eta) \tilde{x} \frac{\partial \tilde{T}}{\partial \tilde{x}} = - D a \tilde{x}^{4/3} \tilde{Y}_F^{n_F} \tilde{Y}_O^{n_O} \tilde{T}^{n_T-n_F-n_O+1} \exp(-\tilde{E}/\tilde{T}) \tag{2.59}$$

$$\frac{1}{S c_F} \frac{\partial^2 \tilde{Y}_F}{\partial \eta^2} + 2(\tanh \eta) \frac{\partial \tilde{Y}_F}{\partial \eta} - 6(\operatorname{sech}^2 \eta) \tilde{x} \frac{\partial \tilde{Y}_F}{\partial \tilde{x}} = D a \tilde{x}^{4/3} \tilde{Y}_F^{n_F} \tilde{Y}_O^{n_O} \tilde{T}^{n_T-n_F-n_O+1} \exp(-\tilde{E}/\tilde{T}) \tag{2.61}$$

$$\frac{1}{S c_O} \frac{\partial^2 \tilde{Y}_O}{\partial \eta^2} + 2(\tanh \eta) \frac{\partial \tilde{Y}_O}{\partial \eta} - 6(\operatorname{sech}^2 \eta) \tilde{x} \frac{\partial \tilde{Y}_O}{\partial \tilde{x}} = D a \tilde{x}^{4/3} \tilde{Y}_F^{n_F} \tilde{Y}_O^{n_O} \tilde{T}^{n_T-n_F-n_O+1} \exp(-\tilde{E}/\tilde{T}) \tag{2.63}$$

$$\eta = 0, \tilde{x} = 1 : \quad \tilde{T} = \tilde{T}_0, \quad \tilde{Y}_F = \tilde{Y}_{F,0}, \quad \tilde{Y}_O = 0$$

$$\eta = 0, \tilde{x} > 1 : \quad \partial \tilde{T} / \partial \eta = \partial \tilde{Y}_F / \partial \eta = \partial \tilde{Y}_O / \partial \eta = 0$$

$$\eta \rightarrow \infty : \quad \tilde{T} \rightarrow \tilde{T}_\infty, \quad \tilde{Y}_F \rightarrow 0, \quad \tilde{Y}_O \rightarrow \tilde{Y}_{O,\infty}$$

## 2.7 Frozen Solution

In the frozen limit (designated by a subscript “f”), there is no reaction

$$(1) \quad \frac{1}{Pr} \frac{\partial^2 \tilde{T}_f}{\partial \eta^2} + 2(\tanh \eta) \frac{\partial \tilde{T}_f}{\partial \eta} - 6(\operatorname{sech}^2 \eta) \tilde{x} \frac{\partial \tilde{T}_f}{\partial \tilde{x}} = 0 \quad (2.64)$$

Since the energy and momentum equations are similar, it is expected that

$$\tilde{T}_f = c_1 + \hat{T}(\eta) \tilde{x}^{1/3}$$

$$\frac{\partial \tilde{T}_f}{\partial \tilde{x}} = -\frac{1}{3} \frac{\hat{T}}{\tilde{x}^{4/3}}, \quad \frac{\partial \tilde{T}_f}{\partial \eta} = \frac{1}{\tilde{x}^{1/3}} \frac{d\hat{T}}{d\eta}, \quad \frac{\partial^2 \tilde{T}_f}{\partial \eta^2} = \frac{1}{\tilde{x}^{1/3}} \frac{d^2 \hat{T}}{d\eta^2}$$

$$\begin{aligned} & \frac{1}{Pr} \frac{\partial^2 \tilde{T}_f}{\partial \eta^2} + 2(\tanh \eta) \frac{\partial \tilde{T}_f}{\partial \eta} - 6(\operatorname{sech}^2 \eta) \tilde{x} \frac{\partial \tilde{T}_f}{\partial \tilde{x}} \\ &= \frac{1}{Pr} \left( \frac{1}{\tilde{x}^{1/3}} \frac{d^2 \hat{T}}{d\eta^2} \right) + 2(\tanh \eta) \left( \frac{1}{\tilde{x}^{1/3}} \frac{d\hat{T}}{d\eta} \right) - 6(\operatorname{sech}^2 \eta) \tilde{x} \left( -\frac{1}{3} \frac{\hat{T}}{\tilde{x}^{4/3}} \right) \\ &= \frac{1}{\tilde{x}^{1/3}} \left[ \frac{1}{Pr} \frac{d^2 \hat{T}}{d\eta^2} + 2(\tanh \eta) \frac{d\hat{T}}{d\eta} + 2(\operatorname{sech}^2 \eta) \hat{T} \right] = \frac{1}{Pr \tilde{x}^{1/3}} \left\{ \frac{d^2 \hat{T}}{d\eta^2} + 2Pr \frac{d[(\tanh \eta) \hat{T}]}{d\eta} \right\} = 0 \end{aligned} \quad (2.65)$$

$$\text{Therefore} \quad \frac{1}{Pr} \frac{d^2 \hat{T}}{d\eta^2} + 2 \frac{d[(\tanh \eta) \hat{T}]}{d\eta} = 0 \quad \text{or} \quad \frac{d\hat{T}}{d\eta} + 2Pr(\tanh \eta) \hat{T} = c_2$$

$$\eta = 0 : \quad \partial \tilde{T}_f / \partial \eta = d\hat{T} / d\eta = 0 \quad \therefore \quad c_2 = 0 \quad (\tanh 0 = 0) \quad \text{and}$$

$$\frac{d\hat{T}}{d\eta} = -2Pr(\tanh \eta) \hat{T}$$

$$\frac{d\hat{T}}{\hat{T}} = -2Pr(\tanh \eta) d\eta = -2Pr \frac{(\sinh \eta)}{(\cosh \eta)} d\eta = -2Pr \frac{d(\cosh \eta)}{(\cosh \eta)} \quad (2.66)$$

Therefore  $\ln(\hat{T}) = -2Pr \ln(\cosh \eta) + c'$  or  $\hat{T} = c_2 (\cosh \eta)^{-2Pr} = c_2 (\operatorname{sech}^{2Pr} \eta)$

leading to  $\tilde{T}_f = c_1 + c_2 (\operatorname{sech}^{2Pr} \eta) \tilde{x}^{1/3}$

$\eta \rightarrow \infty$  :  $\tilde{T}_f \rightarrow \tilde{T}_\infty$  therefore  $c_1 = \tilde{T}_\infty$  and  $\tilde{T}_f = \tilde{T}_\infty + c_2 (\operatorname{sech}^{2Pr} \eta) \tilde{x}^{1/3}$

( $\operatorname{sech}(\infty) \rightarrow 0$ )

$\eta = 0$  ,  $\tilde{x} = 1$  :  $\tilde{T} = \tilde{T}_0$  therefore  $\tilde{T}_0 = \tilde{T}_\infty + c_2$  or  $c_2 = \tilde{T}_0 - \tilde{T}_\infty$  ( $\operatorname{sech}(0) = 1$ )

Thus :  $\tilde{T}_f = \tilde{T}_\infty + (\tilde{T}_0 - \tilde{T}_\infty) (\operatorname{sech}^{2Pr} \eta) \tilde{x}^{1/3}$  (2.67)

$$(2) \frac{1}{Sc_F} \frac{\partial^2 \tilde{Y}_{F,f}}{\partial \eta^2} + 2(\tanh \eta) \frac{\partial \tilde{Y}_{F,f}}{\partial \eta} - 6(\operatorname{sech}^2 \eta) \tilde{x} \frac{\partial \tilde{Y}_{F,f}}{\partial \tilde{x}} = 0$$

Similar to (1), the solution of  $\tilde{Y}_{F,f}$  is  $\tilde{Y}_{F,f} = c_1 + c_2 (\operatorname{sech}^{2Sc_F} \eta) \tilde{x}^{1/3}$

$\eta \rightarrow \infty$  :  $\tilde{Y}_{F,f} \rightarrow 0$  therefore  $c_1 = 0$  and  $\tilde{Y}_{F,f} = c_2 (\operatorname{sech}^{2Sc_F} \eta) \tilde{x}^{1/3}$

$\eta = 0$  ,  $\tilde{x} = 1$  :  $\tilde{Y}_{F,f} = \tilde{Y}_{F,0}$  therefore  $c_2 = \tilde{Y}_{F,0}$

Thus :  $\tilde{Y}_{F,f} = \tilde{Y}_{F,0} (\operatorname{sech}^{2Sc_F} \eta) \tilde{x}^{1/3}$  (2.68)

$$(3) \frac{1}{Sc_O} \frac{\partial^2 \tilde{Y}_{O,f}}{\partial \eta^2} + 2(\tanh \eta) \frac{\partial \tilde{Y}_{O,f}}{\partial \eta} - 6(\operatorname{sech}^2 \eta) \tilde{x} \frac{\partial \tilde{Y}_{O,f}}{\partial \tilde{x}} = 0$$

Similar to (2), the solution of  $\tilde{Y}_{O,f}$  is  $\tilde{Y}_{O,f} = c_1 + c_2 (\operatorname{sech}^{2Sc_O} \eta) \tilde{x}^{1/3}$

$\eta \rightarrow \infty$  :  $\tilde{Y}_{O,f} \rightarrow \tilde{Y}_{O,\infty}$  therefore  $c_1 = \tilde{Y}_{O,\infty}$  and  $\tilde{Y}_{O,f} = \tilde{Y}_{O,\infty} + c_2 (\operatorname{sech}^{2Sc_O} \eta) \tilde{x}^{1/3}$

$\eta = 0$  ,  $\tilde{x} = 1$  :  $\tilde{Y}_{O,f} = 0$  therefore  $0 = \tilde{Y}_{O,\infty} + c_2$  or  $c_2 = -\tilde{Y}_{O,\infty}$

Thus :  $\tilde{Y}_{O,f} = \tilde{Y}_{O,\infty} [1 - (\operatorname{sech}^{2Sc_O} \eta) \tilde{x}^{1/3}]$  (2.69)

#### (4) Summary

$\tilde{T}_f = \tilde{T}_\infty + (\tilde{T}_0 - \tilde{T}_\infty) (\operatorname{sech}^{2Pr} \eta) \tilde{x}^{1/3}$  (2.67)

$$\tilde{Y}_{F,f} = \tilde{Y}_{F,0} (\text{sech}^{2Sc_F} \eta) / \tilde{x}^{1/3} \quad (2.68)$$

$$\tilde{Y}_{O,f} = \tilde{Y}_{O,\infty} [1 - (\text{sech}^{2Sc_O} \eta) / \tilde{x}^{1/3}] \quad (2.69)$$

## 2.8 Summary of Formulation

$$\eta = \sqrt{\frac{\rho_\infty u_0}{3\mu_\infty x_0}} \frac{1}{\tilde{x}^{2/3}} \int_0^y \frac{\rho}{\rho_\infty} dy' \quad , \quad \psi = \sqrt{\frac{3\mu_\infty x_0}{\rho_\infty u_0}} \tilde{x}^{1/3} f(\eta) \quad , \quad x_0 = \frac{3M^2}{32u_0^3 \rho_\infty \mu_\infty}$$

$$\tilde{T} = \frac{c_p T}{q_F} \quad , \quad \tilde{Y}_F = Y_F \quad , \quad \tilde{Y}_O = \frac{v_F W_F}{v_O W_O} Y_O \quad , \quad \tilde{E} = \frac{c_p E}{q_F} \quad ,$$

$$Da = \frac{6x_0 v_O^{n_O} B}{v_F^{n_O-1} W_F^{n_O+n_F-1} u_0} \left( \frac{q_F}{c_p} \right)^{n_T-n_F-n_O+1} \left( \frac{\rho}{R} \right)^{n_F+n_O-1}$$

$$Pr = \frac{\mu}{\lambda / c_p} = \frac{\rho \mu}{\rho \lambda / c_p} \quad , \quad Sc_i = \frac{\mu}{\rho D_i} = \frac{\rho \mu}{\rho^2 D_i} \quad , \quad Le_i = \frac{\lambda / c_p}{\rho D_i} = \frac{Sc_i}{Pr}$$

$$f = \tanh \eta \quad , \quad df / d\eta = \text{sech}^2 \eta \quad , \quad u = u_0 (\text{sech}^2 \eta) \tilde{x}^{1/3}$$

$$\frac{1}{Pr} \frac{\partial^2 \tilde{T}}{\partial \eta^2} + 2(\tanh \eta) \frac{\partial \tilde{T}}{\partial \eta} - 6(\text{sech}^2 \eta) \tilde{x} \frac{\partial \tilde{T}}{\partial \tilde{x}} = -Da \tilde{x}^{4/3} \tilde{Y}_F^{n_F} \tilde{Y}_O^{n_O} \tilde{T}^{n_T-n_F-n_O+1} \exp(-\tilde{E} / \tilde{T})$$

$$\frac{1}{Sc_F} \frac{\partial^2 \tilde{Y}_F}{\partial \eta^2} + 2(\tanh \eta) \frac{\partial \tilde{Y}_F}{\partial \eta} - 6(\text{sech}^2 \eta) \tilde{x} \frac{\partial \tilde{Y}_F}{\partial \tilde{x}} = Da \tilde{x}^{4/3} \tilde{Y}_F^{n_F} \tilde{Y}_O^{n_O} \tilde{T}^{n_T-n_F-n_O+1} \exp(-\tilde{E} / \tilde{T})$$

$$\frac{1}{Sc_O} \frac{\partial^2 \tilde{Y}_O}{\partial \eta^2} + 2(\tanh \eta) \frac{\partial \tilde{Y}_O}{\partial \eta} - 6(\text{sech}^2 \eta) \tilde{x} \frac{\partial \tilde{Y}_O}{\partial \tilde{x}} = Da \tilde{x}^{4/3} \tilde{Y}_F^{n_F} \tilde{Y}_O^{n_O} \tilde{T}^{n_T-n_F-n_O+1} \exp(-\tilde{E} / \tilde{T})$$

$$\eta = 0 \quad , \quad \tilde{x} = 1 \quad : \quad \tilde{T} = \tilde{T}_0 \quad , \quad \tilde{Y}_F = \tilde{Y}_{F,0} \quad , \quad \tilde{Y}_O = 0$$

$$\eta = 0 \quad , \quad \tilde{x} > 1 \quad : \quad \partial \tilde{T} / \partial \eta = \partial \tilde{Y}_F / \partial \eta = \partial \tilde{Y}_O / \partial \eta = 0$$

$$\eta \rightarrow \infty \quad : \quad \tilde{T} \rightarrow \tilde{T}_\infty \quad , \quad \tilde{Y}_F \rightarrow 0 \quad , \quad \tilde{Y}_O \rightarrow \tilde{Y}_{O,\infty}$$

$$\tilde{T}_f = \tilde{T}_\infty + (\tilde{T}_0 - \tilde{T}_\infty) (\text{sech}^{2Pr} \eta) \tilde{x}^{1/3}$$

$$\tilde{Y}_{F,f} = \tilde{Y}_{F,0} (\text{sech}^{2Sc_F} \eta) / \tilde{x}^{1/3}$$

$$\tilde{Y}_{O,f} = \tilde{Y}_{O,\infty} [1 - (\text{sech}^{2Sc_O} \eta) / \tilde{x}^{1/3}]$$

## Chapter 3: Ignition Analysis

### 3.1 Description of Analysis

A total of three ignition analyses will be presented in this chapter. The first two analyses pertain to the cool jet flowing into hot ambient scenario, for two categories of fuels with local  $Le_F < 1$  (hydrogen belongs to this category) and  $Le_F \approx 1$  (for fuels like methane). The third analysis is for the hot jet flowing into cool ambient scenario.

The results and discussion will be based on ignition analysis I (for cool jet case) and analysis III (for hot jet case), as the main focus is on the spontaneous ignition of hydrogen, which occur when the temperature and reaction rate conditions in the inner region (which is the reaction zone) match the outer region (which lies outside the reaction zone). The second analysis is presented for comparison purposes between hydrogen and other common fuels like methane and propane.

### 3.2 Ignition Analysis I: $T_\infty > T_0, Le_F < 1$

Because spontaneous ignition is primarily controlled by temperature, ignition occurs at  $\eta \rightarrow \infty$  if successful. This is the outer edge of the jet.

#### **(A) Outer Solutions**

In the outer region, there is no reaction because of the low temperature. Before ignition, there is only weak reaction. All the variables deviate from the frozen solutions by  $O(\varepsilon)$ .

$$\tilde{T} = \tilde{T}_f + \varepsilon \Theta + O(\varepsilon^2) \quad ; \quad \tilde{T}_f = \tilde{T}_\infty + (\tilde{T}_0 - \tilde{T}_\infty) (\text{sech}^{2Pr} \eta) \tilde{x}^{1/3} = \tilde{T}_\infty - (\tilde{T}_\infty - \tilde{T}_0) (\text{sech}^{2Pr} \eta) \tilde{x}^{1/3}$$

$$\tilde{Y}_F = \tilde{Y}_{F,f} + \varepsilon \Phi_F + O(\varepsilon^2) \quad ; \quad \tilde{Y}_{F,f} = \tilde{Y}_{F0} (\text{sech}^{2Sc_F} \eta) / \tilde{x}^{1/3}$$

$$\tilde{Y}_O = \tilde{Y}_{O,f} + \varepsilon \Phi_O + O(\varepsilon^2) \quad ; \quad \tilde{Y}_{O,f} = \tilde{Y}_{O,\infty} [1 - (\operatorname{sech}^{2Sc_O} \eta) / \tilde{x}^{1/3}]$$

$$\eta = 0, \quad \tilde{x} = 1 : \quad \tilde{T} = \tilde{T}_0, \quad \tilde{Y}_F = \tilde{Y}_{F0}, \quad \tilde{Y}_O = 0 \quad ; \quad \eta = 0, \quad \tilde{x} > 1 :$$

$$\partial \tilde{T} / \partial \eta = \partial \tilde{Y}_F / \partial \eta = \partial \tilde{Y}_O / \partial \eta = 0$$

$$(1) \quad \frac{1}{Pr} \frac{\partial^2 \tilde{T}}{\partial \eta^2} + 2(\tanh \eta) \frac{\partial \tilde{T}}{\partial \eta} - 6(\operatorname{sech}^2 \eta) \tilde{x} \frac{\partial \tilde{T}}{\partial \tilde{x}} = 0$$

$$\frac{1}{Pr} \frac{\partial^2 [\tilde{T}_f + \varepsilon \Theta + O(\varepsilon^2)]}{\partial \eta^2} + 2(\tanh \eta) \frac{\partial [\tilde{T}_f + \varepsilon \Theta + O(\varepsilon^2)]}{\partial \eta} - 6(\operatorname{sech}^2 \eta) \tilde{x} \frac{\partial [\tilde{T}_f + \varepsilon \Theta + O(\varepsilon^2)]}{\partial \tilde{x}} = 0$$

$$\left[ \frac{1}{Pr} \frac{\partial^2 \tilde{T}_f}{\partial \eta^2} + 2(\tanh \eta) \frac{\partial \tilde{T}_f}{\partial \eta} - 6(\operatorname{sech}^2 \eta) \tilde{x} \frac{\partial \tilde{T}_f}{\partial \tilde{x}} \right] + \varepsilon \left[ \frac{1}{Pr} \frac{\partial^2 \Theta}{\partial \eta^2} + 2(\tanh \eta) \frac{\partial \Theta}{\partial \eta} - 6(\operatorname{sech}^2 \eta) \tilde{x} \frac{\partial \Theta}{\partial \tilde{x}} \right] + O(\varepsilon^2) = 0$$

$$\text{Since } \frac{1}{Pr} \frac{\partial^2 \tilde{T}_f}{\partial \eta^2} + 2(\tanh \eta) \frac{\partial \tilde{T}_f}{\partial \eta} - 6(\operatorname{sech}^2 \eta) \tilde{x} \frac{\partial \tilde{T}_f}{\partial \tilde{x}} = 0, \text{ we have}$$

$$\frac{1}{Pr} \frac{\partial^2 \Theta}{\partial \eta^2} + 2(\tanh \eta) \frac{\partial \Theta}{\partial \eta} - 6(\operatorname{sech}^2 \eta) \tilde{x} \frac{\partial \Theta}{\partial \tilde{x}} = 0 \quad (3.1)$$

By the same approach as that for the frozen solution, we obtain

$$\Theta = a_T + \bar{a}_T (\operatorname{sech}^{2Pr} \eta) \tilde{x}^{1/3}$$

$$\eta = 0, \quad \tilde{x} = 1 : \quad \tilde{T} = \tilde{T}_f + \varepsilon \Theta + O(\varepsilon^2) = \tilde{T}_0 \quad \therefore \quad \Theta = 0 \quad \Rightarrow \quad 0 = a_T + \bar{a}_T \quad \text{and}$$

$$\Theta = a_T [1 - (\operatorname{sech}^{2Pr} \eta) \tilde{x}^{1/3}]$$

The condition  $\eta = 0, \quad \tilde{x} > 1 : \quad \partial \tilde{T} / \partial \eta = 0$  is automatically satisfied.

$$\text{Thus : } \quad \tilde{T} = \tilde{T}_f + \varepsilon \Theta + O(\varepsilon^2) = (\tilde{T}_\infty + \varepsilon a_T) - [(\tilde{T}_\infty - \tilde{T}_0) + \varepsilon a_T] (\operatorname{sech}^{2Pr} \eta) \tilde{x}^{1/3} + O(\varepsilon^2)$$

$$(2) \quad \frac{1}{Sc_F} \frac{\partial^2 \tilde{Y}_F}{\partial \eta^2} + 2(\tanh \eta) \frac{\partial \tilde{Y}_F}{\partial \eta} - 6(\operatorname{sech}^2 \eta) \tilde{x} \frac{\partial \tilde{Y}_F}{\partial \tilde{x}} = 0$$

$$\frac{1}{Sc_F} \frac{\partial^2 [\tilde{Y}_{F,f} + \varepsilon \Phi_F + O(\varepsilon^2)]}{\partial \eta^2} + 2(\tanh \eta) \frac{\partial [\tilde{Y}_{F,f} + \varepsilon \Phi_F + O(\varepsilon^2)]}{\partial \eta} - 6(\operatorname{sech}^2 \eta) \tilde{x} \frac{\partial [\tilde{Y}_{F,f} + \varepsilon \Phi_F + O(\varepsilon^2)]}{\partial \tilde{x}} = 0$$

$$\left[ \frac{1}{S_{cF}} \frac{\partial^2 \tilde{Y}_{F,f}}{\partial \eta^2} + 2(\tanh \eta) \frac{\partial \tilde{Y}_{F,f}}{\partial \eta} - 6(\operatorname{sech}^2 \eta) \tilde{x} \frac{\partial \tilde{Y}_{F,f}}{\partial \tilde{x}} \right] +$$

$$+ \varepsilon \left[ \frac{1}{S_{cF}} \frac{\partial^2 \Phi_F}{\partial \eta^2} + 2(\tanh \eta) \frac{\partial \Phi_F}{\partial \eta} - 6(\operatorname{sech}^2 \eta) \tilde{x} \frac{\partial \Phi_F}{\partial \tilde{x}} \right] + O(\varepsilon^2) = 0$$

Since  $\frac{1}{S_{cF}} \frac{\partial^2 \tilde{Y}_{F,f}}{\partial \eta^2} + 2(\tanh \eta) \frac{\partial \tilde{Y}_{F,f}}{\partial \eta} - 6(\operatorname{sech}^2 \eta) \tilde{x} \frac{\partial \tilde{Y}_{F,f}}{\partial \tilde{x}} = 0$ , we have

$$\frac{1}{S_{cF}} \frac{\partial^2 \Phi_F}{\partial \eta^2} + 2(\tanh \eta) \frac{\partial \Phi_F}{\partial \eta} - 6(\operatorname{sech}^2 \eta) \tilde{x} \frac{\partial \Phi_F}{\partial \tilde{x}} = 0 \quad (3.2)$$

By the same approach as that for the frozen solution, we obtain

$$\Phi_F = a_F + \bar{a}_F (\operatorname{sech}^{2S_{cF}} \eta) \tilde{x}^{1/3}$$

$$\eta = 0, \quad \tilde{x} = 1 : \quad \tilde{Y}_F = \tilde{Y}_{F,f} + \varepsilon \Phi_F + O(\varepsilon^2) = \tilde{Y}_{F0} \quad \therefore \quad \Phi_F = 0 \quad \Rightarrow \quad 0 = a_F + \bar{a}_F \quad \text{and}$$

$$\Phi_F = a_F [1 - (\operatorname{sech}^{2S_{cF}} \eta) \tilde{x}^{1/3}]$$

$$\text{Thus :} \quad \tilde{Y}_F = \tilde{Y}_{F,f} + \varepsilon \Phi_F + O(\varepsilon^2) = \varepsilon a_F + (\tilde{Y}_{F0} - \varepsilon a_F) (\operatorname{sech}^{2S_{cF}} \eta) \tilde{x}^{1/3} + O(\varepsilon^2)$$

$$(3) \quad \frac{1}{S_{cO}} \frac{\partial^2 \tilde{Y}_O}{\partial \eta^2} + 2(\tanh \eta) \frac{\partial \tilde{Y}_O}{\partial \eta} - 6(\operatorname{sech}^2 \eta) \tilde{x} \frac{\partial \tilde{Y}_O}{\partial \tilde{x}} = 0$$

$$\frac{1}{S_{cO}} \frac{\partial^2 [\tilde{Y}_{O,f} + \varepsilon \Phi_O + O(\varepsilon^2)]}{\partial \eta^2} + 2(\tanh \eta) \frac{\partial [\tilde{Y}_{O,f} + \varepsilon \Phi_O + O(\varepsilon^2)]}{\partial \eta} - 6(\operatorname{sech}^2 \eta) \tilde{x} \frac{\partial [\tilde{Y}_{O,f} + \varepsilon \Phi_O + O(\varepsilon^2)]}{\partial \tilde{x}} = 0$$

$$\left[ \frac{1}{S_{cO}} \frac{\partial^2 \tilde{Y}_{O,f}}{\partial \eta^2} + 2(\tanh \eta) \frac{\partial \tilde{Y}_{O,f}}{\partial \eta} - 6(\operatorname{sech}^2 \eta) \tilde{x} \frac{\partial \tilde{Y}_{O,f}}{\partial \tilde{x}} \right] +$$

$$+ \varepsilon \left[ \frac{1}{S_{cO}} \frac{\partial^2 \Phi_O}{\partial \eta^2} + 2(\tanh \eta) \frac{\partial \Phi_O}{\partial \eta} - 6(\operatorname{sech}^2 \eta) \tilde{x} \frac{\partial \Phi_O}{\partial \tilde{x}} \right] + O(\varepsilon^2) = 0$$

Since  $\frac{1}{S_{cO}} \frac{\partial^2 \tilde{Y}_{O,f}}{\partial \eta^2} + 2(\tanh \eta) \frac{\partial \tilde{Y}_{O,f}}{\partial \eta} - 6(\operatorname{sech}^2 \eta) \tilde{x} \frac{\partial \tilde{Y}_{O,f}}{\partial \tilde{x}} = 0$ , we have

$$\frac{1}{S_{cO}} \frac{\partial^2 \Phi_O}{\partial \eta^2} + 2(\tanh \eta) \frac{\partial \Phi_O}{\partial \eta} - 6(\operatorname{sech}^2 \eta) \tilde{x} \frac{\partial \Phi_O}{\partial \tilde{x}} = 0 \quad (3.3)$$

By the same approach as that for the frozen solution, we obtain

$$\Phi_O = a_O + \bar{a}_O (\operatorname{sech}^{2S_{cO}} \eta) \tilde{x}^{1/3}$$

$$\eta = 0, \quad \tilde{x} = 1 : \quad \tilde{Y}_O = \tilde{Y}_{O,f} + \varepsilon \Phi_O + O(\varepsilon^2) = 0 \quad \therefore \quad \Phi_O = 0 \quad \Rightarrow \quad 0 = a_O + \bar{a}_O \quad \text{and}$$

$$\Phi_O = a_O [1 - (\text{sech}^{2S_{cO}} \eta) \tilde{x}^{1/3}]$$

$$\text{Thus :} \quad \tilde{Y}_O = \tilde{Y}_{O,f} + \varepsilon \Phi_O + O(\varepsilon^2) = (\tilde{Y}_{O,\infty} + \varepsilon a_O) [1 - (\text{sech}^{2S_{cO}} \eta) \tilde{x}^{1/3}] + O(\varepsilon^2)$$

#### (4) Summary

$$\tilde{T} = (\tilde{T}_\infty + \varepsilon a_T) - [(\tilde{T}_\infty - \tilde{T}_0) + \varepsilon a_T] (\text{sech}^{2P_r} \eta) \tilde{x}^{1/3} + O(\varepsilon^2) \quad (3.4)$$

$$\tilde{Y}_F = \varepsilon a_F + (\tilde{Y}_{F0} - \varepsilon a_F) (\text{sech}^{2S_{cF}} \eta) \tilde{x}^{1/3} + O(\varepsilon^2) \quad ; \quad (3.5)$$

$$\tilde{Y}_O = (\tilde{Y}_{O,\infty} + \varepsilon a_O) [1 - (\text{sech}^{2S_{cO}} \eta) \tilde{x}^{1/3}] + O(\varepsilon^2) \quad (3.6)$$

### (B) Coordination Transformation

Define  $\xi = \text{sech}^2 \eta$  then at  $\eta = 0, \quad \xi = 1$  ; as  $\eta \rightarrow \infty, \quad \xi \rightarrow 0$  ;

$$\tanh^2 \eta = 1 - \text{sech}^2 \eta = 1 - \xi \quad ; \quad d(\tanh \eta) / d\eta = \text{sech}^2 \eta = \xi$$

$$\begin{aligned} \frac{\partial}{\partial \eta} &= \frac{\partial}{\partial \xi} \frac{d\xi}{d\eta} = \frac{d(\text{sech}^2 \eta)}{d\eta} \frac{\partial}{\partial \xi} = 2(\text{sech} \eta) [ -(\text{sech} \eta) (\tanh \eta) ] \frac{\partial}{\partial \xi} = \\ &= -2(\text{sech}^2 \eta) (\tanh \eta) \frac{\partial}{\partial \xi} = -2(\tanh \eta) \xi \frac{\partial}{\partial \xi} \end{aligned}$$

$$\begin{aligned} \frac{\partial^2}{\partial \eta^2} &= \frac{\partial}{\partial \eta} \left[ -2(\tanh \eta) \xi \frac{\partial}{\partial \xi} \right] = -2 \left[ \frac{d(\tanh \eta)}{d\eta} \xi \frac{\partial}{\partial \xi} + (\tanh \eta) \frac{\partial}{\partial \eta} \left( \xi \frac{\partial}{\partial \xi} \right) \right] \\ &= -2 \left\{ \xi^2 \frac{\partial}{\partial \xi} + (\tanh \eta) \left[ -2(\tanh \eta) \xi \frac{\partial}{\partial \xi} \left( \xi \frac{\partial}{\partial \xi} \right) \right] \right\} \\ &= -2\xi^2 \frac{\partial}{\partial \xi} + 4(\tanh^2 \eta) \left( \xi \frac{\partial}{\partial \xi} + \xi^2 \frac{\partial^2}{\partial \xi^2} \right) = 4\xi(1-\xi) \left( \xi \frac{\partial^2}{\partial \xi^2} + \frac{\partial}{\partial \xi} \right) - 2\xi^2 \frac{\partial}{\partial \xi} \end{aligned} \quad (3.7)$$

$$(1) \quad \frac{1}{Pr} \frac{\partial^2 \tilde{T}}{\partial \eta^2} + 2(\tanh \eta) \frac{\partial \tilde{T}}{\partial \eta} - 6(\text{sech}^2 \eta) \tilde{x} \frac{\partial \tilde{T}}{\partial \tilde{x}} = -Da \tilde{x}^{4/3} \tilde{Y}_F^{n_F} \tilde{Y}_O^{n_O} \tilde{T}^{n_T - n_F - n_O + 1} \exp(-\tilde{E}/\tilde{T})$$

$$\begin{aligned} &\frac{1}{Pr} \frac{\partial^2 \tilde{T}}{\partial \eta^2} + 2(\tanh \eta) \frac{\partial \tilde{T}}{\partial \eta} - 6(\text{sech}^2 \eta) \tilde{x} \frac{\partial \tilde{T}}{\partial \tilde{x}} \\ &= \frac{1}{Pr} \left[ 4\xi(1-\xi) \left( \xi \frac{\partial^2 \tilde{T}}{\partial \xi^2} + \frac{\partial \tilde{T}}{\partial \xi} \right) - 2\xi^2 \frac{\partial \tilde{T}}{\partial \xi} \right] + 2(\tanh \eta) \left[ -2(\text{sech}^2 \eta) (\tanh \eta) \frac{\partial \tilde{T}}{\partial \xi} \right] - 6\xi \tilde{x} \frac{\partial \tilde{T}}{\partial \tilde{x}} \end{aligned}$$

$$\begin{aligned}
&= \frac{1}{Pr} \left[ 4\xi(1-\xi) \left( \xi \frac{\partial \tilde{T}}{\partial \xi^2} + \frac{\partial \tilde{T}}{\partial \xi} \right) - 2\xi^2 \frac{\partial \tilde{T}}{\partial \xi} \right] - 4\xi(1-\xi) \frac{\partial \tilde{T}}{\partial \xi} - 6\xi \tilde{x} \frac{\partial \tilde{T}}{\partial \tilde{x}} \\
&= 4\xi(1-\xi) \left[ \frac{1}{Pr} \xi \frac{\partial \tilde{T}}{\partial \xi^2} + \left( \frac{1}{Pr} - 1 \right) \frac{\partial \tilde{T}}{\partial \xi} \right] - \frac{2}{Pr} \xi^2 \frac{\partial \tilde{T}}{\partial \xi} - 6\xi \tilde{x} \frac{\partial \tilde{T}}{\partial \tilde{x}}
\end{aligned}$$

Thus :

$$4(1-\xi) \left[ \frac{1}{Pr} \xi^2 \frac{\partial \tilde{T}}{\partial \xi^2} + \left( \frac{1}{Pr} - 1 \right) \xi \frac{\partial \tilde{T}}{\partial \xi} \right] - \xi \left( \frac{2}{Pr} \xi \frac{\partial \tilde{T}}{\partial \xi} + 6\tilde{x} \frac{\partial \tilde{T}}{\partial \tilde{x}} \right) = -Da \tilde{x}^{4/3} \tilde{Y}_F^{n_F} \tilde{Y}_O^{n_O} \tilde{T}^{n_T - n_F - n_O + 1} \exp(-\tilde{E}/\tilde{T}) \quad (3.8)$$

$$(2) \quad \frac{1}{Sc_F} \frac{\partial^2 \tilde{Y}_F}{\partial \eta^2} + 2(\tanh \eta) \frac{\partial \tilde{Y}_F}{\partial \eta} - 6(\operatorname{sech}^2 \eta) \tilde{x} \frac{\partial \tilde{Y}_F}{\partial \tilde{x}} = Da \tilde{x}^{4/3} \tilde{Y}_F^{n_F} \tilde{Y}_O^{n_O} \tilde{T}^{n_T - n_F - n_O + 1} \exp(-\tilde{E}/\tilde{T})$$

The equation is similar to (1). By the same approach as that of (1), we have

$$4(1-\xi) \left[ \frac{1}{Sc_F} \xi^2 \frac{\partial \tilde{Y}_F}{\partial \xi^2} + \left( \frac{1}{Sc_F} - 1 \right) \xi \frac{\partial \tilde{Y}_F}{\partial \xi} \right] - \xi \left( \frac{2}{Sc_F} \xi \frac{\partial \tilde{Y}_F}{\partial \xi} + 6\tilde{x} \frac{\partial \tilde{Y}_F}{\partial \tilde{x}} \right) = Da \tilde{x}^{4/3} \tilde{Y}_F^{n_F} \tilde{Y}_O^{n_O} \tilde{T}^{n_T - n_F - n_O + 1} \exp(-\tilde{E}/\tilde{T}) \quad (3.9)$$

$$(3) \quad \frac{1}{Sc_O} \frac{\partial^2 \tilde{Y}_O}{\partial \eta^2} + 2(\tanh \eta) \frac{\partial \tilde{Y}_O}{\partial \eta} - 6(\operatorname{sech}^2 \eta) \tilde{x} \frac{\partial \tilde{Y}_O}{\partial \tilde{x}} = Da \tilde{x}^{4/3} \tilde{Y}_F^{n_F} \tilde{Y}_O^{n_O} \tilde{T}^{n_T - n_F - n_O + 1} \exp(-\tilde{E}/\tilde{T})$$

The equation is similar to (1). By the same approach as that of (1), we have

$$4(1-\xi) \left[ \frac{1}{Sc_O} \xi^2 \frac{\partial \tilde{Y}_O}{\partial \xi^2} + \left( \frac{1}{Sc_O} - 1 \right) \xi \frac{\partial \tilde{Y}_O}{\partial \xi} \right] - \xi \left( \frac{2}{Sc_O} \xi \frac{\partial \tilde{Y}_O}{\partial \xi} + 6\tilde{x} \frac{\partial \tilde{Y}_O}{\partial \tilde{x}} \right) = Da \tilde{x}^{4/3} \tilde{Y}_F^{n_F} \tilde{Y}_O^{n_O} \tilde{T}^{n_T - n_F - n_O + 1} \exp(-\tilde{E}/\tilde{T}) \quad (3.10)$$

$$(4) \quad \eta \rightarrow \infty : \quad \tilde{T} \rightarrow \tilde{T}_\infty \quad , \quad \tilde{Y}_F \rightarrow 0 \quad , \quad \tilde{Y}_O \rightarrow \tilde{Y}_{O,\infty} \quad \Rightarrow \quad \xi = 0 : \quad \tilde{T} = \tilde{T}_\infty \quad ,$$

$$\tilde{Y}_F = 0 \quad , \quad \tilde{Y}_O = \tilde{Y}_{O,\infty}$$

(5) Frozen solutions

$$\tilde{T}_f = \tilde{T}_\infty - (\tilde{T}_\infty - \tilde{T}_0) (\operatorname{sech}^{2Pr} \eta) \tilde{x}^{1/3} \quad \Rightarrow \quad \tilde{T}_f = \tilde{T}_\infty - (\tilde{T}_\infty - \tilde{T}_0) \xi^{Pr} \tilde{x}^{1/3} \quad (3.11)$$

$$\tilde{Y}_{F,f} = \tilde{Y}_{F0} (\operatorname{sech}^{2Sc_F} \eta) \tilde{x}^{1/3} \quad \Rightarrow \quad \tilde{Y}_{F,f} = \tilde{Y}_{F0} \xi^{Sc_F} \tilde{x}^{1/3} \quad (3.12)$$

$$\tilde{Y}_{O,f} = \tilde{Y}_{O,\infty} [1 - (\text{sech}^{2S_{Co}} \eta) / \tilde{x}^{1/3}] \quad \Rightarrow \quad \tilde{Y}_{O,f} = \tilde{Y}_{O,\infty} (1 - \xi^{S_{Co}} / \tilde{x}^{1/3}) \quad (3.13)$$

(6) Outer solutions :

$$\tilde{T} = (\tilde{T}_\infty + \varepsilon a_T) - [(\tilde{T}_\infty - \tilde{T}_0) + \varepsilon a_T] \xi^{Pr} / \tilde{x}^{1/3} + O(\varepsilon^2) \quad (3.14)$$

$$\tilde{Y}_F = \varepsilon a_F + (\tilde{Y}_{F0} - \varepsilon a_F) \xi^{S_{CF}} / \tilde{x}^{1/3} + O(\varepsilon^2) \quad ; \quad (3.15)$$

$$\tilde{Y}_O = (\tilde{Y}_{O,\infty} + \varepsilon a_O) (1 - \xi^{S_{Co}} / \tilde{x}^{1/3}) + O(\varepsilon^2) \quad (3.16)$$

(7) Summary

$$4(1-\xi) \left[ \frac{1}{Pr} \xi^2 \frac{\partial^2 \tilde{T}}{\partial \xi^2} + \left( \frac{1}{Pr} - 1 \right) \xi \frac{\partial \tilde{T}}{\partial \xi} \right] - \xi \left( \frac{2}{Pr} \xi \frac{\partial \tilde{T}}{\partial \xi} + 6\tilde{x} \frac{\partial \tilde{T}}{\partial \tilde{x}} \right) = -Da \tilde{x}^{A/3} \tilde{Y}_F^{n_F} \tilde{Y}_O^{n_O} \tilde{T}^{n_T - n_F - n_O + 1} \exp(-\tilde{E}/\tilde{T})$$

$$4(1-\xi) \left[ \frac{1}{S_{CF}} \xi^2 \frac{\partial^2 \tilde{Y}_F}{\partial \xi^2} + \left( \frac{1}{S_{CF}} - 1 \right) \xi \frac{\partial \tilde{Y}_F}{\partial \xi} \right] - \xi \left( \frac{2}{S_{CF}} \xi \frac{\partial \tilde{Y}_F}{\partial \xi} + 6\tilde{x} \frac{\partial \tilde{Y}_F}{\partial \tilde{x}} \right) = Da \tilde{x}^{A/3} \tilde{Y}_F^{n_F} \tilde{Y}_O^{n_O} \tilde{T}^{n_T - n_F - n_O + 1} \exp(-\tilde{E}/\tilde{T})$$

$$4(1-\xi) \left[ \frac{1}{S_{CO}} \xi^2 \frac{\partial^2 \tilde{Y}_O}{\partial \xi^2} + \left( \frac{1}{S_{CO}} - 1 \right) \xi \frac{\partial \tilde{Y}_O}{\partial \xi} \right] - \xi \left( \frac{2}{S_{CO}} \xi \frac{\partial \tilde{Y}_O}{\partial \xi} + 6\tilde{x} \frac{\partial \tilde{Y}_O}{\partial \tilde{x}} \right) = Da \tilde{x}^{A/3} \tilde{Y}_F^{n_F} \tilde{Y}_O^{n_O} \tilde{T}^{n_T - n_F - n_O + 1} \exp(-\tilde{E}/\tilde{T})$$

$$\xi = 0 : \quad \tilde{T} = \tilde{T}_\infty \quad , \quad \tilde{Y}_F = 0 \quad , \quad \tilde{Y}_O = \tilde{Y}_{O,\infty}$$

$$\text{Frozen solutions :} \quad \tilde{T}_f = \tilde{T}_\infty - (\tilde{T}_\infty - \tilde{T}_0) \xi^{Pr} / \tilde{x}^{1/3} \quad ; \quad \tilde{Y}_{F,f} = \tilde{Y}_{F0} \xi^{S_{CF}} / \tilde{x}^{1/3} \quad ;$$

$$\tilde{Y}_{O,f} = \tilde{Y}_{O,\infty} (1 - \xi^{S_{Co}} / \tilde{x}^{1/3})$$

$$\text{Outer solutions :} \quad \tilde{T} = (\tilde{T}_\infty + \varepsilon a_T) - [(\tilde{T}_\infty - \tilde{T}_0) + \varepsilon a_T] \xi^{Pr} / \tilde{x}^{1/3} + O(\varepsilon^2)$$

$$\tilde{Y}_F = \varepsilon a_F + (\tilde{Y}_{F0} - \varepsilon a_F) \xi^{S_{CF}} / \tilde{x}^{1/3} + O(\varepsilon^2) \quad ; \quad \tilde{Y}_O = (\tilde{Y}_{O,\infty} + \varepsilon a_O) (1 - \xi^{S_{Co}} / \tilde{x}^{1/3}) + O(\varepsilon^2)$$

(C) Inner Expansion

Define inner variable :  $\xi^{Pr} = \varepsilon \tilde{x}^{1/3} \zeta / \tilde{Y}_{F0}$  or  $\zeta = \tilde{Y}_{F0} \xi^{Pr} / (\varepsilon \tilde{x}^{1/3})$  ,  $\varepsilon = \tilde{T}_\infty^2 / \tilde{E}$  ,

$$\alpha = (\tilde{T}_\infty - \tilde{T}_0) / \tilde{Y}_{F0} \quad ; \quad \xi = 0 : \quad \zeta = 0 \quad (3.17)$$

$$\tilde{T} = \tilde{T}_f (\xi^{Pr} = \varepsilon \tilde{x}^{1/3} \zeta / \tilde{Y}_{F0}) + \varepsilon \theta + O(\varepsilon^2) = \tilde{T}_\infty - (\tilde{T}_\infty - \tilde{T}_0) (\varepsilon \tilde{x}^{1/3} \zeta / \tilde{Y}_{F0}) \tilde{x}^{1/3} + \varepsilon \theta + O(\varepsilon^2) = \tilde{T}_\infty + \varepsilon (\theta - \alpha \zeta) + O(\varepsilon^2)$$

$$\tilde{Y}_F = \tilde{Y}_{F,f} (\xi^{Pr} = \varepsilon \tilde{x}^{1/3} \zeta / \tilde{Y}_{F0}) + \varepsilon \phi_F + O(\varepsilon^2) = \tilde{Y}_{F0} (\varepsilon \tilde{x}^{1/3} \zeta / \tilde{Y}_{F0})^{S_{CF}/Pr} / \tilde{x}^{1/3} + \varepsilon \phi_F + O(\varepsilon^2) = \varepsilon^{Le_F} (\tilde{Y}_{F0} / \tilde{x}^{1/3})^{1 - Le_F} \zeta^{Le_F} + \varepsilon \phi_F + O(\varepsilon^2)$$

For  $Le_F < 1$  (for hydrogen,  $Le_F \approx 0.5$ ) ,  $\varepsilon^{Le_F} \gg \varepsilon$  and

$$\tilde{Y}_F = \varepsilon^{Le_F} (\tilde{Y}_{F0} / \tilde{x}^{1/3})^{1-Le_F} \zeta^{Le_F} + O(\varepsilon)$$

$$\begin{aligned} \tilde{Y}_O &= \tilde{Y}_{O,f} (\zeta^{Pr} = \varepsilon \tilde{x}^{1/3} \zeta / \tilde{Y}_{F0}) + \varepsilon \phi_O + O(\varepsilon^2) = \tilde{Y}_{O,\infty} [1 - (\varepsilon \tilde{x}^{1/3} \zeta / \tilde{Y}_{F0})^{Sc_O / Pr} / \tilde{x}^{1/3}] \\ &+ \varepsilon \phi_O + O(\varepsilon^2) = \tilde{Y}_{O,\infty} + O(\varepsilon^{Le_O}; \varepsilon) \end{aligned}$$

$$\frac{\partial}{\partial \xi} = \frac{\partial}{\partial \zeta} \frac{\partial \zeta}{\partial \xi} = \frac{\tilde{Y}_{F0} Pr}{\varepsilon \tilde{x}^{1/3}} \zeta^{Pr-1} \frac{\partial}{\partial \zeta} \quad \text{therefore} \quad \xi \frac{\partial}{\partial \xi} = Pr \frac{\tilde{Y}_{F0}}{\varepsilon \tilde{x}^{1/3}} \zeta^{Pr} \frac{\partial}{\partial \zeta} = Pr \zeta \frac{\partial}{\partial \zeta} \quad \text{or}$$

$$\frac{1}{Pr} \xi \frac{\partial}{\partial \xi} = \zeta \frac{\partial}{\partial \zeta}$$

$$\begin{aligned} \frac{\partial^2}{\partial \xi^2} &= \frac{\partial}{\partial \xi} \left( \frac{\partial}{\partial \xi} \right) = \frac{\partial}{\partial \xi} \left( \frac{\tilde{Y}_{F0} Pr}{\varepsilon \tilde{x}^{1/3}} \zeta^{Pr-1} \frac{\partial}{\partial \zeta} \right) = \frac{\tilde{Y}_{F0} Pr}{\varepsilon \tilde{x}^{1/3}} \left[ (Pr-1) \zeta^{Pr-2} \frac{\partial}{\partial \zeta} + \zeta^{Pr-1} \frac{\partial}{\partial \xi} \left( \frac{\partial}{\partial \zeta} \right) \right] \\ &= \frac{\tilde{Y}_{F0} Pr}{\varepsilon \tilde{x}^{1/3}} \left[ (Pr-1) \zeta^{Pr-2} \frac{\partial}{\partial \zeta} + \zeta^{Pr-1} \frac{\tilde{Y}_{F0} Pr}{\varepsilon \tilde{x}^{1/3}} \zeta^{Pr-1} \frac{\partial}{\partial \zeta} \left( \frac{\partial}{\partial \zeta} \right) \right] = \frac{Pr}{\zeta^2} \left[ Pr \zeta^2 \frac{\partial^2}{\partial \zeta^2} + (Pr-1) \zeta \frac{\partial}{\partial \zeta} \right] \end{aligned}$$

$$\frac{1}{Pr} \zeta^2 \frac{\partial^2}{\partial \xi^2} = Pr \zeta^2 \frac{\partial^2}{\partial \zeta^2} + (Pr-1) \zeta \frac{\partial}{\partial \zeta}$$

$$\frac{1}{Pr} \zeta^2 \frac{\partial^2}{\partial \xi^2} + \left( \frac{1}{Pr} - 1 \right) \xi \frac{\partial}{\partial \xi} = Pr \zeta^2 \frac{\partial^2}{\partial \zeta^2} + (Pr-1) \zeta \frac{\partial}{\partial \zeta} + \left( \frac{1}{Pr} - 1 \right) Pr \zeta \frac{\partial}{\partial \zeta} = Pr \zeta^2 \frac{\partial^2}{\partial \zeta^2} \quad (3.18)$$

$$\frac{1}{Sc_j} \xi \frac{\partial}{\partial \xi} = \frac{Pr}{Sc_j} \zeta \frac{\partial}{\partial \zeta} = \frac{1}{Le_j} \zeta \frac{\partial}{\partial \zeta}$$

$$\begin{aligned} \frac{1}{Sc_j} \xi^2 \frac{\partial^2}{\partial \xi^2} + \left( \frac{1}{Sc_j} - 1 \right) \xi \frac{\partial}{\partial \xi} &= \frac{Pr}{Sc_j} \left[ Pr \zeta^2 \frac{\partial^2}{\partial \zeta^2} + (Pr-1) \zeta \frac{\partial}{\partial \zeta} \right] + \left( \frac{1}{Sc_j} - 1 \right) Pr \zeta \frac{\partial}{\partial \zeta} \\ &= \frac{Pr}{Sc_j} \left[ Pr \zeta^2 \frac{\partial^2}{\partial \zeta^2} + (Pr - Sc_j) \zeta \frac{\partial}{\partial \zeta} \right] \end{aligned}$$

$$= \frac{1}{Le_j} \left[ Pr \zeta^2 \frac{\partial^2}{\partial \zeta^2} + Pr \left( 1 - \frac{Sc_j}{Pr} \right) \zeta \frac{\partial}{\partial \zeta} \right] = \frac{Pr}{Le_j} \left[ \zeta^2 \frac{\partial^2}{\partial \zeta^2} + (1 - Le_j) \zeta \frac{\partial}{\partial \zeta} \right] \quad (3.19)$$

$$\tilde{E} / \tilde{T} = \tilde{E} / [\tilde{T}_\infty + \varepsilon (\theta - \alpha \zeta) + O(\varepsilon^2)] = \tilde{E} / \{ \tilde{T}_\infty [1 + (\varepsilon / \tilde{T}_\infty) (\theta - \alpha \zeta) + O(\varepsilon^2)] \}$$

$$= (\tilde{E} / \tilde{T}_\infty) - \varepsilon (\tilde{E} / \tilde{T}_\infty^2) (\theta - \alpha \zeta) + (\tilde{E} / \tilde{T}_\infty) O(\varepsilon^2) = (\tilde{E} / \tilde{T}_\infty) - (\theta - \alpha \zeta) + O(\varepsilon)$$

$$\exp(-\tilde{E} / \tilde{T}) = \exp[-(\tilde{E} / \tilde{T}_\infty) + (\theta - \alpha \zeta) + O(\varepsilon)] = \exp(-\tilde{E} / \tilde{T}_\infty) \exp(\theta - \alpha \zeta) + O(\varepsilon) \quad (3.20)$$

$$(1) \quad \xi = 0 : \quad \zeta = 0 \quad , \quad \tilde{T} = \tilde{T}_\infty \quad , \quad \tilde{Y}_F = 0$$

$$\tilde{T}(\zeta=0) = \tilde{T}_\infty + \varepsilon \theta(\zeta=0) + O(\varepsilon^2) = \tilde{T}_\infty \quad \therefore \quad \theta(\zeta=0) = 0$$

$$\tilde{Y}_F(\zeta=0) = \varepsilon^{Le_F} \phi_F(\zeta=0) + O(\varepsilon^{2Le_F}) = 0 \quad \therefore \quad \phi_F(\zeta=0) = 0$$

(2)

$$\begin{aligned} & 4(1-\xi) \left[ \frac{1}{Pr} \xi^2 \frac{\partial^2 \tilde{T}}{\partial \xi^2} + \left(\frac{1}{Pr}-1\right) \xi \frac{\partial \tilde{T}}{\partial \xi} \right] - \xi \left( \frac{2}{Pr} \xi \frac{\partial \tilde{T}}{\partial \xi} + 6\tilde{x} \frac{\partial \tilde{T}}{\partial \tilde{x}} \right) = -Da \tilde{x}^{4/3} \tilde{Y}_F^{n_F} \tilde{Y}_O^{n_O} \tilde{T}^{n_T-n_F-n_O+1} \exp(-\tilde{E}/\tilde{T}) \\ & 4[1-(\varepsilon\zeta)^{1/Pr}] \left[ Pr \zeta^2 \frac{\partial^2 \tilde{T}}{\partial \zeta^2} + (Pr-1) \zeta \frac{\partial \tilde{T}}{\partial \zeta} + \left(\frac{1}{Pr}-1\right) Pr \zeta \frac{\partial \tilde{T}}{\partial \zeta} \right] - (\varepsilon\zeta)^{1/Pr} \left( \frac{2}{Pr} Pr \zeta \frac{\partial \tilde{T}}{\partial \zeta} + 6\tilde{x} \frac{\partial \tilde{T}}{\partial \tilde{x}} \right) \\ & = -Da \tilde{x}^{4/3} [\varepsilon^{Le_F} (\tilde{Y}_{F0}/\tilde{x}^{1/3})^{1-Le_F} \zeta^{Le_F} + O(\varepsilon)]^{n_F} [\tilde{Y}_{O\infty} + O(\varepsilon^{Le_O}; \varepsilon)]^{n_O} [\tilde{T}_\infty + O(\varepsilon)]^{n_T-n_F-n_O+1} [\exp(-\tilde{E}/\tilde{T}_\infty) \exp(\theta-\alpha\zeta) + O(\varepsilon)] \\ & = -Da \tilde{x}^{4/3} [\varepsilon^{Le_F} (\tilde{Y}_{F0}/\tilde{x}^{1/3})^{1-Le_F} \zeta^{Le_F} + O(\varepsilon)]^{n_F} [\tilde{Y}_{O\infty} + O(\varepsilon^{Le_O}; \varepsilon)]^{n_O} [\tilde{T}_\infty + O(\varepsilon)]^{n_T-n_F-n_O+1} [\exp(-\tilde{E}/\tilde{T}_\infty) \exp(\theta-\alpha\zeta) + O(\varepsilon)] \end{aligned} \quad (3.21)$$

Take the leading order terms in  $\varepsilon$

$$\begin{aligned} & 4Pr \zeta^2 \frac{\partial^2 \{ \tilde{T}_\infty + \varepsilon [ \theta - (\tilde{T}_\infty - \tilde{T}_0) \zeta \tilde{x}^{1/3} ] \}}{\partial \zeta^2} = 4\varepsilon Pr \zeta^2 \frac{\partial^2 \theta}{\partial \zeta^2} \\ & = -\varepsilon^{Le_F n_F} Da \tilde{x}^{4/3} (\tilde{Y}_{F0}/\tilde{x}^{1/3})^{(1-Le_F)n_F} \tilde{Y}_{O\infty}^{n_O} \tilde{T}_\infty^{n_T-n_F-n_O+1} \exp(-\tilde{E}/\tilde{T}_\infty) \zeta^{Le_F n_F} \exp(\theta-\alpha\zeta) \\ & \zeta^2 \frac{\partial^2 \theta}{\partial \zeta^2} = -\varepsilon^{Le_F n_F - 1} \frac{Da \tilde{Y}_{O\infty}^{n_O} \tilde{T}_\infty^{n_T-n_F-n_O+1} \exp(-\tilde{E}/\tilde{T}_\infty)}{4Pr} \tilde{x}^{4/3} (\tilde{Y}_{F0}/\tilde{x}^{1/3})^{(1-Le_F)n_F} \zeta^{Le_F n_F} \exp(\theta-\alpha\zeta) \end{aligned}$$

$$\text{Define } \tilde{D}a = \varepsilon^{Le_F n_F - 1} \frac{Da \tilde{Y}_{O\infty}^{n_O} \tilde{T}_\infty^{n_T-n_F-n_O+1} \exp(-\tilde{E}/\tilde{T}_\infty)}{4Pr} \tilde{x}^{4/3} (\tilde{Y}_{F0}/\tilde{x}^{1/3})^{(1-Le_F)n_F} \quad (3.22)$$

= Reduced Damköhler number

$$\zeta^2 \frac{\partial^2 \theta}{\partial \zeta^2} = -\tilde{D}a \zeta^{Le_F n_F} \exp(\theta-\alpha\zeta) \quad (3.23)$$

## (D) Matching

$$\tilde{T} = (\tilde{T}_\infty + \varepsilon a_T) - [(\tilde{T}_\infty - \tilde{T}_0) + \varepsilon a_T] \zeta^{Pr} \tilde{x}^{1/3} + O(\varepsilon^2) = (\tilde{T}_\infty + \varepsilon a_T) - [(\tilde{T}_\infty - \tilde{T}_0) + \varepsilon a_T] (\varepsilon \zeta / \tilde{Y}_{F0}) + O(\varepsilon^2)$$

$$= \tilde{T}_\infty + \varepsilon (a_T - \alpha \zeta) + O(\varepsilon^2) = \tilde{T}_\infty + \varepsilon (\theta - \alpha \zeta) + O(\varepsilon^2) \Big|_{\zeta \rightarrow \infty}$$

$$\therefore \quad \theta(\zeta \rightarrow \infty) = a_T \quad \text{or} \quad (\partial \theta / \partial \zeta)_{\zeta \rightarrow \infty} = 0$$

### (E) Summary

$$\zeta^2 \frac{\partial^2 \theta}{\partial \zeta^2} = -\tilde{D}a \zeta^{Le_F n_F} \exp(\theta - \alpha \zeta) \quad ; \quad \zeta = 0 : \quad \theta = 0 \quad ; \quad \zeta \rightarrow \infty : \quad \partial \theta / \partial \zeta \rightarrow 0 \quad ,$$

$$\theta \rightarrow a_T$$

$$\alpha = (\tilde{T}_\infty - \tilde{T}_0) / \tilde{Y}_{F0} \quad , \quad \tilde{D}a = \varepsilon^{Le_F n_F - 1} \frac{Da \tilde{Y}_{O_\infty}^{n_O} \tilde{T}_\infty^{n_T - n_F - n_O + 1} \exp(-\tilde{E} / \tilde{T}_\infty) \tilde{x}^{4/3} (\tilde{Y}_{F0} / \tilde{x}^{1/3})^{(1 - Le_F) n_F}}{4 Pr}$$

$$, \quad \varepsilon = \tilde{T}_\infty^2 / \tilde{E}$$

Note: Since there is no differentiation with respect to  $\tilde{x}$ , the problem is locally similar and  $\tilde{x}$  can be considered as a constant in the structure equation.

### (F) Rescaling

when the change of  $\alpha$  is by changing  $T_\infty$  or  $Y_{F,0}$ , or  $n_F$  or  $Le_F$  is varying

Define  $\hat{T}_\infty$  as the reference value of  $\tilde{T}_\infty$  ,  $\hat{n}_F$  as the reference value of  $n_F$  ,

$\hat{Y}_{F0}$  as the reference value of  $\tilde{Y}_{F0}$

$$\hat{\varepsilon} = (\hat{T}_\infty)^2 / \tilde{E} \text{ as the reference value of } \varepsilon \quad \Rightarrow \quad \hat{\varepsilon} / \varepsilon = (\hat{T}_\infty / \tilde{T}_\infty)^2$$

$$\hat{D}a = \hat{\varepsilon}^{Le_F \hat{n}_F - 1} [Da / (4 Pr)] \tilde{Y}_{O_\infty}^{n_O} \hat{T}_\infty^{n_T - \hat{n}_F - n_O + 1} \exp(-\tilde{E} / \hat{T}_\infty) \tilde{x}^{4/3} (\hat{Y}_{F,0} / \tilde{x}^{1/3})^{(1 - Le_F) \hat{n}_F}$$

$$= (\hat{T}_\infty / \tilde{T}_\infty)^{n_T + (2Le_F - 1)\hat{n}_F - n_O - 1} (\tilde{T}_\infty^2 / \tilde{E})^{(Le_F \hat{n}_F - Le_F n_F)} \tilde{T}_\infty^{n_F - \hat{n}_F} (\hat{Y}_{F,0} / \tilde{Y}_{F,0})^{(1 - Le_F) \hat{n}_F} (\tilde{Y}_{F,0} / \tilde{x}^{1/3})^{(1 - Le_F) \hat{n}_F - (1 - Le_F) n_F} \exp[\tilde{E} (\tilde{T}_\infty^{-1} - \hat{T}_\infty^{-1})] \tilde{D}a \quad (3.24)$$

$$\varepsilon a_T = \hat{\varepsilon} \hat{a}_T \quad \therefore \quad \hat{a}_T = (\varepsilon / \hat{\varepsilon}) a_T = (\tilde{T}_\infty^2 / \hat{T}_\infty^2) a_T$$

If only  $T_\infty$  is varying

$$\hat{D}a = (\hat{T}_\infty / \tilde{T}_\infty)^{n_T + (2Le_F - 1)n_F - n_O - 1} \exp[\tilde{E} (\tilde{T}_\infty^{-1} - \hat{T}_\infty^{-1})] \tilde{D}a \quad (3.25)$$

$$\hat{a}_T = (\tilde{T}_\infty^2 / \hat{T}_\infty^2) a_T \quad (3.26)$$

In the calculations, we

(1) Choose a value of  $\alpha$  as the reference value.

(2) Find the value of  $\hat{T}_\infty$  based on this reference value of  $\alpha$ . (need to specify  $\tilde{T}_0$  and  $\tilde{Y}_{F0}$ )

(3) For other values of  $\alpha$ , determine  $\tilde{T}_\infty$  using the same values of  $\tilde{T}_0$  and  $\tilde{Y}_{F0}$ .

(4) Use the values of  $\hat{T}_\infty$  and  $\tilde{T}_\infty$  to determine  $\hat{D}a$ .

$$\text{If only } n_F \text{ is varying, } \hat{D}a = (\tilde{T}_\infty^2 / \tilde{E})^{Le_F(\hat{n}_F - n_F)} \tilde{T}_\infty^{n_F - \hat{n}_F} (\tilde{Y}_{F0} / \tilde{x}^{1/3})^{(1 - Le_F)(\hat{n}_F - n_F)} \tilde{D}a \quad (3.27)$$

$$\text{If only } Y_{F,0} \text{ is varying, } \hat{D}a = (\hat{Y}_{F0} / \tilde{Y}_{F0})^{(1 - Le_F)n_F} \tilde{D}a \quad (3.28)$$

$$\text{If only } Le_F \text{ is varying, } \hat{D}a = (\tilde{T}_\infty^2 / \tilde{E})^{(\hat{Le}_F - Le_F)n_F} (\hat{Y}_{F,0} / \tilde{Y}_{F,0})^{(1 - \hat{Le}_F)n_F} (\tilde{Y}_{F,0} / \tilde{x}^{1/3})^{(Le_F + Le_F)n_F} \tilde{D}a \quad (3.29)$$

### 3.3 Ignition Analysis II : $T_\infty > T_0, Le_F \approx 1$

As in I, ignition occurs at  $\eta \rightarrow \infty$  if successful.

#### **(A) Coordination Transformation and Outer Solutions (From Analysis I)**

Define  $\xi = \text{sech}^2 \eta$  then at  $\eta = 0$ ,  $\xi = 1$ ; as  $\eta \rightarrow \infty$ ,  $\xi = 0$

$$4(1 - \xi) \left[ \frac{1}{Pr} \xi^2 \frac{\partial^2 \tilde{T}}{\partial \xi^2} + \left( \frac{1}{Pr} - 1 \right) \xi \frac{\partial \tilde{T}}{\partial \xi} \right] - \xi \left( \frac{2}{Pr} \xi \frac{\partial \tilde{T}}{\partial \xi} + 6\tilde{x} \frac{\partial \tilde{T}}{\partial \tilde{x}} \right) = -Da \tilde{x}^{A/3} \tilde{Y}_F^{n_F} \tilde{Y}_O^{n_O} \tilde{T}^{n_T - n_F - n_O + 1} \exp(-\tilde{E}/\tilde{T})$$

$$4(1 - \xi) \left[ \frac{1}{Sc_F} \xi^2 \frac{\partial^2 \tilde{Y}_F}{\partial \xi^2} + \left( \frac{1}{Sc_F} - 1 \right) \xi \frac{\partial \tilde{Y}_F}{\partial \xi} \right] - \xi \left( \frac{2}{Sc_F} \xi \frac{\partial \tilde{Y}_F}{\partial \xi} + 6\tilde{x} \frac{\partial \tilde{Y}_F}{\partial \tilde{x}} \right) = Da \tilde{x}^{A/3} \tilde{Y}_F^{n_F} \tilde{Y}_O^{n_O} \tilde{T}^{n_T - n_F - n_O + 1} \exp(-\tilde{E}/\tilde{T})$$

$$\xi = 0 : \quad \tilde{T} = \tilde{T}_\infty, \quad \tilde{Y}_F = 0$$

Outer solutions

$$\tilde{T} = (\tilde{T}_\infty + \varepsilon a_T) - [(\tilde{T}_\infty - \tilde{T}_0) + \varepsilon a_T] \xi^{Pr} / \tilde{x}^{1/3} + O(\varepsilon^2)$$

$$\tilde{Y}_F = \varepsilon a_F + (\tilde{Y}_{F,0} - \varepsilon a_F) \xi^{Sc_F} / \tilde{x}^{1/3} + O(\varepsilon^2)$$

$$\tilde{Y}_O = (\tilde{Y}_{O,\infty} + \varepsilon a_O) (1 - \xi^{Sc_O} / \tilde{x}^{1/3}) + O(\varepsilon^2)$$

## (B) Inner Expansion

Define inner variable :  $\xi^{Pr} = \varepsilon \zeta$  or  $\zeta = \xi^{Pr} / \varepsilon$  ,  $\varepsilon = \tilde{T}_\infty^2 / \tilde{E}$  ;

$$\xi = 0 : \zeta = 0$$

From Analysis I

$$\tilde{T} = \tilde{T}_\infty + \varepsilon[\theta - (\tilde{T}_\infty - \tilde{T}_0)\zeta / \tilde{x}^{1/3}] + O(\varepsilon^2) \quad ; \quad \tilde{Y}_F = \varepsilon^{Le_F} (\tilde{Y}_{F,0} \zeta^{Le_F} / \tilde{x}^{1/3}) + \varepsilon \phi_F + O(\varepsilon^2)$$

$$\frac{1}{Pr} \xi \frac{\partial}{\partial \xi} = \zeta \frac{\partial}{\partial \zeta} \quad ; \quad \frac{1}{Pr} \xi^2 \frac{\partial^2}{\partial \xi^2} + \left(\frac{1}{Pr} - 1\right) \xi \frac{\partial}{\partial \xi} = Pr \zeta^2 \frac{\partial^2}{\partial \zeta^2}$$

$$\frac{1}{Sc_F} \xi \frac{\partial}{\partial \xi} = \frac{1}{Le_F} \zeta \frac{\partial}{\partial \zeta} \quad , \quad \frac{1}{Sc_F} \xi^2 \frac{\partial^2}{\partial \xi^2} + \left(\frac{1}{Sc_F} - 1\right) \xi \frac{\partial}{\partial \xi} = \frac{Pr}{Le_F} \left[ \zeta^2 \frac{\partial^2}{\partial \zeta^2} + (1 - Le_F) \zeta \frac{\partial}{\partial \zeta} \right]$$

$$4\varepsilon Pr \zeta^2 \frac{\partial^2 \theta}{\partial \zeta^2} = -Da \tilde{Y}_{O,\infty}^{n_O} \tilde{T}_\infty^{n_T - n_F - n_O + 1} \exp(-\tilde{E} / \tilde{T}_\infty) \tilde{x}^{4/3} [\varepsilon^{Le_F} (\tilde{Y}_{F,0} \zeta^{Le_F} / \tilde{x}^{1/3}) + \varepsilon \phi_F]^{n_F} \exp[\theta - (\tilde{T}_\infty - \tilde{T}_0)\zeta / \tilde{x}^{1/3}] + O(\varepsilon)$$

$$\zeta = 0 : \quad \theta = 0 \quad , \quad \phi_F = 0$$

Expand  $Le_F$  as  $Le_F = 1 + \varepsilon \ell_F + O(\varepsilon^2)$  , then for any variable  $A$

$$\begin{aligned} A^{Le_F} &= \exp[\ln(A^{Le_F})] = \exp(Le_F \ln A) = \exp[(1 + \varepsilon \ell_F + \dots) \ln A] : \\ &= \exp(\ln A) \exp(\varepsilon \ell_F \ln A + \dots) = A (1 + \varepsilon \ell_F \ln A + \dots) \end{aligned} \quad (3.30)$$

Thus :  $\tilde{Y}_F = \varepsilon^{Le_F} (\tilde{Y}_{F,0} \zeta^{Le_F} / \tilde{x}^{1/3}) + \varepsilon \phi_F + O(\varepsilon^2) = \varepsilon (\phi_F + \tilde{Y}_{F,0} \zeta / \tilde{x}^{1/3}) + O(\varepsilon^2)$

$$\frac{1}{Sc_F} \xi^2 \frac{\partial^2}{\partial \xi^2} + \left(\frac{1}{Sc_F} - 1\right) \xi \frac{\partial}{\partial \xi} = Pr \zeta^2 \frac{\partial^2 \tilde{Y}_F}{\partial \zeta^2} + O(\varepsilon) \quad (3.31)$$

$$(1) \quad 4\varepsilon Pr \zeta^2 \frac{\partial^2 \theta}{\partial \zeta^2} = -Da \tilde{Y}_{O,\infty}^{n_O} \tilde{T}_\infty^{n_T - n_F - n_O + 1} \exp(-\tilde{E} / \tilde{T}_\infty) \tilde{x}^{4/3}$$

$$[\varepsilon^{Le_F} (\tilde{Y}_{F,0} \zeta^{Le_F} / \tilde{x}^{1/3}) + \varepsilon \phi_F]^{n_F} \exp[\theta - (\tilde{T}_\infty - \tilde{T}_0)\zeta / \tilde{x}^{1/3}] + O(\varepsilon)$$

$$\zeta^2 \frac{\partial^2 \theta}{\partial \zeta^2} = -\frac{Da \tilde{Y}_{O,\infty}^{n_O} \tilde{T}_\infty^{n_T - n_F - n_O + 1} \exp(-\tilde{E} / \tilde{T}_\infty) \tilde{x}^{4/3}}{4\varepsilon Pr}$$

$$[\varepsilon (\phi_F + \tilde{Y}_{F,0} \zeta / \tilde{x}^{1/3})]^{n_F} \exp[\theta - (\tilde{T}_\infty - \tilde{T}_0)\zeta / \tilde{x}^{1/3}] + O(\varepsilon)$$

$$= -\varepsilon^{n_F-1} \frac{Da \tilde{Y}_{O,\infty}^{n_O} \tilde{T}_\infty^{n_T-n_F-n_O+1} \exp(-\tilde{E}/\tilde{T}_\infty) \tilde{x}^{4/3}}{4Pr} (\phi_F + \tilde{Y}_{F,0} \zeta / \tilde{x}^{1/3})^{n_F} \exp[\theta + (\tilde{T}_0 - \tilde{T}_\infty) \zeta / \tilde{x}^{1/3}] + O(\varepsilon) \quad (3.32)$$

$$\text{From Section 3.2, } \tilde{D}a = \varepsilon^{n_F-1} \frac{Da \tilde{Y}_{O,\infty}^{n_O} \tilde{T}_\infty^{n_T-n_F-n_O+1} \exp(-\tilde{E}/\tilde{T}_\infty) \tilde{x}^{4/3}}{4Pr}$$

$$\text{The leading order terms are } \zeta^2 \frac{\partial^2 \theta}{\partial \zeta^2} = -\tilde{D}a (\phi_F + \tilde{Y}_{F,0} \zeta / \tilde{x}^{1/3})^{n_F} \exp[\theta - (\tilde{T}_\infty - \tilde{T}_0) \zeta / \tilde{x}^{1/3}]$$

$$(2) \left\{ 4(1-\xi) \left[ \frac{1}{Pr} \xi^2 \frac{\partial^2 \tilde{T}}{\partial \xi^2} + \left(\frac{1}{Pr} - 1\right) \xi \frac{\partial \tilde{T}}{\partial \xi} \right] - \xi \left( \frac{2}{Pr} \xi \frac{\partial \tilde{T}}{\partial \xi} + 6\tilde{x} \frac{\partial \tilde{T}}{\partial \tilde{x}} \right) \right\} \\ + \left\{ 4(1-\xi) \left[ \frac{1}{Sc_F} \xi^2 \frac{\partial^2 \tilde{Y}_E}{\partial \xi^2} + \left(\frac{1}{Sc_F} - 1\right) \xi \frac{\partial \tilde{Y}_E}{\partial \xi} \right] - \xi \left( \frac{2}{Sc_F} \xi \frac{\partial \tilde{Y}_E}{\partial \xi} + 6\tilde{x} \frac{\partial \tilde{Y}_E}{\partial \tilde{x}} \right) \right\} = 0$$

From Section 3.2,

$$4(1-\xi) \left[ \frac{1}{Pr} \xi^2 \frac{\partial^2 \tilde{T}}{\partial \xi^2} + \left(\frac{1}{Pr} - 1\right) \xi \frac{\partial \tilde{T}}{\partial \xi} \right] - \xi \left( \frac{2}{Pr} \xi \frac{\partial \tilde{T}}{\partial \xi} + 6\tilde{x} \frac{\partial \tilde{T}}{\partial \tilde{x}} \right) = 4\varepsilon Pr \zeta^2 \frac{\partial^2 \theta}{\partial \zeta^2} + O(\varepsilon^{1+(1/Pr)}; \varepsilon^2)$$

$$4(1-\xi) \left[ \frac{1}{Sc_F} \xi^2 \frac{\partial^2 \tilde{Y}_E}{\partial \xi^2} + \left(\frac{1}{Sc_F} - 1\right) \xi \frac{\partial \tilde{Y}_E}{\partial \xi} \right] - \xi \left( \frac{2}{Sc_F} \xi \frac{\partial \tilde{Y}_E}{\partial \xi} + 6\tilde{x} \frac{\partial \tilde{Y}_E}{\partial \tilde{x}} \right)$$

$$= 4[1 - (\varepsilon \zeta)^{1/Pr}] \frac{Pr}{Le_F} \left[ \zeta^2 \frac{\partial^2 \tilde{Y}_E}{\partial \zeta^2} + (1 - Le_F) \zeta \frac{\partial \tilde{Y}_E}{\partial \zeta} \right] - (\varepsilon \zeta)^{1/Pr} \left( \frac{2}{Le_F} \zeta \frac{\partial \tilde{Y}_E}{\partial \zeta} + 6\tilde{x} \frac{\partial \tilde{Y}_E}{\partial \tilde{x}} \right)$$

$$= 4Pr \zeta^2 \frac{\partial^2 [\varepsilon (\phi_F + \tilde{Y}_{F,0} \zeta / \tilde{x}^{1/3})]}{\partial \zeta^2} + O(\varepsilon^2; \varepsilon^{1+(1/Pr)}) = 4\varepsilon Pr \zeta^2 \frac{\partial^2 \phi_F}{\partial \zeta^2} + O(\varepsilon^2; \varepsilon^{1+(1/Pr)})$$

$$\text{Thus } 4\varepsilon Pr \zeta^2 \frac{\partial^2 \theta}{\partial \zeta^2} + O(\varepsilon^{1+(1/Pr)}) + 4\varepsilon Pr \zeta^2 \frac{\partial^2 \phi_F}{\partial \zeta^2} + O(\varepsilon^2; \varepsilon^{1+(1/Pr)}) = 0 \quad \text{or} \quad \frac{\partial^2 (\theta + \phi_F)}{\partial \zeta^2} = 0$$

$$\Rightarrow \theta + \phi_F = c \zeta + c_2$$

$$\zeta = 0 : \quad \theta = \phi_F = 0 \quad \therefore \quad c_2 = 0 \quad \text{and} \quad \theta + \phi_F = c \zeta$$

(3) Summary

$$\zeta^2 \frac{\partial^2 \theta}{\partial \zeta^2} = -\tilde{D}a (\phi_F + \tilde{Y}_{F,0} \zeta / \tilde{x}^{1/3})^{n_F} \exp[\theta - (\tilde{T}_\infty - \tilde{T}_0) \zeta / \tilde{x}^{1/3}] \quad ; \quad \zeta = 0 : \quad \theta = 0$$

$$\theta + \phi_F = c \zeta \quad \text{where } c \text{ still needs to be determined.}$$

### (C) Matching

$$\begin{aligned}\tilde{T} &= (\tilde{T}_\infty + \varepsilon a_T) - [(\tilde{T}_\infty - \tilde{T}_0) + \varepsilon a_T] \zeta^{Pr} / \tilde{x}^{1/3} + O(\varepsilon^2) = (\tilde{T}_\infty + \varepsilon a_T) - [(\tilde{T}_\infty - \tilde{T}_0) + \varepsilon a_T] (\varepsilon \zeta) \tilde{x}^{1/3} + O(\varepsilon^2) \\ &= \tilde{T}_\infty + \varepsilon [a_T - (\tilde{T}_\infty - \tilde{T}_0) \zeta / \tilde{x}^{1/3}] + O(\varepsilon^2) = \tilde{T}_\infty + \varepsilon [\theta - (\tilde{T}_\infty - \tilde{T}_0) \zeta / \tilde{x}^{1/3}] + O(\varepsilon^2) \Big|_{\zeta \rightarrow \infty}\end{aligned}$$

$$\therefore \theta(\zeta \rightarrow \infty) = a_T \quad \text{or} \quad (\partial \theta / \partial \zeta)_{\zeta \rightarrow \infty} = 0$$

$$\begin{aligned}\tilde{Y}_F &= \varepsilon a_F + (\tilde{Y}_{F,0} - \varepsilon a_F) \zeta^{ScF} / \tilde{x}^{1/3} + O(\varepsilon^2) = \varepsilon a_F + (\tilde{Y}_{F,0} - \varepsilon a_F) (\zeta^{Pr})^{ScF} / Pr / \tilde{x}^{1/3} + O(\varepsilon^2) \\ &= \varepsilon a_F + (\tilde{Y}_{F,0} - \varepsilon a_F) (\varepsilon \zeta)^{LeF} / \tilde{x}^{1/3} + O(\varepsilon^2) = \varepsilon a_F + (\tilde{Y}_{F,0} - \varepsilon a_F) (\varepsilon \zeta) [1 + \varepsilon \ell_F \ln(\varepsilon \zeta) + \dots] / \tilde{x}^{1/3} + O(\varepsilon^2) \\ &= \varepsilon (a_F + \tilde{Y}_{F,0} \zeta / \tilde{x}^{1/3}) + O(\varepsilon^2) = \varepsilon (\phi_F + \tilde{Y}_{F,0} \zeta / \tilde{x}^{1/3}) + O(\varepsilon^2) \Big|_{\zeta \rightarrow \infty}\end{aligned}$$

$$\therefore \phi_F(\zeta \rightarrow \infty) = a_F$$

From (B) :  $\theta + \phi_F = c \zeta$

$$\zeta \rightarrow \infty : \quad \theta \rightarrow a_T \quad , \quad \phi_F \rightarrow a_F \quad \therefore \quad a_T + a_F = c \zeta \Rightarrow a_T + a_F = c = 0 \quad \text{or}$$

$$a_F = -a_T \Rightarrow \theta + \phi_F = 0 \quad \text{or} \quad \phi_F = -\theta$$

### (E) Summary

$$\zeta^2 \frac{\partial^2 \theta}{\partial \zeta^2} = -\tilde{D} a (-\theta + \tilde{Y}_{F,0} \zeta / \tilde{x}^{1/3})^{n_F} \exp[\theta - (\tilde{T}_\infty - \tilde{T}_0) \zeta / \tilde{x}^{1/3}] \quad ; \quad \zeta = 0 : \quad \theta = 0 \quad ;$$

$$\zeta \rightarrow \infty : \quad d\theta / d\zeta \rightarrow 0 \quad , \quad \theta \rightarrow a_T$$

### Rescaling

From Section 3.2,  $\sigma = \tilde{Y}_{F,0} / \tilde{x}^{1/3}$  ,  $\bar{\zeta} = \sigma \zeta$  ,  $\beta = (\tilde{T}_\infty - \tilde{T}_0) / \tilde{Y}_{F,0}$  , then

$$\bar{\zeta}^2 \frac{\partial^2 \theta}{\partial \bar{\zeta}^2} = -\tilde{D} a (-\theta + \bar{\zeta})^{n_F} \exp(\theta - \beta \bar{\zeta}) \quad ; \quad \bar{\zeta} = 0 : \quad \theta = 0 \quad ;$$

$$\bar{\zeta} \rightarrow \infty : \quad \partial \theta / \partial \bar{\zeta} \rightarrow 0 \quad , \quad \theta \rightarrow a_T$$

Note: Since there is no differentiation with respect to  $\tilde{x}$ , the problem is locally similar and  $\tilde{x}$  can be considered as a constant in the structure equation.

### 3.4 Ignition Analysis III : $T_0 > T_\infty$ , $\tilde{x} \approx 1$ , Thicker Reaction Region

Because spontaneous ignition is primarily controlled by temperature, ignition occurs near  $\eta = 0$ . This is the centerline of the jet.

#### **(A) Outer Solutions**

The outer solution is as follows

$$\tilde{T} = \tilde{T}_\infty + [(\tilde{T}_0 - \tilde{T}_\infty) + \varepsilon a_T] (\text{sech}^{2Pr} \eta) \tilde{x}^{1/3} + O(\varepsilon^2) \quad (3.33)$$

$$\tilde{Y}_F = (\tilde{Y}_{F,0} - \varepsilon a_F) (\text{sech}^{2Sc_F} \eta) \tilde{x}^{1/3} + O(\varepsilon^2) \quad ; \quad (3.34)$$

$$\tilde{Y}_O = \tilde{Y}_{O,\infty} - (\tilde{Y}_{O,\infty} + \varepsilon a_O) (\text{sech}^{2Sc_O} \eta) \tilde{x}^{1/3} + O(\varepsilon^2) \quad (3.35)$$

#### **(B) Inner Expansion**

If successful, ignition occurs in an inner region near  $\eta = 0$  and  $\tilde{x} \approx 1$

Since  $d(\text{sech } \eta) / d\eta = 0$  at  $\eta = 0$ , it seems that the reaction region should be thicker than  $O(\varepsilon)$ .

Define inner variables  $\eta = \sqrt{\varepsilon / (Pr \tilde{Y}_{O,\infty})} \zeta$ ,  $\tilde{x} = 1 + \varepsilon (3\xi / \tilde{Y}_{O,\infty})$ ,  $\varepsilon = \tilde{T}_0^2 / \tilde{E}$ ,

$$\beta = (\tilde{T}_0 - \tilde{T}_\infty) / \tilde{Y}_{O,\infty} \quad ; \quad \text{when } \eta = 0 : \zeta = 0$$

$$\Rightarrow \quad \eta^2 = \varepsilon \zeta^2 / (Pr \tilde{Y}_{O,\infty}) \quad , \quad \partial \eta = \sqrt{\varepsilon / (Pr \tilde{Y}_{O,\infty})} \partial \zeta \quad , \quad \partial \eta^2 = [\varepsilon / (Pr \tilde{Y}_{O,\infty})] \partial \zeta^2 \quad ,$$

$$\partial \tilde{x} = (3\varepsilon / \tilde{Y}_{O,\infty}) \partial \xi$$

$$\text{sech } \eta = 1 - (\eta^2 / 2) + \dots = 1 - \varepsilon [\zeta^2 / (2Pr \tilde{Y}_{O,\infty})] + O(\varepsilon^2)$$

$$\text{sech}^2 \eta = \{1 - \varepsilon [\zeta^2 / (2Pr \tilde{Y}_{O,\infty})] + O(\varepsilon^2)\}^2 = 1 - 2\varepsilon [\zeta^2 / (2Pr \tilde{Y}_{O,\infty})] + O(\varepsilon^2) = 1 - \varepsilon [\zeta^2 / (Pr \tilde{Y}_{O,\infty})] + O(\varepsilon^2)$$

$$\text{sech}^{2Pr} \eta = \{1 - \varepsilon [\zeta^2 / (2Pr \tilde{Y}_{O,\infty})] + O(\varepsilon^2)\}^{2Pr} = 1 - \varepsilon 2Pr [\zeta^2 / (2Pr \tilde{Y}_{O,\infty})] + O(\varepsilon^2) = 1 - \varepsilon (\zeta^2 / \tilde{Y}_{O,\infty}) + O(\varepsilon^2)$$

$$\text{sech}^{2Sc_i} \eta = \{1 - \varepsilon [\zeta^2 / (2Pr \tilde{Y}_{O,\infty})] + O(\varepsilon^2)\}^{2Sc_i} = 1 - \varepsilon 2Sc_i [\zeta^2 / (2Pr \tilde{Y}_{O,\infty})] + O(\varepsilon^2)$$

$$= 1 - \varepsilon (Sc_i / Pr) (\zeta^2 / \tilde{Y}_{O,\infty}) + O(\varepsilon^2) = 1 - \varepsilon Le_i (\zeta^2 / \tilde{Y}_{O,\infty}) + O(\varepsilon^2) \quad (3.36)$$

$$\tanh \eta = \eta - (\eta^3/3) + \dots = \sqrt{\varepsilon/(Pr\tilde{Y}_{O,\infty})} \zeta + O(\varepsilon^{3/2}) \quad (3.37)$$

$$1/\tilde{x}^{1/3} = 1/[1 + \varepsilon(3\xi/\tilde{Y}_{O,\infty})]^{1/3} = 1/[1 + \varepsilon(\xi/\tilde{Y}_{O,\infty}) + O(\varepsilon^2)] = 1 - \varepsilon(\xi/\tilde{Y}_{O,\infty}) + O(\varepsilon^2) \quad (3.38)$$

$$\begin{aligned} \tilde{T} &= \tilde{T}_f[\eta = \sqrt{\varepsilon/(Pr\tilde{Y}_{O,\infty})} \zeta, \tilde{x} = 1 + 3\varepsilon(\xi/\tilde{Y}_{O,\infty})] + \varepsilon\theta + O(\varepsilon^2) \\ &= \tilde{T}_\infty + (\tilde{T}_0 - \tilde{T}_\infty)[1 - \varepsilon(\zeta^2/\tilde{Y}_{O,\infty}) + O(\varepsilon^2)][1 - \varepsilon(\xi/\tilde{Y}_{O,\infty}) + O(\varepsilon^2)] + \varepsilon\theta + O(\varepsilon^2) \\ &= \tilde{T}_0 + \varepsilon\{\theta - (\tilde{T}_0 - \tilde{T}_\infty)[(\zeta^2/\tilde{Y}_{O,\infty}) + (\xi/\tilde{Y}_{O,\infty})]\} + O(\varepsilon^2) = \tilde{T}_0 + \varepsilon\{\theta - [(\tilde{T}_0 - \tilde{T}_\infty)/\tilde{Y}_{O,\infty}](\zeta^2 + \xi)\} + O(\varepsilon^2) \\ &= \tilde{T}_0 + \varepsilon[\theta - \beta(\zeta^2 + \xi)] + O(\varepsilon^2) \end{aligned} \quad (3.39)$$

$$\begin{aligned} \tilde{Y}_F &= \tilde{Y}_{F,f}[\eta = \sqrt{\varepsilon/(Pr\tilde{Y}_{O,\infty})} \zeta, \tilde{x} = 1 + 3\varepsilon(\xi/\tilde{Y}_{O,\infty})] + \varepsilon\phi_F + O(\varepsilon^2) \\ &= \tilde{Y}_{F,0}[1 - \varepsilon Le_F(\zeta^2/\tilde{Y}_{O,\infty}) + O(\varepsilon^2)][1 - \varepsilon(\xi/\tilde{Y}_{O,\infty}) + O(\varepsilon^2)] + \varepsilon\phi_F + O(\varepsilon^2) = \tilde{Y}_{F,0} + O(\varepsilon) \end{aligned} \quad (3.40)$$

$$\begin{aligned} \tilde{Y}_O &= \tilde{Y}_{O,f}[\eta = \sqrt{\varepsilon/(Pr\tilde{Y}_{O,\infty})} \zeta, \tilde{x} = 1 + 3\varepsilon(\xi/\tilde{Y}_{O,\infty})] + \varepsilon\phi_O + O(\varepsilon^2) \\ &= \tilde{Y}_{O,\infty}\{1 - [1 - \varepsilon Le_O(\zeta^2/\tilde{Y}_{O,\infty}) + O(\varepsilon^2)][1 - \varepsilon(\xi/\tilde{Y}_{O,\infty}) + O(\varepsilon^2)]\} + \varepsilon\phi_O + O(\varepsilon^2) \\ &= \varepsilon\{\phi_O + \tilde{Y}_{O,\infty}[Le_O(\zeta^2/\tilde{Y}_{O,\infty}) + (\xi/\tilde{Y}_{O,\infty})]\} + O(\varepsilon^2) = \varepsilon(\phi_O + Le_O\zeta^2 + \xi) + O(\varepsilon^2) \end{aligned} \quad (3.41)$$

$$\begin{aligned} \tilde{E}/\tilde{T} &= \tilde{E}/\{\tilde{T}_0 + \varepsilon[\theta - \beta(\zeta^2 + \xi)] + O(\varepsilon^2)\} = \tilde{E}/\tilde{T}_0\{1 + \varepsilon[\theta - \beta(\zeta^2 + \xi)]/\tilde{T}_0 + O(\varepsilon^2)\} \\ &= (\tilde{E}/\tilde{T}_0)\{1 - \varepsilon[\theta - \beta(\zeta^2 + \xi)]/\tilde{T}_0 + O(\varepsilon^2)\} = (\tilde{E}/\tilde{T}_0) - \varepsilon(\tilde{E}/\tilde{T}_0^2)[\theta - \beta(\zeta^2 + \xi)] + (\tilde{E}/\tilde{T}_0)O(\varepsilon^2) \\ &= (\tilde{E}/\tilde{T}_0) - [\theta - \beta(\zeta^2 + \xi)] + O(\varepsilon) \end{aligned}$$

$$\exp(-\tilde{E}/\tilde{T}) = \exp\{-(\tilde{E}/\tilde{T}_0) - [\theta - \beta(\zeta^2 + \xi)] + O(\varepsilon)\} = \exp(-\tilde{E}/\tilde{T}_0) \exp[\theta - \beta(\zeta^2 + \xi)] + O(\varepsilon) \quad (3.42)$$

$$(1) \quad \eta = 0, \quad \tilde{x} = 1 : \quad \tilde{T} = \tilde{T}_0, \quad \tilde{Y}_O = 0 \quad \Rightarrow \quad \zeta = 0, \quad \xi = 0 : \quad \theta = \phi_O = 0$$

$$(2) \quad \eta = 0, \quad \tilde{x} > 1 : \quad \partial\tilde{T}/\partial\eta = \partial\tilde{Y}_O/\partial\eta = 0 \quad \Rightarrow \quad \zeta = 0, \quad \xi > 0 :$$

$$\partial\theta/\partial\zeta = \partial\phi_O/\partial\zeta = 0$$

$$(3) \quad \left[ \frac{1}{Pr} \frac{\partial^2 \tilde{T}}{\partial \eta^2} + 2(\tanh \eta) \frac{\partial \tilde{T}}{\partial \eta} - 6(\operatorname{sech}^2 \eta) \tilde{x} \frac{\partial \tilde{T}}{\partial \tilde{x}} \right] + \left[ \frac{1}{Sc_O} \frac{\partial^2 \tilde{Y}_O}{\partial \eta^2} + 2(\tanh \eta) \frac{\partial \tilde{Y}_O}{\partial \eta} - 6(\operatorname{sech}^2 \eta) \tilde{x} \frac{\partial \tilde{Y}_O}{\partial \tilde{x}} \right] = 0$$

$$\frac{1}{Pr} \frac{\partial^2 \{\tilde{T}_0 + \varepsilon[\theta - \beta(\zeta^2 + \xi)] + O(\varepsilon^2)\}}{[\varepsilon/(Pr\tilde{Y}_{O,\infty})] \partial \zeta^2} + 2[\sqrt{\varepsilon/(Pr\tilde{Y}_{O,\infty})} \zeta + O(\varepsilon^{3/2})] \frac{\partial \{\tilde{T}_0 + \varepsilon[\theta - \beta(\zeta^2 + \xi)] + O(\varepsilon^2)\}}{\sqrt{\varepsilon/(Pr\tilde{Y}_{O,\infty})} \partial \zeta}$$

$$\begin{aligned}
& -6\{1-\varepsilon[\zeta^2/(Pr\tilde{Y}_{O,\infty})]+O(\varepsilon^2)\}[1+3\varepsilon(\xi/\tilde{Y}_{O,\infty})]\frac{\partial\{\tilde{T}_0+\varepsilon[\theta-\beta(\zeta^2+\xi)]+O(\varepsilon^2)\}}{(3\varepsilon/\tilde{Y}_{O,\infty})\partial\xi} \\
& +\frac{1}{Sc_0}\frac{\partial^2[\varepsilon(\phi_0+Le_0\zeta^2+\xi)+O(\varepsilon^2)]}{[\varepsilon/(Pr\tilde{Y}_{O,\infty})]\partial\zeta^2}+2[\sqrt{\varepsilon/Pr}\zeta+O(\varepsilon^{3/2})]\frac{\partial[\varepsilon(\phi_0+Le_0\zeta^2+\xi)+O(\varepsilon^2)]}{\sqrt{\varepsilon/(Pr\tilde{Y}_{O,\infty})}\partial\zeta} \\
& -6\{1-\varepsilon[\zeta^2/(Pr\tilde{Y}_{O,\infty})]+O(\varepsilon^2)\}[1+3\varepsilon(\xi/\tilde{Y}_{O,\infty})]\frac{\partial[\varepsilon(\phi_0+Le_0\zeta^2+\xi)+O(\varepsilon^2)]}{(3\varepsilon/\tilde{Y}_{O,\infty})\partial\xi}=0 \quad (3.43)
\end{aligned}$$

The leading order terms are

$$\tilde{Y}_{O,\infty}\left\{\frac{\partial^2[\theta-\beta(\zeta^2+\xi)]}{\partial\zeta^2}-2\frac{\partial[\theta-\beta(\zeta^2+\xi)]}{\partial\xi}+\frac{Pr}{Sc_0}\frac{\partial^2(\phi_0+Le_0\zeta^2+\xi)}{\partial\zeta^2}-2\frac{\partial(\phi_0+Le_0\zeta^2+\xi)}{\partial\xi}\right\}=0$$

$$\frac{\partial^2\theta}{\partial\zeta^2}-2\beta-2\frac{\partial\theta}{\partial\xi}+2\beta+\frac{1}{Le_0}\left(\frac{\partial^2\phi_0}{\partial\zeta^2}+2Le_0\right)-2\frac{\partial\phi_0}{\partial\xi}-2=0 \quad \text{or}$$

$$\frac{\partial^2\theta}{\partial\zeta^2}-2\frac{\partial\theta}{\partial\xi}+\frac{1}{Le_0}\frac{\partial^2\phi_0}{\partial\zeta^2}-2\frac{\partial\phi_0}{\partial\xi}=0$$

$$(4) \quad \frac{1}{Pr}\frac{\partial^2\tilde{T}}{\partial\eta^2}+2(\tanh\eta)\frac{\partial\tilde{T}}{\partial\eta}-6(\operatorname{sech}^2\eta)\tilde{x}\frac{\partial\tilde{T}}{\partial\tilde{x}}=-Da\tilde{x}^{4/3}\tilde{Y}_F^{n_F}\tilde{Y}_O^{n_O}\tilde{T}^{n_T-n_F-n_O+1}\exp(-\tilde{E}/\tilde{T})$$

$$\tilde{Y}_{O,\infty}\left[\frac{\partial^2\theta}{\partial\zeta^2}-2\frac{\partial\theta}{\partial\xi}+O(\varepsilon)\right]$$

$$=-Da[1+O(\varepsilon)]^{4/3}[\tilde{Y}_{F,0}+O(\varepsilon)]^{n_F}[\varepsilon(\phi_0+Le_0\zeta^2+\xi)+O(\varepsilon^2)]^{n_O}[\tilde{T}_0+O(\varepsilon)]^{n_T-n_F-n_O+1}$$

$$\cdot\exp(-\tilde{E}/\tilde{T}_0)\exp[\theta-\beta(\zeta^2+\xi)]+O(\varepsilon)$$

$$=-\varepsilon^{n_O}Da\tilde{Y}_{F,0}^{n_F}\tilde{T}_0^{n_T-n_F-n_O+1}\exp(-\tilde{E}/\tilde{T}_0)(\phi_0+Le_0\zeta^2+\xi)^{n_O}\exp[\theta-\beta(\zeta^2+\xi)]+O(\varepsilon)$$

$$\text{Define } \tilde{D}a=\varepsilon^{n_O}Da(\tilde{Y}_{F,0}^{n_F}/\tilde{Y}_{O,\infty})\tilde{T}_0^{n_T-n_F-n_O+1}\exp(-\tilde{E}/\tilde{T}_0) \quad (3.44)$$

= Reduced Damköhler number

$$\text{Then : } \frac{\partial^2\theta}{\partial\zeta^2}-2\frac{\partial\theta}{\partial\xi}=-\tilde{D}a(\phi_0+Le_0\zeta^2+\xi)^{n_O}\exp[\theta-\beta(\zeta^2+\xi)] \quad (3.45)$$

### (C) Matching

$$\tilde{T}=\tilde{T}_\infty+[(\tilde{T}_0-\tilde{T}_\infty)+\varepsilon\alpha_T](\operatorname{sech}^{2Pr}\eta)\tilde{x}^{1/3}+O(\varepsilon^2)$$

$$\begin{aligned}
&= \tilde{T}_\infty + [(\tilde{T}_0 - \tilde{T}_\infty) + \varepsilon a_T] [1 - \varepsilon(\zeta^2 / \tilde{Y}_{O,\infty})] [1 - \varepsilon(\xi / \tilde{Y}_{O,\infty})] + O(\varepsilon^2) \\
&= \tilde{T}_0 + \varepsilon \{ a_T - [(\tilde{T}_0 - \tilde{T}_\infty) / \tilde{Y}_{O,\infty}] (\zeta^2 + \xi) \} + O(\varepsilon^2) = \tilde{T}_0 + \varepsilon [\theta - \beta(\zeta^2 + \xi)] + O(\varepsilon^2) \Big|_{\zeta \rightarrow \infty}
\end{aligned}$$

$$\therefore \theta(\zeta \rightarrow \infty) \rightarrow a_T \quad \text{and} \quad (\partial\theta / \partial\zeta)_{\zeta \rightarrow \infty} \rightarrow 0$$

$$\begin{aligned}
\tilde{Y}_O &= \tilde{Y}_{O,\infty} - (\tilde{Y}_{O,\infty} + \varepsilon a_O) (\operatorname{sech}^{2Sc} \eta) \tilde{x}^{1/3} + O(\varepsilon^2) \\
&= \tilde{Y}_{O,\infty} - (\tilde{Y}_{O,\infty} + \varepsilon a_O) [1 - \varepsilon Le_O (\zeta^2 / \tilde{Y}_{O,\infty})] [1 - \varepsilon(\xi / \tilde{Y}_{O,\infty})] + O(\varepsilon^2) \\
&= \varepsilon(-a_O + Le_O \zeta^2 + \xi) + O(\varepsilon^2) = \varepsilon(\phi_O + Le_O \zeta^2 + \xi) + O(\varepsilon^2) \Big|_{\zeta \rightarrow \infty}
\end{aligned}$$

$$\therefore \phi_O(\zeta \rightarrow \infty) \rightarrow -a_O \quad \text{and} \quad (\partial\phi_O / \partial\zeta)_{\zeta \rightarrow \infty} \rightarrow 0$$

### (D) Ignition Criterion

(1) Ignition is successful when  $(\partial\tilde{T} / \partial\tilde{x})_{\eta=0} \geq 0$

Since  $\eta = 0$  is in the inner, reactive region, the ignition condition becomes

$$(\partial\tilde{T}_{in} / \partial\tilde{x})_{\zeta=0} \geq 0$$

$$(\partial\tilde{T}_{in} / \partial\tilde{x})_{\zeta=0} = \langle \partial\{ \tilde{T}_0 + \varepsilon[\theta - \beta(\zeta^2 + \xi)] + O(\varepsilon^2) \} / \partial\tilde{x} \rangle_{\zeta=0} = \varepsilon [(\partial\theta / \partial\zeta)_{\zeta=0} - \beta] + O(\varepsilon^2) \geq 0$$

$$\text{or} \quad (\partial\theta / \partial\zeta)_{\zeta=0} \geq \beta$$

(2) Ignition is successful when  $\partial\tilde{T} / \partial\eta \geq 0$  at any  $\tilde{x}$

In the inner, reactive region, the ignition condition becomes  $\partial\tilde{T}_{in} / \partial\zeta \geq 0$  at any  $\tilde{x}$

$$\partial\tilde{T}_{in} / \partial\zeta = \partial\{ \tilde{T}_0 + \varepsilon[\theta - \beta(\zeta^2 + \xi)] + O(\varepsilon^2) \} / \partial\zeta = \varepsilon [(\partial\theta / \partial\zeta) - 2\beta\zeta] + O(\varepsilon^2) \geq 0$$

$$\text{or} \quad \partial\theta / \partial\zeta \geq 2\beta\zeta \quad \text{at any } \zeta$$

### (E) Initial condition

At the nozzle exit, there is no reaction. Thus

$$\theta(\xi=0) = \phi_O(\xi=0) = 0$$

**(F) Summary**

$$\frac{\partial^2 \theta}{\partial \zeta^2} - 2 \frac{\partial \theta}{\partial \xi} + \frac{1}{Le_0} \frac{\partial^2 \phi_0}{\partial \zeta^2} - 2 \frac{\partial \phi_0}{\partial \xi} = 0$$

$$\frac{\partial^2 \theta}{\partial \zeta^2} - 2 \frac{\partial \theta}{\partial \xi} = -\tilde{D}a(\phi_0 + Le_0 \zeta^2 + \xi)^{n_0} \exp[\theta - \beta(\zeta^2 + \xi)]$$

$$\theta(\xi=0) = \phi_0(\xi=0) = 0$$

$$\zeta = 0, \quad \xi > 0 : \quad \partial \theta / \partial \zeta = \partial \phi_0 / \partial \zeta = 0$$

$$\zeta \rightarrow \infty : \quad \partial \theta / \partial \zeta \rightarrow 0 \quad ; \quad \partial \phi_0 / \partial \zeta \rightarrow 0$$

If  $Le_0 = 1$ , we have  $\phi_0 = -\theta$  and the problem is reduced to

$$\frac{\partial^2 \theta}{\partial \zeta^2} - 2 \frac{\partial \theta}{\partial \xi} = -\tilde{D}a(\zeta^2 + \xi - \theta)^{n_0} \exp[\theta - \beta(\zeta^2 + \xi)]$$

$$\zeta = 0 : \quad \xi = 0 : \quad \theta = 0 \quad , \quad \xi > 0 : \quad \partial \theta / \partial \zeta = 0 \quad ; \quad \zeta \rightarrow \infty : \quad \partial \theta / \partial \zeta \rightarrow 0$$

Ignition criterion :  $(\partial \theta / \partial \xi)_{\zeta=0} \geq \beta$  or  $\partial \theta / \partial \zeta \geq 2\beta\zeta$  at any  $\xi$

**(G) Rescaling when the change of  $\gamma$  is by changing  $T_0$  or  $Y_{O,\infty}$ , or  $n_0$  is varying**

Define  $\hat{T}_0$  as the reference value of  $\tilde{T}_0$  ,  $\hat{n}_0$  as the reference value of  $n_0$  ,

$\hat{Y}_{O,\infty}$  as the reference value of  $\tilde{Y}_{O,\infty}$

$$\hat{\varepsilon} = \hat{T}_0^2 / \tilde{E} \text{ as the reference value of } \varepsilon \Rightarrow \hat{\varepsilon} / \varepsilon = (\hat{T}_0 / \tilde{T}_0)^2$$

$$\begin{aligned} \hat{D}a &= \hat{\varepsilon}^{\hat{n}_0} Da (\tilde{Y}_{F0})^{n_F} / \hat{Y}_{O,\infty} \hat{T}_0^{n_T - n_F - \hat{n}_0 + 1} \exp(-\tilde{E} / \hat{T}_0) \\ &= (\hat{T}_0 / \tilde{T}_0)^{n_T - n_F + \hat{n}_0 + 1} (\tilde{T}_0 / \tilde{E})^{\hat{n}_0 - n_0} (\tilde{Y}_{O,\infty} / \hat{Y}_{O,\infty}) \exp[\tilde{E}(\tilde{T}_0^{-1} - \hat{T}_0^{-1})] \tilde{D}a \end{aligned} \quad (3.46)$$

$$\text{If only } T_0 \text{ is varying: } \hat{D}a = (\hat{T}_0 / \tilde{T}_0)^{n_T - n_F + n_0 + 1} \exp[\tilde{E}(\tilde{T}_0^{-1} - \hat{T}_0^{-1})] \tilde{D}a \quad (3.47)$$

In the calculations, we

(1) Choose a value of  $\beta$  as the reference value.

(2) Find the value of  $\hat{T}_0$  based on this reference value of  $\beta$ . (need to specify  $\tilde{T}_\infty$  and  $\tilde{Y}_{O,\infty}$ )

(3) For other values of  $\beta$ , determine  $\tilde{T}_0$  using the same values of  $\tilde{T}_\infty$  and  $\tilde{Y}_{O,\infty}$ .

(4) Use the values of  $\hat{T}_0$  and  $\tilde{T}_0$  to determine  $\hat{D}a$ .

If only  $n_O$  is varying :  $\hat{D}a = (\tilde{T}_0 / \tilde{E})^{\hat{n}_O - n_O} \tilde{D}a$  (3.47)

If only  $Y_{O,\infty}$  is varying :  $\hat{D}a = (\tilde{Y}_{O,\infty} / \hat{Y}_{O,\infty}) \tilde{D}a$  (3.48)

### 3.5 Analysis Scenarios

#### 3.5.1 Cool jet flowing into a hot ambient ( $T_\infty > T_0$ )

(With reference to Section 3.2 Ignition Analysis I) In the presence of a weak reaction, the temperature is increased from its frozen value by a small,  $O(\epsilon)$  amount where  $\epsilon = \tilde{T}_\infty^2 / \tilde{E}$  while the reactant concentrations are reduced from their respective frozen values by an  $O(\epsilon)$  amount. Because ignition is primarily controlled by temperature, ignition occurs near  $\eta \rightarrow \infty$  if successful. Fig.3.1 shows a schematic of the inner and outer regions for the scenario.

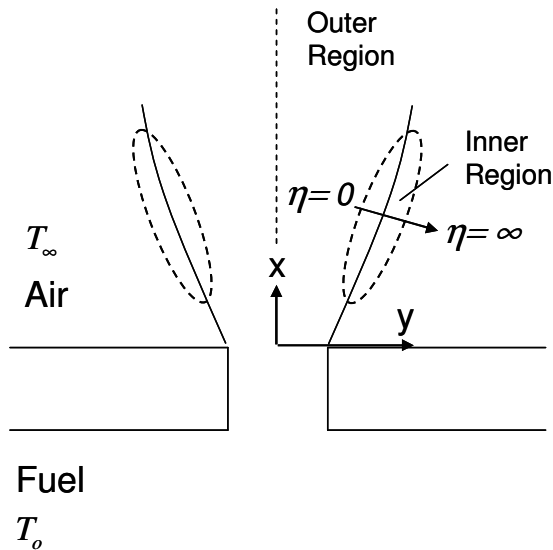


**Fig. 3.1: Schematic of inner and outer regions for cool jet, hot ambient case.**

Away from this high temperature region, the reaction is frozen. In the outer, chemically frozen region, the outer solutions are similar to Eqns. 3.4 – 3.6, but with an  $O(\varepsilon)$  change in their values. In the inner, reactive region, defining a stretched inner variable as

$$\zeta = \tilde{Y}_{F,0}(\operatorname{sech} \eta)^{2Pr} / (\varepsilon \tilde{x}^{1/3}) \quad (3.49)$$

and substituting into Parts (C) to (E) of Ignition Analysis I, yields, when  $Le_F$  is sufficiently smaller than unity, as for hydrogen,

$$\zeta^2 (\partial^2 \theta / \partial \zeta^2) = -\tilde{D}a \zeta^{Le_F} \exp(\theta - \alpha \zeta) \quad , \quad (3.50)$$

where  $\alpha = (\tilde{T}_\infty - \tilde{T}_0) / \tilde{Y}_{F,0}$  and the reduced Damköhler number is defined as

$$\tilde{D}a = Da \tilde{Y}_{O,\infty} \tilde{x}^{4/3} [\tilde{Y}_{F,0} / (\varepsilon \tilde{x}^{1/3})]^{1-Le_F} \exp(-\tilde{E} / \tilde{T}_\infty) / (4Pr\tilde{T}_\infty) \quad . \quad (3.51)$$

The boundary conditions required to solve this equation can be found by matching the inner and outer solutions as

$$\zeta = 0 : \quad \theta = 0 \quad ; \quad \zeta \rightarrow \infty : \quad \partial \theta / \partial \zeta \rightarrow 0 \quad , \quad \theta \rightarrow a_T \quad (3.52)$$

For the case of  $Le_F$  close to unity, Eqn. (3.2) is modified to

$$\zeta^2 (\partial^2 \theta / \partial \zeta^2) = -\tilde{D}a (\zeta - \theta) \exp(\theta - \alpha \zeta) \quad . \quad (3.53)$$

### 3.5.2 Hot jet flowing into a cool ambient ( $T_0 > T_\infty$ )

(With reference to Section 3.4 Ignition Analysis III) For the case of a hot jet issuing into a cold ambient, any ignition will occur near the jet centerline,  $\eta = 0$ . Fig.3.2 shows a schematic of the inner and outer regions for the scenario.

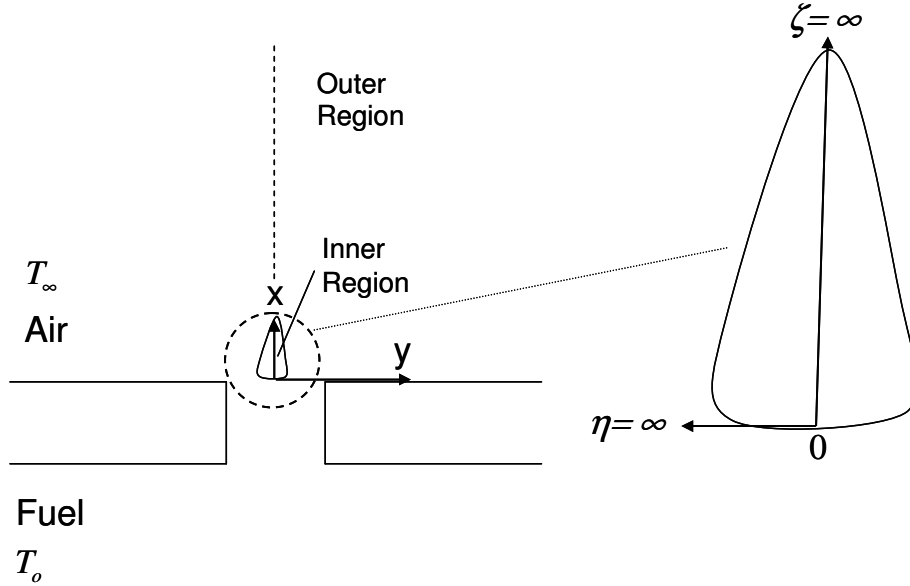


**Fig. 3.2: Schematic of inner and outer regions for hot jet, cool ambient case.**

Moreover, because the jet will be cooled by the cold ambient gas along the flow, ignition is expected to occur near the slot exit. The analysis is similar to that in

Section 3.1, except that  $\varepsilon = \tilde{T}_0^2 / \tilde{E}$  and the inner variables are defined as

$$\zeta = \eta \sqrt{Pr \tilde{Y}_{O,\infty} / \varepsilon} \quad , \quad \xi = \tilde{Y}_{O,\infty} (\tilde{x} - 1) / (3\varepsilon) \quad , \quad (3.54)$$

leading to

$$\frac{\partial^2 \theta}{\partial \zeta^2} - 2 \frac{\partial \theta}{\partial \xi} + \frac{1}{Le_0} \frac{\partial^2 \phi_0}{\partial \zeta^2} - 2 \frac{\partial \phi_0}{\partial \xi} = 0 \quad , \quad (3.55)$$

$$\frac{\partial^2 \theta}{\partial \zeta^2} - 2 \frac{\partial \theta}{\partial \xi} = -\tilde{D}a(\phi_0 + Le_0 \zeta^2 + \xi) \exp[\theta - \beta(\zeta^2 + \xi)] \quad , \quad (3.56)$$

with the initial and boundary conditions

$$\theta(\xi=0) = \phi_0(\xi=0) = 0 \quad ,$$

$$\zeta = 0 \text{ and } \zeta \rightarrow \infty \quad , \quad \xi > 0 : \quad \partial \theta / \partial \zeta = \partial \phi_0 / \partial \zeta = 0 \quad ,$$

where  $\beta = (\tilde{T}_0 - \tilde{T}_\infty) / \tilde{Y}_{O,\infty}$  and the reduced Damköhler number is

$$\tilde{D}a = \varepsilon [Da \tilde{Y}_{F,0} / (\tilde{T}_0 \tilde{Y}_{O,\infty})] \exp(-\tilde{E} / \tilde{T}_0) \quad . \quad (3.57)$$

Ignition is considered successful when the heat generation through reaction is sufficient to compensate the heat loss from the jet to the ambient at any location, and the ignition criterion is given by

$$(\partial \theta / \partial \xi)_{\zeta=0} \geq \beta \quad \text{or} \quad \partial \theta / \partial \zeta \geq 2\beta\zeta \quad \text{at any } \xi \quad . \quad (3.58)$$

## Chapter 4: Results and Discussions

### 4.1 Recapitulation

Limits of spontaneous ignition were identified as functions of slot width, flow rate, and temperatures of the hydrogen jet and ambient air for the two scenarios of a cool jet flowing into a hot ambient and a hot jet flowing into a cool ambient. Specifically, Sections 3.2 (for the cool jet case) and 3.4 (for the hot jet case) were referenced for the analysis of hydrogen due to its low local  $Le_F$  of 0.6. Equations balancing diffusive terms with reaction terms were obtained for the cool jet case (Eqn. 3.50), and equations balancing the transverse diffusive, streamwise convective terms and reaction terms were obtained for the hot jet case (Eqn. 3.56). The solutions from the equations are discussed in greater detail in the following sections.

### 4.2 Cool jet flowing into a hot ambient ( $T_\infty > T_0$ )

Equations (3.50) and (3.53), subject to Eqns. (3.51) – (3.52), were solved by a fourth order Runge-Kutta method (using computer codes). The results are shown in Fig. 4.1, a plot of the reaction temperature increase ( $a_T$ ) versus reduced Damköhler number. This reveals the lower and middle branches of an S-curve [5]. In each such curve, there is a maximum value of  $\tilde{D}a$  above which a solution does not exist. For values of  $\tilde{D}a$  smaller than this ignition  $\tilde{D}a$ , there are two solutions. This represents the transition from weak reaction to vigorous burning, and is defined as the ignition state. The lower branch, showing an increase of temperature with higher reaction rate,

is the physically realistic branch. The middle branch represents conditions that are not physically possible, owing to the negative slope. Spontaneous ignition is predicted for any  $\tilde{D}a$  greater than this critical value.

Three curves are included in Fig. 4.1, each with a different value of  $\alpha$ , where

$$\alpha = (\tilde{T}_\infty - \tilde{T}_0) / \tilde{Y}_{F,0} \quad (4.1)$$

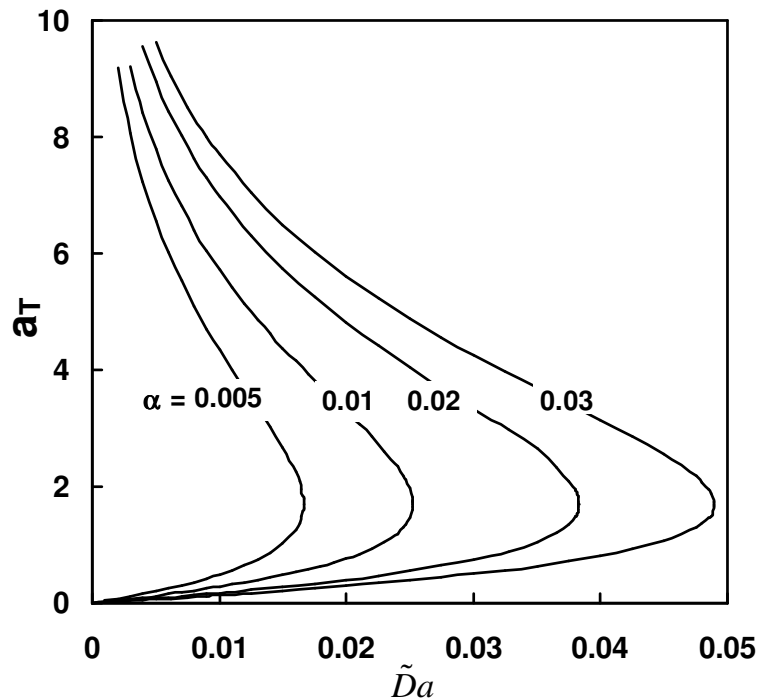


**Fig. 4.1:  $a_T$  versus  $\tilde{D}a$  for varying  $\alpha$  (which is changed by variations in  $\tilde{T}_0$  or  $\tilde{Y}_{F,0}$ ), with  $Le_F = 0.6$  and constant  $\tilde{T}_\infty = 0.0123$ , hot ambient. Definitions of  $\tilde{D}a$  and  $a_T$  are in Section 3.2(Part C-2).**

Fig. 4.1 indicates that a decrease in  $\alpha$  reduces the critical  $\tilde{D}a$  at ignition, which means that ignition is favored. Such a decrease can be accomplished either by increasing the reactant mass fraction in the fuel supply,  $\tilde{Y}_{F,0}$ , or by increasing the jet temperature,  $\tilde{T}_0$ . Both findings are physically realistic. A fuel such as hydrogen

(which has  $Le_F$  of 0.6 or less in mixtures with  $N_2$ , is hence more ignitable as compared to fuels such as isooctane and methane (which have higher  $Le_F$ , under the same conditions). Table 1 lists the typical values of  $\alpha$  and  $q_F$  for hydrogen and 2 other fuels.

Properties/Fuel	Hydrogen (H <sub>2</sub> )	Methane (CH <sub>4</sub> )	Iso-octane (C <sub>8</sub> H <sub>18</sub> )
Typical $\alpha$	0.0064	0.024	0.024
$q_F$ (kJ/g)	120.9	54.8	46.4

**Table 1: Values of  $\alpha$  and specific heat of combustion ( $q_F$ ) from [4].**

Parameter  $\alpha$  also can be changed by variations in the ambient temperature,  $\tilde{T}_\infty$ , but this changes  $\tilde{Da}$  simultaneously. To investigate the effects of  $\tilde{T}_\infty$  variations at fixed  $\tilde{Da}$  requires a rescaling. The rescaling is performed here by specifying a reference value of  $\tilde{T}_\infty$  as  $\hat{T}_\infty$ , defining rescaled parameters:

$$\hat{\epsilon} = (\hat{T}_\infty)^2 / \tilde{E}, \quad (4.2)$$

$$\hat{a}_T = (\tilde{T}_\infty^2 / \hat{T}_\infty^2) a_T \text{ and} \quad (4.3)$$

$$\hat{Da} = \tilde{Da} \tilde{Y}_{O,\infty} \tilde{x}^{4/3} [\tilde{Y}_{F,0} / (\hat{\epsilon} \tilde{x}^{1/3})]^{(1-Le_F)} \exp(-\tilde{E} / \hat{T}_\infty) / (4Pr\hat{T}_\infty) \quad (4.4)$$

and plotting the results in terms of rescaled variables  $\hat{a}_T$  and  $\hat{Da}$ . The results are shown in Fig. 4.2. Here an increase in  $\tilde{T}_\infty$ , which increases  $\alpha$  without changing  $\hat{Da}$ , is seen to favor ignition. This also is physically realistic because more heat is transferred to the cold fuel flow at a higher rate when the ambient is at a higher temperature. By the same reason, when the kinetic data are unchanged, an increased  $\tilde{T}_\infty$  yields ignition to occur nearer the edge of the jet. Note that the Damköhler number shown is a

function of the axial distance from the virtual origin of the jet (see Eqn. 2.50).

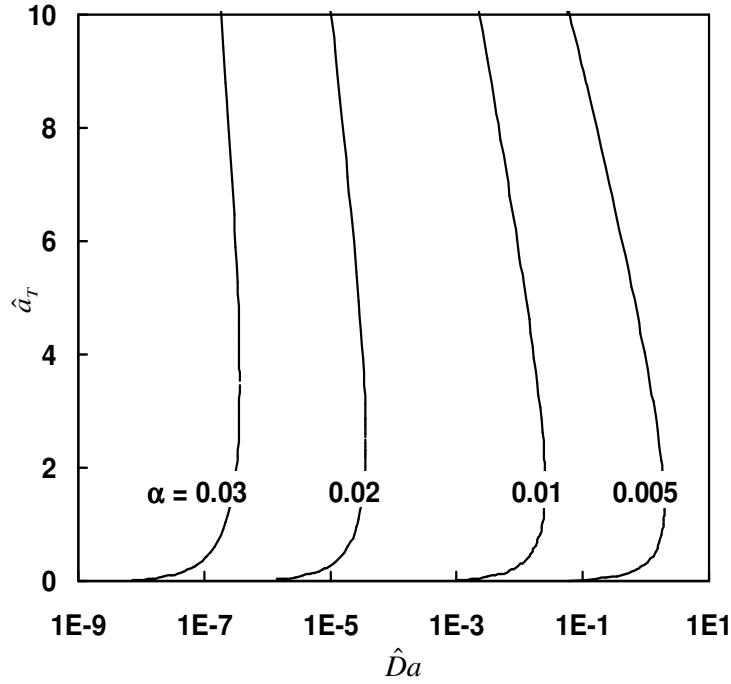


**Fig. 4.2: Rescaled plot of  $\hat{a}_T$  versus  $\hat{Da}$  (rescaled  $\tilde{Da}$  values due to changes in  $\tilde{T}_\infty$ ) for varying  $\alpha$  (which is changed by variations in  $\tilde{T}_\infty$ ), with  $Le_F = 0.6$ ,  $\tilde{T}_0 = 0.00226$ ,  $\tilde{E} = 1.79$ ,  $Y_{F,0} = 1$ , and  $\alpha = 0.01$  as reference, hot ambient.**

The influence of reactant Lewis number on ignition is considered in Fig. 4.3. Here  $Le_F$  is defined as the mixture thermal diffusivity divided by the mass diffusivity of fuel into the mixture. A decrease in  $Le_F$  for fixed  $\hat{Da}$  is seen to favor ignition. This occurs because a smaller  $Le_F$  implies that fuel species diffuse more quickly into the hot oxidizer. A fuel such as a mixture of hydrogen and nitrogen has a small  $Le_F$ , is hence easier to ignite than other fuels of higher  $Le_F$  at the same conditions. Nayagam and Williams [23] found that in a one-dimensional model of steady motion of edges of reaction sheets, increasing the Lewis number decreases the propagation velocity at small Damköhler numbers.

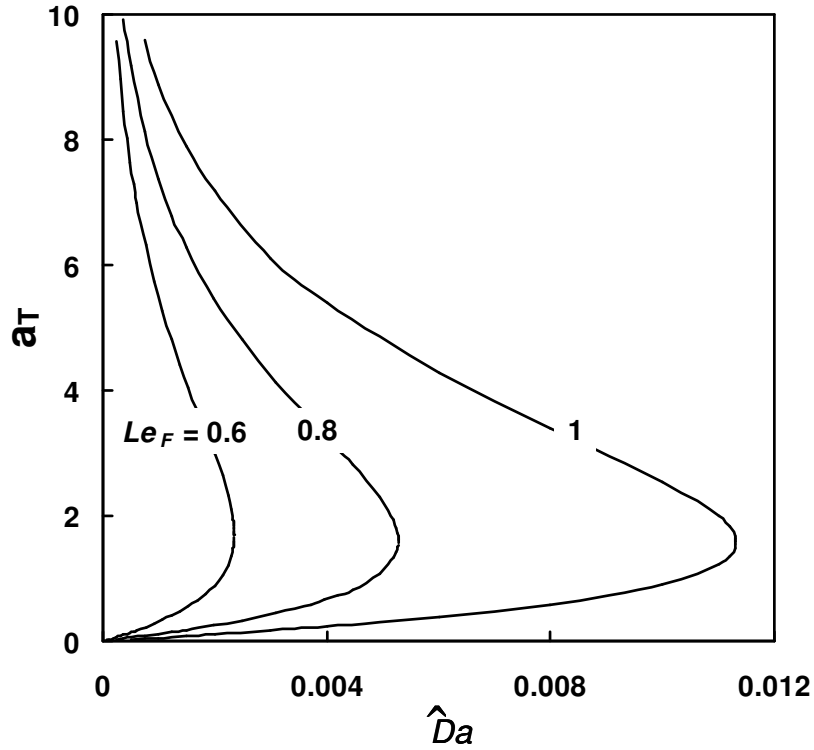


**Fig. 4.3:**  $a_T$  versus  $\hat{D}a$  (rescaled  $\tilde{D}a$  values due to changes in  $Le_F$ ) for varying  $Le_F$ , with  $\alpha = 0.02$ ,  $\tilde{T}_0 = 0.00226$ ,  $\tilde{E} = 1.79$ , hot ambient.

#### 4.2.1 Ignition states that separate the ignitable and non-flammable regions

Plots of ignition  $\hat{D}a$  versus  $\alpha$  under several conditions for the cool jet scenario are shown in Figs. 4.4 - 4.6. In Fig. 4.4, ignition  $\hat{D}a$  versus  $\alpha$  is plotted for varying  $Le_F$ , with  $Le_F = 1$  as the reference. The plot shows that as the  $Le_F$  decreases, ignition is favored (similar to explanation for Fig. 4.3) for decreasing  $\alpha$  (at fixed  $\tilde{T}_\infty$ ), resulting in a larger ignitable region. This is consistent with the findings shown in Fig. 4.2.

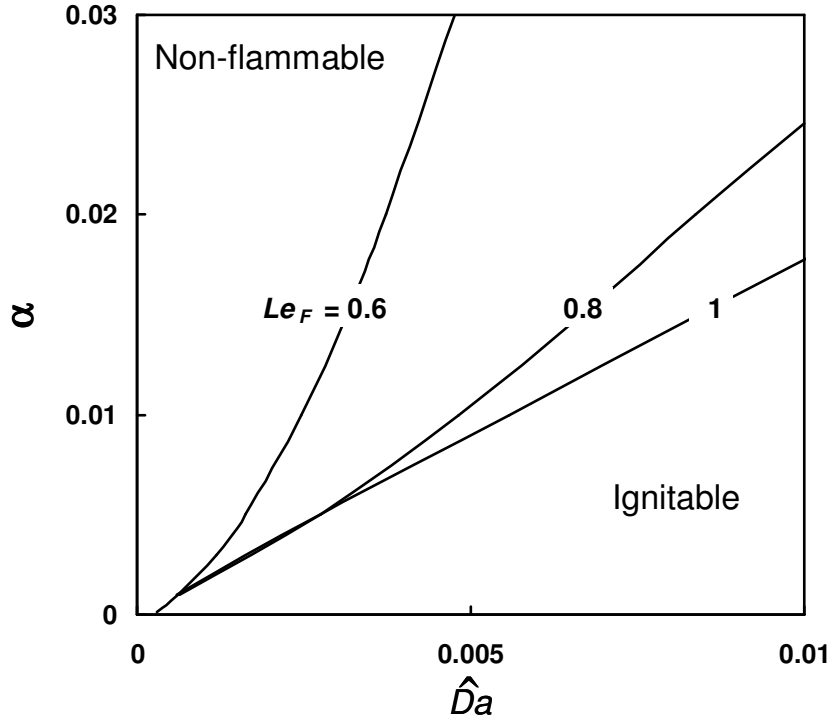


**Fig. 4.4:**  $\alpha$  (which is changed by variations in  $\tilde{T}_0$  or  $\tilde{Y}_{F,0}$ ) versus  $\hat{Da}$  (rescaled  $\tilde{Da}$  values due to changes in  $Le_F$ ) for varying  $Le_F$ , with  $Le_F = 1$  as reference and constant  $\tilde{T}_\infty = 0.0123$ , hot ambient.

In Fig. 4.5, ignition  $\hat{Da}$  versus  $\alpha$  is plotted for varying  $Le_F$ . The plot shows that as the  $Le_F$  decreases, ignition is favored (similar to explanation for Fig. 4.3) for increasing  $\alpha$  (due to increases in  $\tilde{T}_\infty$ ), resulting in a larger ignitable region, which is physically realistic.

In Fig. 4.6, ignition  $\hat{Da}$  versus  $\alpha$  is plotted for varying  $n_F$ . The plot shows that as the  $n_F$  increases, ignition is favored due to an increased reaction rate, resulting in a larger ignitable region. The effect of increasing  $n_F$  on ignition, however, is weaker as compared to the effects of reducing  $Le_F$  or increasing  $\tilde{T}_\infty$ .

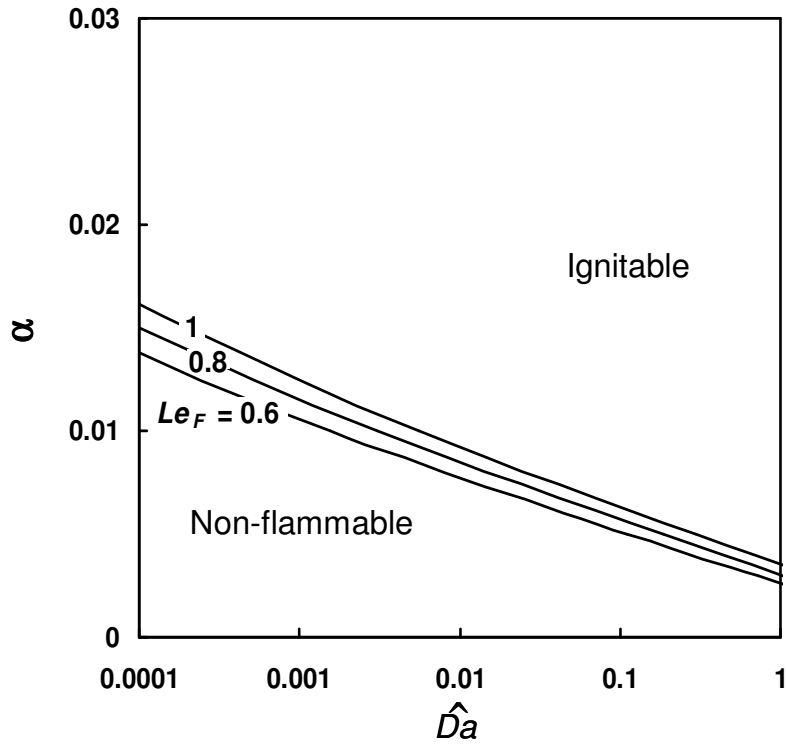


Fig. 4.5:  $\alpha$  (which is changed by variations in  $\tilde{T}_\infty$ ) versus  $\hat{D}a$  (rescaled  $\tilde{D}a$  values due to changes in  $\tilde{T}_\infty$ ) for varying  $Le_F$ , and  $\tilde{T}_0 = 0.00226$ , hot ambient.

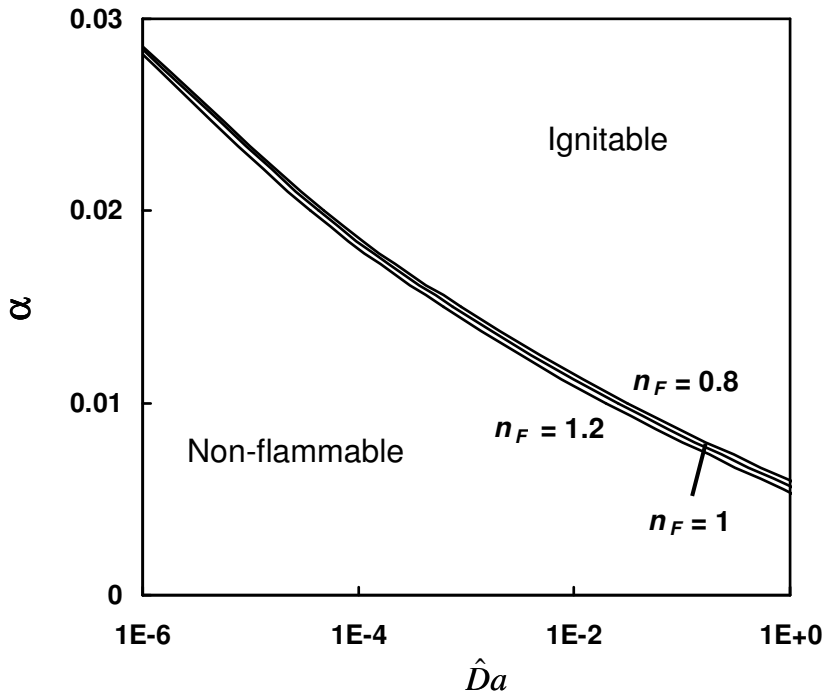


Fig. 4.6:  $\alpha$  (which is changed by variations in  $\tilde{T}_\infty$ ) versus  $\hat{D}a$  (rescaled  $\tilde{D}a$  values due to changes in  $\tilde{T}_\infty$ ) for varying  $n_o$  at  $Le_F = 0.6$ , and  $\tilde{T}_0 = 0.00226$ , hot ambient.

#### 4.3 Hot jet flowing into a cool ambient ( $T_0 > T_\infty$ )

Eqns. (3.55) – (3.56) were solved by the Crank-Nicholson method and the resulting matrix was inverted by LU decomposition (using computer codes). Selected results are shown in Figs. 4.7 and 4.8. In Fig. 4.7,  $\theta_{\max}$  represents the maximum value of temperature increase through reaction before ignition occurs. The corresponding ignition location,  $X$ , is shown in Fig. 4.8.

Three curves are included in Figs. 4.7 and 4.8, each with a different value of  $\beta$ , where

$$\beta = (\tilde{T}_0 - \tilde{T}_\infty) / \tilde{Y}_{O,\infty} \quad (4.5)$$

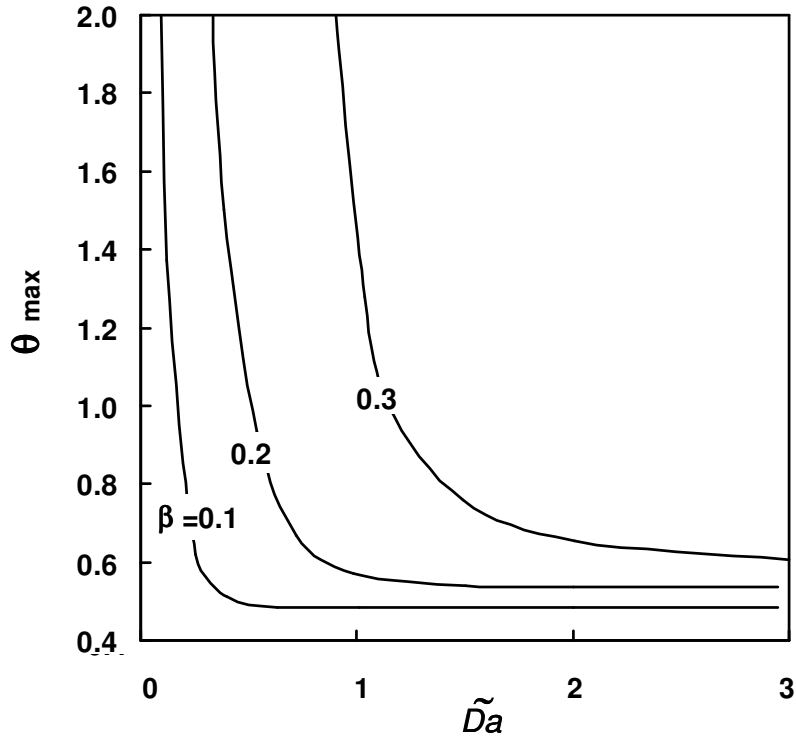
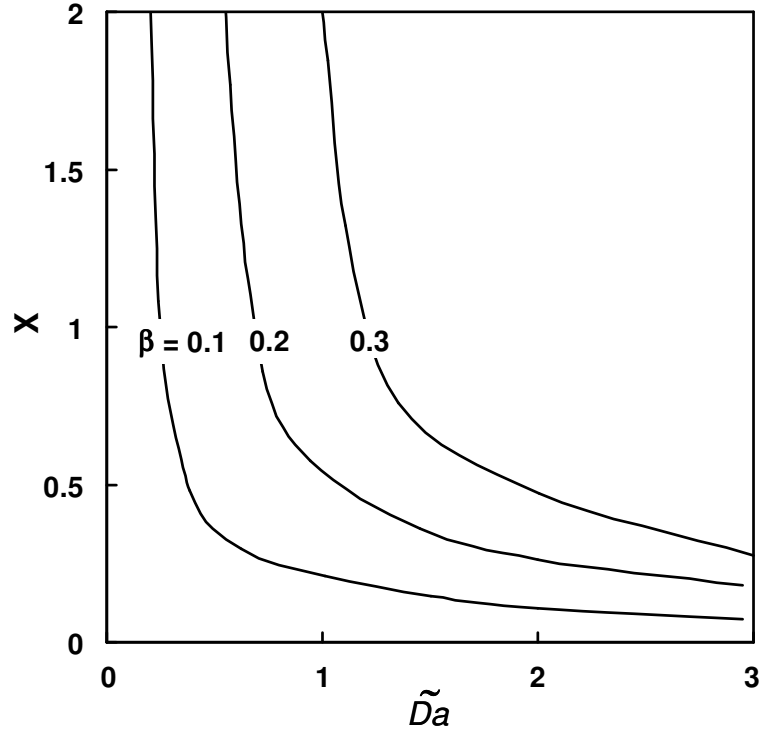


Fig. 4.7:  $\theta_{\max}$  versus  $\tilde{D}a$  for varying  $\beta$  (which is changed by variations in  $\tilde{T}_\infty$  or  $\tilde{Y}_{O,\infty}$ ) at  $Le_o = 1$ , and constant  $\tilde{T}_0 = 0.0388$ , hot jet.



**Fig. 4.8:  $X$  versus  $\tilde{D}a$  for varying  $\beta$  (which is changed by variations in  $\tilde{T}_\infty$  or  $\tilde{Y}_{O,\infty}$ ) at  $Le_o = 1$ , and constant  $\tilde{T}_0 = 0.0388$ , hot jet.**

These curves do not have the shape of an S-curve because the solutions are derived from a partial differential equation (since it is dependent on both transverse and streamwise stretched coordinates), in contrast to the ordinary differential equation of the cool jet (which is only dependent on the transverse diffusive term). On each curve, by increasing the reaction rate,  $\tilde{D}a$ , a smaller temperature increase and a shorter ignition location is observed before ignition, as is reasonable to expect. A higher value of  $\tilde{D}a$  yields an increased heat generation rate, which compensates for some heat loss from the hot jet to the cold ambient, favors ignition, and moves the point of ignition closer to the jet exit. In contrast, a reduction in  $\tilde{D}a$  weakens the reaction and makes ignition more difficult such that both  $\theta_{\max}$  and  $X$  increase.

Although an increase of  $X$  provides longer residence time for the reaction so that ignition can occur at a smaller  $\tilde{D}a$ , the reaction rate decreases with  $X$  because the jet is cooled by the cold ambient, as can be seen from the reaction term of Eq. (3.56). A sharp increase in  $\theta_{\max}$  and  $X$ , as shown the low  $\tilde{D}a$  side of the curves in Figs. 4.7 and 4.8, means that the reduction of reaction rate dominates over the residence time increase, and defines the smallest  $\tilde{D}a$  for which ignition occurs.

Figures 4.7 and 4.8 also indicate that a decrease in  $\beta$  for any fixed  $\tilde{D}a$  favors ignition, as ignition occurs at a lower temperature increase,  $\theta_{\max}$ , and at a shorter ignition location,  $X$ . More importantly, a decrease in  $\beta$  permits ignition at a lower value of  $\tilde{D}a$ . Such a decrease can be accomplished either by increasing the reactant mass fraction in the oxidizer supply,  $\tilde{Y}_{O,\infty}$ , or by increasing the ambient temperature,  $\tilde{T}_\infty$ . Both findings are physically realistic.

Parameter  $\beta$  also can be changed by variations in the jet temperature,  $\tilde{T}_0$ , but this changes  $\tilde{D}a$  simultaneously. To investigate the effects of  $\tilde{T}_0$  variations at fixed  $\tilde{D}a$  requires a rescaling similar to that performed for the cool jet scenario. The rescaling is performed here by specifying a reference value of  $\tilde{T}_0$  as  $\hat{T}_0$ , defining rescaled parameters :

$$\hat{\varepsilon} = (\hat{T}_0)^2 / \tilde{E}, \quad (4.6)$$

$$\hat{\theta}_{\max} = (\tilde{T}_0 / \hat{T}_0)^2 \theta_{\max} \quad \text{and} \quad (4.7)$$

$$\hat{D}a = \hat{\varepsilon} [Da \tilde{Y}_{F,0} / (\hat{T}_0 \tilde{Y}_{O,\infty})] \exp(-\tilde{E} / \hat{T}_0) \quad (4.8)$$

and plotting the results in terms of rescaled variables  $\hat{\theta}_{\max}$  and  $\hat{Da}$ . The results are shown in Figs. 4.9 and 4.10. Here an increase in  $\tilde{T}_0$ , which increases  $\beta$  without changing  $\hat{Da}$ , is seen to favor ignition because ignition can occur at a lower reaction rate, or lower  $\hat{Da}$ . This also is physically realistic. Ignition is predicted to occur near the centerline if the fuel is hotter than the air because this is where the highest temperature is attained.

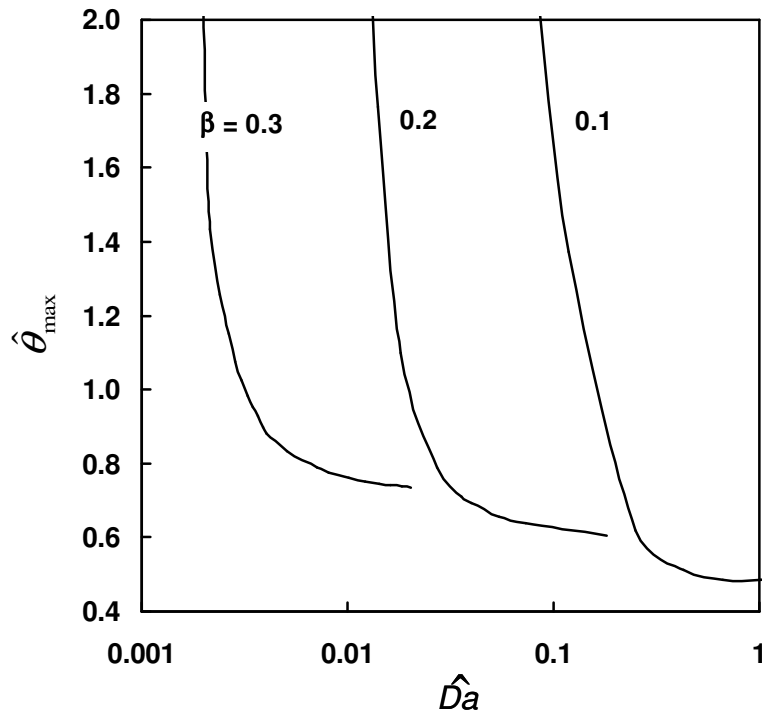


**Fig. 4.9:** Rescaled plot of  $\hat{\theta}_{\max}$  versus  $\hat{Da}$  (rescaled  $\tilde{Da}$  values due to changes in  $\tilde{T}_0$ ) for varying  $\beta$  (which is changed by variations in  $\tilde{T}_0$ ), with  $Le_o = 1$ ,  $\tilde{T}_\infty = 0.0358$ ,  $\tilde{E} = 1.79$ ,  $\tilde{Y}_{O_\infty} = 0.029$ , and  $\beta = 0.1$  as reference value, hot jet.

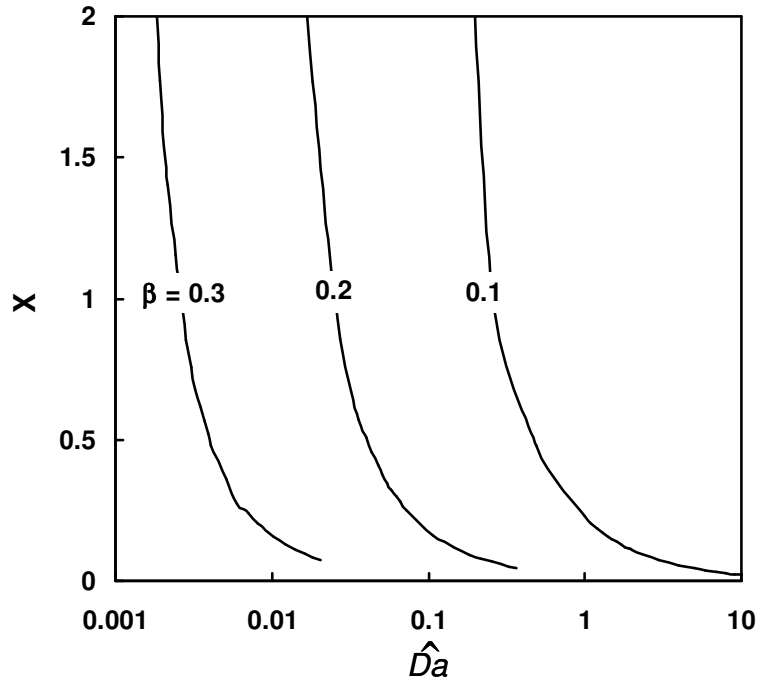


**Fig. 4.10: X versus  $\hat{D}a$  (rescaled  $\tilde{D}a$  values due to changes in  $\tilde{T}_0$ ) for varying  $\beta$  (which is changed by variations in  $\tilde{T}_0$ ), with  $Le_o = 1$ ,  $\tilde{T}_\infty = 0.0358$ ,  $\tilde{E} = 1.79$ ,  $\tilde{Y}_{O,\infty} = 0.029$ , and  $\beta = 0.1$  as reference value, hot jet.**

The effects of oxidizer Lewis number on spontaneous ignition are considered in Fig. 4.11. This plot shows that decreased  $Le_O$  makes ignition more difficult. For an increase in the mass diffusivity of the oxidizer (or a decreased  $Le_O$ ) at a fixed value of  $\tilde{D}a$ ,  $\theta_{\max}$  increases. In addition, the minimum  $\tilde{D}a$  for ignition increases with decreased  $Le_O$ . This differs from the ignition behavior with respect to fuel Lewis number in the cool jet case (Fig. 4.3). In a cool jet, there is unlimited heat transfer from the hot ambient gas to preheat the fuel so that a higher fuel diffusion rate (lower

$Le_F$ ) results in a higher fuel concentration in the reaction region, more heat generation through the reaction and, hence, easier ignition.

In the hot jet, only limited heat is available from the fuel flow. An increased oxidizer mass diffusivity increases the transport rate of oxidizer to the center of the jet, thus requiring more heat to preheat the oxidizer, decreasing the temperature in the hot zone, and making ignition more difficult. Furthermore, unlike the cool jet case, the Lewis number of the oxidizer only has a weak effect on the ignition state (see Fig. 4.11) because ignition occurs near the jet exit if successful. In the reaction region, the flow velocity is high such that streamwise convection dominates over transverse diffusion. Moreover, because  $Le_O$  is close to unity for oxygen in air, the effect of  $Le_O$  in a hot-hydrogen cold-air system is secondary. As in Fig. 4.10, the effect of  $Le_O$  on the ignition location is similar to that on the ignition state, shown in Fig. 4.12.

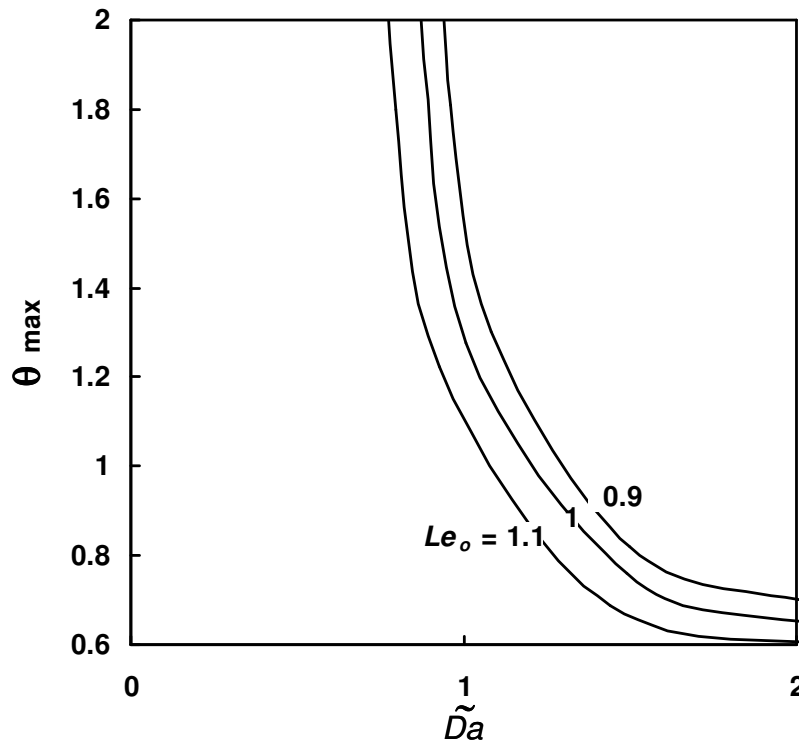


**Fig. 4.11:**  $\theta_{\max}$  versus  $\tilde{D}a$  for varying  $Le_o$ , with  $\beta = 0.3$  and constant  $\tilde{T}_0 = 0.0388$ , hot jet.

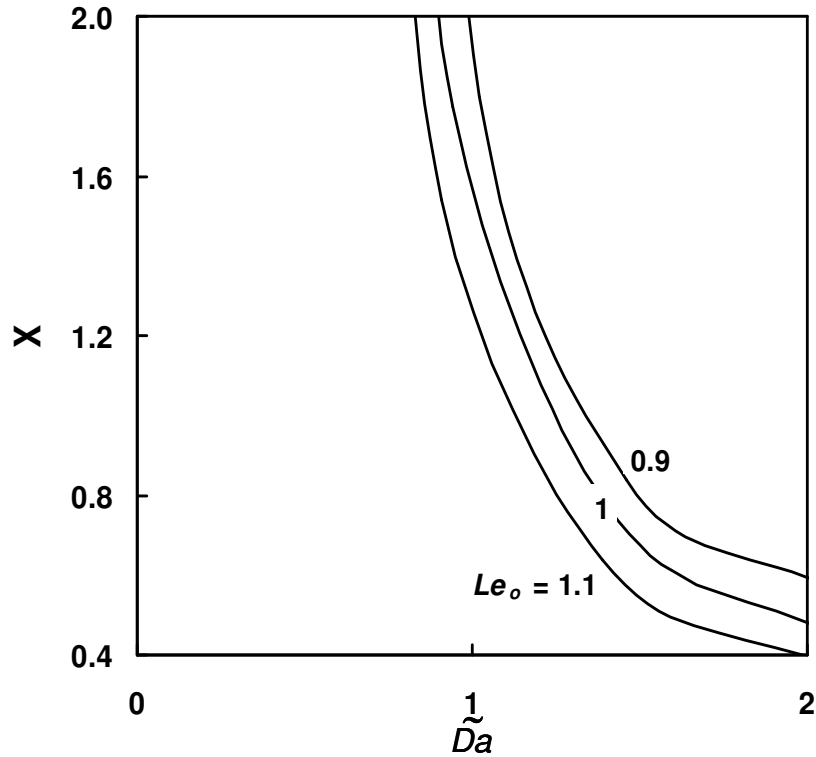


**Fig. 4.12: X versus  $\tilde{D}a$  for varying  $Le_o$ , with  $\beta = 0.3$  and constant  $\tilde{T}_0 = 0.0388$ , hot jet.**

#### 4.3.1 Ignition states that separate the ignitable and non-flammable regions

Plots of ignition  $\hat{D}a$  versus  $\beta$  under several conditions for the hot jet scenario are shown on Figs. 4.13 – 4.14. In Fig. 4.13, ignition  $\hat{D}a$  versus  $\beta$  was plotted for varying  $n_o$  and constant  $\tilde{T}_0$ . The plot shows that as the oxidizer reaction order increases, ignition is favored, resulting in a larger ignitable region, which is physically realistic.

In Fig. 4.14, ignition  $\hat{D}a$  versus  $\beta$  was plotted for varying  $n_o$  and  $\tilde{T}_0$ . The plot shows that as the  $n_o$  and  $\tilde{T}_0$  increases, ignition is favored, resulting in a larger ignitable region covering lower values of  $\hat{D}a$ .

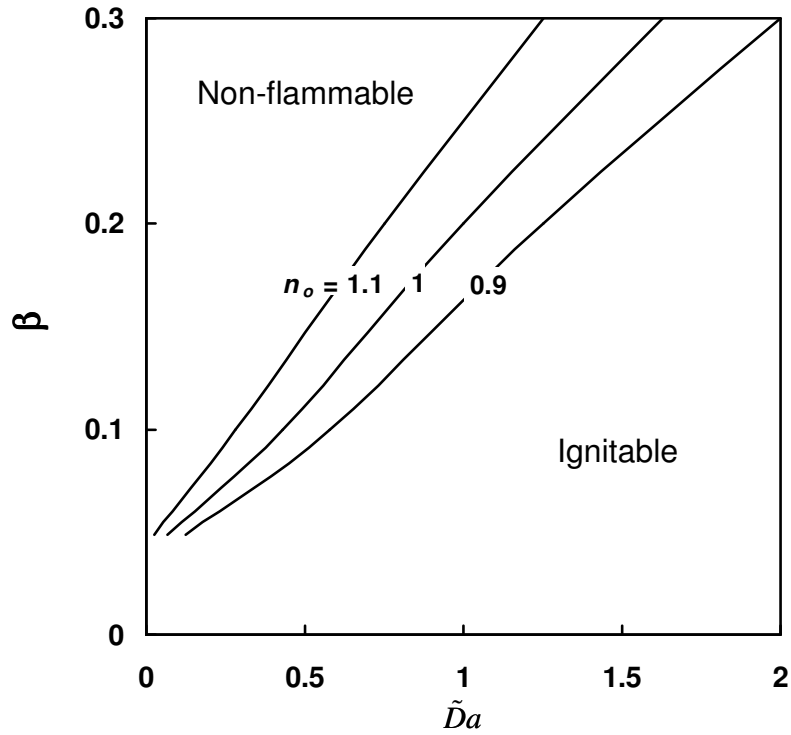


Fig. 4.13:  $\beta$  (which is changed by variations in  $\tilde{T}_\infty$  or  $\tilde{Y}_{O,\infty}$ ) versus  $\tilde{D}a$  for varying  $n_o$ , and constant  $\tilde{T}_0 = 0.0388$ , hot jet.

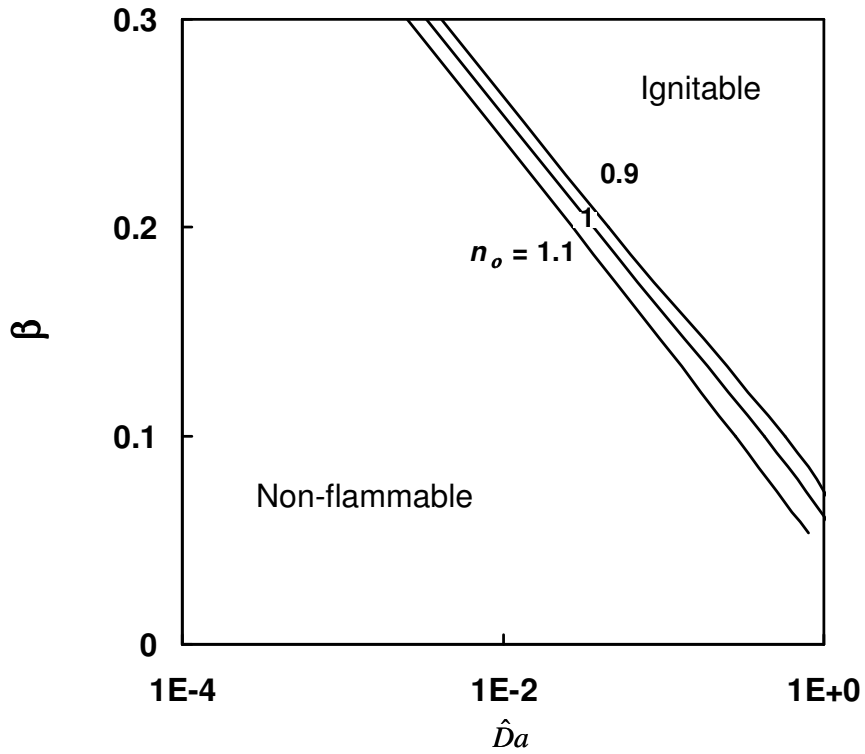


Fig. 4.14:  $\beta$  (which is changed by variations in  $\tilde{T}_0$ ) versus  $\hat{D}a$  (rescaled  $\tilde{D}a$  values due to changes in  $\tilde{T}_0$ ) for varying  $n_o$ , with  $Le_o = 1$ ,  $\tilde{T}_\infty = 0.0358$ ,  $\tilde{E} = 1.79$ ,  $\tilde{Y}_{O,\infty} = 0.029$ , and  $\beta = 0.1$  as reference value, hot jet.

## Chapter 5: Conclusions

### 5.1 Conclusions

The spontaneous ignition of a hydrogen jet emanating from a slot into air has been considered analytically. A similarity solution of the flowfield was obtained for the scenario of cool jet flowing into hot ambient, which was then combined with the species and energy conservation equations. Solutions were found using activation energy asymptotics.

The analysis yielded limiting conditions for spontaneous ignition of fuel jets. For a cool jet flowing into a hot ambient, ignition is found to be a strong function of ambient temperature and fuel Lewis number. Ignition was favored by an increase in ambient temperature or a decrease in Lewis number. For the hot jet scenario, ignition was significantly affected by the jet temperature, but only weakly affected by the oxidizer Lewis number.

Because spontaneous ignition is very sensitive to temperature, ignition is predicted to occur near the edge of the jet if the fuel is cooler than the air and on the centerline if the fuel is hotter than the air.

The value of the mixture fraction  $Z$  at which ignition occurs can be extracted from

the AEA solutions as 
$$Z = \frac{\sigma Y_F + (Y_{o,\infty} - Y_o)}{\sigma Y_{F,o} + Y_{o,\infty}} .$$

In the first scenario of cool jet flowing into a hot ambient, ignition occurs at  $Z \rightarrow 0$  since it occurs at the jet edge where  $\tilde{Y}_O \rightarrow \tilde{Y}_{O,\infty}$  and  $Y_F$  is very small and of the order  $\epsilon$ . In the second scenario of the hot jet, ignition occurs at the jet centerline, where  $Z \rightarrow 1$  since  $\tilde{Y}_O \rightarrow 0$  and  $Y_F \rightarrow Y_{F,0}$ .

The present model can be extended to studies of flame extinction and to circular jet configurations. When experimental data becomes available, parametric comparisons can also be made to establish reaction rates for use in the present model.

## Bibliography

- [1] E.C. Magison, *Electrical Instruments in Hazardous Locations*, 2<sup>nd</sup> Edition, Instrument Society of America, Pittsburg, Pennsylvania, pp.304, 1972.
- [2] J. Hord, *Is Hydrogen a Safe Fuel?*, *International journal of hydrogen energy*, 3:157, 1978.
- [3] R.C. Weast, *CRC Handbook of Chemistry and Physics*, CRC Press, West Palm Beach (1979).
- [4] A.M. Kanury, *Introduction to Combustion Phenomena*, Gordon and Breach Publishers, Amsterdam (1975).
- [5] F.A. Williams, *Combustion Theory*, 2nd Edition, Addison-Wesley Publishing Company, Redwood City, CA, pp.76-84, 1985.
- [6] N. Peters, *Turbulent Combustion*, Cambridge University Press, Cambridge, England, pp.178-186, 2000.
- [7] A. Liñán, F.A. Williams, *Fundamental Aspects of Combustion*, Vol. 34 of Oxford Engineering Science Series, Oxford University Press, New York, pp.57-81, 1993.
- [8] H.G. Im, S.R. Lee, C.K. Law., *Ignition in the Supersonic Hydrogen/Air Mixing Layer with Reduced Reaction Mechanisms*, AIAA-1994-548 Aerospace Sciences Meeting and Exhibit, 32nd, Reno, NV, Jan 10-13, 1994
- [9] H.G. Im, B.H. Chao, J.K. Bechtold, C.K. Law, *Analysis of Thermal Ignition in the Supersonic Mixing Layer*, AIAA J 32, pp.341-349, 1994.

- [10] S.R. Lee, S.H. Chung, On the structure of Hydrogen Diffusion Flames with Reduced Kinetic Mechanisms, *Combust. Sci. Tech.*, 96, pp.247.
- [11] B.T Helenbrook, C.K. Law, Ignition of Hydrogen and Oxygen in Counterflow at High Pressures, *Proc. Combust. Inst.*, pp.815-822, 1996.
- [12] H.G. Im, B.T Helenbrook, S.R. Lee, C.K. Law, Ignition in the supersonic hydrogen/air mixing layer with reduced reaction mechanisms, *J. Fluid Mech.*, vol 322, pp.275-296, 1996.
- [13] X.L. Zheng, C.K. Law, Ignition of Premixed Hydrogen/Air by Heated Counterflow under Reduced and Elevated Pressures, *Combust. Flame*, pp.136-168, 2004.
- [14] V.V. Toro, A.V. Mokhov, H.B. Levinsky, M.D. Smooke, Combined Experimental and Computational Study of Laminar, Axisymmetric Hydrogen-air Diffusion Flames, *Proc. Combust. Inst.* 30:485, 2005.
- [15] M. Chaos, R.-H Chen, E.J. Welle, W.L., Roberts, Fuel Lewis Number Effects in Unsteady Burke Schumann Hydrogen Flames, *Combust. Sci. Tech.* 177:75, 2005.
- [16] Y., Liu, P., Pei , Asymptotic analysis on autoignition and explosion limits of hydrogen-oxygen mixtures in homogeneous systems, *International J. Hydrogen Energy* , Vol. 31, No. 5, pp.639-647, 2006.
- [17] F.L. Dryer, M.Chao, Z. Zhao, J.N. Stein, J.Y. Alpert, C.J. Homer, Spontaneous Ignition of Pressurized Releases of Hydrogen and Natural Gas into Air, *Combust. Sci. Tech.*, v179, pp.663-694, 2007.

- [18] C.K. Law, Combustion Physics, C.K. Law, Cambridge University Press, New York, pp.313-315, 2006.
- [19] R.W. Bilger, Combust. Flame, 30, pp.227-228, 1977.
- [20] M.H. Holmes, Introduction to Perturbation Methods, p1-5 ,Springer, New York, 1994.
- [21] G. Damköhler, Zeit.Elektrochem. 42, 846, 1936.
- [22] D.A. Frank-Kamenetskii, Diffusion and Heat Transfer in Chemical Kinetics, New York, Plenum Press, 64-72, 1969.
- [23] D.R Kasoy and F.A. Williams, Phys Fluids 11, 1343, 1968.
- [24] D.R Kasoy, M.K., Liu and F.A. Williams, Phys Fluids 12, 265, 1969.
- [25] F.E. Fendell, J. Fluid Mech.21, 281, 1965.
- [26] H. Schlichting, Boundary-Layer Theory, Seventh Edition, McGraw-Hill, Inc.,p. 127-200, 1979.
- [27] W. Bickey, The Plane Jet, Phil. Mag. Ser. 7, 23: 727, 1939.
- [28] V. Nayagam, F.A. Williams, Lewis-number effects on edge-flame propagation, Journal of fluid mechanics, 458: 219-228, 2002.

## ABSTRACT

Title of Document: FLAME QUENCHING LIMITS OF  
HYDROGEN LEAKS

Christopher W. Moran, Master of Science  
in Fire Protection Engineering, 2008

Directed By: Assistant Professor, Peter B. Sunderland,  
Department of Fire Protection Engineering

This study examines flame quenching limits of hydrogen leaks in compression fittings and tube burners. Experimental work is presented. Measurements included ignition limits for leaking compression fittings on tubes of 3.16-12.66 mm in diameter and the ignition and quenching limits of tube burners with diameters of 0.15 – 0.56 mm. Minimum ignition flow rates of 0.028 mg/s for hydrogen, 0.378 mg/s for methane, and 0.336 mg/s for propane were found in the compression fitting experiments. The upstream pressure does not play a role in the ignition flowrate limit. The minimum quenching limits of hydrogen found in tube burners were 2.1 and 3.85  $\mu\text{g/s}$  in oxygen and air, respectively. These correspond to heat release rates of 0.252 and 0.463 W, respectively, the former being the weakest observed flame ever.

FLAME QUENCHING LIMITS OF HYDROGEN LEAKS

By

Christopher W. Moran

Thesis submitted to the Faculty of the Graduate School of the  
University of Maryland, College Park, in partial fulfillment  
of the requirements for the degree of  
Master of Science  
2008

Advisory Committee:  
Assistant Professor Peter B. Sunderland, Chair  
Professor Marino di Marzo  
Associate Professor Arnaud Trouvé

© Copyright by  
Christopher W. Moran  
2008

## Acknowledgements

This work was supported by NIST (Grant 60NANB5D1209) under the technical management of J. Yang. I also very much appreciate the support that was offered me through the Clark School of Engineering Distinguished Graduate Fellowship that allowed me to work and study here.

I would like to express my gratitude to my advisor Dr. Peter Sunderland, for his guidance, support, and encouragement. Never before have I met a professor as enthusiastic about teaching and helping his students. It has been my privilege.

I also thank Dr. James Milke, for guiding me through the program and involving me in the department. His enthusiasm and guidance while I considered the pursuit of this degree was invaluable.

I thank my advisory committee, Dr. Arnaud Trouvé and Dr. Marino di Marzo for their time, input and help.

The faculty of the Department of Fire Protection Engineering has been exceptional for their help and support. I would not have been able to get through my years here without them.

I would also like to thank my colleagues, for their assistance, reminders, and friendship. Specifically, Richard Axelbaum and Michael Butler of Washington University were instrumental in the completion of this work. Beei-Huan Chao (of University of Hawaii) assisted with the choked-flow calculations.

Lastly, I would like to thank my parents for their encouragement and support. I never would have been able to have the college experience that I did without them.

# Table of Contents

Acknowledgements.....	ii
List of Tables .....	iv
List of Figures .....	v
Chapter 1: Introduction.....	1
1.1 Hydrogen Chemistry.....	1
1.2 Hydrogen Economy .....	2
1.3 Hydrogen Fire Safety.....	4
1.4 Objectives .....	5
Chapter 2: Flame Quenching Limits of Leaky Compression Fittings.....	7
2.1 Experimental Background and Procedure .....	7
2.1.1 <i>Experimental Introduction</i> .....	7
2.1.2 <i>Fittings</i> .....	10
2.1.3 <i>Flow System</i> .....	13
2.1.4 <i>Lab Safety</i> .....	14
2.1.5 <i>Procedures</i> .....	15
2.1.6 <i>Sources of Error</i> .....	17
2.2 Results.....	18
2.2.1 <i>Ignition Flowrate Limits</i> .....	19
2.2.2 <i>Effects of Fitting Orientation</i> .....	24
2.2.3 <i>Effects of Leak Type</i> .....	25
2.2.4 <i>Effects of Tube Diameter</i> .....	26
Chapter 3: Weak Flames.....	30
3.1 Experimental Background and Procedure .....	30
3.1.1 <i>Experimental Introduction</i> .....	30
3.1.2 <i>Burners</i> .....	31
3.1.3 <i>Flow System</i> .....	32
3.1.4 <i>Procedures</i> .....	35
3.1.5 <i>Sources of Error</i> .....	36
3.2 Results.....	37
3.2.1 <i>Ignition Flowrate Limits</i> .....	38
3.2.2 <i>Effects of Orientation on Ignition Flowrate Limits</i> .....	39
3.2.3 <i>Quenching Flowrate</i> .....	41
3.2.4 <i>Weakest Flame Ever Observed</i> .....	43
Chapter 4: Conclusions.....	46
4.1 Compression Fittings .....	46
4.2 Weak Flames.....	47
Appendix A: Fuel Properties .....	49
References.....	50

## List of Tables

Table 2.1. Compression Fitting Burner Summary .....	10
Table 2.2. Round Orifice Diameters .....	23
Table 3.1. Tube Burner Summary.....	32
Table 3.2. Volumetric Flowrates and Exit Velocities.....	34
Table 3.3. Ignition Flowrate Limits for Burner Heights and Oxygen Velocities. ....	38
Table 3.4. Quenching Flowrates and Heat Release Rates. ....	41
Table A.1. Fuel Properties .....	49

## List of Figures

Fig. 2.1	Image of Fitting Assembly	11
Fig. 2.2	Image of Weak Flame on Platinum Burner	12
Fig. 2.3	Hydrogen Flow System Schematic	14
Fig. 2.4	Image of Fitting Assembly and Gas Collection Device	17
Fig. 2.5	Image of Flames on Burner 8L	19
Fig. 2.6	Image of Flames on Burner 4L	19
Fig. 2.7	Image of Flames on Burner 2L	19
Fig. 2.8	Plot of $m_{fuel}$ versus Upstream Pressure	21
Fig. 2.9	Plot of $V_{fuel}$ versus Upstream Pressure	22
Fig. 2.10	Plot of Leak Diameter versus Upstream Pressure	24
Fig. 2.11	Plot of $m_{fuel}$ versus Orientation	25
Fig. 2.12	Plot of $m_{fuel}$ versus Leak Type	26
Fig. 2.13	Plot of $m_{fuel}$ versus Burner Diameter	27
Fig. 2.14	Image of Hydrogen Flames	28
Fig. 2.15	Image of Methane Flames	28
Fig. 2.16	Image of Propane Flames	29
Fig. 3.1	Image of Coflow Burner	33
Fig. 3.2	Hydrogen Flow System Schematic	34
Fig. 3.3	Oxygen Flow System Schematic	35
Fig. 3.4	Plot of $m_{fuel}$ versus Diameter	39
Fig. 3.5	Plot of $m_{fuel}$ versus Orientation	40
Fig. 3.6	Plot of Quenching $m_{fuel}$ versus Diameter	42
Fig. 3.7	Plot of Power versus Diameter	43
Fig. 3.8	Image of Weakest Flame	44
Fig. 3.9	Image of Weak Flame on Platinum Burner	45

# **Chapter 1: Introduction**

## ***1.1 Hydrogen Chemistry***

Hydrogen is a very unusual fuel. It is the lightest fuel and has very wide flammability limits, 4-75% by volume (Kanury, 1975). Hydrogen has the lowest quenching distance (0.51 mm), the smallest ignition energy of any fuel in air (0.028 mJ), the lowest auto-ignition temperature of any fuel ignited by a heated air jet (640 °C), the highest laminar burning velocity of any fuel in air (2.91 m/s), and the highest heat of combustion (119.9 MJ/kg) (Kanury, 1975). Hydrogen flames are the dimmest of any fuel. Hydrogen also embrittles many metals more than any other fuel.

Despite these unusual aspects of hydrogen, it is attractive as an energy carrier. It can be produced from water and electricity. It can power fuel cells or engines with only water vapor as exhaust. Its combustion produces no carbon dioxide.

Hydrogen may not be any more intrinsically hazardous from a fire safety standpoint than gasoline or diesel. However, over a century of experience with these traditional fuels in widespread vehicle use has resulted in good fire safety records. Further research is necessary if hydrogen vehicles are to be introduced with a similar safety record.

One of the most attractive aspects of using hydrogen as an alternative fuel source is that there are no carbon products produced. No greenhouse gases are produced during the reaction. The lack of carbon in the reaction eliminates the main source of radiation and visible light as compared to hydrocarbon flames (Bregeon et al., 1978). This makes detecting hydrogen flames especially difficult. The flames are also typically hotter than hydrocarbon flames as the adiabatic flame temperature is approximately 2400 K (Turns, 2000).

Although hydrogen leaks can be extremely dangerous, there are aspects of hydrogen that are

safer than other combustible gases. Because hydrogen is so light, it rises at 20 m/s, much faster than most combustible gases and 6 times faster than natural gas (DOE, 2007). Hydrogen also diffuses 3.8 times faster than natural gas (DOE, 2007). This makes it more difficult for the gas to collect and reach flammable concentrations in open spaces. If the gas is not contained, it diffuses too quickly to reach explosive concentrations. It is much more likely that the hydrogen leak would be ignited near the source and form a flame as opposed to forming an explosive mixture.

Hydrogen can cause steel embrittlement and permeation leaks. While permeation leaks are generally not flammable, they do present a challenge in the storage of hydrogen. Hydrogen's low molecular weight motivates its storage at higher pressures (or liquification). Due to hydrogen's low molecular weight, it has the highest volumetric leak propensity of any fuel.

## ***1.2 Hydrogen Economy***

As gasoline prices climb and concerns grow about the extensive release of greenhouse gases into the atmosphere, hydrogen has emerged as one of the leading alternative fuel sources. Oil currently supplies 33% of the world's primary energy (Marban and Valdes-Solis, 2007). Hydrogen as an energy carrier can help mitigate concerns about fossil fuel consumption (Yamawaki et al., 2007). Some benefits of hydrogen are that it can be converted to electricity with a high efficiency, its products of combustion are mainly water, it can be stored as liquid, gas or solid, and it can be transported using pipelines, tankers or rail trucks over long distances (Sherif et al., 2005). It is also projected that hydrogen can be produced efficiently using nuclear sources or renewable methods such as wind (Von Jouanne et al., 2005). Hydrogen, however, is also unique in that it has unusual fire hazards that must be taken into account before widespread

use of this fuel can be considered safe.

The United States government has experienced itself over the past few years to moving towards a hydrogen fueled economy. In 2003, President Bush announced the Hydrogen Fuel Initiative to accelerate the research and development of hydrogen for the use in transportation (DOE, 2007). It was thought that widespread use of hydrogen could help reduce the dependence on foreign oil as well as reduce pollutants. In 2005, the Energy Policy Act was created to reinforce government support for hydrogen and alternative fuel technology (DOE, 2007). The Advanced Energy Initiative was enacted in 2006 to again help accelerate research with the potential to reduce near term oil use and advance activities under the Hydrogen Fuel Initiative (DOE, 2007). Presently, however, there are few codes or standards to regulate the hydrogen transportation industry. These codes and standards are currently being experienced.

Hydrogen is being considered as a fuel source for transportation purposes largely owing to its lack of carbon emissions after combustion. Veziroglu and Babir (1992) argue that hydrogen is one of the safest fuels owing to its high diffusivity and buoyancy. In case of a leak, hydrogen will be released into the atmosphere as opposed to gasoline, which will pool and presents a longer danger. Hydrogen also radiates much less heat as it does not produce carbon compounds. This means that people are rarely burned by a hydrogen flame unless they are in the flame. Lovins (2003) compares hydrogen to gasoline and natural gas as an energy source and states that "a good fuel cell system is about 50-70% efficient, hydrogen to electricity, while a typical car engine's efficiency from gasoline to output shaft averages only about 15-17%."

Bossel and Eliasson (2002) believe that the upstream energy costs of a hydrogen economy have not been adequately assessed. The energy necessary to form hydrogen either through electrolysis or the conversion of another gas does not make it efficient enough to use as an energy carrier.

They state that "the production, packaging, storage, transfer, and delivery of the gas are so energy consuming that other solutions must be considered."

### ***1.3 Hydrogen Fire Safety***

Owing to its low molecular weight, hydrogen is often stored at high pressures. It is predicted that hydrogen will need to be stored at up to 40 MPa to be an effective vehicle fuel (Takeno et al., 2007). Hydrogen's safety hazards resulted in a Department of Energy report (Cadwallader and Herring, 1999) finding that hydrogen containment was the chief safety concern associated with using hydrogen as a transportation fuel. One characteristic of hydrogen that makes it more prone to risk is that it is easier to ignite than most other common fuels. The minimum ignition energy for hydrogen is an order of magnitude lower than those for methane and propane (Ge and Sutton, 2006). This means that a small spark might be able to ignite a hydrogen leak, whereas the same spark might not be able to ignite a methane or propane leak. It has also been noted that hydrogen flames have weak luminosity (Cheng et al., 2005), hence a hydrogen leak sustaining a flame would be difficult to detect by the human eye.

Swain and Swain (1992) did a comparison study of hydrogen, methane and propane fuel leakage in a residential setting. Only pressures less than 0.965 bar (14 psi) were used in the study. In their research, they found three times more hydrogen volume than methane would escape through a leak. As relatively high leakage rates can lead to combustible fuel clouds, they discovered that propane produces a cloud much faster than hydrogen or methane.

Hydrogen is odorless and colorless, which makes detecting hydrogen leaks extremely difficult. Odorants are not used with hydrogen as no known odorant is light enough to diffuse as fast as hydrogen and odorants poison fuel cells. Hydrogen is nontoxic although death can occur due to

asphyxiation if too much oxygen is displaced.

Hydrogen's unique fire hazards present a challenge to firefighters. Currently, firefighters are taught to detect hydrogen flames with a straw broom. Thermal imaging firefighting cameras are effective but not all departments have them. When near a possible hydrogen leak, firefighters listen for leaking gas, look for heat shimmering, and use their detection methods. If a leak is found, they are taught to stop the flow if possible. If they are unable to stop the flow, then the flame is allowed to consume the gas supply if safe. Extinguishing the flame without stopping the leak can result in an explosive mixture.

#### ***1.4 Objectives***

Codes and standards are currently being experienced for hydrogen system fire safety. One issue of interest is permissible leak rates. However, prior to the present work no measurements had been performed to establish the maximum leak rate for nonflammable conditions.

Thus motivated, the objects of this work are:

1. Measure the minimum flowrates that are necessary to support flames from compression fittings in air. Three different gases were used in the experiments; hydrogen, methane and propane.
2. Identify the minimum ignition and quenching hydrogen flowrates possible for any choice of burner and oxidizer. Determine whether this produces the weakest flame ever observed.

The results of this work are expected to be helpful in the creation of the codes and standards governing the safe use of hydrogen and in the field of micro-combustion. The data found during these experiments gives the ignition flowrate limits for leaky compression fittings, which can be

used when deciding the minimum allowable leaks in a commercial application. Micro-combustion is a growing field as electronics get smaller and batteries make up most of the device weight. A lighter, more efficient (more environmentally friendly) power supply can be found using micro-combustors (Federici, 2006).

## **Chapter 2: Flame Quenching Limits of Leaky Compression Fittings**

### ***2.1 Experimental Background and Procedure***

As many high pressure systems are made with compression fittings, it is important to determine the possible leakage scenarios and the ignition flowrate limits associated with these fittings. Three different fuels were used to determine the ignition flowrate limits for a number of different possible failure scenarios. The first, hydrogen, is being considered for use in alternative fuel source applications but many of the dangers are still unknown. The second gas is methane. This gas is commonly used as a fuel in many applications and its properties are better known. In many cases, it is known as natural gas and is used to heat homes and power vehicles. Methane's advantage over other hydrocarbons is that it produces less CO<sub>2</sub> when combusted. The third gas used is propane. Propane is most commonly used for cooking on grills and portable stoves. It is also used in refrigeration and as an automotive fuel.

Although the main purpose of the experimentation was to find the flame quenching limits for hydrogen, the same tests were also done on methane and propane to have a comparison of the different fuels as they are used in many of the same applications.

#### ***2.1.1 Experimental Introduction***

Quenching and blowoff limits bound the leak flowrates that can support combustion. Matta et al. (2002) found that a propane flame is not able to exist when its predicted length is less than the measured standoff distance. Experiments verified this analytical method of finding the quenching flowrate by establishing a propane flame over a hypodermic, stainless steel tube and decreasing the fuel flowrate until extinction. It was also found that the flowrate at quenching is practically independent of the tube diameter. Work in this laboratory has extended this work to hydrogen fuel and diverse burners (Butler et al., 2008).

There are three classifications for laminar jet flames: diffusion controlled flames (e.g., Burke and Schuman, 1928), diffusion and momentum controlled flames (e.g., Roper et al., 1977) and micro diffusion flames controlled by momentum and diffusion (e.g., Ban et al., 1994). Extensive research has been done on the first two types, but only a limited amount has been done on micro diffusion flames. Baker et al. (2002) devised a flame height expression for purely diffusion controlled flames capable of accurately predicting micro-slot diffusion flame heights. Useful parameters for characterizing dominant flame mechanisms were defined: a diffusion-buoyancy and a diffusion-momentum parameter. This work extended the investigation of Roper et al. (1977) to smaller slot sizes. Ban et al. (1994) investigated flames established on circular burners with inner diameters of 0.15, 0.25, and 0.40 mm. The experiments worked to verify the predicted flame shapes of laminar flames for three fuels: ethane, ethylene and acetylene. The work found that buoyancy effects are negligible for small flames; nearly spherical flames were established that were unaltered by rotating the burner. An in depth analysis of a micro diffusion hydrogen flame was performed by Cheng et al. (2005); their numerical solution for species was compared with experimental data. It was found that buoyancy effects were insignificant. Nakamura et al. (2006) numerically studied methane micro diffusion flames on a circular burner of diameter less than 1 mm. They found that small flames have the same, nearly spherical structure as those in microgravity, citing weak buoyancy forces. Also, the existence of a minimum flame size necessary for combustion was predicted.

Lee et al. (2003) conducted leak rate experiments on micro-machined orifices of different sizes and shapes. They examined the differences in flowrates among square and elliptical slit orifices. In almost every case, the flow was choked in the orifice, which caused large underestimates in the flow using the helium signature test. Schefer et al. (2006) also presented equations to

calculate choked flow, as well as subsonic laminar and turbulent flows. They considered leaks owing to pressure-driven convection and permeation through metals.

Research has been conducted on hydrogen interface leakage in national pipe thread (NPT) fittings by Ge and Sutton (2006). They found that the best threaded fittings investigated leaked hydrogen with leak rates of 1 µg/s. Leak rates under non-ideal conditions were far higher. Ge and Sutton (2006) found that a larger tightening torque is not as important in sealing the threads as the Teflon material and properties. The tests were run at a pressure drop of 70 bar. They determined that two wraps of Teflon experiences had better performance than one wrap and the Swagelok™ anaerobic pipe thread sealant out performed the Teflon.

Compression fittings are typically used with gases at high pressure. Compression fittings are a reliable, easy to use method that allows fittings to be taken apart and attached with ease. A large benefit of using compression fittings over NPT fittings is the lack of Teflon tape that is necessary to prevent leakage. Any time an NPT fitting is taken apart, it must be cleaned and rewrapped before it can be used again.

Swagelok has made available product test reports that give information on the leakage of their fittings. Product test report (PTR) 396 shows for 144 samples of 6 and 12 mm fittings tested at 310 and 200 bar nitrogen, respectively, there were no detectable leaks found after 10 minutes. In PTR-865, the fittings were tested again at 512 and 312 bar nitrogen, respectively, and leaked less than one bubble per minute during the 10 minute test period. Leaks were detected by submerging the fittings under water and watching for bubbles. Using hydrogen instead of nitrogen would dramatically increase any leak rates.

### 2.1.2 Fittings

The compression fitting experiments were conducted using three types of leaky fittings of three different diameters. Each leaky fitting was made by attaching a steel tube to a Swagelok union and capping the other end of the union. The leaks occurred at the connection between the steel tube and the union. A sample leaky fitting can be seen in Fig. 2.1. Compression fittings with outside tube diameters of 3.16, 6.33 and 12.66 mm were used. The leaks were caused using three different methods: loosened, over-tightened, and scratched fittings. These methods were chosen as possible leak modes that compression fittings used in commercial applications would experience. All of the fittings used can be found in Table 2.1.

**Table 2.1. Leaky fittings used in compression fitting experiments**

Fitting Number	Tube Diameter		Description
	in	mm	
Fitting 8L	1/8	3.16	Correctly made, then loosened
Fitting 4L	1/4	6.33	Correctly made, then loosened
Fitting 4T	1/4	6.33	Correctly made, then over-tightened
Fitting 4S	1/4	6.33	Correctly made, then scratched
Fitting 2L	1/2	12.66	Correctly made, then loosened

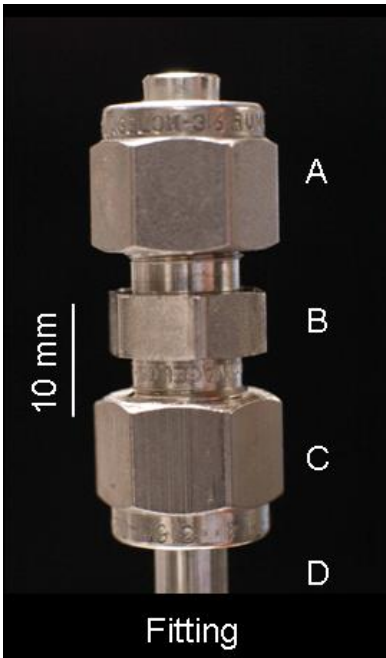


**Figure 2.1.** An example fitting assembly is shown. (A) Stainless steel plug for Swagelok tube fitting. (B) Swagelok union. (C) Swagelok nut. (D) Steel tube.

Figure 2.2 shows a cross-sectional view of a compression fitting. The steel tube, nut, fitting body and ferrules are shown. Leak paths seen in the experiments are shown with the dotted line. The leak travels from the tube exit, around the front and back ferrule, and exits between the nut and the tube. Leaks were not seen coming from threads of the compression fitting.

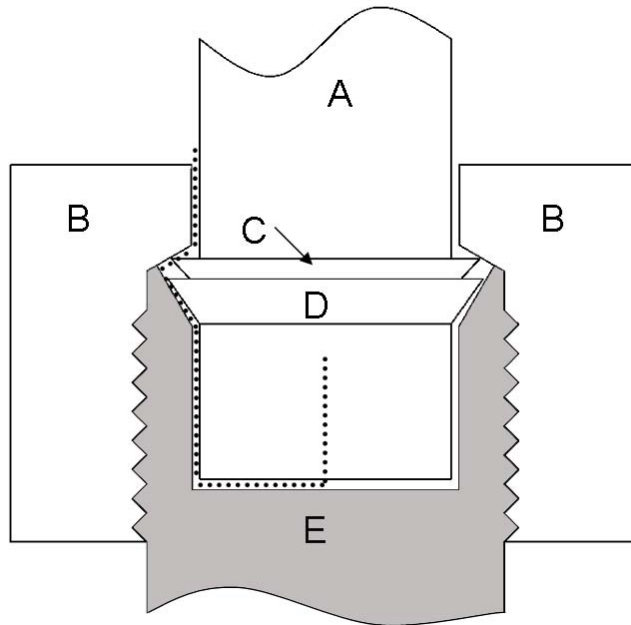


**Figure 2.2. Cross-sectional view of the fitting connection with proposed leak path. (A) Steel tube. (B) Swagelok nut. (C) Back ferrule. (D) Front ferrule. (E) Fitting body.**

### **Loosened Fittings**

This method simulates a fitting that has not been retightened properly and then pressurized. Each fitting was made using the manufacturer's directions and confirmed to be leak free at 6.89 bar (100 psi) using hydrogen. If no leaks were present, the fitting was then loosened until the ignition flowrate limit was found. This was done at several different pressures to show that there is no change in minimum flowrate necessary for combustion for different pressures.

### **Over-tightened Fittings**

This method simulates a fitting that has been over-tightened. Over-tightening damages the ferrule in the compression fitting, allowing leaks to occur. This method was done only for the 6.33 mm fitting. It is difficult to over tighten a 12.66 mm fitting as it is so large that a high torque is required. The fittings were made using the manufacturer's directions and confirmed to be leak free at 6.89 bar (100 psi) using hydrogen. The fitting between the steel tube and union was taken apart and then retightened to finger tight. The fitting was then tightened one full turn

(3/4 turn past manufacturer's instructions). The fitting was then taken apart again and tightened until the ignition flowrate limit was found for several different pressures.

### **Scratched**

This method simulates a ferrule being damaged by insertion into a fitting and was done only for the 6.33 mm fitting. The fittings were made using the manufacturer's directions and confirmed to be leak free at 6.89 bar (100 psi) using hydrogen. The ferrule on the steel tube was then scratched using a small triangular file. The fitting was then reassembled properly and the ignition flowrate limit was found by slowly tightening the fitting.

### ***2.1.3 Flow System***

Methane and propane were used in the experiments as well as hydrogen. Each test was completed using all three fuels so that comparisons could be made. Hydrogen, methane, and propane were tested in pressure ranges of 1-135 bar, 1-100 bar, and 1-7 bar, respectively. Propane could not be tested at pressures higher than 7 bar as this is its vapor pressure at room temperature.

The fuel flow system is shown in Fig. 2.3. For safety reasons, the flow was passed through a filter and relief valve to keep the downstream pressure below 6.89 bar in the event of any failure of the bottle pressure regulator. When experiments were done at pressures higher than this, the filter and relief valve were temporarily taken out of the system. The upstream pressure was controlled by a pressure regulator located just before the leaky fitting.

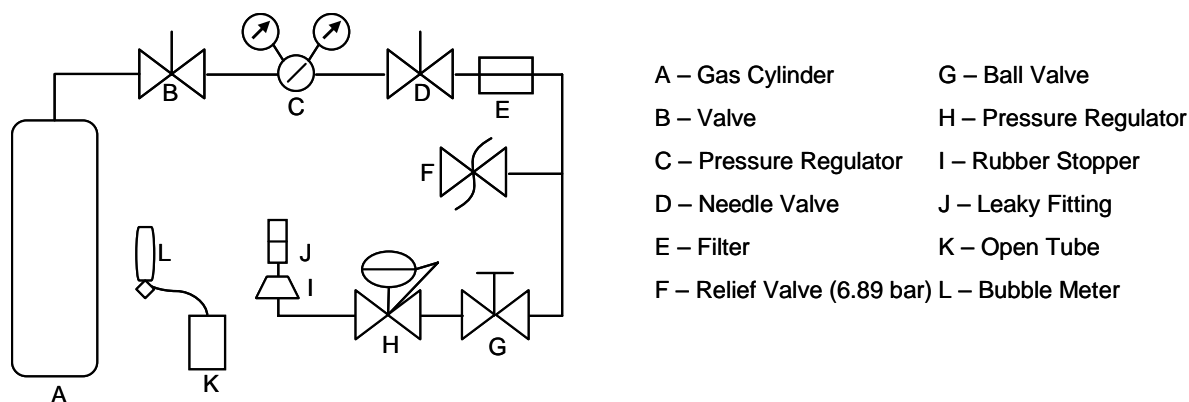


**Figure 2.3. Experimental setup of flow system.**

### **2.1.4 Lab Safety**

Fire safety is one of the primary concerns with the use of hydrogen. Methane and propane exhibit many normal characteristics of hydrocarbon flames, such as high radiant energy and brightly visible flames. Hydrogen on the other hand does not have these characteristics. Larger hydrogen flames can be seen in a dim room but flames near the quenching limit are not visible even in a darkened room. Due to this, the following methods of flame detection were compiled to allow for safe flame detection.

1. Hot Plume Check with Thermocouple: This is the safest method and the method that was primarily used during these experiments. A thermocouple is slowly inserted above the flame region to check for a change in temperature owing to the hot plume. This method allows the researcher to get close to the flame region without burning. At the quenching limits, temperature rises on the order of 15-50 °C were observed. A Fluke 179 with thermocouple probe was used to measure temperature. The thermocouple was a type K.
2. Thin Paper Check: This method involves slowly inserting a piece of paper into the flame region and looking for ignition. This method works better for larger flames as small

drafts can extinguish the smaller flames. Also, this method should not be used when combusting in a pure oxygen environment as any paper in the oxygen will burn violently.

As the automatic detection of hydrogen is difficult and there are no odorants available with hydrogen, it was important to frequently check for leaks in the system. Excess hydrogen buildup in an enclosed space can lead to an explosion. To prevent this, the lab was well ventilated so that any hydrogen buildup would have been difficult. Also the flowrates used during the experiments were so small that a potential explosive buildup was very unlikely.

### ***2.1.5 Procedures***

A Nikon D100 camera with a 50 mm lens was used to photograph the different experiments. In most cases, extender rings were used to allow closer photographs of the experiments. The camera was connected to a computer and controlled using the Nikon capture control software. This allowed many camera settings to be controlled on the computer and direct transfer of pictures from the camera.

Before each test, the system was pressurized and tested for leaks. This was done by squirting a small amount of soap water on each fitting. If any bubbles were seen, the fitting was tightened until the leak stopped. The only exception to this was the fitting between the steel tube and union that was purposely made to leak. This detection method allowed for quick discovery of leaks as well as being an accurate detector of small leaks.

To determine the minimum pressure and flow necessary for a sustained flame, the fitting was tightened and the pressure was slowly raised until a flame occurred. The upstream pressure in the system was controlled by the pressure regulator located before the fitting. Ignition of the fuel was caused by a butane lighter held briefly to the fitting. It was considered to be a sustained

ignition if the flame lasted a minimum of 10 s. After a successful ignition of any flame, the steel tube and fitting were allowed to cool to room temperature before the next test was attempted. This kept the gas from being preheated in the fitting. Also, as the metal fitting heats, it expands, causing the leak path to shrink and changing the minimum flowrate. Allowing the fitting to cool between tests minimized these sources of error.

For each test, the fitting was imaged against a black background to make the flames more visible. Flames for the propane and methane tests were visible to the naked eye and ignition was determined visually. This was backed up by the use of a thermocouple to determine if a flame was present. The hydrogen flames were too small and dim to be seen by eye and therefore only the thermocouple was used to determine if a flame existed. The thermocouple was placed slightly off and above the flaming region so that it would not interfere with the flame. When the hydrogen gas ignited, an audible pop was heard that signaled ignition. In some cases however, the fuel ignited but the flame was immediately extinguished. Several fitting orientations were tested to see the effect fitting orientation had on the ignition flowrate limit. Flames were never observed inside the fitting owing to the quenching limits of each fuel. Each test was repeated to establish repeatability.

To measure the flowrate from the leaky fittings, an apparatus was built to capture the escaping gas. This can be seen in Fig. 2.4. An open tube was created that fit over the leaky fitting assembly and created an air tight seal that allowed the gas to be collected and sent to a bubble meter. All flames were extinguished and the fittings were allowed to cool before any flow measurements were taken. As the gas traveled to the bubble meter, it was bubbled through water to give the gas 100% relative humidity. This was done so that partial humidification in the bubble meter did not interfere with the results. A humidity adjustment of 2.645% was then made

when calculating the flowrate (Incropera, 2002). In the bubble meter, the time for the bubble to travel 10 cc was clocked and recorded.

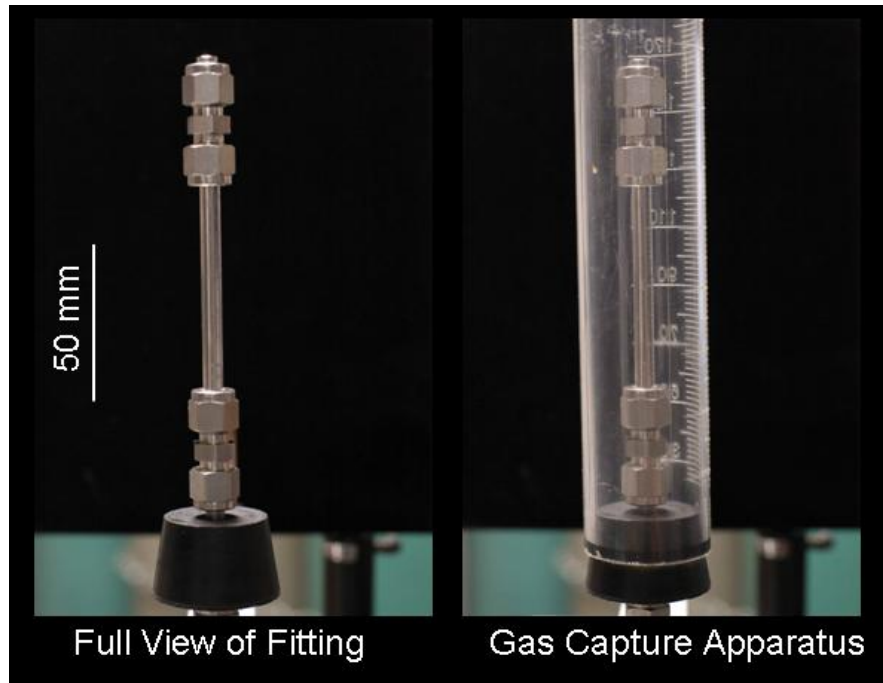


**Figure 2.4. The fitting assembly and the gas capture apparatus.**

Equation 2.1 shows the conversion of gas volumetric flow to mass flow.

$$M = 0.97355Q \frac{pMW}{R_u T} \quad (2.1)$$

where M is the mass flowrate, Q is the volumetric flowrate, p is ambient pressure, MW is fuel molecular weight,  $R_u$  is the universal gas constant, and T is ambient temperature. Measurements for the laboratory temperature and pressure were measured when tests were run. Ambient pressures were obtained online ([www.weather.com](http://www.weather.com)).

### **2.1.6 Sources of Error**

There is some uncertainty with each flow measurement. The volumetric flowrate was timed using a stopwatch. Most flows were small enough that being slightly off would not affect the measurement significantly. All flows were measured multiple times so that the results could be

averaged and uncertainty lowered.

One issue in the lab was the inability to control the airflow. The ventilation in the lab space caused air currents and it was not possible to close or turn off the air circulation system. A draft curtain was deployed around the experiment to try to minimize these air currents. These air currents were sometimes problematic when attempting to find the ignition limit flowrates. Care was taken to limit the air currents around the experiments but it is possible that lower ignition flowrates could be obtained in a more controlled environment.

## ***2.2 Results***

Figure 2.5 shows that the hydrogen flames at quenching are much smaller than the methane and propane flames. The hydrogen flames were also much dimmer than the other flames.

Figures 2.5, 2.6 and 2.7 show images of hydrogen, methane, and propane flames on leaky compression fittings in the vertical orientation for the different sized fittings. The images were recorded slightly above the quenching limits. The hydrogen flame is significantly smaller than the methane and propane flames in each figure. This is due to the smaller flowrate as hydrogen has a lower quenching limit. The quenching distance of hydrogen is approximately a quarter of the distance of methane and propane. This allows the flame to burn much closer to the metal. As the fitting size increases, it can be seen that the flame size also increases.

The flames were isolated to one side of the fitting where the most damage to the ferrule occurred. This is most evident in the hydrogen photo as the flame is much smaller. The photos below are from the loosened fittings. These flowrates were slightly larger than those from the scratched and over-tightened fittings. This could be seen from the increased flowrate in Fig. 2.12.

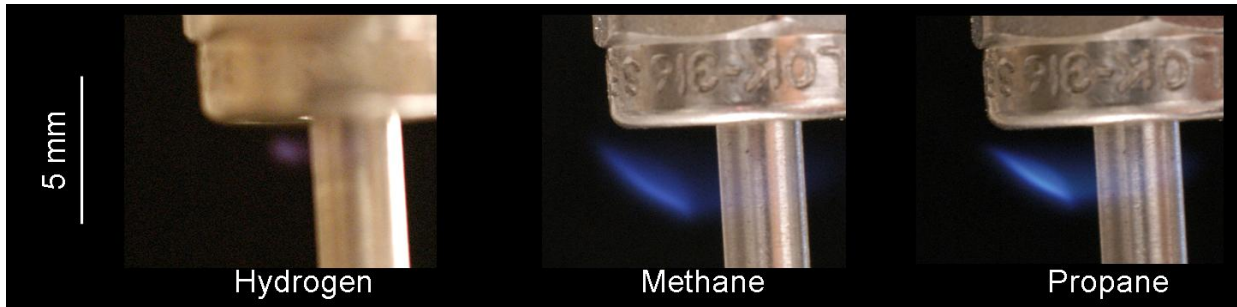


**Figure 2.5.** Color images of Fitting 8L flames for each fuel. Each fuel is flowing at the minimum flowrate possible for ignition. The camera settings for hydrogen were 20 s, F1.4, ISO 1600. The camera settings for methane/propane were 1 s, F1.4, ISO 800.

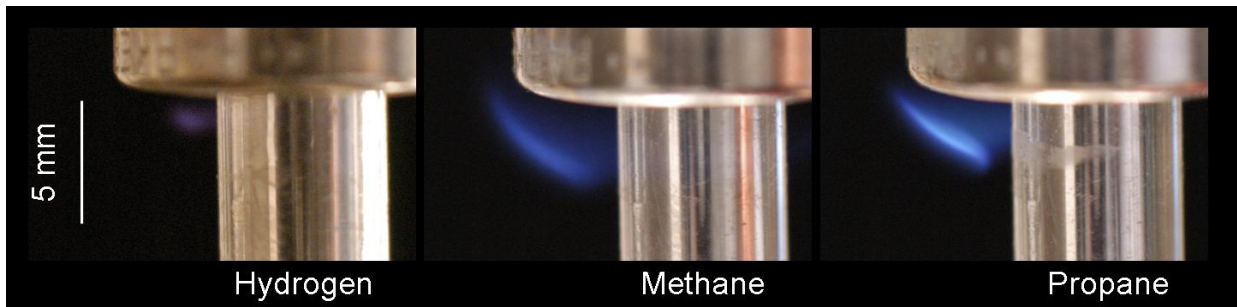


**Figure 2.6.** Color images of Fitting 4L flames for each fuel. Each fuel is flowing at the minimum flowrate possible for ignition. The camera settings for hydrogen were 20 s, F1.4, ISO 1600. The camera settings for methane/propane were 1/10 s, F1.4, ISO 800.

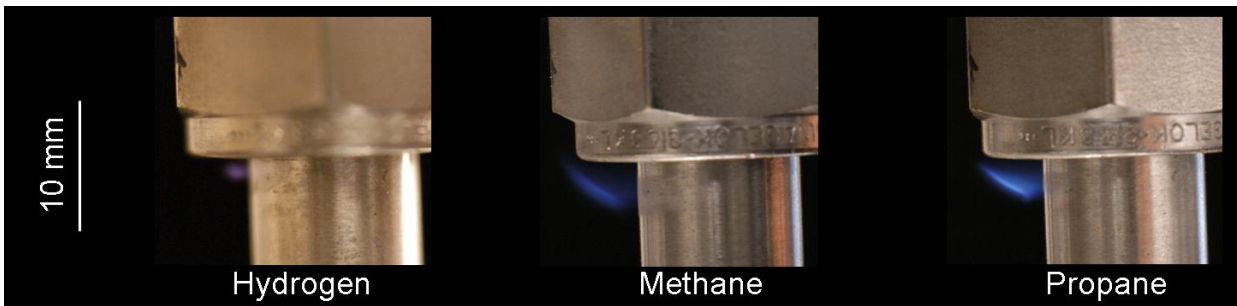


**Figure 2.7.** Color images of Fitting 2L flames for each fuel. Each fuel is flowing at the minimum flowrate possible for ignition. The camera settings for hydrogen were 20 s, F1.4, ISO 1600. The camera settings for methane/propane were 1/10 s, F1.4, ISO 800.

### 2.2.1 Ignition Flowrate Limits

Figure 2.8 shows the measured ignition flowrates for hydrogen, methane, and propane for the vertical orientation. The minimum flowrate necessary for sustained ignition is plotted versus pressure. For each fuel, the measurements at increased pressures are associated with an increase

in torque on the fitting. The upper limit on pressure for propane is lower than that of the other gases because the vapor pressure of propane at room temperature is 9.1 bar (142 psia).

Within experimental uncertainties, the ignition limits of Fig. 2.8 are independent of pressure for each fuel. This indicates that, as expected, at a fixed fuel mass flowrate the upstream pressure has little or no effect on the velocity profile of the jet entering the surrounding air. The mean hydrogen flowrate, 28  $\mu\text{g/s}$ , is about an order of magnitude lower than for the other fuels owing to its low quenching distance and low molecular weight. The mean methane and propane flowrate limits were 378 and 336  $\mu\text{g/s}$ , respectively. The quenching distance of hydrogen is approximately one fourth that of methane and propane and its molecular weight is an order of magnitude smaller than that of both propane and methane. This explains why the hydrogen flowrate is an order of magnitude smaller than that of both methane and propane. Butler et al. (2007, 2008) found the same behavior in their experiments using round burners. This is an important finding in that it shows that the upstream pressure does not play a role in the ignition flowrate limit.

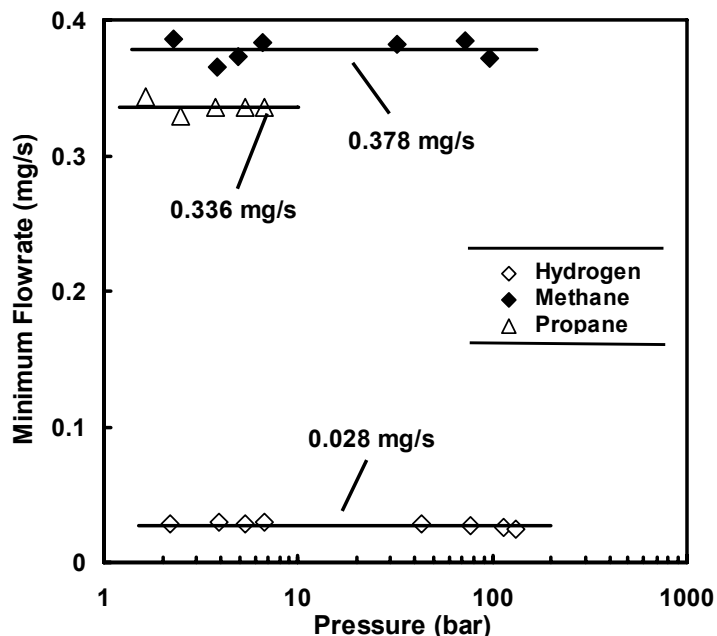


**Figure 2.8. Ignition mass flowrate limit versus upstream pressure in the vertical orientation.**

The measured ignition mass flowrates of Fig. 2.8 were converted to volumetric flowrates using the measured temperature and pressure of the laboratory that day. The resulting volumetric flowrates are plotted in Fig. 2.9 with respect to upstream pressure. Within experimental uncertainties, the minimum fuel volumetric flowrates of Fig. 2.9 are independent of pressure. Propane requires the lowest volumetric flowrate for ignition while methane requires the highest. The volumetric flowrates for hydrogen, methane and propane are 0.337, 0.581, and 0.187 mL/s, respectively. While hydrogen has the lowest mass flowrate necessary for ignition, propane has the lowest volumetric flowrate for ignition.

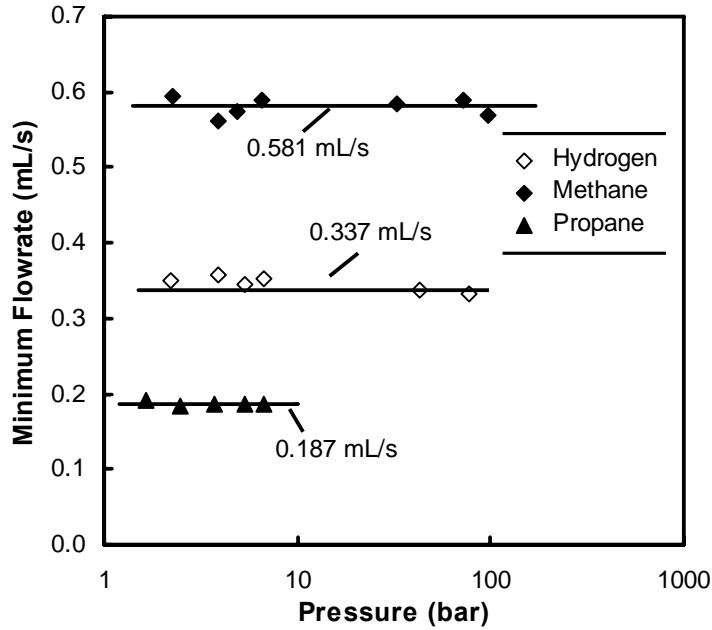


**Figure 2.9. Ignition volumetric flowrate limit versus upstream pressure in the vertical orientation.**

The pressure and flowrate measurements at the ignition limits can provide insight into the associated leak paths. For simplicity, it is assumed here that the leak paths are choked round orifices. Using equations from Munson et al. (2006) for isentropic compressible flow, the orifice areas and diameters were found. Equation (2.2) was used to find the static pressure  $P$  in the orifice, where  $P_0$  is the stagnation (upstream) pressure, and  $k$  is fuel specific heat ratio.

$$\frac{P}{P_0} = \left( \frac{2}{k+1} \right)^{\frac{k}{k-1}} \quad (2.2)$$

Equation (2.3) was used to find the static temperature in the orifice,  $T$ , where  $T_0$  is the stagnation (upstream) temperature. As there is a decrease in static pressure, there is a decrease in static temperature in the orifice. This static temperature was used to find the speed of sound,  $c$ , for the fuel using Eq. (2.4) where  $R_u$  is the universal gas constant and  $MW$  is the fuel molecular weight.

$$\frac{T}{T_0} = \frac{2}{k+1} \quad (2.3)$$

$$c = \sqrt{\frac{R_u T k}{MW}} \quad (2.4)$$

After finding the static pressure and temperature in the orifice, the density of the fuel,  $\rho$ , can be found using the ideal gas law using Eq. (2.5). The orifice area can be found from Eq. (2.6), where  $M$  is fuel mass flowrate at the ignition limit. The minimum and maximum calculated leak areas and leak diameters are given in Table 2.2.

$$\rho = \frac{PMW}{R_u T} \quad (2.5)$$

$$M = \rho c A \quad (2.6)$$

**Table 2.2. Round orifice diameters assuming choked flow**

Fuel	Upstream Pressure (Bar)	Speed of Sound (m/s)	Mass Flowrate (mg/s)	Leak Area ( $\mu\text{m}^2$ )	Leak Diameter ( $\mu\text{m}$ )
Hydrogen	344.7	1193.1	0.028	0.687	0.936
	4.14			57.3	8.54
Methane	206.8	416.4	0.378	5.81	2.72
	4.14			290.5	19.2
Propane	6.89	244.2	0.336	103.3	11.5
	4.14			172.1	14.8

Figure 2.10 shows a plot of leak diameter for the minimum ignition flowrate versus the upstream pressure assuming choked flow. The diameter of the leak decreases sharply with an increase in pressure. Hydrogen requires the smallest leak diameters to reach its minimum ignition flowrate while methane requires the largest leak diameter. The curves in Fig. 2.10 span the typical ranges of fuel pressures for vehicle tanks.

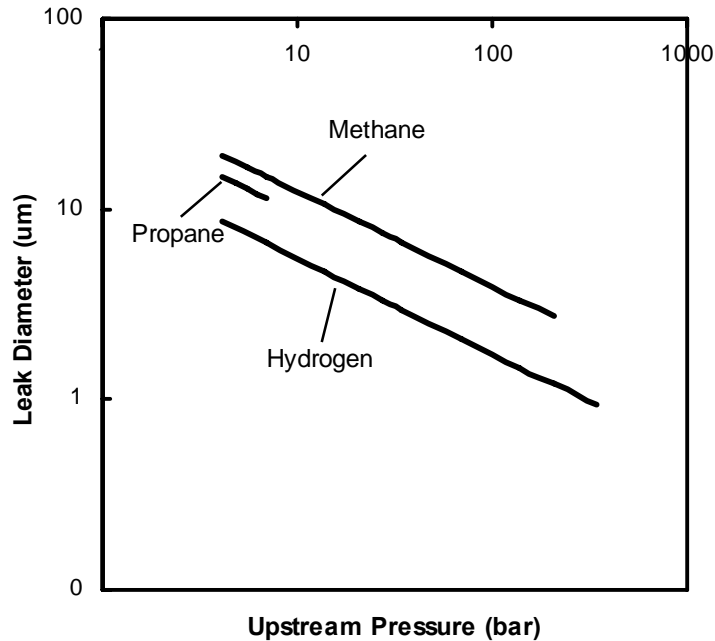


**Figure 2.10. Leak diameter for minimum ignition flowrate versus upstream pressure assuming choked flow.**

### ***2.2.2 Effects of Fitting Orientation***

Figure 2.11 shows the effect of fitting orientation on the ignition flowrate limit for Fitting 4L. The orientation of the leak does not have an effect on the flowrate of hydrogen owing to its lower quenching limit and ease of ignition. Fitting orientation did have an effect on propane and methane with the horizontal configuration requiring the highest flowrate and inverted orientation requiring the lowest. The inverted orientation required the lowest flowrate of each fuels as this kept the flame away from the fitting so that less heat was lost to the surrounding metal. The horizontal and vertical orientations gave a large surface to absorb the heat from the flame causing a larger flowrate to be necessary for sustained ignition. This can be seen in Fig. 2.5 where the flames are directly below the compression fitting and lose a significant portion of their energy through convection and radiation.

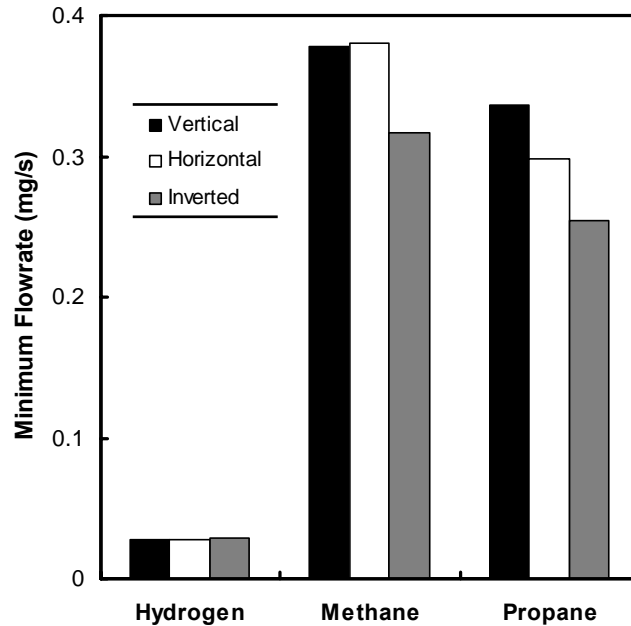


**Figure 2.11. Minimum flaming flow rate for Fitting 4L in vertical, horizontal and inverted orientations.**

### ***2.2.3 Effects of Leak Type***

Figure 2.12 shows the effect of the different leaky fittings on the ignition flowrate limits. The loosened fittings had the highest flowrate for ignition among the leakage configurations. The flowrates for the loosened fittings had a 26% higher flowrate than the over-tightened configuration. The flowrates for the over-tightened and scratched fittings were comparable for hydrogen. Only a slight difference was found and this is within the experimental uncertainties. Methane and propane followed the same trend with the loosened fitting having the highest flowrate and the scratched fitting having the lowest.

The trends for the methane and propane ignition flowrates are as expected. In the loosened fitting, there is no damage to the ferrule and therefore no easy leakage path for the gas. This means that the gas exits over a wider area surrounding the tube so that a larger flowrate is necessary to sustain the flame. The next higher flowrate was from the over-tightened fitting.

This method damages the ferrule, allowing for a small leak. This leak can spread before exiting the ferrule, making it more difficult to ignite. However, the damage is confined to a small area on the ferrule so that leak will not spread as much as the loosened fitting. The smallest flowrate came from the scratched fitting. The leak was caused by filing a straight path from one end of the ferrule to the other. This gave a very specific leak path for the gas to follow. As the gas exited the fitting in one location, it was less spread out than the other two configurations. This allowed for a smaller ignition flowrate limit. The less the gas spreads before exiting the fitting, the smaller the flowrate necessary for ignition.

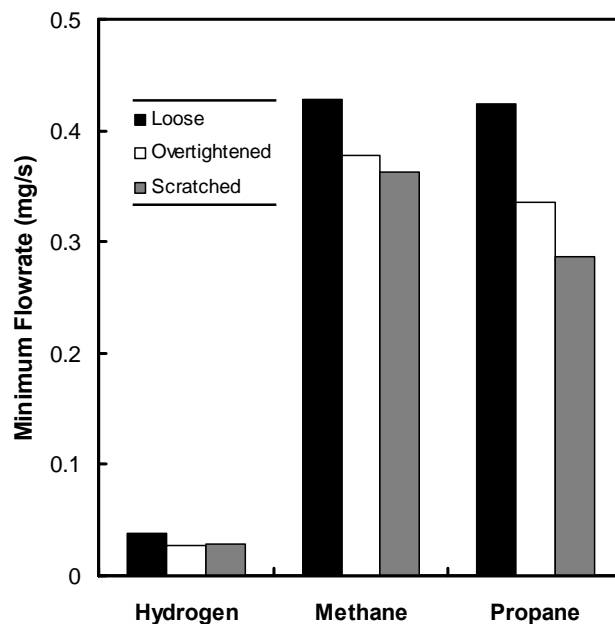


**Figure 2.12. Minimum flaming flowrate for each gas with different kinds of leaks.**

### ***2.2.4 Effects of Tube Diameter***

Figure 2.13 shows a comparison of flowrates against fitting size. The trends seen are as expected for each fuel. The smallest flowrate came from the smallest fitting while the largest flowrate came from the largest fitting. The leak types for each size fitting were the same so that the only difference was the fitting diameter. It can then be expected that the smaller fittings would need a

smaller flowrate for ignition as there is less surrounding metal to transfer heat away from the reaction. Each larger fitting size has four times as much surface area as the fitting below it allowing for more heat loss to the surroundings. For the most part, it is approximately a 20% increase in flowrate as the fitting size doubles. The only difference was a 50% increase in flowrate for hydrogen and propane when going from fitting 8L to 4L. Also, in the smaller fittings, the gas will leak in a smaller area allowing for a higher concentration of fuel. For the larger fittings, the gas has a larger leakage area, making for a smaller concentration of fuel.

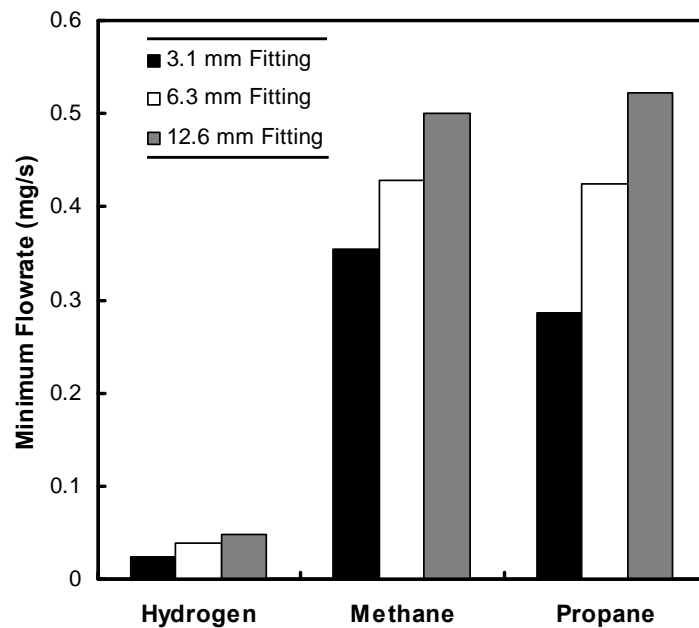


**Figure 2.13. Minimum flaming flowrate for each gas at differently sized compression fittings.**

Hydrogen flames in Fig. 2.14 are all similar regardless of the fitting size. The flowrates for each fitting diameter were similar in size and would correspond to flames of approximately the same size. The flames were not visible to the naked eye and an extended exposure at a high ISO was necessary to obtain a picture of them. Each flame is approximately 1.35 mm in diameter.

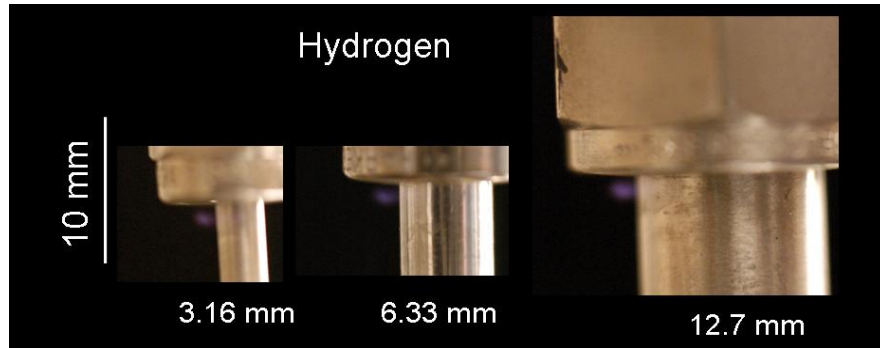


**Figure 2.14. Color images of hydrogen flames in vertical position for different sized fittings. Each flame is at its minimum flowrate. The camera settings are 20 s, F1.4, ISO 1600.**

In Fig. 2.15 and 2.16 the methane and propane flames are all approximately the same size even though Fig. 2.13 showed the flowrate increased with increasing fitting size. As the flame width and height are the same, there could be an increase in flame depth that is not readily visible through the image. The flowrates also are possibly not large enough that an increase in flame size would be visible. Each flame is approximately 3.85 mm wide and 3.85 mm from the flame tip to the base.

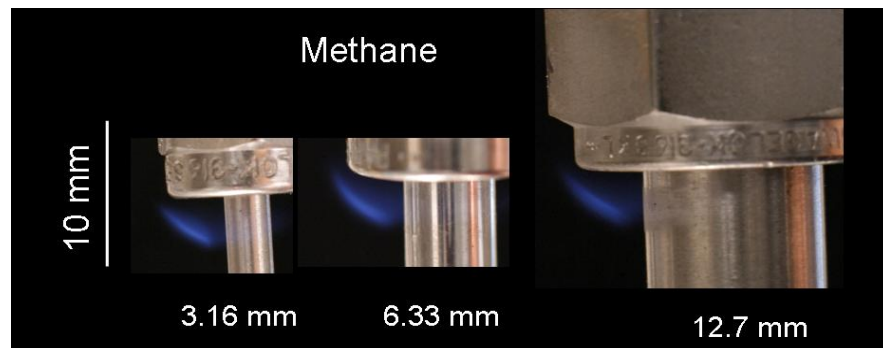


**Figure 2.15. Color images of methane flames in vertical position for different sized fittings. Each flame is at its minimum flowrate. The camera settings are 1/10 s, F1.4, ISO 800.**

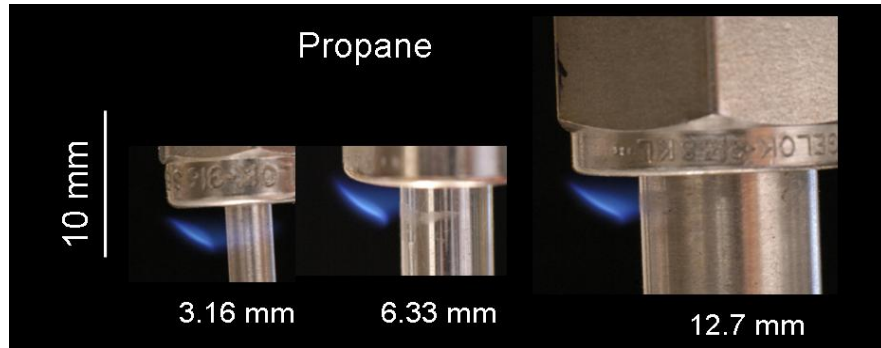


**Figure 2.16.** Color images of propane flames in vertical position for different sized fittings. Each flame is at its minimum flowrate. The camera settings are 1/10 s, F1.4, ISO 800.

## **Chapter 3: Weak Flames**

### ***3.1 Experimental Background and Procedure***

Weak flames have an important role in the field of micro-combustors. These weak flames hold the ability to replace electrical igniters. The ability to produce weak but stable flames can increase the turndown ratio of micro-combustors. The weak flames are also important in fundamental combustion models. If these simple flames can be modeled correctly, then the results can be expanded to the extinction behavior of larger, more complex flames.

#### ***3.1.1 Experimental Introduction***

Ronney et al. (1998) did experiments in microgravity using weak fuel pre-mixtures to produce flame balls. A flame ball is a steady, spherical flame in a premixed gas. Fuel and oxygen diffuse in while the combustion products and heat diffuse out. Ronney et al. (1998) found that the flame balls released 1.0-1.8 W per ball. Later, flame balls with energy releases as low as 0.5 W were recorded (Philips, 2003). At the time, they were the weakest flames ever recorded.

Butler et al. (2007, 2008) did experiments on curved wall, pinhole and tube burners measuring quenching flowrates. They found that the lowest flowrates occurred for tube burners and had a minimum for burners with an internal diameter of approximately 0.15 mm. They later showed that tube burners in an inverted configuration allowed for the smallest necessary flow to sustain combustion.

Hydrogen is being used in micro-electrical-mechanical systems (MEMS) that are found in many commercial applications. Hydrogen is the fuel of choice for these systems owing to its high heating value, rapid rate of vaporization, fast diffusion velocity, short reaction time, and high flame speed (Yang et al., 2002). Yang et al. (2002) found that hydrogen fuels are 24 times more

powerful than state of the art lithium batteries of the same size. Hydrogen is also cheaper, provides a more constant voltage, has no memory effect and instant recharge capability (Yang et al., 2002). Zhang et al. (2006) also noted that the quenching distance of hydrogen is much shorter than that of hydrocarbons and the combustion of hydrogen is more stable than other fuels. Zhang et al. (2006) performed experiments where hydrogen was mixed with hydrocarbons to lower the quenching distance and increase the flame speed of the mixture. They found that hydrogen was able to ignite but that pure methane and ethane were not unless platinum was present. The main issues when working with micro-combustion are the thermal and radical quenching effects. The high surface-to-volume ratio of micro-combustion devices poses challenges to researchers (Chen et al., 2007). These issues can be reduced or eliminated by increasing the wall temperature or preventing heat losses to the wall (Fernandez-Pello, 2002).

As the increase of the surface-to-volume ratio of the combustor becomes a problem for gas-phase combustion, it begins to favor catalytic combustion. This reaction is typically slower than a gas-phase reaction and heat loss is still a problem, but the increase in surface area and lower temperatures of the catalytic reaction may allow easier implementation (Fernandez-Pello, 2002). These catalytic systems are typically easier to start, self-sustaining at leaner fuel/air ratios and can be designed with no moving parts (Federici et al., 2006).

### ***3.1.2 Burners***

Experiments were performed to attempt to observe the weakest flame observed to date. Tube burners were used as Butler et al. (2007, 2008) found that tube burners in the inverted position allowed for the smallest flowrates with sustained combustion. The three burners used during the experiment can be found in Table 3.1. Steel hypodermic tubes (Small Parts, Inc.) were obtained

with an inside diameter of 0.152 mm. Platinum hypodermic tubes (Goodfellow Cambridge Limited) were obtained with an inside diameter of 0.16 mm. Graphite/polyimide ferrules (Small Parts, Inc) were used to attach the steel and platinum tubes to a 3.16 mm Swagelok fitting. This allowed for easy switching of burners as well as leak-proof connections. Each burner was tested at 5.52 bar (80 psi) with hydrogen for leaks. The ferrules maximum operating pressure was 6.89 bar (100 psi). Soap water was placed along the connections to test for leaks.

Tests were run with an inverted burner (downward discharge) using air as an oxidizer as well as pure oxygen. Burner SS56 was used during these tests. It was important to determine the advantage of burning hydrogen in a pure oxygen environment over combustion in ambient air.

**Table 3.1. Tube burners used during smallest flame tests. The steel tubes were 152 mm in length and the platinum tube was 100 mm in length.**

Name	Material	ID (mm)	OD (mm)
SS56	Stainless Steel 304	0.559	1.57
SS15	Stainless Steel 316	0.152	0.305
PT16	Platinum (99.95% Pure)	0.16	0.4

### **3.1.3 Flow System**

As oxygen was found to allow smaller flames, it was primarily used as the oxidizer in the weak flame experiments. The oxygen used was 99.994% purity from Airgas. To provide a steady, laminar flow of oxygen to the flame, it was supplied through a coflow burner. Oxygen was run through a ceramic honeycomb in the coflow burner to make the flow laminar. Tests were run with oxygen flowing at several velocities from the coflow burner to determine the velocity that allowed for the minimum ignition and quenching limits. Velocities of 4.5, 9, and 18 cm/s were used. The base value of 9 cm/s was taken from the literature (Santoro, 1987) and then halved and doubled to find the most beneficial velocity.

To determine the velocity at which the air exited the coflow burner, the volumetric flowrate measured by a flowmeter was divided by the coflow burner area. The coflow burner had a diameter of 102 mm. The center of the coflow burner was hollow and can be used to flow fuel. It was capped off underneath and not used in these experiments. The top of the burner can be seen in Fig. 3.1. The oxygen flow created a pure oxygen atmosphere above the burner. The volumetric flowrates and corresponding oxygen velocities can be found in Table 3.2.

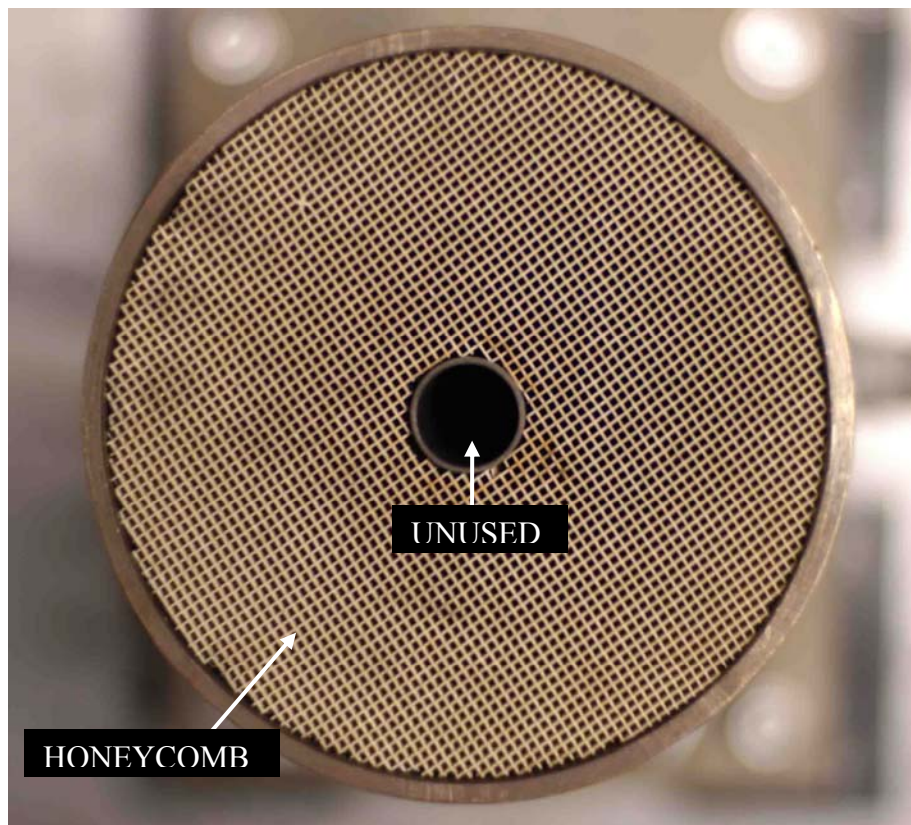


**Figure 3.1. Color image of top view of coflow burner. Internal diameter of the ceramic honeycomb is 102 mm and outside diameter of central tube is 16 mm.**

In addition to running tests at several different oxygen velocities, the burner height above the coflow burner was varied to determine the height that allowed for the smallest flowrate. Each height measurement was made at each oxygen velocity so that a variety of values could be analyzed. Heights of 10, 20, and 30 mm above the coflow burner were measured.

**Table 3.2. Volumetric flowrates and corresponding exit velocities of oxygen.**

Volumetric Flowrate (m <sup>3</sup> /s)	Oxygen Flow Velocity (m/s)
3.59E-4	0.045
7.17E-4	0.09
1.43E-3	0.18

The hydrogen flow system (Fig. 3.2) for the smallest flame experiments was almost identical to the setup used in the compression fitting experiments. The main difference was that a very sensitive needle valve with very low flow coefficient was placed before the burner to allow fine changes in flow. This was critical with the small flowrates that were achieved. Experiments were run at 2.76 bar (40 psi) into the flow valve. The oxygen system (Fig. 3.3) ran from the pressure regulator on the tank, past a relief valve and through a flowmeter. The flowmeter was used to determine the velocity of the oxygen exiting the coflow burner. The flowmeter used was an Omega, model FL-2063-NV.

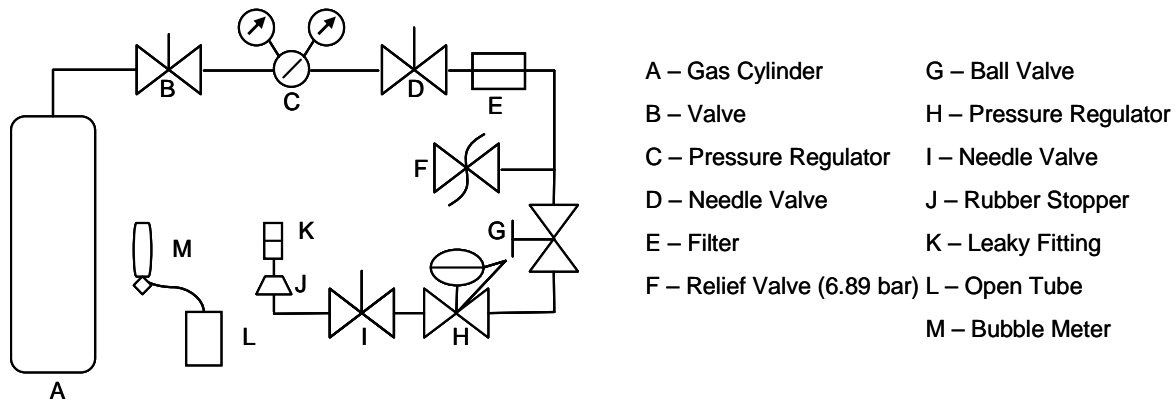


**Figure 3.2. Experimental setup of hydrogen flow system.**

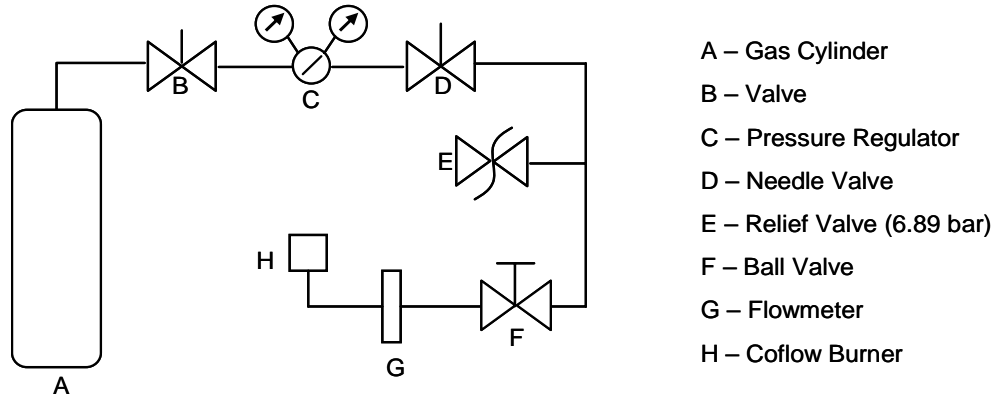


**Figure 3.3. Experimental setup of oxygen flow system.**

### **3.1.4 Procedures**

After the optimum height and coflow burner speeds were determined, tests were run using burners SS15 and PT16. Care had to be taken when igniting the flame with the butane lighter as the flame from the lighter could ignite the stainless steel in burner SS15 in the pure oxygen atmosphere. The hydrogen flames were too small for a pop to be heard upon ignition as in the compression fitting experiments. Ignition was determined by placing the thermocouple slightly to the side and above the burner and looking for a temperature rise. If flames were sustained for more than 10 s, the test was considered successful. The burners were photographed against a black background with the lights off for image contrast. Photographs were taken of the weak flames using the Nikon D100. Most pictures required extended exposure times.

The mass flowrate was found using the same method as the compression fitting experiments. The gas exiting the burner was captured and run through a bubble meter where the volumetric flowrate could be measured. Due to the extremely low flowrate, the gas was not bubbled through water on the way to the bubble meter as in the compression fitting experiments. The bubbling caused fluctuations in the measured volumetric flowrate. The power heat release rate was found by multiplying the hydrogen mass flowrate by the lower heating value. The lower

heating value was taken from literature as 119.9 kJ/g (Kanury, 1975).

It is expected that not all of the hydrogen flowing from the burner was combusted. This means that the power measured by using the mass flowrate could be higher than the actual heat release rate. However, as there was no means to verify this, the power measured is the power output as if all the hydrogen were converted to water. Tests were repeated to show repeatability.

### ***3.1.5 Sources of Error***

The weak flame experiments were also susceptible to similar errors as the compression fitting experiments concerning the airflow in the laboratory and timing of the volumetric flowrate. The airflow in the laboratory was not a problem for the experiments in the oxygen environment as the oxygen velocity negated the air currents. The airflow did still cause issues when combusting in the ambient air. These sources of error were controlled and minimized as much as possible as explained previously.

There are several potential sources of error during the experimental measuring of the gas flowrates. The humidity of the lab is one potential source of error affecting the minimum ignition and quenching flowrates of the fuels. It has been shown that that humidity has no significant influence on the minimum ignition energy on a hydrogen-air mixture (Ono et al., 2007), however this did not show the effect of humidity on ignition or quenching flowrate limits. When measuring the flowrate for the compression fitting experiments, the gas was bubbled through water so that the humidity of the gas would not affect the volumetric flowrate measurement. This was not possible during the weak flame experiments as it caused too many fluctuations during the measurement.

One issue that arose during the weak flame experiments was the ignition of the SS15 burners. Several burners caught fire during the experiments and had to be replaced. This occurred while

trying to ignite the hydrogen exiting the burner in the pure oxygen environment. This was not a problem when the burner was first introduced to the pure oxygen environment, but only after extended periods of time in the oxygen. Ignition of the fuel occurred by a butane lighter, which burns much hotter when it enters the pure oxygen atmosphere. If the lighter was brought too close to the burner, there were instances where the burner ignited and was not extinguished until both the hydrogen and oxygen flows were stopped. There were also several cases where the burner would glow as if from the hydrogen combustion heating but would continue even after the hydrogen flow was stopped. This made finding the ignition and quenching flowrate limits difficult as it was not known whether only a flame existed or a flame with the metal reaction. It is possible that the quenching flowrate for the stainless steel burner was lower owing to a chemical reaction between the iron and oxygen. This would allow for a smaller hydrogen flowrate to be found than would occur without metal oxidation. To avoid this, anytime a measurement was taken, the flow was backed off afterwards to ensure that hydrogen combustion was the only reaction taking place. The best method to avoid this was to frequently replace the stainless steel burners. However, using the methods and tools available, it was impossible to tell whether the measurements were only due to the flame or a combination of the flame and metal oxidation on burner SS15. The platinum burner did not have this problem as it is a noble metal and does not oxidize.

### ***3.2 Results***

Data collected from the weak flame experiments was used to investigate the ignition and quenching limits of hydrogen in both air and oxygen. Hypodermic stainless steel and platinum tubes were used to observe the weakest flames in the world to date.

### 3.2.1 Ignition Flowrate Limits

The oxygen versus air experiments (done with burner SS56) showed that a smaller quenching flowrate can be obtained by flowing hydrogen into pure oxygen. It was found that combustion in pure oxygen gave a 30% reduction in the minimum mass flowrate compared to air. The hydrogen quenching limit in air was 5.64  $\mu\text{g/s}$  while in oxygen it was 3.97  $\mu\text{g/s}$ . This is expected as burning in pure oxygen results in higher flame temperatures, which raises the reaction rate. Table 3.3 shows the different ignition flowrate limits that were obtained at various burner heights and oxygen velocities. For each oxygen velocity, the highest mass flowrate corresponded to the highest burner height. This is likely due to air mixing in with the oxygen flow at this height, especially at the weakest oxygen velocity. Diluting the oxygen flow would increase the minimum fuel flowrate necessary for ignition.

**Table 3.3. Burner height and oxygen velocity versus ignition flowrate limits of hydrogen for Burner SS15.**

Burner Height (mm)	Mass Flowrate ( $\mu\text{g/s}$ )
Oxygen Velocity = 45 mm/s	
10	5.28
20	5.15
30	6.37
Oxygen Velocity = 90 mm/s	
10	5.18
20	5.05
30	5.33
Oxygen Velocity = 180 mm/s	
10	4.85
20	5.02
30	5.12

Figure 3.4 shows the ignition flowrate limits of hydrogen found in both oxygen and air. Also shown are the quenching limits of hydrogen in air found by Butler et al. (2007, 2008). As expected, the ignition flowrate limits of hydrogen in air are larger than the quenching limits found by Butler et al. (2007, 2008). A higher flowrate is necessary to have sustained ignition as there is less preheating of the burner. The minimum ignition flowrate in air was 4.67  $\mu\text{g/s}$  while

the quenching limit was 3.93  $\mu\text{g/s}$ . As Fig. 3.4 shows, a 16% higher flowrate is necessary to have sustained ignition than is needed at the quenching limit. The ignition flowrate limit of hydrogen in pure oxygen was lower than the hydrogen quenching limit in air. As the flame temperature is higher in oxygen, the reaction is faster allowing for the smaller flowrate. The minimum ignition flowrate in oxygen was 2.7  $\mu\text{g/s}$ . This is a 45% lower flowrate than the quenching limit in air and 73% lower than the ignition flowrate limit in air.

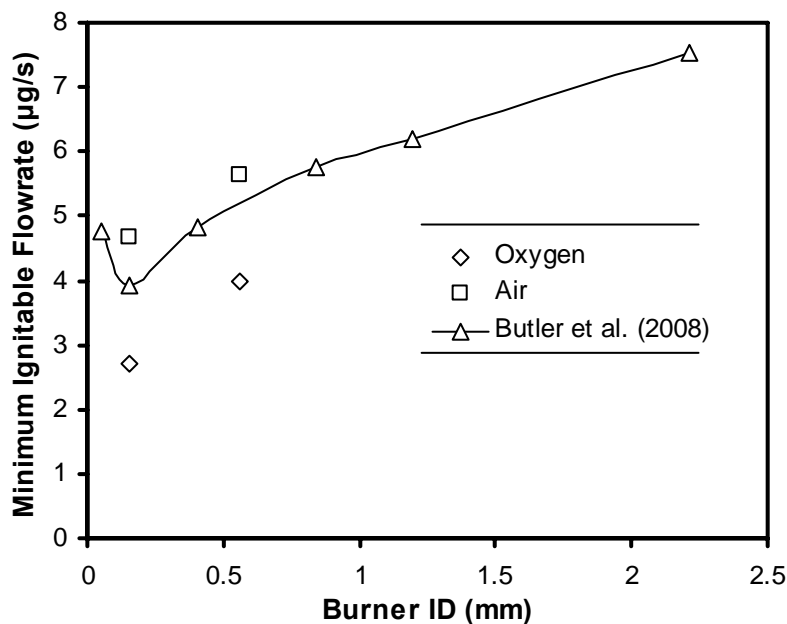


**Figure 3.4. Ignition flowrate limits of hydrogen in air and oxygen with burner in vertically downward position. Butler et al (2007, 2008) data is the quenching limit in air.**

### 3.2.2 Effects of Orientation on Ignition Flowrate Limits

Figure 3.5 shows the ignition flowrate limits in both oxygen and air for different tube burner orientations. The initial hypothesis was that the lowest flowrate would occur when the burner was facing upwards as there is less surrounding metal to take heat away from the reaction. However, when the burner is facing downwards, a portion of the heat is being used to preheat the unburned hydrogen. Thus this becomes a heat-recirculating burner, for which temperatures

exceeding the adiabatic flame temperature are possible. Raising the temperature of the hydrogen supply allows for a higher temperature in the flame and a faster reaction so that a smaller flowrate can be achieved. The horizontal configuration required the highest flowrate as it does not preheat the gas as effectively.

There is a difference between the flowrate trends necessary for sustained ignition in air and oxygen. The lowest flowrate for both comes in the downward orientation. However, the horizontal orientation has the highest flowrate for ignition in oxygen while the upward orientation has the highest flowrate for ignition in air. Butler et al. (2007, 2008) found that the horizontal configuration gave the highest quenching flowrate in air. As the ignition flowrate limit in oxygen follows this trend, it is likely that the higher minimum ignition flowrate for air in the upward orientation is due to error, although it is within the range of experimental uncertainty.

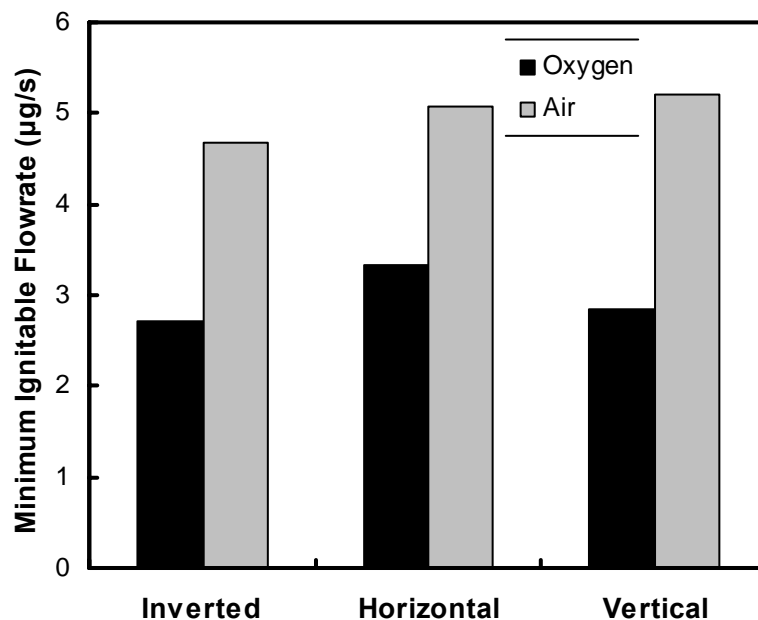


**Figure 3.5. Ignition flowrate limits of hydrogen in oxygen and air for different burner orientations.**

### 3.2.3 Quenching Flowrate

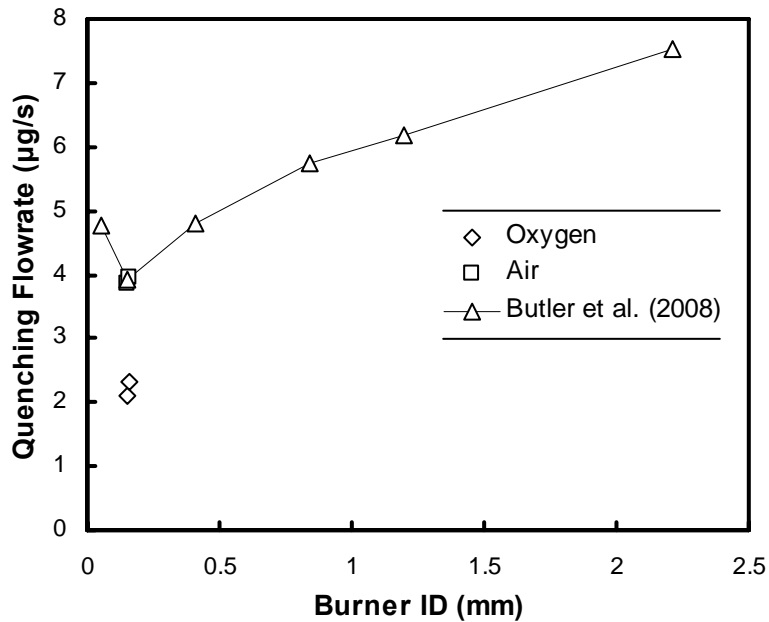
The quenching flowrates for burners SS15 and PT16 can be found in Table 3.4. These were the only two burners used when attempting to create the weakest, sustained flame. Butler et al. (2007, 2008) found that the lowest quenching flowrate came from tube burners in the downward configuration of approximately 0.15 mm internal diameter. From experimentation, minimum quenching flowrates of 2.1  $\mu\text{g/s}$  were found, which corresponds to a power output of 0.252 W.

Ronney et al. (1998) obtained a minimum power of approximately 1 W in his SOFBALL experiments, later achieving a power of 0.5 W (Phillips, 2003). These were done in a microgravity environment and recorded on video. Butler et al. (2007, 2008) found a minimum heat release rate of 0.55 W in his tube burner quenching experiments. It can be seen that the quenching limit in oxygen provided a flowrate approximately half that of Butler et al. (2007, 2008) found. This allowed for a heat release rate of 0.252 W, the weakest flame ever observed.

**Table 3.4. Hydrogen quenching flowrates in oxygen and corresponding power output.**

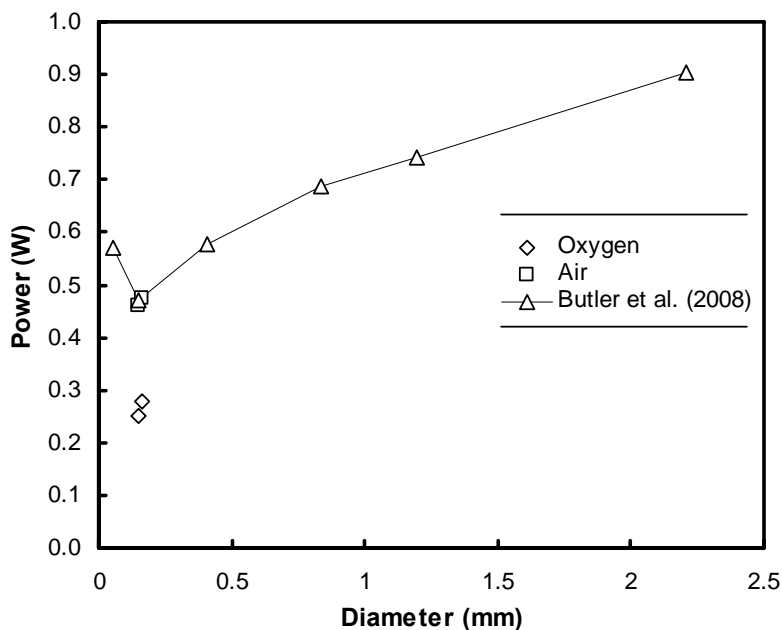
Burner	Quenching Flowrate ( $\mu\text{g/s}$ )	Power (W)
SS15	2.1	0.252
PT16	2.3	0.276

A slight difference in the measured flowrate for the platinum and stainless steel burner can be seen. Although there is an 8  $\mu\text{m}$  difference between the internal diameters of the burners, the main reason that different flowrates were found is attributed to the properties of the burners. Platinum and stainless steel 316 have thermal conductivities of 71.6 and 16.3 W/m-K, respectively (Incropera, 2002). Platinum transfers the heat away from the burner tip much better than stainless steel so that more heat is lost from the reaction region. There is a delicate balance between the combustion heating and the heat loss to the surroundings. If the heat loss is too great, the reaction rate will slow and the flame will extinguish.



**Figure 3.6. Quenching flowrates of hydrogen in air and oxygen with burner in vertically downward position. Butler et al (2007, 2008) data is quenching limit of air.**

Figure 3.6 shows the hydrogen quenching limits obtained in both air and oxygen. The data from Butler et al. (2007, 2008) is also plotted. The quenching flowrates in air were the same within experimental uncertainties as the Butler et al. (2007, 2008) data. Quenching flowrates of 3.85 and 3.94  $\mu\text{g/s}$  were found in air for burners SS15 and PT16, respectively. The hydrogen quenching flowrate in oxygen was much lower than that in air. This was expected as the previous data has shown that the minimum ignition and quenching flowrates are lower in oxygen than air. There was a 40-45% drop in quenching flowrate from air to oxygen.



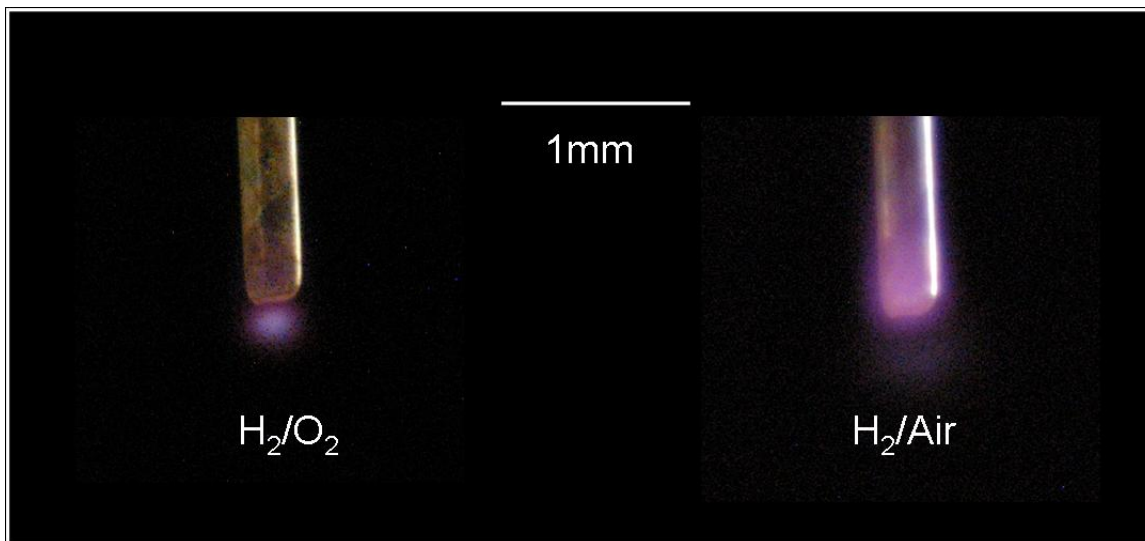
**Figure 3.7. Heat release rate in air and oxygen with burner in vertically downward position. Butler et al (2007, 2008) data is for air only.**

Figure 3.7 shows the effects of burner diameter on the heat release rate. The heat release rate is directly proportional to the mass flowrate from Fig. 3.6. Butler et al. (2007, 2008) showed that an increase in burner diameter causes the heat release rate to increase owing to an increase in quenching flowrate. A minimum in terms of flowrate and power occurs at an approximate internal diameter of 0.15 mm.

### ***3.2.4 Weakest Flame Ever Observed***

Representative quenching limit flames from burner SS15 can be seen in Fig. 3.8. These are images of the world's weakest observed flame to date. The flame diameter is approximately that of the burner for the  $H_2/O_2$  reaction. A faint outline of the flame for the  $H_2$ /air reaction is visible beneath the burner. It is difficult to maintain the flame at the quenching limit in the  $H_2$ /air reaction due to the air currents in the laboratory. The  $H_2/O_2$  reaction did not have this problem as the oxygen velocity negated any airflow currents. The glowing in the  $H_2$ /air reaction is

attributed to the higher flowrate exiting the burner.



**Figure 3.8. Color image of world's weakest flame using burner SS15 for hydrogen in oxygen (left) and air (right). The H<sub>2</sub>/O<sub>2</sub> flame has a power of 0.252 W while the H<sub>2</sub>/air flame has a power of 0.463 W. The camera settings were 30 s, F2.8, ISO 800.**

Flames from the burner PT16 are shown in Fig. 3.9. These were taken just before the quenching flowrate. The H<sub>2</sub>/O<sub>2</sub> flame is approximately the same size as the internal diameter of the platinum burner. The H<sub>2</sub>/air flame is slightly larger, which would correspond to the higher quenching flowrate. A slight glow can be seen coming off the burner from the H<sub>2</sub>/O<sub>2</sub> flame. This could be due to a surface reaction on the burner or the heating of the burner due to the flame.

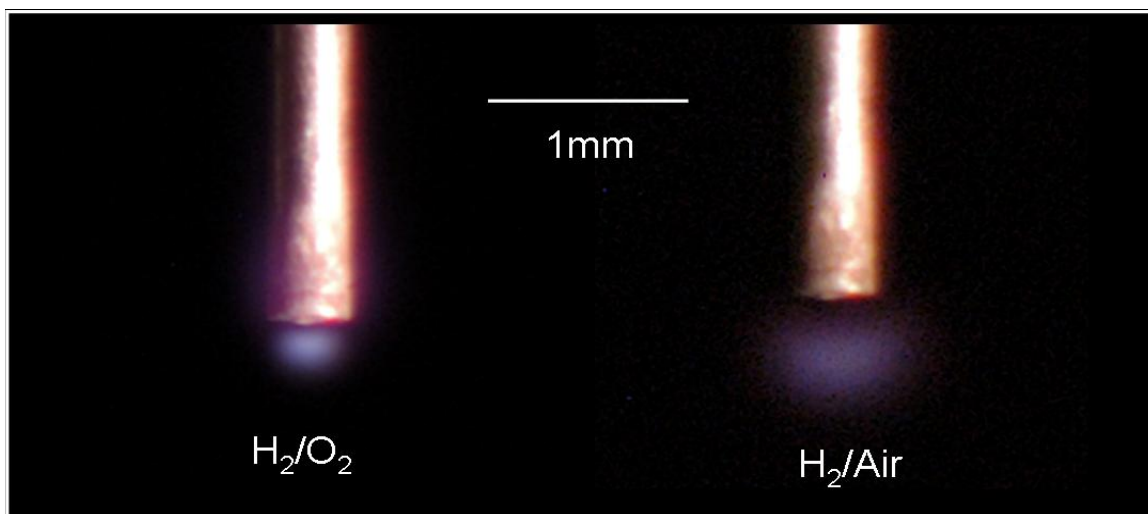


**Figure 3.9.** Color image of weak flame using burner PT16 for hydrogen in oxygen (left) and air (right). The H<sub>2</sub>/O<sub>2</sub> flame has a power of 0.276 W while the H<sub>2</sub>/air flame has a power of 0.474 W. The camera settings were 30 s, F1.4, ISO 200.

## **Chapter 4: Conclusions**

This was a study of the ignition and quenching flowrates of hydrogen flames from compression fittings and tube burners using both air and oxygen as oxidizers. Methane and propane were also used as fuels in the compression fitting experiments to give a scale to the hydrogen limits and find their ignition limits. This work is expected to be useful in the creation of hydrogen safety codes and in the field of micro-combustors.

### ***4.1 Compression Fittings***

The minimum flowrates necessary for igniting and sustaining hydrogen, methane, and propane flames on a leaky compression fitting is 0.028, 0.378, and 0.336 mg/s, respectively. This was due to hydrogen's lower molecular weight and smaller quenching distance. It was found that the ignition flowrate limit of each fuel was independent of upstream pressure for pressures of 1-100 bar (1-7 bar for propane).

The leaky fitting orientation has no statistically significant effect on the ignition flowrate limit of hydrogen. Burner orientation did play a significant role in the minimum flowrate for propane and methane. The lowest flowrate occurred with the burner in an inverted orientation and the highest flowrate with the burner in a vertical orientation. Orientation had an effect due to the amount of surrounding metal that the flames impinged upon. The less heat lost to the surroundings, the lower the flowrate was.

For each fuel, the leaky fitting with the scratched ferrule had the lowest flowrate necessary for sustained ignition. This burner had the straightest path for the fuel to flow before exiting the fitting, which allowed for smaller flowrates. The burners with the loosened fittings had the highest flowrate necessary for sustained ignition. There was a larger area for the fuel to spread

before exiting the fitting, which made for a higher flowrate to sustain ignition.

The ignition flowrate limit increased with increasing burner size. As the burners got larger, the flames impinged on a wider, thicker surface. As more heat was drawn from the flame, a higher flowrate was necessary for sustained ignition. Also, the flow was less concentrated at the fitting exit for the larger burners, which made for larger flowrates.

In every case, the hydrogen flames were too small and dim to see with the naked eye. Photos of the hydrogen flames required extended exposures at a high ISO. When the lighter was brought near the burner, a pop typically signaled that ignition of the hydrogen had occurred. The methane and propane limit flames were visible for every burner but did not omit a popping sound upon ignition.

Applying a soap water solution is an effective way to check for hydrogen leaks at fittings. Leak rates above the quenching limits produce visible bubbles in the solution.

#### ***4.2 Weak Flames***

The weakest flames were obtained when the burner height above the coflow burner was 10 mm with an oxygen velocity of 0.18 m/s. The optimal burner orientation was downwards. The ignition and quenching flowrates were lower in a pure oxygen environment than in air. As in the compression fitting experiments, the hydrogen flame was not visible to the naked eye and could only be seen using extended exposures with the camera.

This study led to the discovery of the weakest flames observed to date. The weakest flame ever recorded was found using a stainless steel burner with an internal diameter of 0.152 mm. A quenching flowrate of 2.1  $\mu\text{g/s}$  was found in a pure oxygen atmosphere. This corresponds to a power output of 0.252 W, half the size of the previous weakest observed flame. In comparison, a

birthday candle flame produces 50 W. The platinum burner with an internal diameter of 0.16 mm gave a quenching flowrate of 2.3  $\mu\text{g/s}$ , which corresponds to a power of 0.28 W. This is slightly higher than that found with the stainless steel burner and could be the result of a lack of surface reactions on the burner.

MEMS systems can benefit from these flames owing to the high turndown ratios and use of pilot flames. These flames have such low flowrates that they can be used as pilot flames, removing the need for electrical igniters. Using a weak hydrogen flame, especially in an oxygen atmosphere, would allow these systems to be made even smaller.

## Appendix A: Fuel Properties

Hydrogen	
Molecular Weight	2.016 g/mol
Lower Heating Value	119.9 MJ/kg
Spontaneous Ignition Temperature	571.1 °C
Maximum Flame Speed	291.19 cm/s
Quenching Distance	0.51 mm
Specific Heat Ratio	1.41
Methane	
Molecular Weight	16.04 g/mol
Lower Heating Value	50 MJ/kg
Spontaneous Ignition Temperature	632.2 °C
Maximum Flame Speed	37.71 cm/s
Quenching Distance	2.03 mm
Specific Heat Ratio	1.31
Propane	
Molecular Weight	44.096 g/mol
Lower Heating Value	46.3 MJ/kg
Spontaneous Ignition Temperature	504.4 °C
Maximum Flame Speed	42.89 cm/s
Quenching Distance	1.78 mm
Specific Heat Ratio	1.15

**Table A.1. Values obtained from Appendix C of SFPE Handbook (2002)**

## References

- Baker J., Calvert M.E., Murphy D.W. *Structure and dynamics of laminar jet micro-slot diffusion flames*. Journal of Heat Transfer 2002; 124:783-790.
- Ban H., Venkatesh S., Saito K. *Convection-diffusion controlled laminar micro flames*. Transactions of the ASME 1994;116:954-959.
- Bossel, U.B., Eliasson, B. *The Future of the Hydrogen Economy: Bright or Bleak?.* Proc. Of Fuel Cells World, Lucerne, Switzerland, July 2002.
- Bregeon B., Gordon A.S., and Williams, F.A. *Near-Limit Downward Propagation of Hydrogen and Methane Flames in Oxygen-Nitrogen Mixtures*. Combustion and Flame, 1978; 33:33-45.
- Burke S.P., Schuman T.E.W. *Diffusion flames*. Industrial and Engineering Chemical Research. 1928; 20:998-1004.
- Butler M.S., Axelbaum R.L., Moran C.W., Sunderland P.B. *Flame Quenching Limits of Hydrogen Diffusion Flames*, Eastern States Section of the Combustion Institute, Charlottesville, 2007.
- Butler M.S., Axelbaum R.L., Moran C.W., Sunderland P.B. *Flame Quenching Limits of Hydrogen Leaks*, SAE World Congress, Detroit, SAE Paper 2008-01-0726, 2008.
- Cadwallader L.C., Herring J.S. *Safety issues with hydrogen as a vehicle fuel*. Report INEEL/EXT-99-00522 prepared for U.S. Department of Energy 1999.
- Chao Y.C., Chen G.B., Hsu C.J., Leu T.S., Wu C.Y., Cheng T.S. *Operational characteristics of catalytic combustion in a platinum microtube*. Combustion Science and Technology, 2004; 176:1755-1777.
- Chen G.B., Chen C.P., Wu C.Y., Chao Y.C. *Effects of catalytic walls on hydrogen/air combustion inside a micro-tube*. Applied Catalysis A: General, 2007; 332:89-97.
- Cheng T.S., Chao Y-C., Wu C-Y., Li Y-H., Nakamura Y., Lee K-Y., Yuan T., Leu T.S. *Experimental and numerical investigation of microscale hydrogen diffusion flames*. Proceedings of the Combustion Institute, 2005; 30:2489-2497.
- Federici J.A., Norton D.G., Bruggemann T., Voit K.W., Wetzel E.D., Vlachos D.G. *Catalytic microcombustors with integrated thermoelectric elements for portable power production*. Journal of Power Sources, 2006; 161:1469-1478.
- Fernandez-Pello A.C. *Micropower generation using combustion: issues and approaches*. Proceedings of the Combustion Institute, 2002; 29:883-899.

- Ge X., Sutton W.H. *Analysis and test of compressed hydrogen interface leakage by commercial stainless steel (NPT) fittings*. SAE International, 2006:35-47.
- Incropera F.P., DeWitt D.P. *Fundamentals of Heat and Mass Transfer*. Hoboken, NJ: Wiley, 2002: 906-907.
- Jacobson A.S., Epstein A.H. *An informal survey of power MEMS*. The International Symposium on Micro-Mechanical Engineering, December 2003.
- Jouanne A., Husain I., Wallace A., Yokochi A. *Gone with the wind*. IEEE Industry Applications Magazine July/Aug 2005:12-19.
- Kanury A.M. *Introduction to Combustion Phenomena*. New York, NY: Gordon and Breach, 1975: 130-131.
- Lee I.D., Smith O.I., Karagozian A.R. *Hydrogen and helium leak rates from micromachined orifices*. AIAA Journal, 2003; 41(3):457-463.
- Lovins, A.B. *Twenty Hydrogen Myths, Final Report*. Rocky Mountain Institute Snowmass, CO, 2003.
- Marban G., Valdes-Solis T. *Towards the hydrogen economy?* International Journal of Hydrogen Energy 2007; 32:1625-1637.
- Matta L.M., Neumeier Y., Lemon B., Zinn B.T. *Characteristics of microscale diffusion flames*. Proceedings of the Combustion Institute, 2002; 29:933-938.
- Munson B.R., Young D.F., Okiishi T.H. *Fundamentals of Fluid Mechanics*. Hoboken, NJ: Wiley, 2006.
- Nakamura Y., Yamashita H., Saito K. *A numerical study on extinction behaviour of laminar micro-diffusion flames*. Combustion Theory and Modeling, 2006; 10(6):927-938.
- Ono R., Nifuku M., Fujiwara S., Horiguchi S., Oda T. *Minimum Ignition Energy of Hydrogen-Air Mixtures: Effects of Humidity and Spark Duration*. Journal of Electrostatics, 2007; 65(2):87-93.
- Peterson, R.B. *Small Packages*. Mechanical Engineering Magazine 2001.
- Phillips T. NASA, 2003. <[http://spaceresearch.nasa.gov/general\\_info/31jan\\_kelly\\_lite.html](http://spaceresearch.nasa.gov/general_info/31jan_kelly_lite.html)>
- Ronney P.D., Wu M.S., Pearlman H.G. *Structure of Flame Balls at Low Lewis-Number (SOFBALL): Preliminary Results from the STS-83 and STS-94 Space Flight Experiments*. Aerospace Sciences Meeting and Exhibit, Reno (1998).
- Ronney P.D., Wu M.S., Pearlman H.G. *Experimental study of flame balls in space: preliminary*

- results from STS-83. *AIAA Journal*, 1998; 36(8): 1361-1368.
- Roper F.G. *The prediction of laminar jet diffusion flame sizes: Part 1. Theoretical model.* *Combustion and Flame*, 1977; 29:219-226.
- Santoro R.J., Yeh T.T., Horvath J.J., Semerjian H.G. *The Transport and Growth of Soot Particles in Laminar Diffusion Flames.* *Combustion Science and Technology*, 1987; 53:89-115.
- Schefer R.W., Houf W.G., San Marchi C., Chernicoff W.P., Englom L. *Characterization of leaks from compressed hydrogen dispensing systems and related components.* *International Journal of Hydrogen Energy*, 2006; 31:1247-1260.
- Sherif S.A., Barbir F., Veziroglu T.N. *Wind energy and the hydrogen economy - review of the technology.* *Solar Energy*, 2005; 78:647-660.
- Swain M.R., Swain M.N. *A Comparison of H<sub>2</sub>, CH<sub>4</sub>, and C<sub>3</sub>H<sub>8</sub> Fuel Leakage in Residential Settings.* *International Journal of Hydrogen Energy*, 1992; 17:807-815.
- Takeo K., Okabayashi K., Kouchi A., Nonaka T., Hashiguchi K., Chitose K. *Dispersion and explosion field tests for 40 MPa pressurized hydrogen.* *International Journal of Hydrogen Energy*, 2007; 32(13):2144-2153.
- Turns, S.R., *An Introduction to Combustion.* McGraw-Hill, (2000).
- U.S. Department of Energy, Hydrogen Program, *Hydrogen and Our Energy Future*, DOE/EE-0320, U.S. Department of Energy 2007.
- Veziroglu T.N., Babir F. *Hydrogen: The Wonder Fuel.* *International Journal of Hydrogen Energy*, 1972; 17, 391-404.
- Yang W.M., Chou S.K., Shu C., Li Z.W., Xue H. *Combustion in micro-cylindrical combustors with and without a backward facing step.* *Applied Thermal Engineering*, 2002; 22:1777-1787 (2002).
- Yamawaki M., Nishihara T., Inagaki Y, Minato K., Oigawa H., Onuki K., Hino R., Ogawa M. *Application of nuclear energy for environmentally friendly hydrogen generation.* *International Journal of Hydrogen Energy*, 2007; 32:2719-2725.
- Zhang Y., Zhou J., Yang W., Liu M., Cen K.. *Effects of hydrogen addition on methane catalytic combustion in a microtube.* *International Journal of Hydrogen Energy*, 2006; 32:1286-1293.